Investigation of Drag Reduction in Turbulent Flow using Superhydrophobic Surfaces

Andrew Kenneth Baglin

School of Mechanical and Manufacturing Engineering

University of New South Wales

A thesis submitted for the degree of

Doctor of Philosophy

January 2016

THE UNIVERSITY OF NEW SOUTH WALES
Thesis/Dissertation Sheet

Surname or Family name: Baglin

First name: Andrew Other name/s: Kenneth

Abbreviation for degree as given in the University calendar: PhD

School: Mechanical and Manufacturing Engineering Faculty: Engineering

Title: Investigation of Drag Reduction in Turbulent Flow using Superhydrophobic Surfaces

Abstract 350 words maximum: (PLEASE TYPE)

Superhydrophobic surfaces have been shown to be able to reduce drag in laminar flows; however, in turbulent flows, the literature is divided with drag reductions between 0% and 70% being achieved. With frictional drag accounting for over half of the resistance of most ships, a method of decreasing drag would result in both significant fuel savings, and a reduction in carbon dioxide emissions. In order to ascertain whether these surfaces can provide a reduction in drag in turbulent flows, experimental and detailed computational fluid dynamics studies have been undertaken. As well as determining whether turbulent flow drag reduction is achievable, this work investigated both the mechanics and conditions under which the drag reduction occurs.

The experimental program was aimed to determine if drag reduction in high Reynolds number flows were achievable. As part of the research, a test rig was designed and constructed that allowed measurement of skin friction drag whilst minimising the effects of pressure drag. A hydrophobic surface was compared to a smooth plate across a range of turbulent flow Reynolds numbers with no noticeable drag reductions shown. Further investigations into the reasons for the lack of drag reduction were then achieved using computational fluid dynamics.

To accurately simulate the interactions between air and water at a scale where surface tension dominates, a lattice Boltzmann method was used. A code featuring methods which include fractional propagation, a novel technique of mesh refinement, a multiphase model and pseudo direct numerical simulation of turbulence has been devised and implemented. Validation across a range of benchmark tests was performed and the code proven to produce accurate results. An optimisation process was also undertaken to maximise efficiency.

This code was then used to simulate laminar, transitional and turbulent flows through a smooth walled channel, and over a series of roughened and hydrophobic surfaces.

The results of this research have confirmed that drag reductions in laminar and transitional flows are achievable; however, at Reynolds numbers greater than $Re_\tau = 390$, minimal benefit was found as the air layer against the surface was removed. The drag reduction effect has been shown to be dependent on the location of the free-surface, and the way in which it insulates the ridges and posts on the hydrophobic surface from the water.

FOR OFFICE USE ONLY Date of completion of requirements for Award:

ORIGINALITY STATEMENT

I hereby declare that this submission is my own work and to the best of my knowledge it contains no materials previously published or written by another person, or substantial proportions of material which have been accepted for the award of any other degree or diploma at UNSW or any other educational institution, except where due acknowledgment is made in the thesis. Any contribution made to the research by others, with whom I have worked at UNSW or elsewhere, is explicitly acknowledged in the thesis. I also declare that the intellectual content of this thesis is the product of my own work, except to the extent that assistance from others in the project's design and conception or in style, presentation and linguistic expression is acknowledged.

Signed: ..... Date: January 20, 2016

Publications

Journal Articles

- Baglin, A., Barber, T. & Rosengarten, G. (2014)
  Development of an effective FVLBM code for the study of turbulent and multiphase flows.
  Applied Mechanics and Materials, 553, 180-186, [3]

Conference Papers

- Baglin, A., Barber, T. & Rosengarten, G. (2013)
  Development of an effective FVLBM code for the study of turbulent and multiphase flows.
  Australian Conference on Computational Mechanics 2013
  University of Sydney
  Sydney, Australia

- Baglin, A., Barber, T. & Rosengarten, G. (2014)
  Investigation of turbulent flow over superhydrophobic surfaces using the lattice Boltzmann method.
  Discrete Simulation of Fluid Dynamics Conference 2014
  Ecole Normale Supèrieure
  Paris, France

Abstract

Superhydrophobic surfaces have been shown reduce drag in laminar flows; however, in turbulent flows, the literature is divided with drag reductions between 0% and 70% being achieved. With frictional drag accounting for over half of the resistance of most ships, a method of decreasing drag would result in both significant fuel savings, and a reduction in carbon dioxide emissions. In order to ascertain whether these surfaces can provide a reduction in drag in turbulent flows, experimental and detailed computational fluid dynamics studies have been undertaken. In addition to determining whether turbulent flow drag reduction is achievable, this work investigated both the mechanics and conditions under which the drag reduction occurs, and quantified the interaction between the hydrophobic surface and the turbulent multiphase flow.

The experimental program aimed to determine if drag reduction in high Reynolds number flows were achievable. As part of the research, a test rig was designed and constructed that allowed measurement of skin friction drag whilst minimising the effects of pressure drag. A hydrophobic surface was compared to a smooth plate across a range of turbulent flow Reynolds numbers with no noticeable drag reductions shown. Further investigations into the reasons for the lack of drag reduction were then achieved using computational fluid dynamics.

The lattice Boltzmann method was used to accurately simulate the interactions between air and water at a scale where surface tension dominates. A code featuring methods which include fractional propagation, a novel technique of mesh refinement, a multiphase model and pseudo direct numerical simulation of turbulence has been devised and implemented. Validation across a range of benchmark tests was performed and the code proven to produce accurate results. An optimisation process was also undertaken to maximise efficiency.

This code was then used to simulate laminar, transitional and turbulent flows through a smooth walled channel, and over a series of roughened and hydrophobic surfaces.

The results of this research have confirmed that drag reductions in laminar and transitional flows are achievable; however, at Reynolds numbers greater than $Re_\tau = 390$, minimal benefit was found because the air layer against the surface was removed. The drag reduction effect has been shown to be dependent on the location of the free-surface, and the way in which it insulates the ridges and posts on the hydrophobic surface from the water. The geometry of the surface has also been shown to have an effect on both the overall drag and the ability of the surface to maintain the insulating air layer.

Acknowledgements

With a project of this size, there are numerous people to whom I am indebted, as without their support and assistance I never would have made it this far:

Thank you to DSTO for providing partial funding of this work, particularly in regards to the experimental program.

The guys in the UNSW workshop, Ian Cassipi, Andy Higley & Rahda Pullambil. Thank you for building anything and everything I asked for, including all the time spent working on the ever changing experimental rig.

To Dr Alex Wu and his team at the Department of Chemistry, Melbourne University; thank you for preparing and applying the surface coatings, and the discussion that ensued before, during and after their use.

Thanks to my undergraduate helper monkeys, Sue-Ellen Jahshan and James Burgess. I hope you both had as much fun working with me as I did with you.

The team at the Cavitation Research Lab at AMC. A big thank you to Assoc. Prof. Paul Brander, Dr Bryce Pearce, and Rob Wrigley, for their assistance in the design of the experimental rig, and the hours they spent with me trying to make it all work the way it was supposed to. A special thanks to Rob, who had the arduous task of assembling all the components I sent him and getting it all to fit together.

To my friends and family, thank you for always being interested in what I have been doing, and supporting me in whatever ways you could. Whether it be intelligent conversation, a chance to relax, or just someone to listen to me rant about whatever was going wrong at the time, this would not have been possible without your help. Special thanks to my parents, who as well as proof reading this work,

were the ones who convinced me that I should take on this challenge in the first place. Thank you again for your love and support.

My co-supervisors, Assoc. Prof. Gary Rosengarten, and Phil Helmore. Gary, thank you for your assistance, especially in the area of superhydrophobic surfaces. Your knowledge and driving influence in this project allowed it to progress further than I sometimes thought it might. Phil, thank you for helping where ever you could. Although most of this work was vastly outside your areas of expertise, you were still able to assist whenever I required your help. Thank you both for your support and friendship.

My supervisor, Assoc. Prof. Tracie Barber. Tracie, thank you for your never failing support through both the ups and the downs. Whenever things seemed to fall apart you always managed to find a way that we could move forward. Your advice and optimism were always enormous encouragement, and without your help, this project would never have succeeded.

Last but definitely not least, Rosie Collins. Thank you for putting up with me doing this Phd, and all the stress, anxiety and frustration that it must have entailed. Thank you for your patience, support, and most importantly, love.

Contents

List of Figures

List of Tables

Nomenclature

δ	Channel Half Height
ν	Fluid Kinematic Viscosity
ρ	Fluid Density
τ_w	Wall Shear Stress
A	Atwood Number $((\rho_2 - \rho_1)/(\rho_2 + \rho_1))$
Eo	Eötvos Number $(\Delta\rho g L^2/\sigma)$
Re	Reynolds Number $(\rho U L/\mu)$
Re_ϕ	Reynolds Number based on Channel Diameter $(U_0 D/\nu)$
Re_τ	Friction Reynolds Number $(u^*\delta/\nu)$
u	Velocity
u^*	Friction Velocity
We	Weber Number $(\rho u^2 L/\sigma)$
δ_t	Lattice Time Step Length
δ_x	Lattice Unit Length
τ	Relaxation Parameter
c_s	Lattice Speed of Sound
f_i^{eq}	Fluid Equilibrium Probability Density Function

g_i	Phase Probability Density Function
g_i^{eq}	Phase Equilibrium Probability Density Function
lu	Lattice Length Unit
n	Mesh Refinement Level Parameter
p	Fluid Fractional Propagation Parameter
q	Phase Fractional Propagation Parameter
ts	Time Step
μ	Chemical Potential
ω	Wall Concentration Gradient Magnitude
σ	Surface Tension
θ_w	Wall Contact Angle
W	Interface Thickness
f_i	Fluid Probability Density Function

Chapter 1

Introduction and Overview

1.1 Motivation

There are currently an estimated 106,000 merchant ships comprising tankers, bulk carriers, container ships and general cargo ships steaming on the world's oceans [70]. Between them, they carry up to 90% of the world's cargo and have been shown to be the most efficient method of transporting goods around the planet. In order to do this, it is reported that these ships burn over 411 million tonnes of fuel annually, and with fuel prices currently at around $650 USD per tonne, this equates to an annual fuel bill of roughly $267 billion USD. Burning this much fuel also releases significant amounts of carbon dioxide (CO_2) into the atmosphere with reports stating that in 2007, carbon dioxide emissions totalling 870 million tonnes, or 2.7% of global emissions were produced by the marine shipping industry [67].

With the price of fuel still increasing, and the push towards lower emissions and greenhouse gas targets, the transport industry as a whole is trying to find more efficient ways of carrying cargo. Nowhere is this demonstrated more than in the maritime shipping industry. There are a number of methods of improving shipping efficiencies. These methods include improvements to the engines and drive trains, reducing the speed of the ships, or decreasing the resistance of the ships through hull optimisation or drag reduction techniques. Some drag reduction techniques that have been investigated include micro bubble injection [69], aqueous detergent solutions [98], superheating of the hull [131],

electrolysis [86], and various surface coatings [43], but none of these have been shown to provide both significant and commercial benefits.

A novel surface coating that has shown significant drag reducing abilities in laminar flow environments are super hydrophobic surfaces. These are surfaces that have a low affinity for water and as a result are extremely hard to wet. By coating the hull of a ship with these surfaces, it may be possible to substantially reduce the drag of the ship, and correspondingly, reduce both the fuel use and carbon emissions.

1.2 Introduction

To determine whether superhydrophobic surfaces can be beneficially applied to ships, they must be studied in the conditions they will experience on a ship's hull. As ships move through the water, the viscous flow around the hull is characterised by the Reynolds number. For an average sized cargo ship travelling at its normal operating speed, the Reynolds number (Re) can be of the order of 10^9, indicating that the flow is highly turbulent. If superhydrophobic surfaces are to provide a reduction of drag, it is clear that they must be able to do so in turbulent flow.

As will be presented in Chapter 2, super hydrophobic surfaces rely on micro or nano scale roughness on a hydrophobic surface. In order to properly analyse and investigate the details of flow over a surface with these micro structures, numerical simulation offers the most advantages. Simulations at this sub-micrometre scale are in the realm of mesoscopic physics, that is, in the range between the upper bounds of molecular dynamics, and the lower bounds of continuum mechanics. As a result, standard computational fluid dynamics (CFD) solvers are not really suitable for modelling this flow problem, and a different method needs to be used. First implemented in the late 1980s, the lattice Boltzmann method is a relatively new numerical method that can be used for simulating fluid flow. Instead of directly solving the Navier-Stokes equations, it instead solves a form of the Boltzmann transport equation. The fluid is modelled as a population of particles as opposed to a continuum, allowing extremely accurate control of the underlying physics. Although there are some lattice Boltzmann codes available, none of them have the ability to accurately model both turbulence and multiphase

flow over micro scale geometries. A code therefore needed to be designed and implemented so that this flow problem could be properly researched, a process which was undertaken throughout the course of this work.

This lattice Boltzmann code was then used to investigate both laminar and turbulent flows over a range of surfaces. These surfaces included micro features such as grooves and posts that were aligned in various arrangements. As well as subjecting each surface to both laminar and turbulent flow, each geometry was tested under two different flow conditions. The first of these conditions corresponded to a surface that was fully wetted, where only a single phase representing water was used. The second condition was then simulated which modelled both air and water phases to show the effect that the superhydrophobicity had on the drag reducing abilities of the surface.

A brief experimental study has also been completed to validate the results of the simulations. A test panel coated with a superhydrophobic surface was tested in high Reynolds number flows, with the results compared to an uncoated panel. In order to perform this study, an experimental rig was designed and constructed.

The results of this work enable a better understanding of the drag reducing abilities of superhydrophobic surfaces. With this knowledge, decisions can be made as to whether the application of these surfaces to ships is likely to yield beneficial results. In addition to the broad scale goal of showing viable drag reduction, this work will also serve to detail the processes that occur at the micro scale level which give rise to these macroscopic drag reductions.

1.3 Overview of Research

Full details of the research will be presented throughout the following chapters; however, a brief summary is first presented below:

- Chapter 2 introduces the present state-of-the-art position in both turbulent boundary layer control and superhydrophobic surface research. Both experimental and numerical research in this area is considered, and shows

the divide in opinion on whether superhydrophobic surfaces can adequately reduce drag in turbulent flow.

- Chapter 3 details the experiments undertaken to determine if turbulent drag reduction is attainable. This includes the design of the experimental rig, the tests undertaken, and the results found.

- Chapter 4 details the theory of the lattice Boltzmann method, and explains the extensions that were necessary in order to simulate turbulent multiphase flow at micro scales. Implementation and validation of the code are covered for a range of test cases including laminar and turbulent channel flows, bubble and droplet dynamics, and Rayleigh-Taylor instabilities.

- Chapter 5 covers the setup and initialisation of the main body of simulations for this research. This explains the details of the simulations undertaken with emphasis on the geometric and physical parameters for the system.

- Chapters 6, 7 and 8 present results of the simulations based on a minimisation in wetted surface area. Analysis and discussion explaining the results and the reasons for them are provided.

- Chapter 9 presents some additional results based on an analysis of the velocity profiles through the channels with differing walls. Results are based on the location of the peak velocity, and the centroid of the moment of area of the profiles. Also discussed are the Reynolds stresses measured over some of the surfaces.

- Chapter 10 presents the conclusions drawn from the research, and outlines potential directions for future work.

Chapter 2

Literature Review

2.1 General Fluid Principles

2.1.1 Boundary Layers

Although ships have been operating for thousands of years, it is only relatively recently that any scientific studies have been undertaken to investigate the resistance of a ship as it moves through the water. The first research in this area was performed by William Froude [45] in 1872 where he found that the drag on a ship could be considered in two mutually exclusive components, the frictional component, and what he referred to as the residuary component which is made up of both form or pressure drag and wave making drag. There is much work being done to minimize the drag from both of these components of resistance however only the frictional drag will be discussed in this review. To better understand the way that frictional drag works, the concept of a boundary layer, first proposed in 1904 by Prandtl [101] must be introduced. When there is fluid flow past a solid body there exists no relative motion of the fluid on the surface of the body. This then leads to the conclusion that there must be a region between the zero velocity at the surface and the free stream velocity of the flow. This region is referred to as the boundary layer, and is depicted in Figure 2.1.

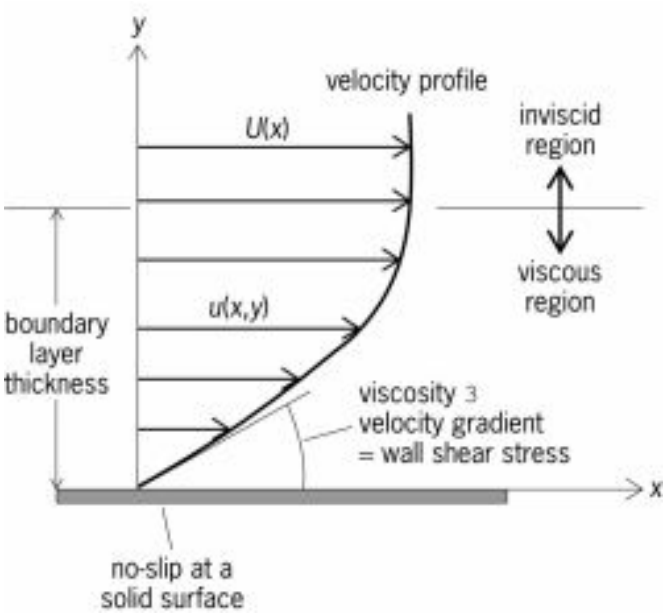

Figure 2.1: Velocity Profile in a Boundary Layer.[39]

The boundary layer can be divided into four main regions, the first of these being the laminar region. This is typically at the forward most point of the body where the fluid first comes into contact with the surface. The flow at this region has a profile typical of that seen in Figure 2.1, however as the flow moves further downstream, and the boundary layer thickness increases, the instability within this laminar flow also increases. The motion of the fluid then becomes more disturbed and leads to a breakdown of the laminar flow structure. This area of instability is referred to as the transition region. These breakdowns and instabilities grow quickly and a turbulent boundary layer develops. The flow within this turbulent region is difficult to predict and undergoes rapid fluctuations in velocity. However because of the condition that the flow at the surface of the body must be zero, the region close to the surface tends to retain a laminar profile. This laminar region is known as the viscous sublayer, in which the viscous forces still dominate. Each of these regions are depicted in Figure 2.2.

Frictional resistance, or shear drag as it will be referred to throughout this work, is due to the fluid exerting a shear stress on the wall. The wall shear stress, indicated by τ_w, is a function of the viscosity of the fluid (μ) and the rate at

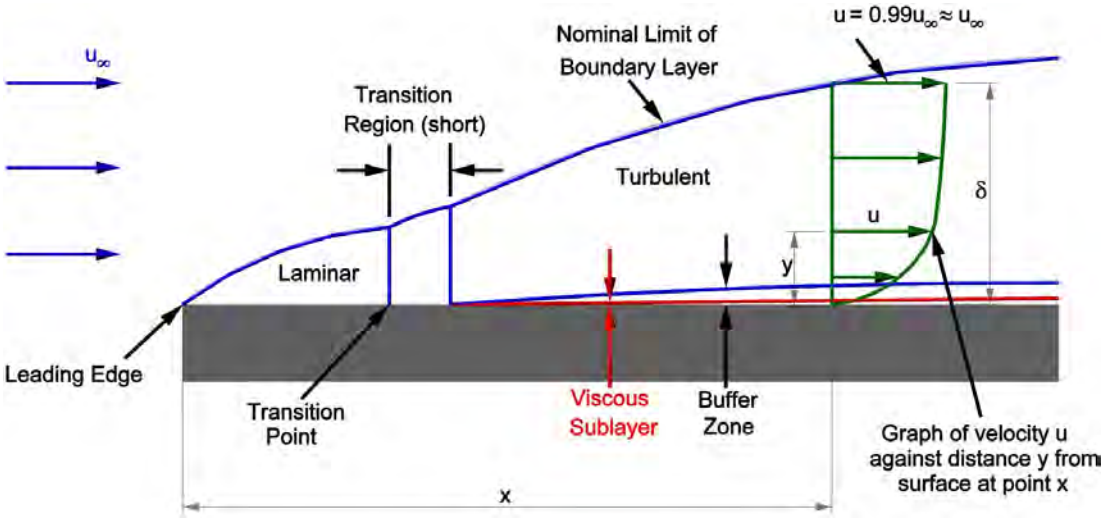

Figure 2.2: Regions of a Boundary Layer.[85]

which the fluid velocity (U) changes in respect of its distance from the wall (y). Combined, this results in the well known wall shear stress equation, shown as Equation 2.1.

$$\tau_w = \mu \frac{\partial U}{\partial y} \tag{2.1}$$

The significance of the frictional drag can easily be seen when we look at boats, specifically large ships such as container ships or oil tankers. Van Manen and Van Oossanen [132] reported that the frictional drag component could constitute between 80 and 85 percent of the total drag of a slow ship and up to 50 percent of high speed ships. Other work by Couser [28] shows values for high speed ferries with frictional drag in the order of 40 to 70 percent depending on the vessel's speed. A summary of findings can be seen in Figure 2.3 giving the breakdown between the frictional and the residuary resistance. In both cases, the vast majority of the total resistance is due to the frictional resistance so any reduction that can be made would be beneficial.

Various methods of drag reduction have been researched with two predominant approaches. The first approach is to delay the onset of the flows transition from laminar to turbulent, thereby reducing the drag by holding the flow in the laminar regime. A number of different approaches to this problem have been attempted which include both compliant walls (Kramer [74, 75],

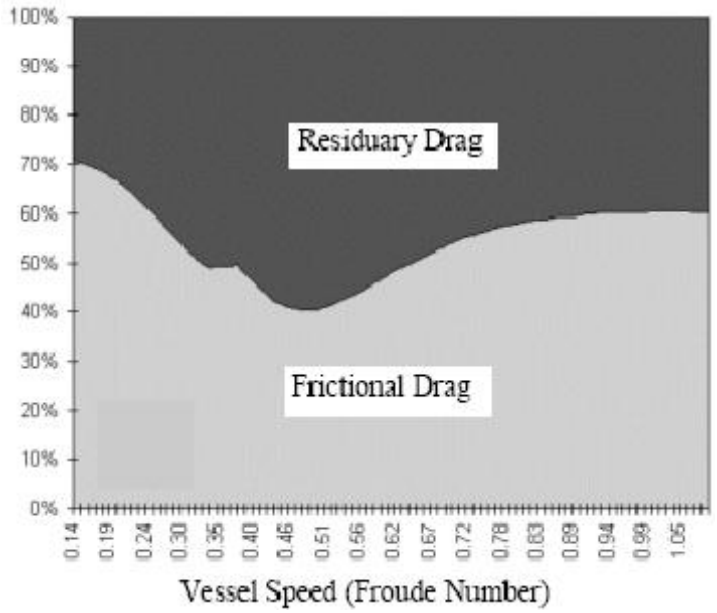

Figure 2.3: Percentage contributions of total drag of a typical high speed catamaran across it's speed range. (Couser [28])

Grosskreutz [49]) and heating and cooling of the surface (Reshotko [105]) with the aim of reducing the viscosity of the fluid near the wall resulting in a smaller wall shear stress and hence less drag.

The alternate approach is to try and control or minimize the drag associated with fully turbulent flow, which is what the present study aims to investigate.

2.1.2 Fluid Flow Equations

Before an analysis of a turbulent fluid dynamics problem can take place, the equations concerning the motion of fluids first need to be presented. There are four main equations that govern the way fluid flows. The first three of these are conservation equations (conservation of mass, conservation of momentum and conservation of energy) while the fourth is known as the Navier-Stokes equation. Each of these equations are shown and discussed below.

2.1.2.1 Conservation of Mass

Mass conservation is often described by the phrase *"Matter can neither be created nor destroyed."* When applied to fluid dynamics, a more approprate description is that *"The rate of increase of mass within a control volume equals the rate at which mass enters the control volume'.* If the flow through the surfaces of a control volume are calculated, the conservation of mass can be expressed as Equation 2.3.

$$\frac{\partial \rho}{\partial t} + \nabla \cdot (\rho \mathbf{u}) = \frac{\partial \rho}{\partial t} + \frac{\partial (\rho u)}{\partial x} + \frac{\partial (\rho v)}{\partial y} + \frac{\partial (\rho w)}{\partial z} = 0 \tag{2.2}$$

where ρ is the fluid density, and u, v and w are the velocity components in the x, y and z directions respectively. In the case of incompressible flows, where the density of the fluid is constant, this equation can be simplified to

$$\nabla \cdot \mathbf{u} = \frac{\partial u}{\partial x} + \frac{\partial v}{\partial y} + \frac{\partial w}{\partial z} = 0 \tag{2.3}$$

2.1.2.2 Conservation of Momentum

Conservation of momentum stems from Newton's Second Law ($F = ma$) which can be stated as *'The rate of change of the momentum of a fluid element is equal to the sum of all the forces acting on that element'.* Mathematically, this can be expressed as

$$\begin{aligned}
\rho \frac{Du}{Dt} &= -\frac{\partial P}{\partial x} + \frac{\partial \tau_{xx}}{\partial x} + \frac{\partial \tau_{yx}}{\partial y} + \frac{\partial \tau_{zx}}{\partial z} + \sum F_x \\
\rho \frac{Dv}{Dt} &= -\frac{\partial P}{\partial y} + \frac{\partial \tau_{xy}}{\partial x} + \frac{\partial \tau_{yy}}{\partial y} + \frac{\partial \tau_{zy}}{\partial z} + \sum F_y \\
\rho \frac{Dw}{Dt} &= -\frac{\partial P}{\partial z} + \frac{\partial \tau_{xz}}{\partial x} + \frac{\partial \tau_{yz}}{\partial y} + \frac{\partial \tau_{zz}}{\partial z} + \sum F_z
\end{aligned} \tag{2.4}$$

where the ∂P term represents the normal stresses due to the pressure acting on the fluid element and the τ terms represent the normal and tangential viscous stresses acting on the element. The additional forcing terms represent body forces which could be due to gravity, Coriolis effect and/or electro-magnetic forces.

2.1.2.3 Conservation of Energy

The conservation of energy equation is based on the First Law of Thermodynamics, and can be stated as *'The rate of change of energy in a fluid element equals the net rate of heat added to the element plus the net rate of work done on the element'*. The equation for this conservation rule is

$$\begin{aligned}\rho\frac{DE}{Dt} &= \nabla\cdot(k\cdot\nabla T) - (\nabla\cdot(\rho\mathbf{u})) \\ &+ \left[\frac{\partial(u\sigma_{xx})}{\partial x} + \frac{\partial(u\tau_{yx})}{\partial y} + \frac{\partial(u\tau_{zx})}{\partial z}\right. \\ &+ \frac{\partial(v\tau_{yx})}{\partial x} + \frac{\partial(v\sigma_{yy})}{\partial y} + \frac{\partial(v\tau_{yz})}{\partial z} \\ &+ \left.\frac{\partial(w\tau_{zx})}{\partial x} + \frac{\partial(w\tau_{yz})}{\partial y} + \frac{\partial(w\sigma_{zz})}{\partial z}\right] \\ &+ S_e\end{aligned} \tag{2.5}$$

where σ represents the sum of the pressure and normal viscous stresses and τ again represents the tangential viscous stresses, k is thermal conductivity, T is temperature and S_e is a term that includes energy other sources of energy (e.g. potential energy, heat from chemical reactions etc).

The energy equation will not be used in this work as the flows being investigated are considered to be incompressible isothermal flows. thus negating the need to specifically include this equation.

2.1.2.4 Navier-Stokes Equations

The Navier-Stokes equations are fundamental equations in fluid dynamics. Described here are the continuity and motion equations which are based on the mass and momentum conservation equations shown above. The motion equation is formed by expressing the viscous stress terms in the momentum equation as functions of the deformations. Linear deformations are represented by using an isotropic dynamic viscosity μ, while volumetric deformations are represented with a second viscosity $\lambda = -2/3\mu$. The stress tensor can then be written as

$$\tau = \begin{bmatrix} \tau_{xx} & \tau_{xy} & \tau_{xz} \\ \tau_{yx} & \tau_{yy} & \tau_{yz} \\ \tau_{zx} & \tau_{zy} & \tau_{zz} \end{bmatrix}$$

$$= \begin{bmatrix} 2\mu\frac{\partial u}{\partial x} - \frac{2}{3}\mu\left(\nabla\cdot\mathbf{u}\right) & \mu\left(\frac{\partial u}{\partial y} + \frac{\partial v}{\partial x}\right) & \mu\left(\frac{\partial u}{\partial z} + \frac{\partial w}{\partial x}\right) \\ \mu\left(\frac{\partial u}{\partial y} + \frac{\partial v}{\partial x}\right) & 2\mu\frac{\partial v}{\partial y} - \frac{2}{3}\mu\left(\nabla\cdot\mathbf{u}\right) & \mu\left(\frac{\partial v}{\partial z} + \frac{\partial w}{\partial y}\right) \\ \mu\left(\frac{\partial u}{\partial z} + \frac{\partial w}{\partial x}\right) & \mu\left(\frac{\partial v}{\partial z} + \frac{\partial w}{\partial y}\right) & 2\mu\frac{\partial w}{\partial z} - \frac{2}{3}\mu\left(\nabla\cdot\mathbf{u}\right) \end{bmatrix} \tag{2.6}$$

by inserting these terms into the momentum equation shown in Equation 2.4, simplifying, and using the relationship $\nu = \frac{\mu}{\rho}$, the Navier-Stokes motion equation is found.

$$\frac{\partial\rho}{\partial t} + \nabla\cdot\left(\rho\mathbf{u}\right) = 0 \qquad \text{Continuity Equation} \tag{2.7}$$

$$\rho\left(\frac{\partial\mathbf{u}}{\partial t} + \left(\mathbf{u}\cdot\nabla\right)\mathbf{u}\right) = -\nabla p - \nu\nabla^2\mathbf{u} + \frac{1}{3}\nu\nabla\left(\nabla\cdot\mathbf{u}\right) + \mathbf{F} \qquad \text{Motion Equation} \tag{2.8}$$

As can be seen, the continuity equation is identical to the conservation of mass equation shown as Equation 2.3. In incompressible flow, this equation ensures that the fluid flowing into and out of a control volume are equal. The terms in the momentum equation also have physical significance with the $\frac{\partial\mathbf{u}}{\partial t}$ term representing the local acceleration of the fluid. The $\left(\mathbf{u}\cdot\nabla\right)\mathbf{u}$ term gives the equation an advection term while the $\nu\nabla^2\mathbf{u}$ term contributes a diffusion term. Pressure gradient and body force terms are represented by the ∇P and $\mathbf{F}$ terms respectively.

Using these equations, the flow velocity at any point in space should in theory be able to be calculated, however in practice, especially in the regions of turbulent flow, the analytical solutions to these equations are far too complex to solve. This means that other methods of invoking and studying turbulence are needed.

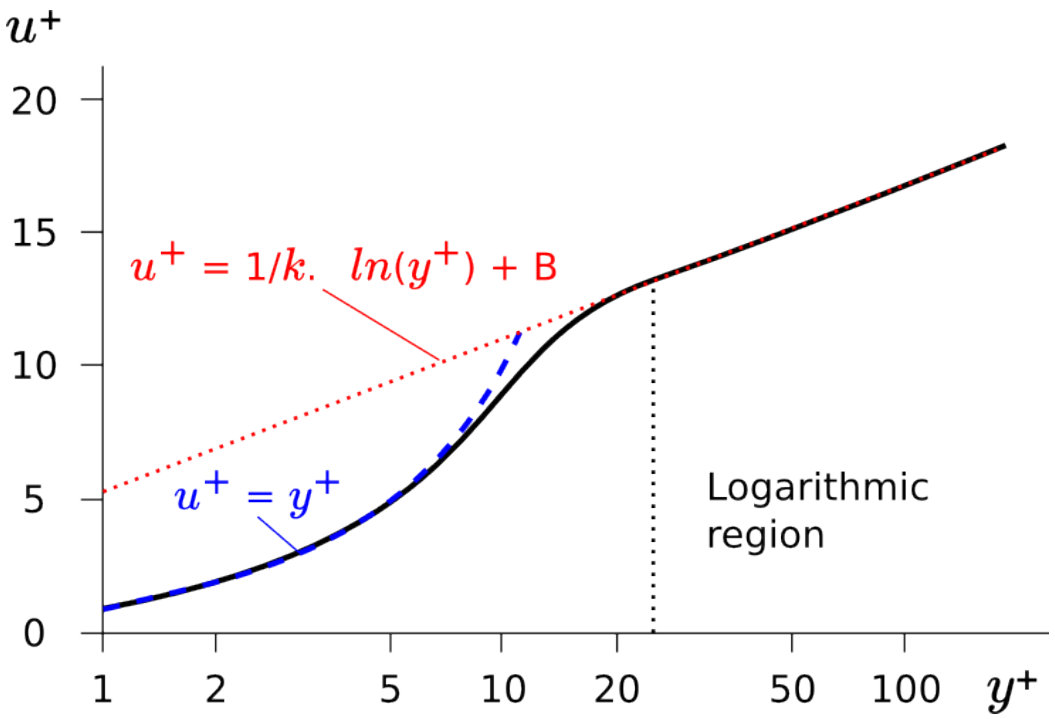

Figure 2.4: Comparison of experimental results (black line) with the Law of the Wall equations in fully developed turbulent flow over a flat plate. [30]

2.1.3 Turbulence

In order to understand how turbulent flows can be controlled, a brief overview of turbulence will first be undertaken. This section does not aim to be an all encompassing work on turbulence, but merely to introduce some of the concepts that will be frequently used within this work.

Reynolds [106, 107] established that turbulent flow could be classified by a single number known as the Reynolds number, the equation for which is shown as Equation 2.9. Reynolds also concluded that due to the random nature of turbulence there is little benefit in directly studying its details, and instead, a better approach is to view it in its separate mean and fluctuating components. This practice is still the primary way turbulence is viewed today.

$$Re = \frac{\rho U L}{\mu} \tag{2.9}$$

In 1922, Richardson presented the concept of energy cascades [108]. This was the understanding that turbulent flow is composed of eddies of various sizes

with the big eddies breaking down into smaller eddies, and so on until the eddies become small enough that viscous effects dissipate the remaining energy. Further advances were made by Von Kármán [135] who in 1930 published the law of the wall, a mathematical construct that closely approximates the velocity of fluid as it flows over a flat boundary as a function of its distance from that boundary. This can be seen diagramatically in Figure 2.4 with the black line showing the experimental values of the fluid velocity above the wall and the red and blue lines showing the analytical values making up the law of the wall. As was mentioned earlier, the near wall region of the turbulent boundary layer is known as the viscous sub-layer. This layer extends from the wall out to $y^+ = 5$, where y^+ is a non-dimensional wall distance found using $y^+ = \frac{u^* y}{\nu}$, and u^* is the wall friction velocity ($u^* = \sqrt{\frac{\tau_w}{\rho}}$). In this region, the velocity varies linearly with wall distance, which can be expressed as $u^+ = y^+$, where u^+ is a non-dimensional velocity ($u^+ = \frac{U}{u^*}$). Above $y^+ = 30$, the velocity profile follows the line published by Von Kármán, as shown in Equation 2.10.

$$u^+ = \frac{1}{\kappa}\, ln(y^+) \; + \beta \tag{2.10}$$

where κ and β have been experimentally determined as 0.4 and 5.0 respectively. The range of $5 \leqslant y^+ \leqslant 30$ between the linear region and the log region is known as the buffer or overlap region.

As can be seen with the work documented so far, the number of non-dimensional numbers used is quite high. This trend continues with some more key values being introduced, specifically, the wall shear Reynolds number. Where the original Reynolds number based on velocity and characteristic length was shown in Equation 2.9, a more commonly used version in the study of boundary layer flows is a version based on the wall shear velocity (u^*) and the a length scale of the boundary layer thickness (δ), and is shown as Equation 2.11. In a channel flow where the boundary layers overlap, δ represents thee half channel height.

$$Re_\tau = \frac{u^* \delta}{\nu} \tag{2.11}$$

With a basic understanding of the turbulent boundary layer, some methods of control are now presented.

2.1.4 Control of a Turbulent Boundary Layer

Previous research into the area of boundary layer control can be divided into two categories, passive control and active control. The most basic of the active control methods involves wall blowing and suction. As the name suggests, this involves either forcing fluid through the wall and into the flow (blowing), or removing fluid from the flow by sucking it back through openings in the wall (suction). This method was investigated by Choi, Moin and Kim [25] who in 1994 studied these methods using direct numerical simulations. They implemented a strategy whereby when the velocities in the boundary layer were directed towards the surface, blowing would be applied. Conversely, when the velocity of the near wall flow was directed away from the wall, suction was applied. They reported that theoretical drag reductions of up to 20% should be attainable; however, in 2007 Segawa *et. al.* [118] showed a value of only half this amount when they performed an experiment using blowing and suction in a water channel. A similar method of control is also possible using wall oscillations. Like blowing and suction, the boundary layer is manipulated by creating velocity disturbances in the flow. Choi and Clayton [26] demonstrated this method by introducing spanwise oscillations in a wind tunnel which lead to a frictional drag reduction of 45%. It was then proposed by Dhanak and Si [35] that this reduction was due to the destruction of low speed streaks, a flow structure inherent in turbulence.

Electro-hydro-dynamics (EHD) is another candidate for controlling turbulent boundary layers, as shown by the work of Roth [112, 113]. This method works by interacting an ion field with an electric field. The electric field accelerates the ions which then collide with fluid particles in the boundary layer. This is akin to applying a body force directly on the fluid. Roth generated an ion field on a flat plate in air using a method now known as the One Atmosphere Uniform Glow Discharge Plasma (OAUGDP). Although this method seems to be useful for boundary layers in air, as can be clearly seen in Figure 2.5, its applications in water are not as useful. This is due to the fact that the ions have less effect on the higher momentum fluid particles in water, as well as the ions achieving lower velocities travelling through the liquid than they do through the air.

Although EHD control in water seems to be unfeasible, water does have one distinct advantage, that is that it is an electrical conductor, albeit a weak

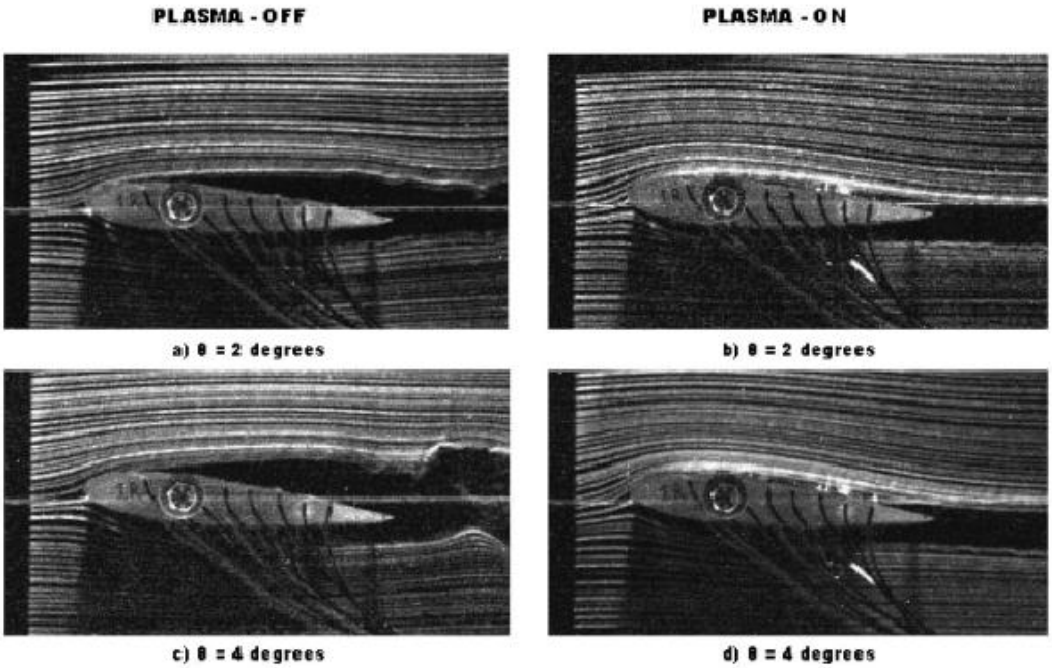

Figure 2.5: Boundary Layer control of air using One Atmosphere Uniform Glow Discharge Plasma (OAUGDP) over a foil. When turned on, the flow stays attached to the foil at higher angles of attack than it otherwise would. [113]

conductor. Magneto-hydro-dynamic (MHD) control attempts to benefit by this conductivity by passing a magnetic flux through the water and inducing an electric field. The interaction between the electric field and the magnetic field results in a force being applied to the fluid particles. A study by Lim, Choi and Kim [80] found that this method of control did indeed work if the conductivity of the fluid was high enough, however their testing was all performed on molten iron. Further work by Crawford and Karniadakis [29] revealed that for weakly conductive fluids, an external electric field as well as a magnetic field would need to be applied to get beneficial results. Studies on this method of control, dubbed as electro-magneto-hydro-dynamic (EMHD) have been proven to work, as shown by Bandyopadhyay [5], Berger *et. al.* [7] and Du *et. al.* [37], with drag reductions of up to 40% being shown possible. This reduction in drag however comes at the cost of the increased power usage to drive the system. Indeed, the power required to generate these drag reductions is an order of magnitude higher

than the reductions themselves. Techniques to increase this efficiency have been attempted (Spong [120]) however EMHD still appears not to be commercially viable.

The active control systems described above all require an input of energy to control the boundary layer. An alternative to this is to use passive control methods. Passive systems are far simpler than their active counterparts as they require no additional energy expenditure to operate. Possibly the simplest of the passive techniques are riblets.

Riblets are geometric features on the wall that can be a range of shapes and sizes of grooves, posts, or other three-dimensional forms. Early work studying riblets and their influence on turbulent boundary layers was completed by Walsh [138, 139] who studied two-dimensional grooves of several shapes including notched, sawtoothed and sinusoidal, as can be seen in Figure 2.6. Walsh was able to show drag reductions of up to 8% using these riblets, which were later applied to the 1987 winning America's Cup yacht. Shortly thereafter, riblets were prohibited on racing yachts by the International Yacht Racing Union.

DNS studies of turbulent flow over riblets have been performed by Choi *et. al.* [25], leading to the hypothesis that the drag reduction by riblets is produced by minimising the surface area with which the high speed flow can interact.

Experimental work by Berchert, Bruse and Hage [6] working with three dimensional riblets designed to mimic shark skin was undertaken, however did not offer the same levels of drag reduction as the two-dimensional riblets. Recent work by Dean [33] has detailed optimised riblet geometries akin to those of shark skin that have performed better than the original tests by Berchert. Dean has also hypothesised that the mucus on the skin of the sharks results in the skin being somewhat hydrophobic which in some way alters the flow over the skin.

A different method of surface geometry known as large eddy break up units (LEBUs) has also been tested. These are devices that extend into the flow and as the name suggests, break up the large turbulent flow structures. Unlike riblets, which only act across a small area of the boundary layer, the LEBUs are of the order of size of the boundary layer as can be seen in Figure 2.7. Hefner, Weinstein and Bushnell [58] found frictional drag reductions of the order of 24% using these devices, however the reduction in total resistance, that is frictional and pressure drag was negligible.

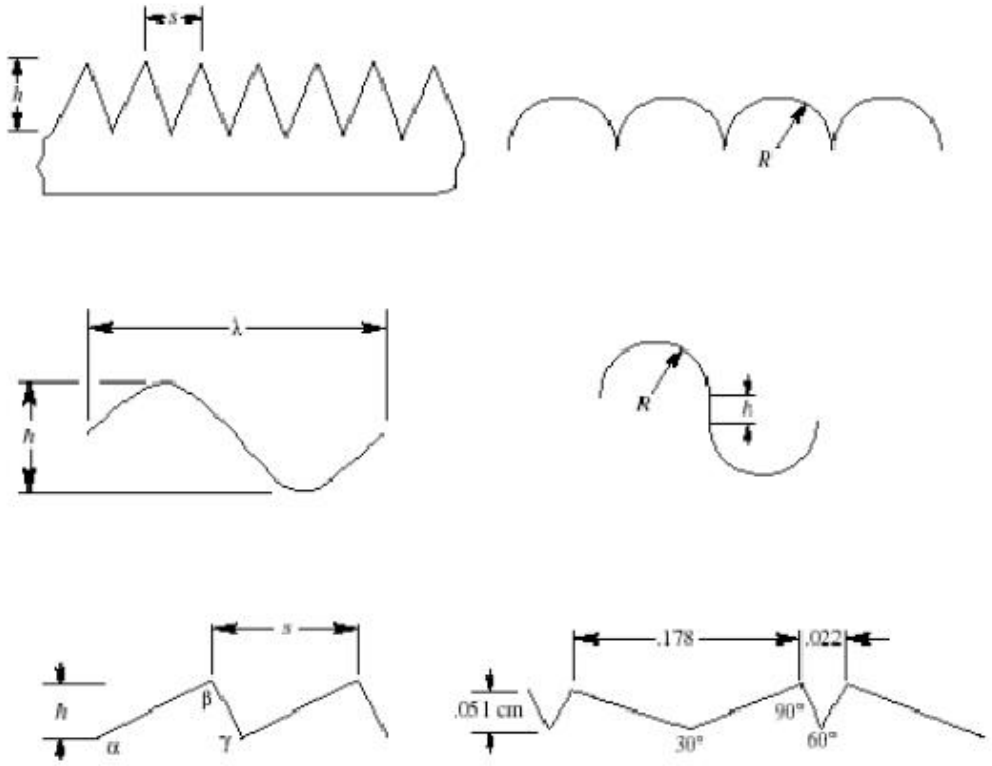

Figure 2.6: Two-dimensional riblet geometries studied by Walsh [138]

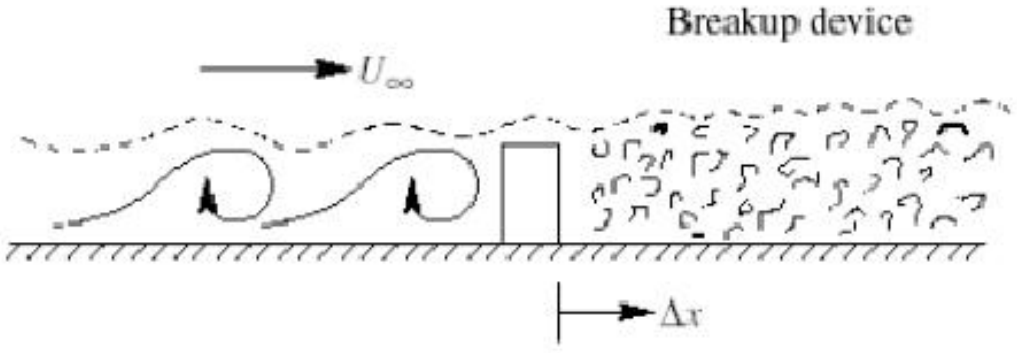

Figure 2.7: Large Eddy Break Up Device. [58]

One of the most commonly used drag reduction methods in the shipping industry today is known as polymer injection. Although the initial injection of the polymer into the flow requires some external energy it can still be considered to be a passive technique as no energy is required for the polymers to interact with the flow. There are various ways that the polymer can modify the flow structure, with the most common being to change the viscosity of the fluid, and hence reduce the shear stress. The best example of polymer injection has been shown in the Trans Alaskan Pipeline, as reported by Motier, Chou and Kommareddi [91]. Originally this pipeline was to have 12 pump stations to drive the flow through the pipeline, however due to the success of the polymer injection system, only 10 of these stations were required and built. There is a large difference however between flow through a pipe, where the fluid is contained and the polymers cannot escape, and the flow around a ship hull, where the polymers can quickly be moved away from their area of intended influence. The winner of the 2010 America's Cup was also fitted with a polymer injection system, however it was removed before the final races both to save weight, and as it regularly malfunctioned. Had this system worked it would have reputably given them 4 to 5 percent improvement in boat speed. [119]

The final method of boundary control to be discussed is based again on a geometric surface topology like that of the riblet and LEBU, however at a much smaller scale. Recent work has focused on surfaces that employ both chemical and geometric attributes to achieve high levels of drag reduction by utilising the physical property of surface tension to keep water away from the surface minimising the wetted surface area.

2.1.5 Surface Tension and Contact Angles

The key to these new surfaces lies in the ability to exploit the surface tension of the fluid, a concept that was first proposed by Young in 1805 [143]. Surface tension is molecular in nature, and occurs because of an imbalance in molecular forces at the surface of a fluid. In the bulk of the fluid, molecules are surrounded on all sides meaning molecular attraction forces between them are relatively isotropic. At the surface of the fluid there is no outward attraction to balance the inward pull as there are substantially less molecules on the vapor side of the interface.

This inward pull on the surface molecules is what we refer to as surface tension. In a liquid-vapor system, a droplet of liquid will form a sphere to balance the inward forces from the bulk of the liquid.

When dealing with a solid-liquid-vapor system, such as a stationary droplet resting on a surface, as well as the liquid-vapor interface described above, there are also solid-liquid and solid-vapor interfaces. The droplet will find an equilibrium state where the surface tension forces from these three interfaces are balanced. At the three-phase boundary, that is where each of the three phases meet, the angle between the liquid-vapor interface and the solid surface is referred to as the contact angle, indicated by θ_w [1]. In cases where the droplet is moving across the surface, two dynamic contact angles also exist, known as the advancing and receding contact angles, θ_a and θ_r respectively. The value of the contact angle gives information about the surface energy of the solid. A solid with high surface energy attracts the molecules of the fluid, resulting in a thin layer of fluid across the surface. This occurs as the energy of the solid surface exerts a greater attractive force on the molecules than the rest of the molecules in the bulk of the fluid. Conversely, if the solid surface energy is low, the droplet will have a high contact angle, as the molecules are again attracted inwards by the bulk of the fluid, and a near spherical droplet will again result. Knowing the surface tensions of these interfaces, the static contact angle can be found using the Young's equation, shown as Equation 2.12, where σ_{sg}, σ_{sl} and σ are the surface tension between the solid-gas, solid-liquid, and liquid-gas respectively. Figure 2.8a also illustrates these concepts.

$$\cos\theta_w = \frac{\sigma_{sg} - \sigma_{sl}}{\sigma} \tag{2.12}$$

Young's equation predicts the contact angle of the fluid in ideal conditions, that is, when there are only the 3 phases present, and the surface is perfectly flat. In reality, surfaces tend to have some amount of roughness. Wenzel [141], in 1936 studied droplets on rough surfaces and formulated an equation to account for the surface roughness, $\theta^* = r\cos\theta_w$, where r is a roughness ratio, and θ^* is the apparent contact angle due to the roughness of the surface. Droplets fully wetting a rough surface are said to be in a Wenzel state, illustrated in Figure 2.8b.

[1] This is also sometimes called the wetting angle hence the subscript w

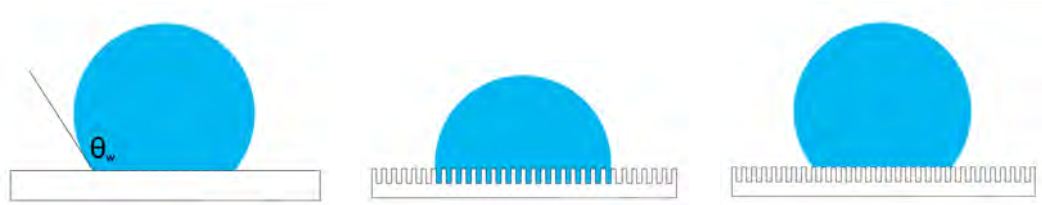

(a) Droplet on an ideal surface.

(b) Droplet in the fully wetted Wenzel state.

(c) Droplet in the partially wetted Cassie-Baxter state.

Figure 2.8: States of droplets.

The Cassie-Baxter state, proposed by Cassie and Baxter [20] in 1944, instead deals with a rough surface that has not been fully wetted, as can be seen in Figure 2.8c. In this case, small pockets of vapor are still present beneath the droplet. This again causes the apparent contact angle of the liquid to change, and results in a reduced wetted area of the surface. It is this principle that is responsible for super hydrophobicity.

2.2 Hydrophobic Surfaces

Surfaces can be classified by their contact angle, with those having contact angles $\theta_w < 90°$ known as hydrophillic, or water attracting, and those with $\theta_w > 90°$ known as hydrophobic, or water repelling. More recently, surfaces with contact angles $\theta_w > 150°$ have been receiving quite a lot of attention by the research community. With such high contact angles, they strongly repel water, and have been termed super hydrophobic surfaces.

Super hydrophobic surfaces are able to maintain such a high contact angle by combining both hydrophobicity, and micro or nano scale roughness. These micro or nano scale surface features tend to be either grooves and ridges, or arrays of posts. In both of these cases, the alignment with the flow can also be varied to give a multitude of differing geometries. Figure 2.9 shows a schematic diagram of a super hydrophobic surface.

As well as drag reduction, super hydrophobic surfaces have been shown to be useful for other purposes such as self cleaning surfaces [11, 47], minimising heat transfer [110, 111], and bio-fouling [117, 128].

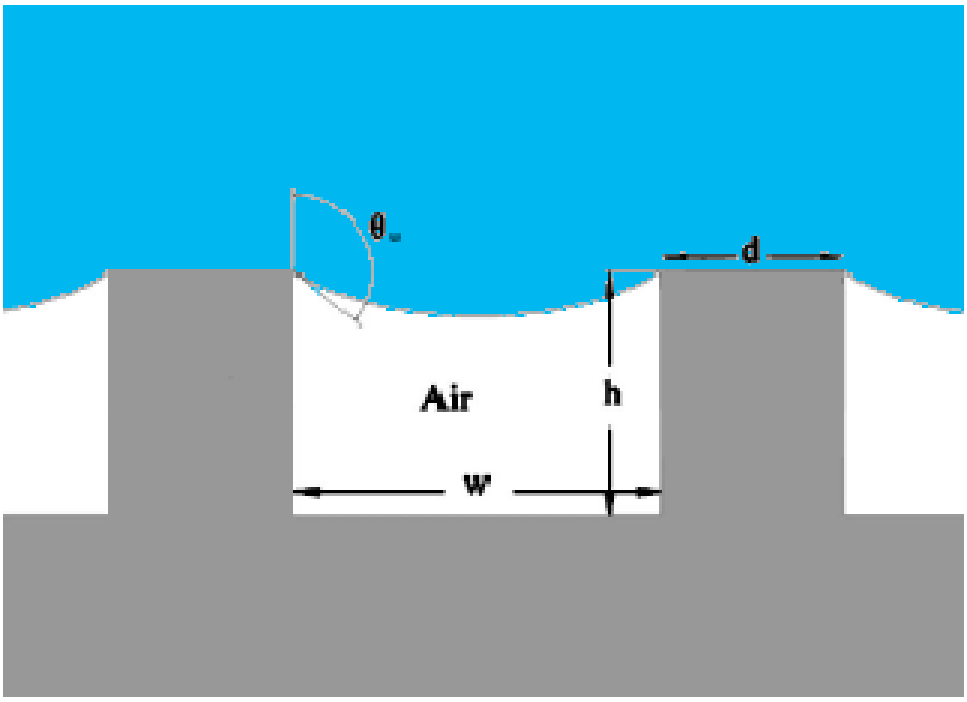

Figure 2.9: Schematic model of a super hydrophobic surface showing the post height (h), post diameter (d), and the post spacing (w) and contact angle (θ_w). The radius of curvature of the surface is a function of many variables including the wetting contact angle, the surface tension, and the hydrostatic pressure the fluid is applying at the air-water interface.

2.2.1 Experimental Research

Although the phenomenon of super hydrophobicity has been apparent for hundreds of years in places like the leaves of the lotus flower (Figure 2.10), or on the legs of water striders, it was not until 1944 that Cassie and Baxter actually quantified this effect. Vinogradova [133, 134] first performed theoretical studies on hydrophobicity showing that drag reduction using these types of surfaces was possible. It was shown that there was an experimentally discernible increase in the flow of water across hydrophobic surfaces in simulations of thin film draining between hydrophobic spheres, results which were later also shown experimentally. The first experimental work in the area was performed by Udugawa and Watanabe [130], who in 1997 investigated flow through a pipe which was lined with a hydrophobic coating. Pressure drop measurements along the pipe indicated that

(a) Droplet of water of a lotus leaf.

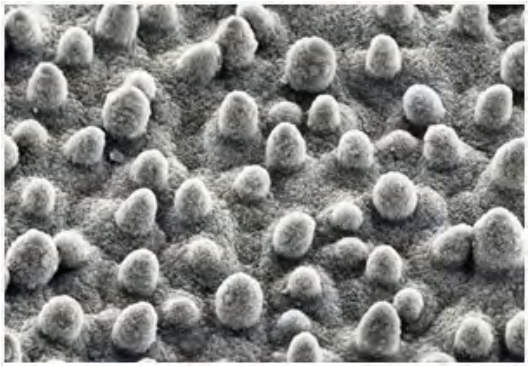

(b) Micro scale features on the lotus leaf.

Figure 2.10: Images of the leaf of a Lotus flower. [23]

there was a 14% reduction in drag compared to an uncoated pipe. Figure 2.11 shows an example of the surface coating Udugawa and Watanabe used in their experiments.

In 2000, Öner and McCarthy [93] tested a series of structured surfaces with photo lithographically created posts of varying shapes and sizes, examples of which can be seen in Figure 2.12. This work was instrumental in investigating the contact line dynamics, that is, the line where the droplet makes contact with the surface. Although all of the tests were undertaken with posts of the same height on horizontal surfaces, Öner and McCarthy theorized that introducing posts of varying heights would add to the contact line instability and hence increase the hydrophobic nature of the surface. This was later proven by Bittoun and Marmur [10] who undertook a study optimizing the surface geometry of super hydrophobic surfaces. They too investigated the use of different shaped posts; however, unlike previous studies that had only varied the cross sectional shape of the posts, Bittoun and Marmur trialled a variety of other topographies including parabolids and hemispheres which can also be seen in Figure 2.12.

Tretheway and Meinhart [125, 126] studied pressure variation on flow within microchannels with a unstructured chemically created hydrophobic surface. Instead of the fully structured surfaces used by Öner and McCarthy, chemically manufactured surfaces create a somewhat random array of posts and gaps. Using this type of surface, they showed that slip at a wall with water as the working

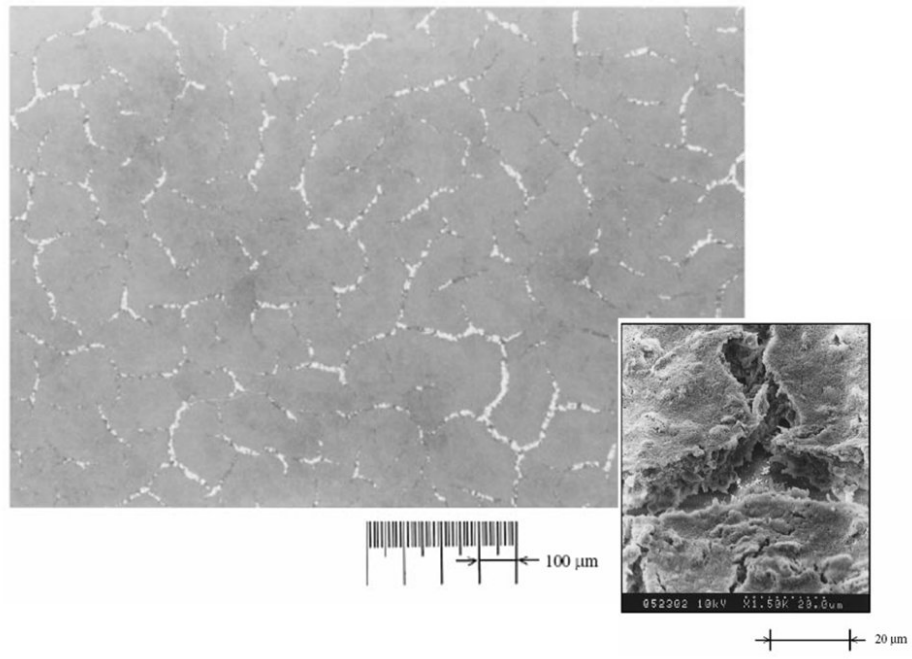

Figure 2.11: Chemically created super hydrophobic surface used by Udugawa and Watanabe. [130]

fluid was possible, and the zero velocity condition at a wall as propsed by Prandtl was not a binding physical phenomenon. An extract of these results is shown in Figure 2.14 showing the non-zero velocity at the wall on the hydrophobic surface.

The first work directly targeting drag reduction was undertaken by Ou *et. al.* [94] who investigated laminar flow in microchannels. Ou *et. al.* again used structured surfaces, and brought about drag reductions using carefully controlled microscopic topologies which were fabricated on silicon wafers. One of the surfaces tested can be seen in Figure 2.13a. Ou credited the reduced resistance to the microscale roughness preventing the water from moving into the pores between the peaks of the posts. Instead of wetting the entire surface, the water only touches as many peaks as is required to support the free surface. Tests of surfaces with varying geometries were also undertaken and compared against a flat hydrophobic surface with drag reduction effects of over 40% reported. This result was also confirmed by Truesdell [127] who additionally reported on the minimum effective slip length required to gain the reduction in drag.

A similar study was repeated by Danniello [31] this time in turbulent flow.

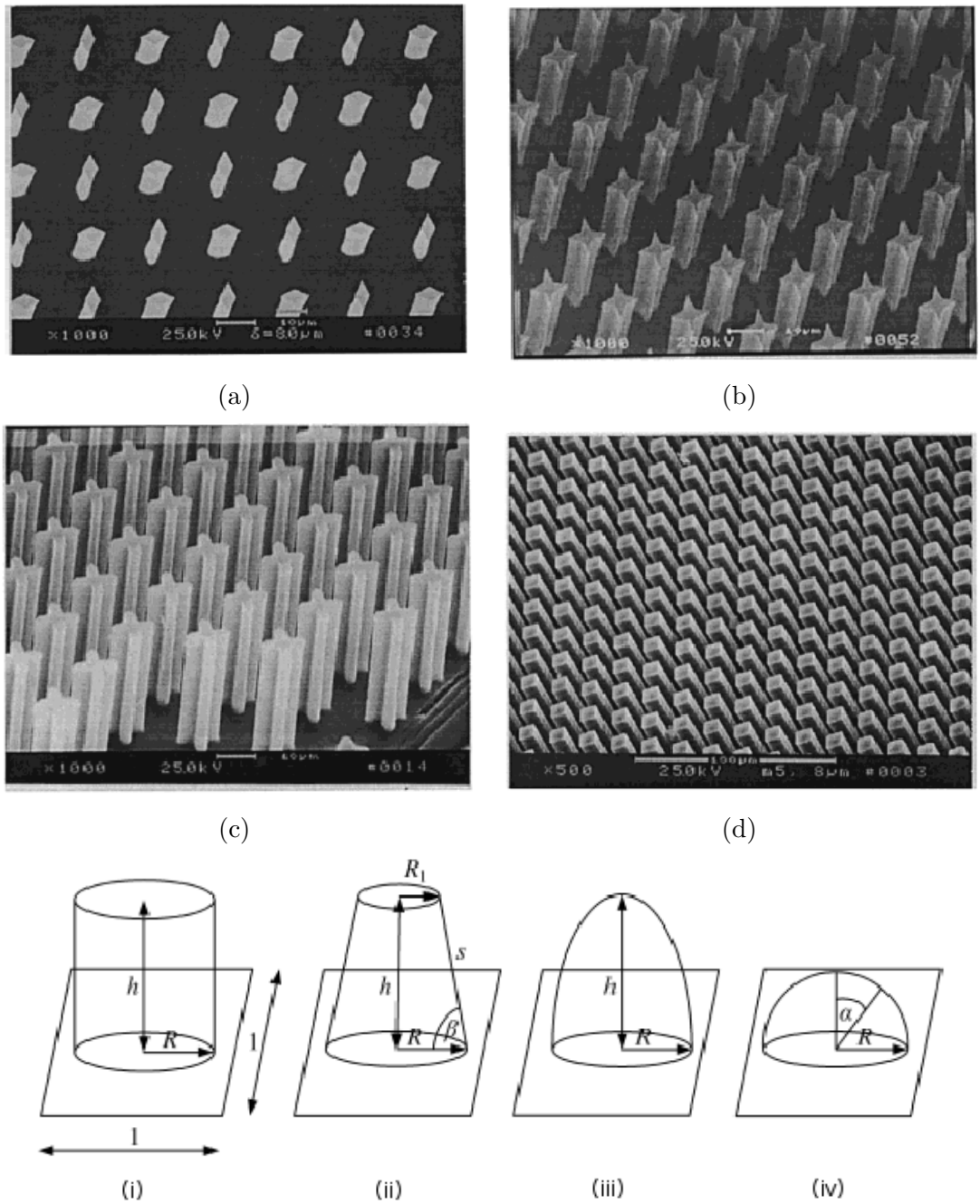

(e) (i) Cylindrical (ii) Truncated Cone
(iii) Paraboloid (iv) Hemisphere

Figure 2.12: (a) - (d) Post shapes tested by Öner and McCarthy
(e) Optimised post shapes tested by Bittoun and Marmur. Note the resemblance between the paraboloid in this work and the surface of the lotus leaf shown in Figure 2.10b.

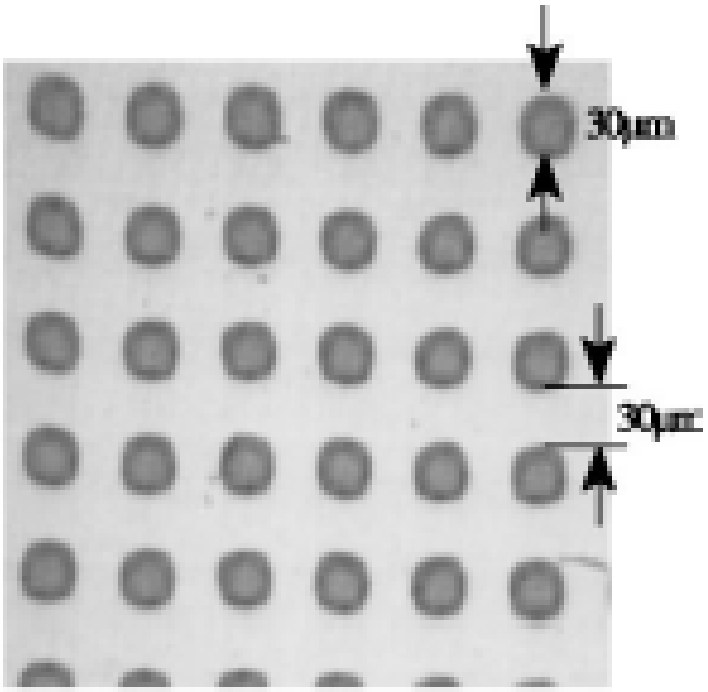

(a) $30\mu m$ cubic posts with $30\mu m$ spacings.

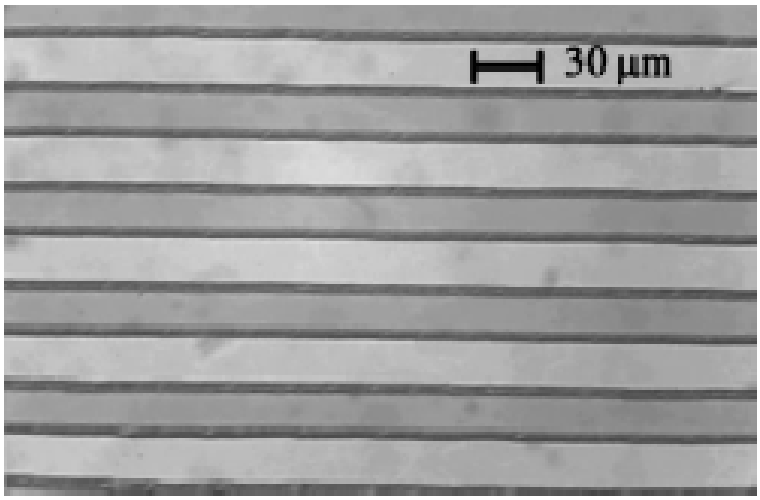

(b) $30\mu m$ ridges and grooves.

Figure 2.13: Photo-lithographically produced super hydrophobic surfaces.[94]

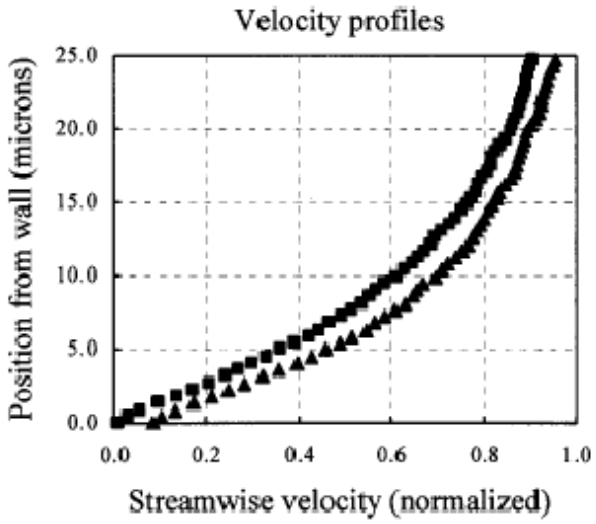

Figure 2.14: Velocity profiles for flow over a hydrophilic (square) and hydrophobic (triangle) surface.[125]

Again using a structured surface with streamwise grooves, and testing flow rates with Reynolds numbers between 2000 and 8000, Daniello measured drag reduction of up to 50% using pressure drop and PIV measurements. Studies by Woolford [142] also using PIV measurement of turbulent flow over a structured super hydrophobic surface gave slightly different results, with an 11% decrease in friction found when grooves were aligned with the flow and a small increase in drag when the grooves were aligned transversely. With the previous work studying internal flows in micro fluidic devices, the first external flow experiments were completed by Henoch *et. al* [59]. Henoch manufactured fields of 400 nm diameter posts with a 1.25 μm spacing on silicon wafers. These fields were stitched together to form a test plate 416mm x 175mm, which can be seen in Figure 2.15 which was tested in a recirculating water tunnel between speeds of 0 and 1.4 meters per second. A comparison was made by also testing a smooth PVC plate in identical conditions with drag reductions in the laminar regime reported of up to 50%.

Another recent study by Park *et. al.* [96] have reported drag reduction in turbulent flow of up to 70%. Using methods which they claim to be error-less, a comparison between a monolithically fabricated super hydrophobic surface featuring streamwise grooves, and a hydrophobic flat plate were performed. The two plates were run simultaneously in a water channel with flow at a Reynolds

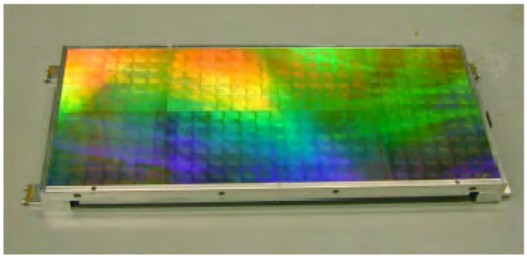

(a) Micro grass plate used by Henoch.

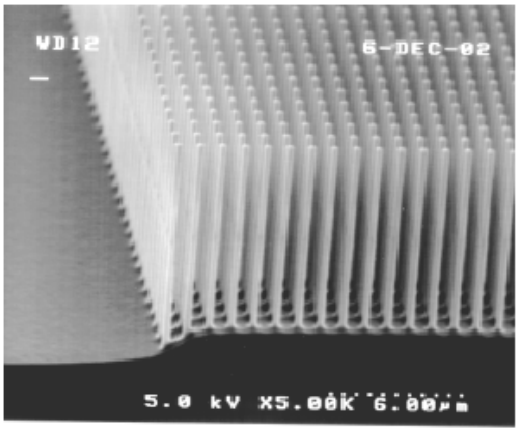

(b) Microscopic image of micro grass surface. The posts are each 400 nm diameter and spaced 1.25μm apart.

Figure 2.15: Micro grass test plate. [59]

number measured to be 2×10^5, corresponding to about $Re_\tau = 250$.

Not all experiments have shown such reductions are achievable, with work by Zhao et. al. [150] having undertaken a theoretical and experimental study in which they claim that the maximum attainable drag reductions are 8.76% for low Reynolds number flows, and 2.63% for high Reynolds number flows. Further to this, experiments by Peguero and Breuer [97] testing surfaces similar to those used by Daniello, also showed no definitive evidence of any appreciable reduction in drag. Additionally, Aljallis *et. al.* [1] tested flat aluminium plates with differing spray-on super hydrophobic surfaces by towing them in a high-speed towing tank. They found drag reductions of up to 30% in the laminar / transitional regime; however, at higher speeds in the turbulent regime, an increase of drag was again reported. This increase was credited to the surface wetting which occurred as a result of the high shear at the surface removing the air from the gaps.

Work by Emami *et. al.* [40] further supports the conclusions of those who claim significant drag reduction is not possible. They developed a mathematical framework to predict the length of time that a submerged super hydrophobic surface could stay in the Cassie-Baxter state before transitioning into the Wenzel state. This work was based on the fact that over time, air dissolves into the water, reducing the volume of the air in the grooves and gaps, and allowing the

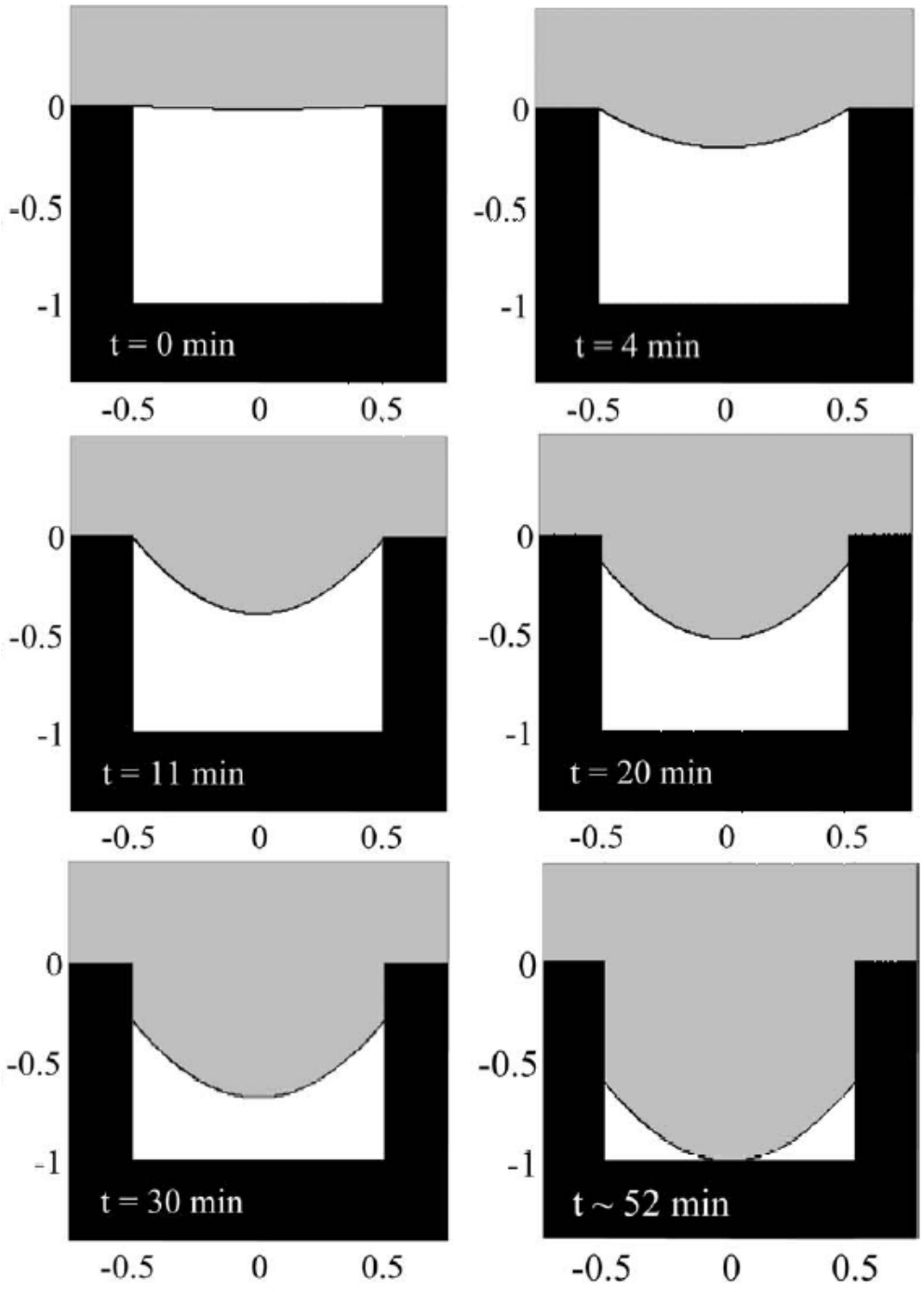

Figure 2.16: Water ingress into groove due to dissolution of air into the water. [40]

water to instead fill them. Figure 2.16 shows the progression of the water into a $100\mu m$ wide, $30\mu m$ high groove where the contact angle of the fluid is 115°. They predict the life time of a surface with this size and shaped geometry to be just under an hour before the air layer has been removed. Work by Lee and Kim [78] hopes to overcome this issue with specially shaped surface features that allow the submerged surfaces to be de-wetted while still underwater.

2.2.2 Numerical Research

As well as experiments on super hydrophobic surfaces, a range of simulations have also been performed. These simulations can be split into two distinct groups: those with droplets, and those with immersed super hydrophobic surfaces. It is the second group that is more relevant to this work.

Numerical studies by Min and Kim [88, 89] on the effects of hydrophobic surfaces on wall bounded shear flows revealed that frictional drag reduction was possible. Using direct numerical simulation, they simulated flow over the surface at $Re_\tau = 180$ and represented the hydrophobic surface by setting an arbitrary slip length on the wall. When this boundary condition was applied in a streamwise direction, the frictional drag decreased, and the turbulence intensities and structures were significantly weakened. However, when the slip condition was applied spanwise to the flow, they found the turbulent structures changed and the drag increased. They determined that there is a minimum value of slip required to have an effect on the turbulence and hence a reduction in drag. Due to the slip lengths of current hydrophobic surfaces they concluded that these surfaces would be unlikely to cause drag reductions in fully turbulent flow.

The results of Min and Kim was extended in a theoretical model by Fukagata, Kasagi and Koumoutsakos [46]. They again assumed a boundary condition with slip velocities and extended the underlying equations to deal with higher Reynolds numbers. Their work predicted that in flow of $Re_\tau = 2 \times 10^5$, or roughly that of a 300 m cargo ship at 16 knots, a drag reduction of 10% should be attainable.

Work by Martell, Perot and Rothstein [83] contradicted the conclusions of Min and Kim. Martell *et. al.* also used direct numerical simulations with turbulent flow; however, instead of setting an arbitrary slip length, a series of alternating slip / no-slip walls was used to form a post like pattern. Martell further argued

that the curvature of the free-surface between the posts on the super hydrophobic surface was negligible and the free surface could be thought of as having no out-of-plane deflection. These simulations showing drag reductions of up to 40% in fully turbulent flow.

More recently, Samaha [116] has undertaken simulations of laminar flow over both structured and unstructured super hydrophobic surfaces. This was achieved using a commercial CFD code and again modelled the air/water interface with a variable shear wall. Analysis was done to find the point at which the water would intrude into the air gaps and the surface transition into the Wenzel state. They found that the structured surface results in more drag reduction, and is less likely to allow the air gaps to flood.

In each of the cases so far the air water interface has been assumed to be flat and stable. As has been shown by some of the experiments, this is not always the case. This means that modelling these super hydrophobic surfaces as slip/no-slip walls is not entirely accurate. This has been partially addressed by the work done by Byun [18] who simulated of flow over the actual geometry. In his work, the flow over the surface features was only modelled as a single phase fluid, however with some of the geometries tested, namely those with high aspect ratios of the gap to post, there was an appreciable reduction in drag. This was attributed to the vortices created in the gaps between the posts and is therefore similar to the experimental studies into riblets.

Another study performed by Teo and Khoo [124] actually modelled the air water interface as a curved free-slip surface under laminar flow conditions. They trialled grooves running both streamwise and spanwise and found that the streamwise grooves were the better performers, as unlike the spanwise grooves, they did not exhibit negative slip lengths.

2.3 Summary

This review of the literature in the area of boundary layer control and resistance reduction has showed that frictional drag accounts for a large part of the total resistance experienced by a ship. A reduction of this drag is a worthwhile goal as it would directly influence the speed of the ship and lead to a reduction in costs of

shipping. Although various methods of controlling flows over surfaces have been investigated, super hydrophobic surfaces may yet be able to provide the greatest benefits.

As was shown, there has already been some research completed in the field of turbulent flow over super hydrophobic surfaces. The results of this research however vary wildly, with some researchers claiming almost no measurable drag reductions, whilst other claim reductions of up to 70%. By detailed analysis of the mechanisms responsible for the apparent drag reduction, this work aims to reveal which of the claims made are correct, and whether the application of super hydrophobic surfaces to ships will increase their efficiency.

This page is intentionally left blank.

Chapter 3

Surface Experiments

As was detailed in the previous chapter, there have been a range of experiments conducted investigating super hydrophobic surfaces in both laminar, and low Reynolds number turbulent flows [1, 59, 96]. To properly assess whether super hydrophobic surfaces are capable of reducing the drag on a ship, tests of these surfaces at higher Reynolds numbers need to be undertaken. This chapter details the equipment, method, and the results of an experiment testing super hydrophobic surfaces at Reynolds numbers up to 6×10^6 performed in a cavitation tunnel. As no suitable equipment was available, a significant component of the project involved designing and building the required experimental apparatus. Detailed design drawings for the resulting components can be seen in Appendix D.

3.1 Cavitation Tunnel Details

Physical experiments were conducted in the Tom Fink Cavitation tunnel at the Australian Maritime College, Launceston. The cavitation tunnel is a recirculating water tunnel, similar in principle to a wind tunnel, but using water as the working fluid. It has an operating velocity range of between 2 and 12 m/s, and a centreline pressure range of 0.4 to 400 kPa absolute, allowing the pressure at which the surfaces are tested to be varied. This pressure and velocity range allows the tunnel to reach Reynolds numbers of up to 6×10^6, and a minimum cavitation number of 0.07[1].

[1]Cavitation number ($Ca = \frac{P - P_v}{\frac{1}{2}\rho U^2}$) is a dimensionless number relating the absolute pressure of a fluid to the fluids vapor pressure and the kinetic energy per volume.

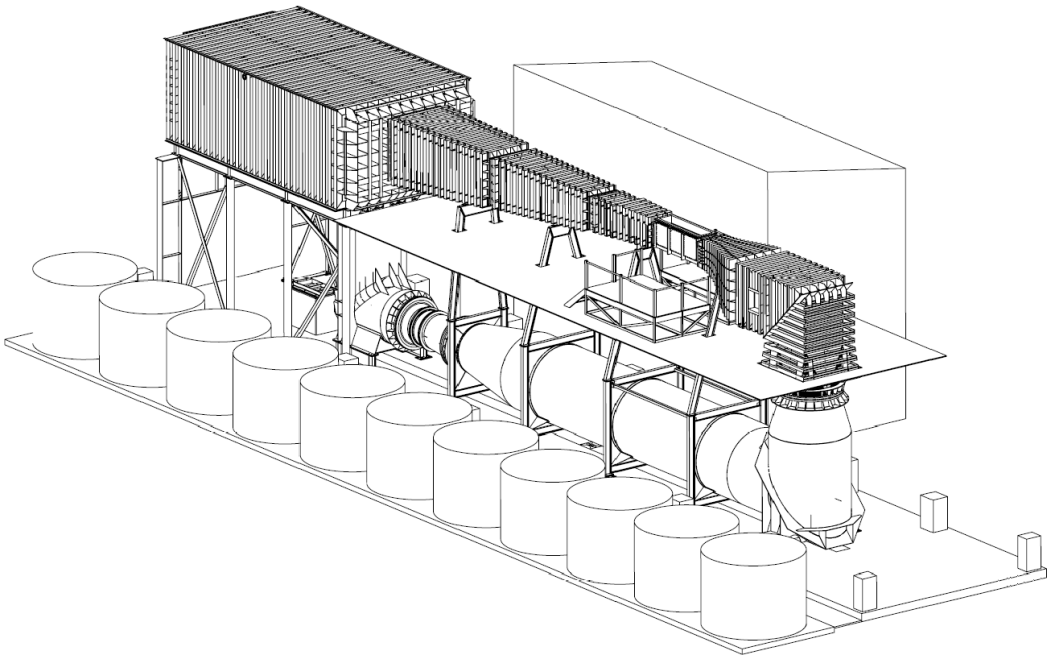

Figure 3.1: Three-dimensional cavitation tunnel general arrangement. [13]

The cavitation tunnel, as shown in Figure 3.1, contains $365m^3$ of water and is composed of a number of parts including an upstream contraction, downstream linear expansion region, bubble separation chamber and a test section. The test section itself consists of a $0.6 \times 0.6 \times 2.6$ metre long rectangular box with windows on the sides and bottom made of a high quality acrylic which has been machined and finished to a precision suitable for the use of laser diagnostics. The top of the test section features a series of openings, referred to as "windows", that allow a range of apparatus to be positioned within the test section. The ceiling of the test section is horizontal, whereas the floor slopes downward by 20 mm over its length to maintain constant speed and a zero-pressure gradient throughout. Pressure and velocity measurements are made using high and low range Siemens Sitransp differential pressure transducers with estimated precisions of 0.007 and 0.018 m/s for the high and low range transducers respectively. The tunnel is also capable of both injecting and ingesting water at the entry to the test section so as to vary the boundary layer thickness. Further details on both the design and operation of the cavitation tunnel can be found in the work of Brandner *et. al.* [13, 14, 15].

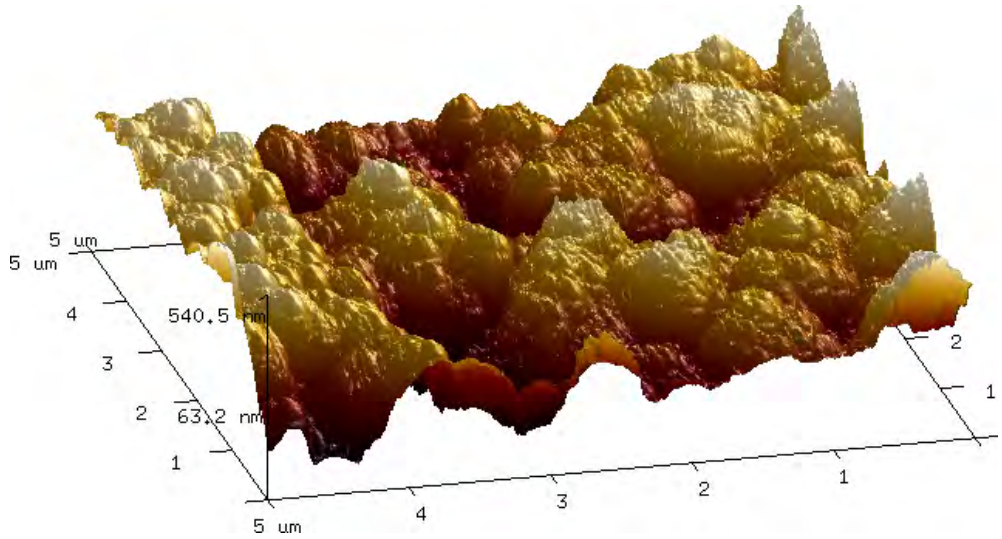

Figure 3.2: Atomic force microscopy image of the superhydrophobic surface tested. This images covers a $5\mu m \times 5\mu m$ area meaning that the microfeatures on this surface are orders of magnitude smaller than those tested in the simulations later in this work.

3.2 Superhydrophobic Surfaces

Two test panels were used in this experimental work, one of which was coated with a superhydrophobic coating, and the other left uncoated to act as a control. Both surfaces were laser cut from 0.9 mm stainless steel plate and finished to a 2B standard[1]. The superhydrophobic panels were coated by the Department of Chemistry, University of Melbourne [24, 129, 140].

Although full details of the method used to apply the superhydrophobic coating can be found in work by Zhang, Lamb and Jones [72], a brief overview will be given here. Firstly, reactants including nano-silica particles, a polymer linking agent, and a platinum catalyst were mixed and left to vibrate in an ultrasonic bath for between 15 and 30 minutes to disperse the nano silica particles and form a uniform solution. This solution was then applied to the substrate using spray coating and was left at room temperature for 3 hours, then cured at $150°C$ for a further 10 minutes. The method of spray coating the solution onto the surface

[1] A 2B finish implies the plate has been annealed, descaled, and cold rolled leaving it bright and moderately reflective.

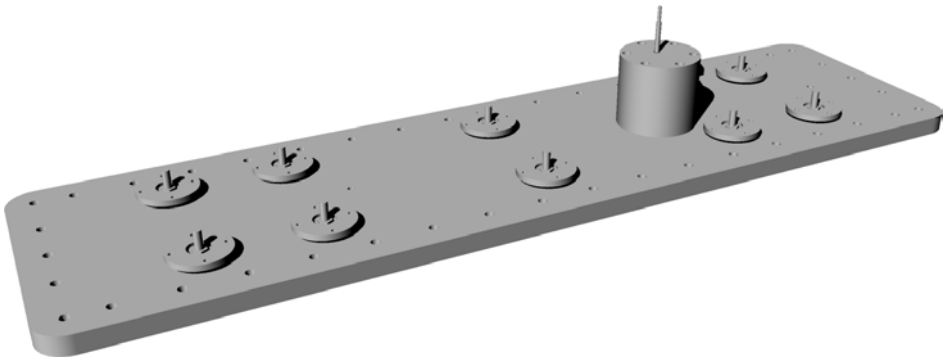

(a) Illustration of the top surface of the fixed side of the experimental rig. The load cell housing, flexures, and the keeper plates locking the flexures in position can be seen. The holes around the edge of the plate allow it to be bolted into the window on the top of the cavitation tunnel test section.

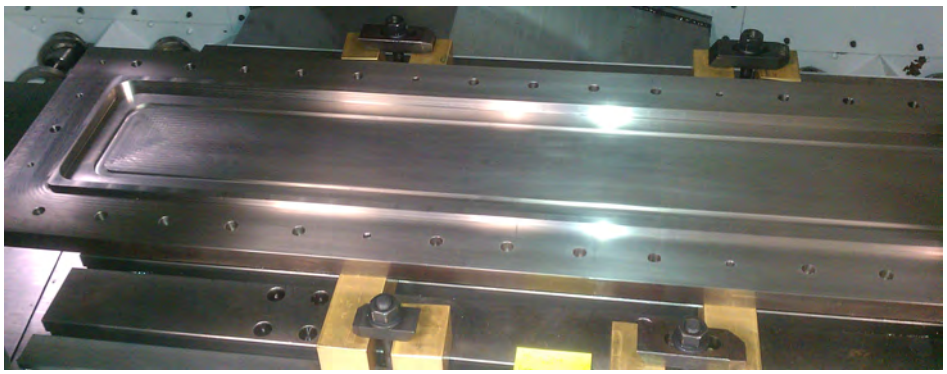

(b) Bottom surface of fixed side during machining. The air removal groove and alignment lip are both visible.

Figure 3.3: Fixed side of experimental rig.

meant that the contact angle varied across the surface due to an uneven particle distribution. Contact angle measurements made by the chemists who performed the coating operation found the contact angle of the surface was 164° (±5°) indicating it was indeed superhydrophobic.

3.3 Experimental Rig

In order to accurately measure the frictional drag on each test surface, it was critical to minimise any forms of drag other than those due to skin friction. This was best accomplished by using a "floating" test rig that aligned the coated test panel with the ceiling of the cavitation tunnel test section.

Making use of an existing "window" in the top of the test section, with a clear opening of 1500×250 mm allowed test panels of 1498×248 mm to be used, giving a nominal 1 mm clearance around the test panel. The rest of the test rig can be divided into two groups, the fixed side, and the measurement side. The fixed side, illustrated in Figure 3.3, is bolted to the top of the cavitation tunnel test section and forms a stiff platform that supports the measurement side and the load cell. With the entirety of the cavitation tunnel manufactured from stainless steel, it was required that all components in the experimental rig also be stainless steel to avoid electrolysis and issues with dis-similar metals. In order to provide both the depth required for bolting points, and to withstand the maximum pressure of the cavitation tunnel, the fixed side needed to be machined from a 50 mm thick stainless steel plate. The fixed side plate also contains features such as an alignment lip, an air removal groove, alignment holes for the load cell housing, and openings and bolting points for the flexures.

The measurement side was suspended below the the fixed side, and was supported by a series of flexures. As can be seen in Figure 3.4, flexures are essentially 10 mm pins that have been machined in such a way that they have minimal resistance to forces in the streamwise direction, whilst being able to withstand forces in the spanwise and wall normal directions. This has been achieved by machining two flats of 0.5 mm thickness roughly eqi-distantly from the middle of the pin. This geometry allowed the pin to be able to flex and allow movement in one dimension but remain rigid in the other two. Using these

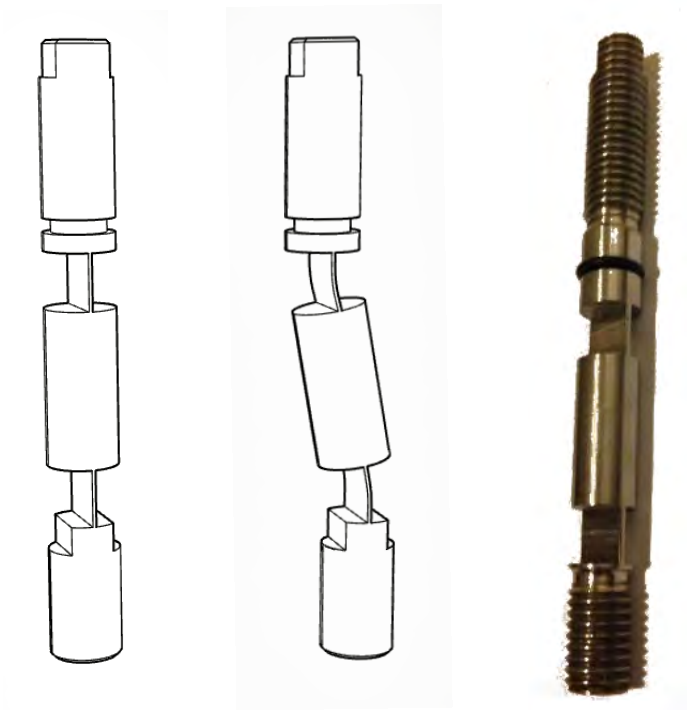

(a) Un-deformed. (b) Deformed. (c) Actual flexure used.

Figure 3.4: Flexures. These connect the fixed and measurement sides and allow freedom of movement of the measurement side in only a single direction.

flexures, the measurement side was supported and held in place, while allowing the majority of the forces acting in the streamwise direction to be measured by the load cell. Although the flexures do absorb a small portion of the force, this was accounted for through a calibration process.

The measurement side is connected to the fixed side through the flexures and by the load cell. Calibration of the load cell over the expected force range was performed with an accuracy shown of within 0.05% of the global load. The load cell was also rigidly attached to the fixed side, and connected to the measurement side by a longitudinal flexure to ensure no out of plane forces were applied to the load cell.

Like the fixed side, the measurement side was also comprised of a number of components. It was required to be stiff and strong to support the test panels and ensure the superhydrophobic surface remain flat during testing, while also

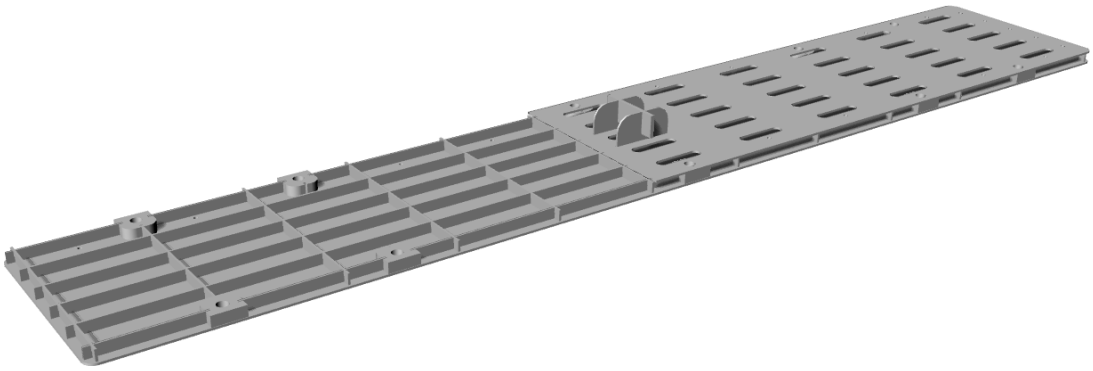

Figure 3.5: Measurement side strongback structure. Part of the top surface has been removed so the egg-crate structure inside is visible. The holes in the top surface also allow water to get into the structure to remove any effects due to buoyancy.

being light weight so as to minimise inertia and momentum. To achieve this, an "egg-crate" structure was created and sandwiched between two 1 mm sheets of stainless steel, as is illustrated in Figure 3.5. This lightweight rigid structure, referred to as the strongback, was glued together on a perfectly flat surface to ensure the test surfaces would remain flat when tested. The top surface of the measurement side is also covered in openings to allow water to fill the structure. Without this, the air trapped inside the strongback would cause it to be buoyant, potentially leading to it applying a small force in the streamwise direction as it tried to float.

The 0.9 mm test panels were bonded to 5 mm stainless steel backing plates which had large cut-outs to minimise the bending strength, and a series of pre-drilled and tapped holes. As the laser cutting process introduced curves into the plates, the reduced bending strength of the backing plates allowed them to be pulled perfectly flat against the strongback when they were attached. With the test surface attached to the strongback, the entire rig was lowered into the window in the cavitation tunnel. Figure 3.6 shows the assembled rig before it was bolted into the window. Detailed constructions drawings for some of the major components can also be seen in Appendix D.

Figure 3.6: The assembled experimental rig. The measurement side can be seen suspended below the fixed side. The window into which the rig fits is also visible below the assembly.

Table 3.1: Measurement sample times for different velocity flows to ensure a similar amount of water flows past the test panel in each case. These values correspond to 250 m of water flowing past the panel.

Re ($\times 10^6$)	Velocity (m/s)	Time (sec)	Sample Time (sec)
2	3.74	66.84	67
3	5.61	44.55	45
4	7.48	33.42	35
5	9.35	26.74	27
6	11.22	22.29	23

3.4 Experimental Method

With the experimental rig assembled and installed in the test section, the first tests undertaken were conducted on an uncoated test panel. The cavitation tunnel was set at a constant pressure of 107 kPa, and the flow velocity increased with measurements taken at nominal Reynolds numbers of 2, 3, 4, 5 and 6×10^6. For each measurement made, an constant volume of water was allowed to pass over the plate, meaning that measurements taken at lower speeds were run for a longer period than tests taken at higher speed. Table 3.1 shows the required and the utilised sample times to allow 250 metres of water to pass over the test panel. Each measurement recorded a time average dataset of drag on the test panel, flow velocity, pressure and fluid properties allowing the Cavitation number, Reynolds number and drag co-efficient of the surface to be calculated.

The rig was then removed from the test section and the uncoated panel replaced with the superhydrophobic panel. Due to the nature of the superhydrophobic surface, any contact can cause damage to the micro-features resulting in the surface losing its superhydrophobicity. To avoid this problem, the test panel was supported by its edges while being attached to the measurement side. The rig was then re-inserted into the test section.

Two tests were undertaken with the coated test panel. The first was identical to the process previously described with the uncoated plate, and involved the hydrophobic surface being tested at the same pressure and velocities. A second test was also conducted which kept the velocity constant at a nominal Reynolds number of 4×10^6 and varied the cavitation number between 4.63 and 0.59 (corresponding to lowering the pressure from an initial value of 130.2 kPa down to 18.2 kPa). The theory behind this test was that by decreasing the pressure, any air trapped on the surface would be able to expand and change the air cavity geometry, potentially leading to a change in the flow over the surface and a possible reduction of drag.

A comparison for this test was also undertaken by performing an identical experiment with no flow over the surface allowing any pressure dependencies to be accounted for within the experimental rig.

Table 3.2: Tabulated experimental results. The differences in the velocity between the smooth and hydrophobic panel tests is due to a difference in water temperature which corresponds to differences in density and viscosity. As can be seen, the actual Reynolds numbers for both tests are almost identical.

Nominal		Smooth Panel				Hydrophobic			
Re ($\times 10^6$)	Re_τ	Velocity (m/s)	Drag (N)	C_d ($\times 10^{-3}$)	Re ($\times 10^6$)	Velocity (m/s)	Drag (N)	C_d ($\times 10^{-3}$)	Re ($\times 10^6$)
2	2590	3.46	4.15	2.8221	1.985	3.74	4.95	2.8758	1.983
3	3601	5.17	8.53	2.5954	2.976	5.61	10.33	2.6644	2.975
4	4641	6.93	14.50	2.4594	3.978	7.48	17.55	2.5543	3.963
5	5616	8.65	21.71	2.3615	4.971	9.35	26.60	2.4770	4.952
6	6578	10.35	30.03	2.2824	5.948	11.22	37.38	2.4187	5.948

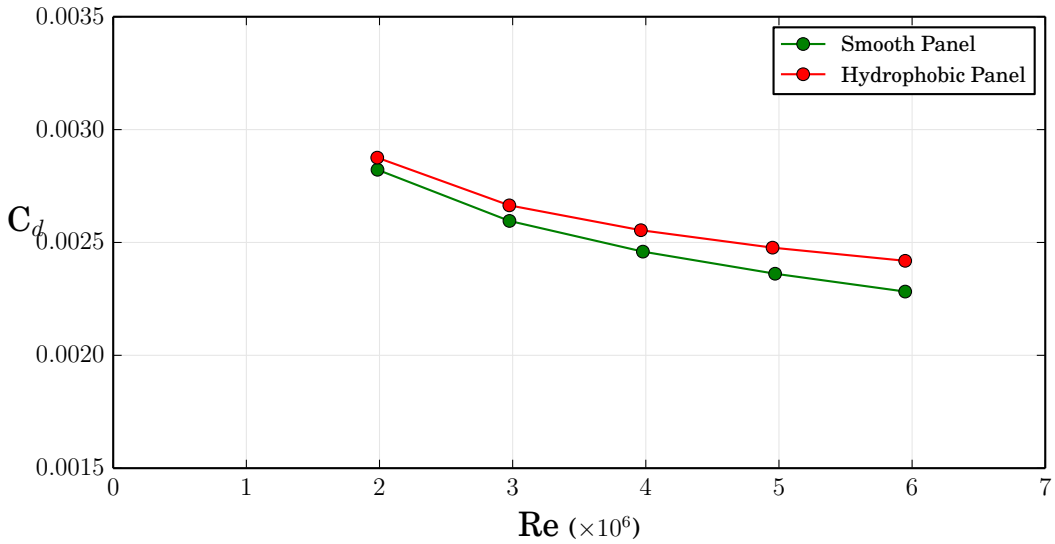

Figure 3.7: Comparison of the hydrophobic and uncoated panels. The hydrophobic panel has a higher drag across the tested Reynolds number range with the difference in drag between the two surfaces appearing to increase with Reynolds number.

3.5 Results

Results of the first test comparing the hydrophobic and uncoated panels can be seen in Table 3.2, and illustrated in Figure 3.7. As is immediately obvious, the hydrophobic test panel appears to have a higher drag co-efficient across the entirety of the Reynolds number range investigated, with the difference between the drag values of the two surfaces increasing with Reynolds number.

As was discussed in Chapter 2, the increased drag of the hydrophobic surface can be at least partially explained by the air layer on the surface being removed. Without a layer of air trapped against the micro structures in the coating, the surface effectively becomes a roughened panel.

Evidence of the air layer being depleted can be seen by looking at photographs of the superhydrophobic surface before, during and after the tests were performed, as can be seen in Figures 3.8 to 3.14.

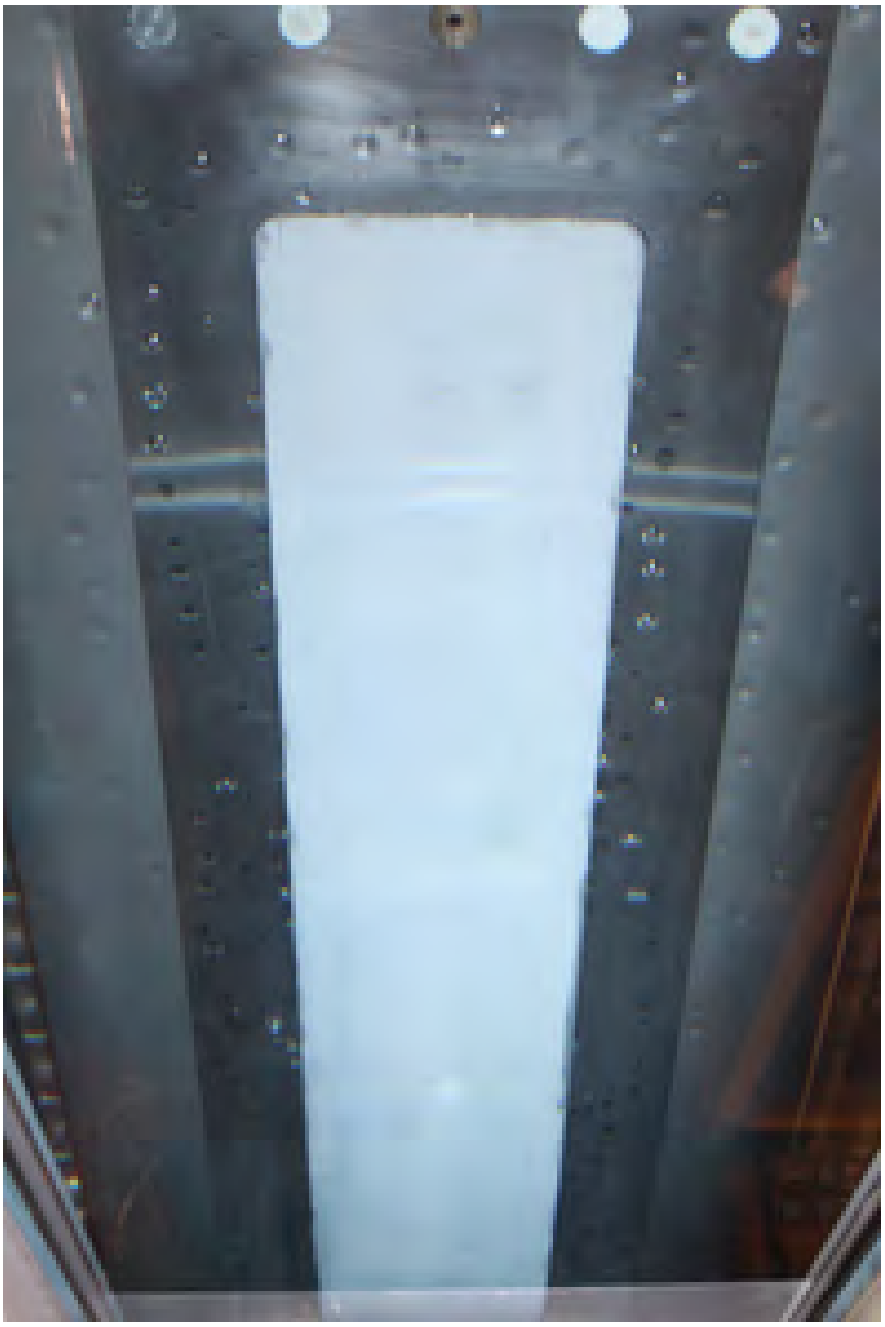

Figure 3.8: Test panel before testing. In this image, the experimental rig has been installed in the top of the test section. The water level in the test section is still below the ceiling height and at this time, the test panel (white rectangle) is completely dry; however, droplets can be seen on the ceiling surrounding the test panel due to earlier wetting. The image is orientated with the upstream end at the bottom of the image, and the downstream end at the top. The circles visible at the very top are blanking plates, and static and dynamic pressure tappings.

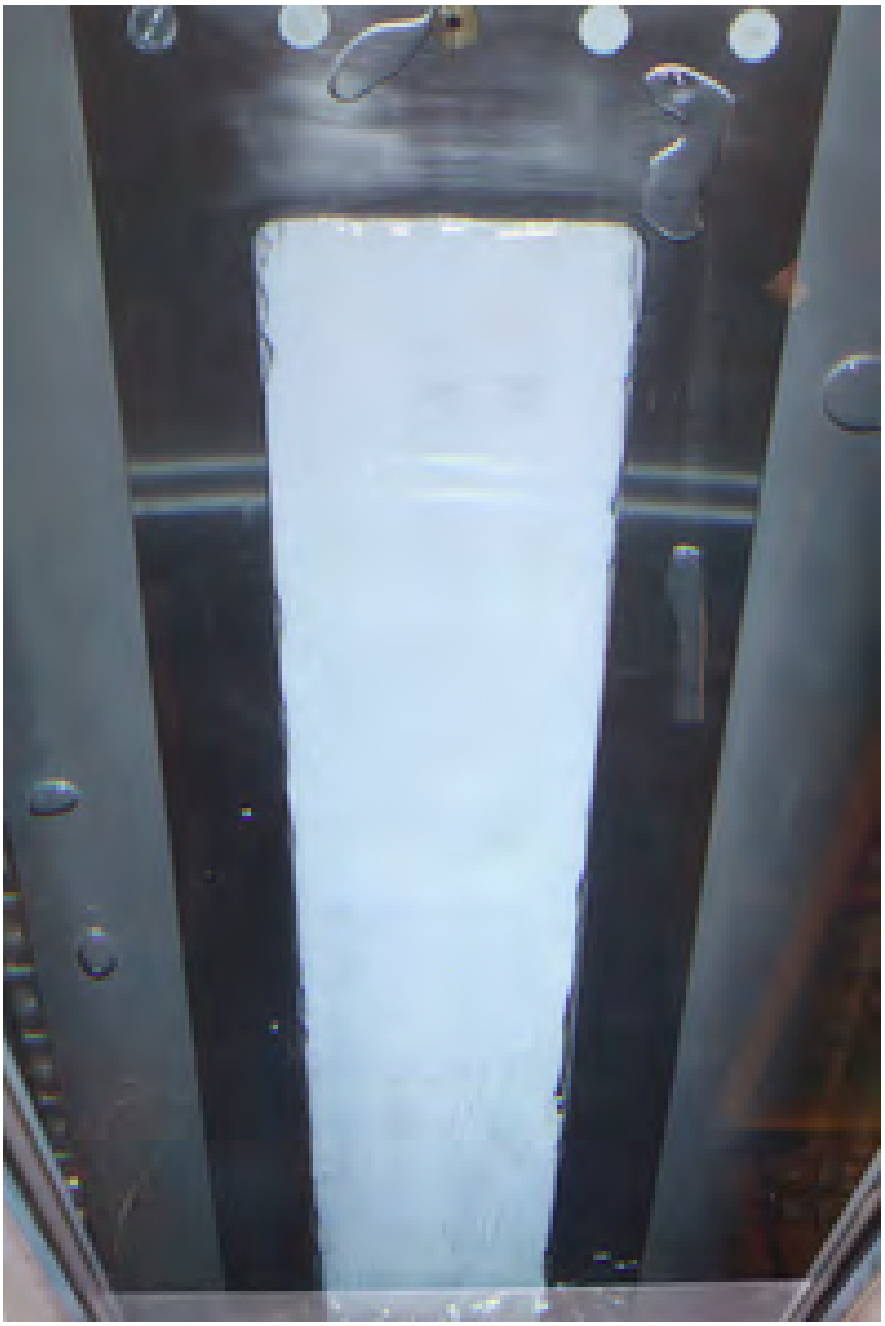

Figure 3.9: Test panel with zero flow. At this time the tunnel has been filled with water up to the operating level. With no flow, some bubbles are still present against the ceiling of the test section. The majority of the test panel is still dry and can be seen to be covered with a layer of air; however, due to damage to the surface around the edges during the installation process, some of the panel has become wet.

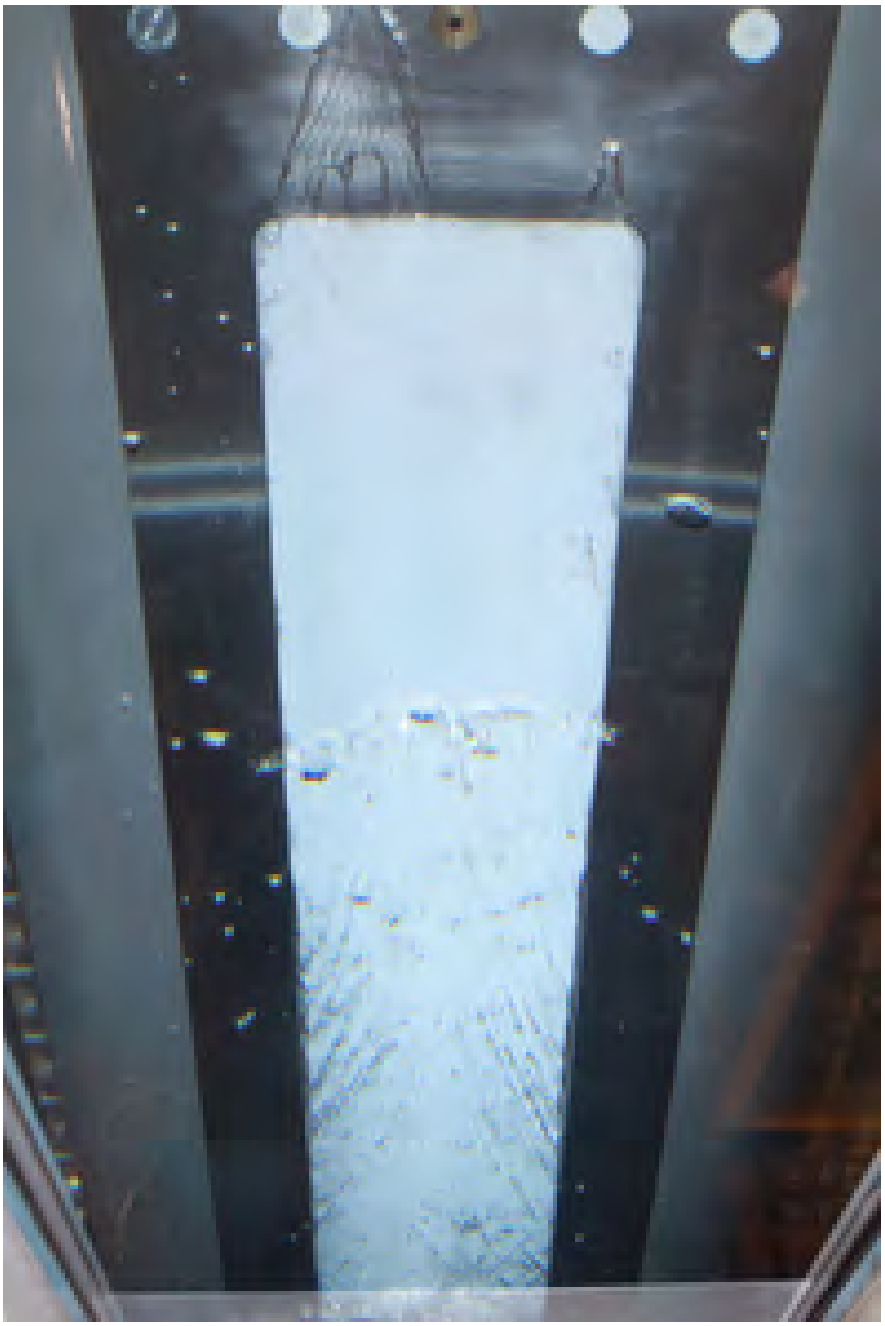

Figure 3.10: Test panel with low speed flow. With the pump driving the cavitation tunnel started and flow beginning to occur over the panel, the air layer on the surface can be seen to be distorted. Also visible at the downstream end of the panel is air being washed off the surface. This image was taken at flow speed significantly lower than the minimum operating velocity of the tunnel.

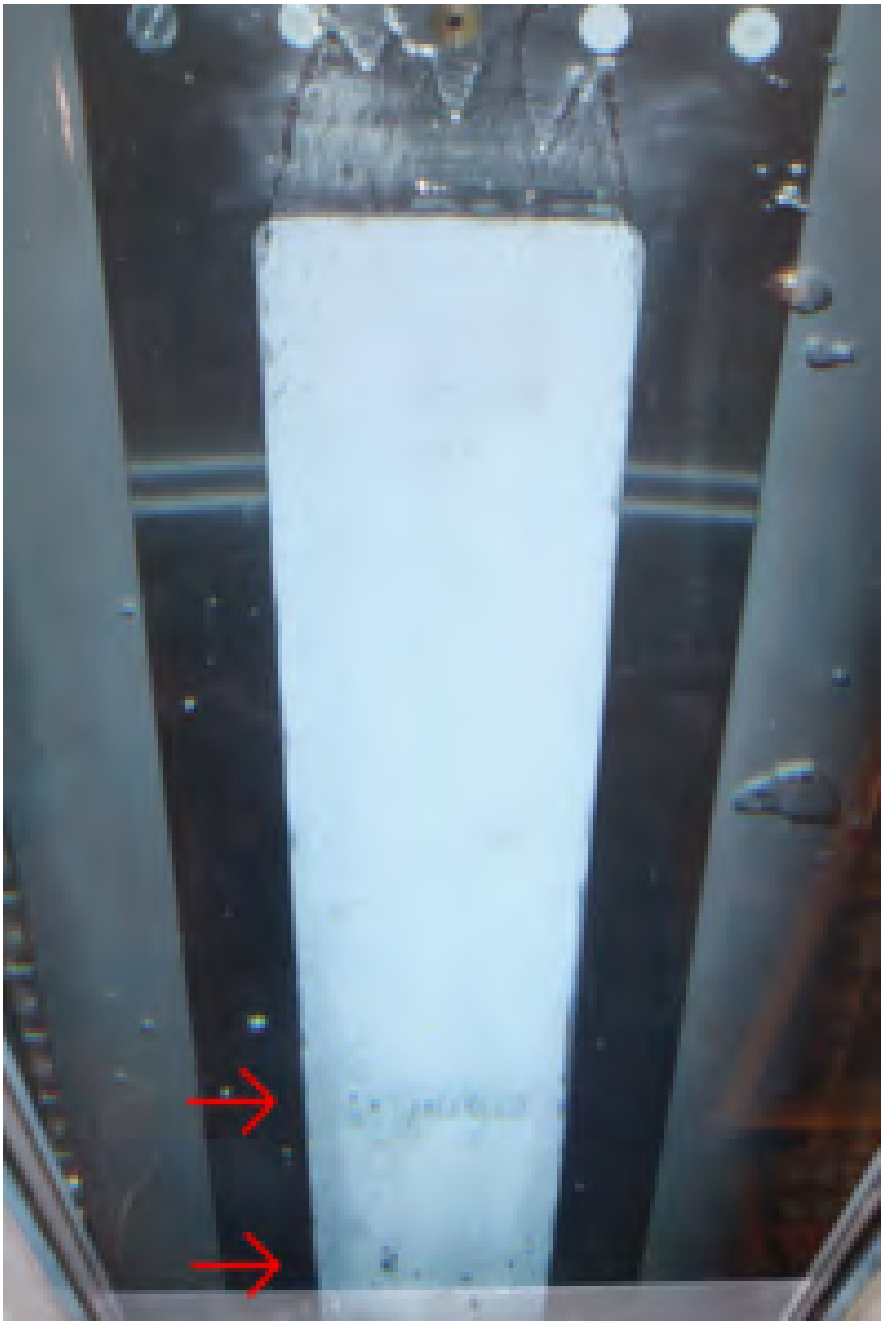

Figure 3.11: Additional image of test panel with low speed flow taken moments after the previous image. Portions of the panel have become completely wetted, particularly towards the leading edge, and are indicated by the red arrows. As was evident in the last image, air is again being washed off the downstream end of the panel. The tunnel is still well below the minimum operating velocity at the time this photograph was taken.

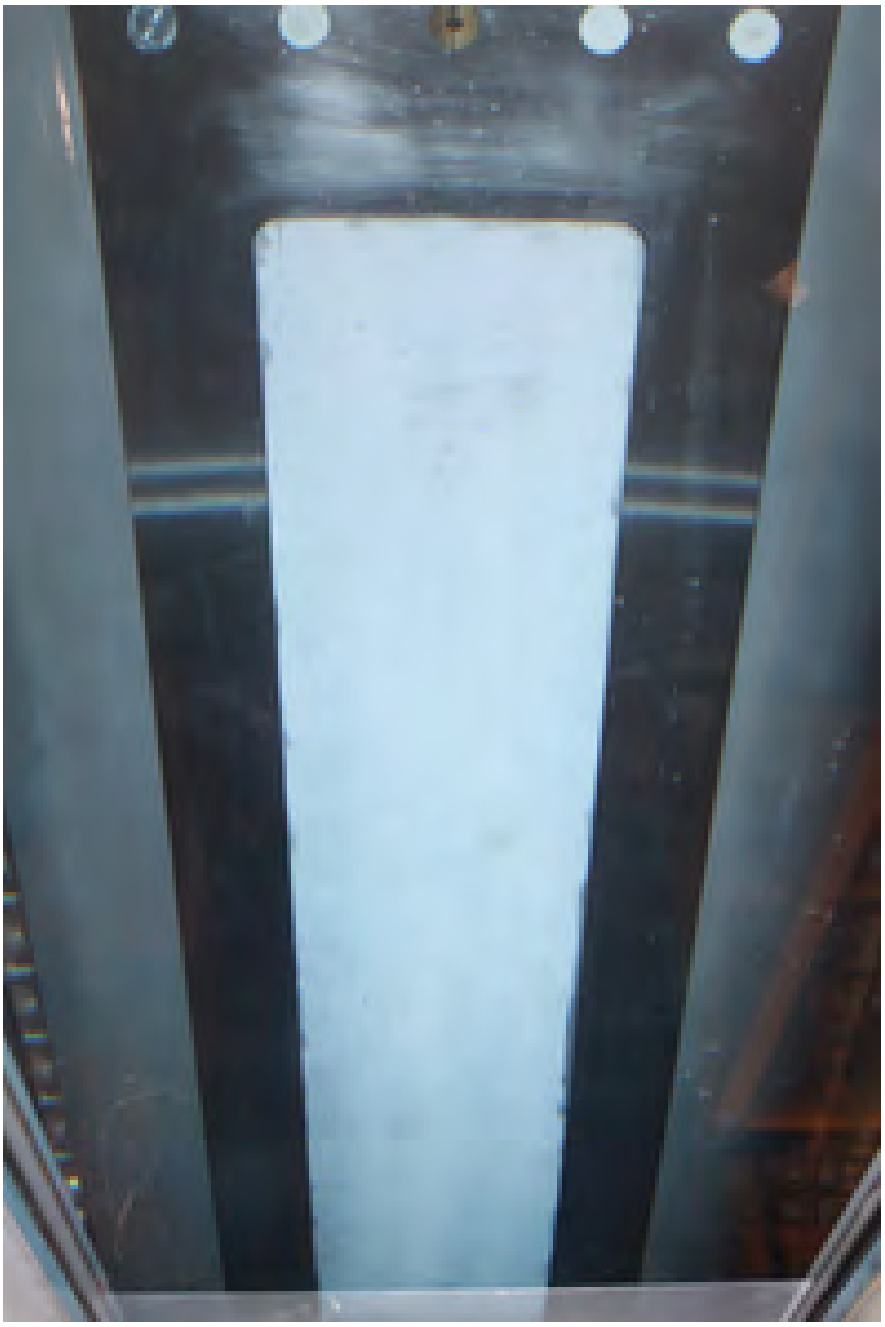

Figure 3.12: Test panel at $Re = 1.175 \times 10^6$. At the time of this photograph, the tunnel is operating at its minimum velocity of 2 m/s. The air layer that was seen in previous images is no longer visible. At this stage, the surface has become completely wetted. The damage around the edges of the panel is also more visible without the air layer obstructing the view.

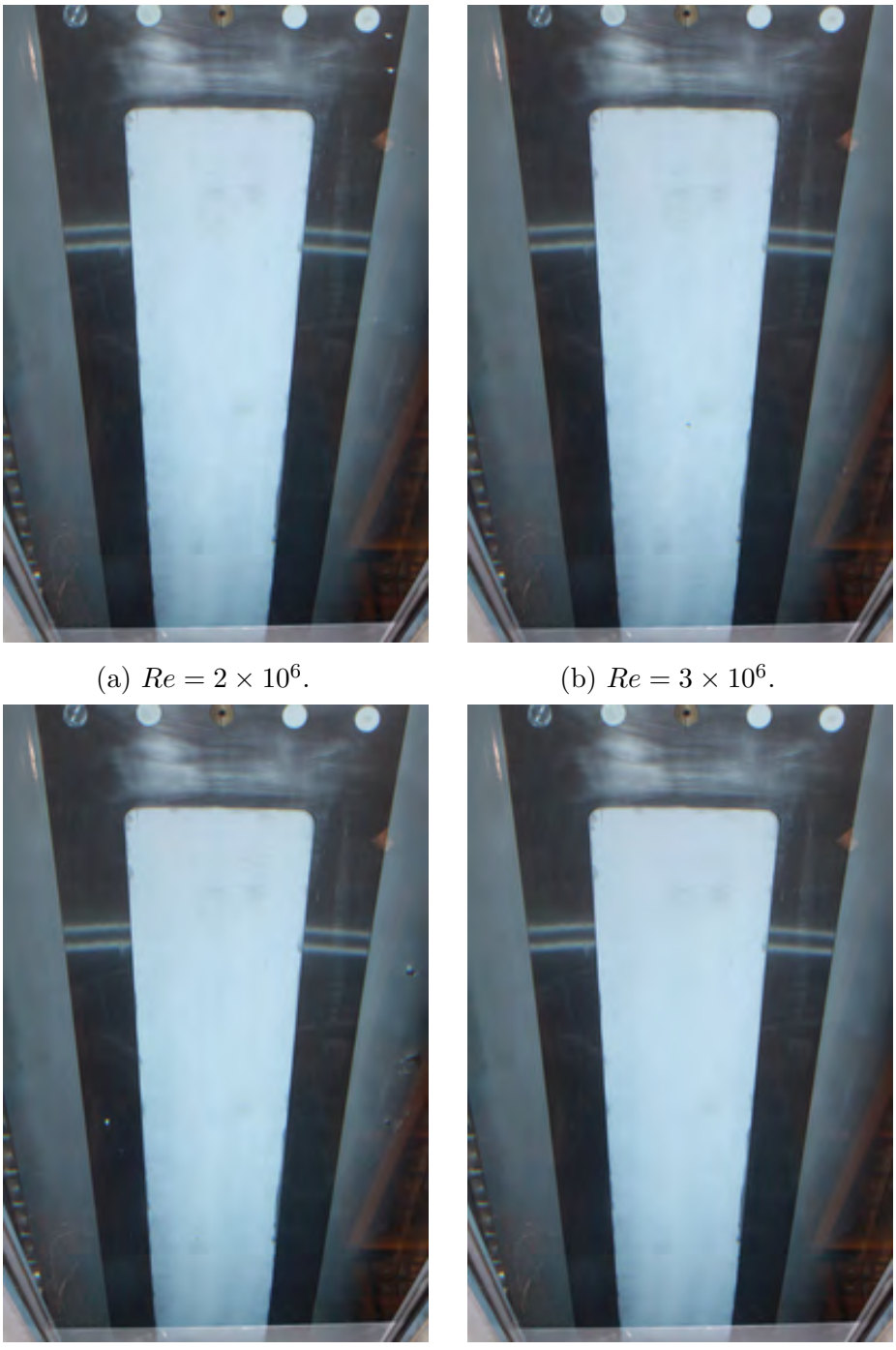

(a) $Re = 2 \times 10^6$. (b) $Re = 3 \times 10^6$.

(c) $Re = 4 \times 10^6$. (d) $Re = 5 \times 10^6$.

Figure 3.13: Test panel at various Reynolds numbers. Each of these photographs are almost identical to the image taken at $Re = 1.175 \times 10^6$. After the initial removal of the air layer already shown, no further observable changes occurred throughout the course of the experiments.

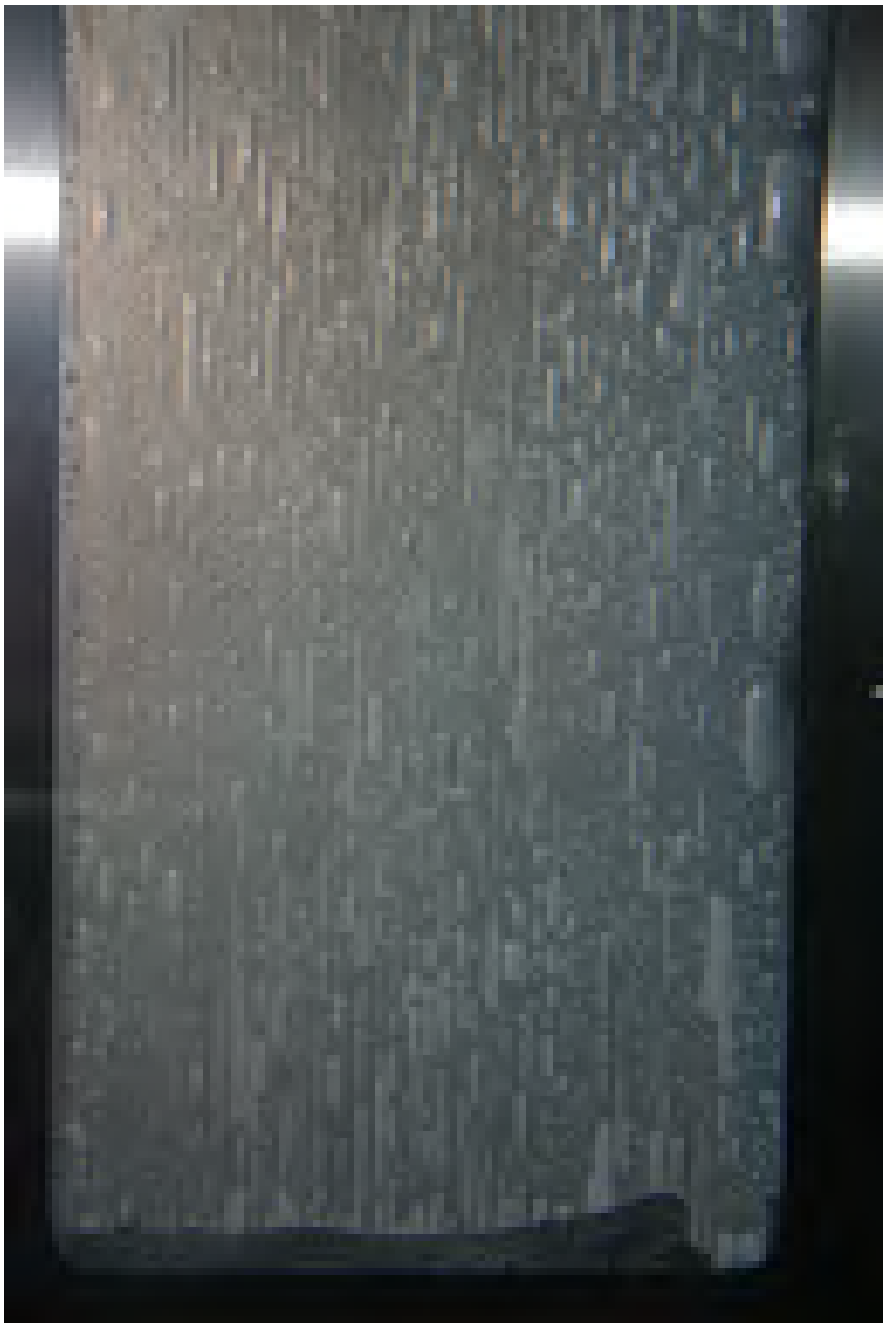

Figure 3.14: Close up image of the test panel after testing. After the testing was stopped and with pressure in the tunnel remaining at about 18 kPa, some air from the nuclei injection system was re-introduced into the test section. Upon reaching the ceiling of the test section, the air immediately de-wetted sections of the panel in the streamwise streaky pattern shown here. This image is of the leading edge of the panel and shows evidence of further damage to the panel that can only have been caused by the water flowing over it.

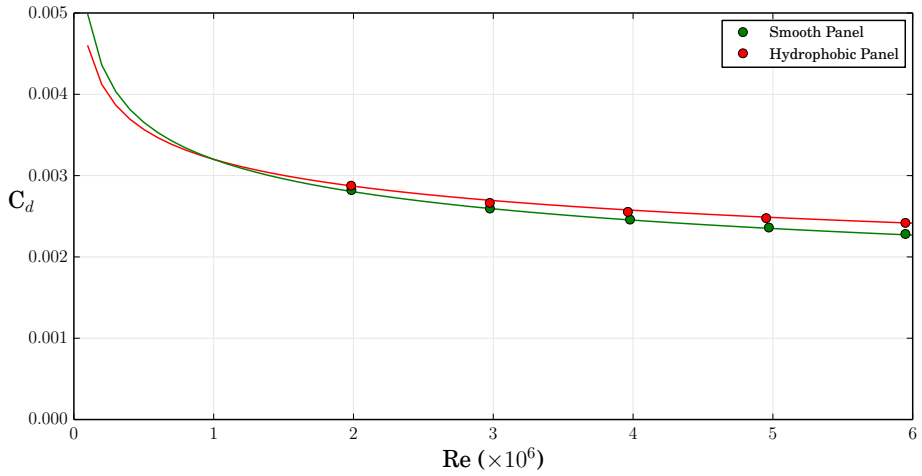

Figure 3.15: Results from the drag measurements of the smooth and hydrophobic surfaces. Logarithmic curves have been fitted to the results and extrapolated to lower Reynolds numbers. This indicates that at low speeds, the drag on the hydrophobic surface may be less than that of the smooth plate.

With the air layer seemingly removed before any drag measurements had been taken, the increased drag of the hydrophobic surface over that of the smooth plate is not unexpected. Figure 3.7 showed that as the Reynolds number increased, the difference between the drag of the smooth and hydrophobic test panels also increased. The drag on a surface due to turbulent channel flow can be approximately empirically calculated by an implicit relation known as the Colebrook equation ($\frac{1}{\sqrt{f}} = -2.0 \log\left(\frac{\epsilon/D}{3.7} + \frac{2.51}{Re\sqrt{f}}\right)$) which allows calculation of the friction factor (f) as a function of the relative roughness of the surface (ϵ/D) and the Reynolds number. This means that the results from the experiment can have logarithmic curves fitted to them. If this is done, and the values extrapolated to lower Reynolds numbers, the curves intersect and cross over, indicating the potential for drag reduction at lower speeds, an assumption that is consistent with the drag reduction shown by super hydrophobic surfaces in laminar flow.

Results of the second experiment that varied the cavitation number and pressure for a constant velocity can be seen in Figure 3.16. These results indicate that for the measured drag at $Re = 4 \times 10^6$, some drag reduction occurs as the cavitation number increases. Unfortunately, this same pattern was observed in

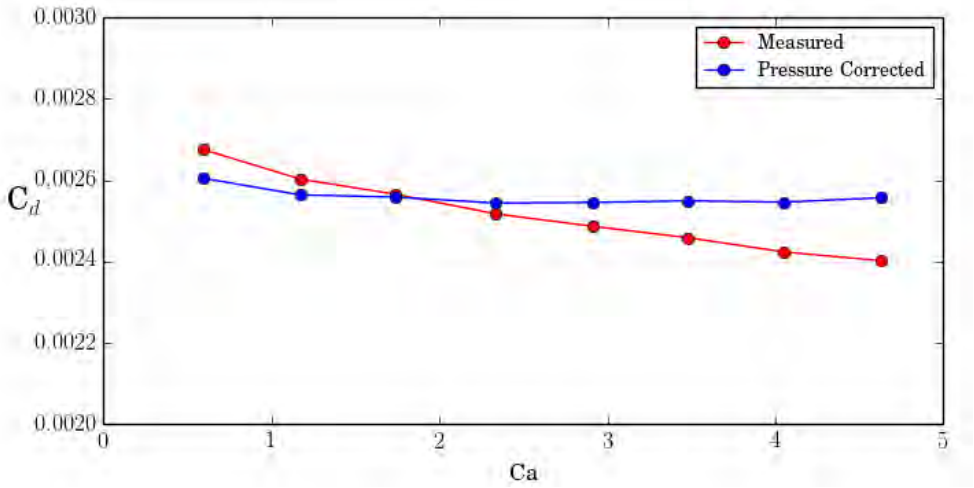

Figure 3.16: Variation of cavitation number results. The red points are the measured drag values for at $Re = 4 \times 10^6$. The blue points have been pressure corrected by performing the same measurements in a zero flow condition and applying the correction to the measured results.

the zero flow case to which is was compared. This indicates that the experimental rig has some structural dependence on the pressure within the test section. When the measured values were corrected to take this dependency into account, the results showed no drag reduction was achieved.

3.6 Summary

Although these experiments did not indicate any reduction in drag, they support the literature that shows the removal of air from the surface as a major obstacle in the pursuit of drag reduction. Further investigation into what causes the air to be removed could therefore assist in finding ways to maintain the air layer, and potentially find a method whereby these surfaces can be used to reduce drag in turbulent flow. In order to better study the behaviour of the surfaces at speeds lower than the minimum operating velocity of the facility, combined with the size of structures on the surface being measured in nano or micro metres, computational fluid dynamics offers the best method of further investigating flow over these surfaces.

Chapter 4

Lattice Boltzmann Method: Theory and Implementation

In order to simulate turbulent flow over a superhydrophobic surface, a method is required that is capable of replicating the numerous physical phenomena specific to hydrophobic surfaces at a nanometre to micrometre scale. With the topological features of the surfaces in that nanometre to micrometer scale (as explained in the previous chapter), mesoscopic modelling is the most appropriate choice.

Although standard computational fluid dynamics (CFD) codes which directly solve the Navier-Stokes equations are able to add and solve turbulence equations, they have significant drawbacks when simulating multiphase flow at this small scale. This is because at these scales, the forces resulting from surface tension dominate, which leads to spurious velocities at the interface between the fluids. These spurious velocities disrupt both the interface and the surrounding fluid and hence destroy the accuracy of the simulation. As a result of these problems, another method is needed to simulate multiphase flow at this scale.

The lattice Boltzmann method is a relatively new addition to the family of CFD techniques. It is based on the Boltzmann transport equation which describes the evolution of a system based on the transport of fictitious particles and is rooted in statistical mechanics[1]. It can be shown that the method is also able to recover the Navier-Stokes equations, meaning that hydrodynamic

[1]Statistical mechanics is a branch of physics which links the microscopic behaviour of atoms and molecules to the macroscopic behaviour of gases, fluids and solids.

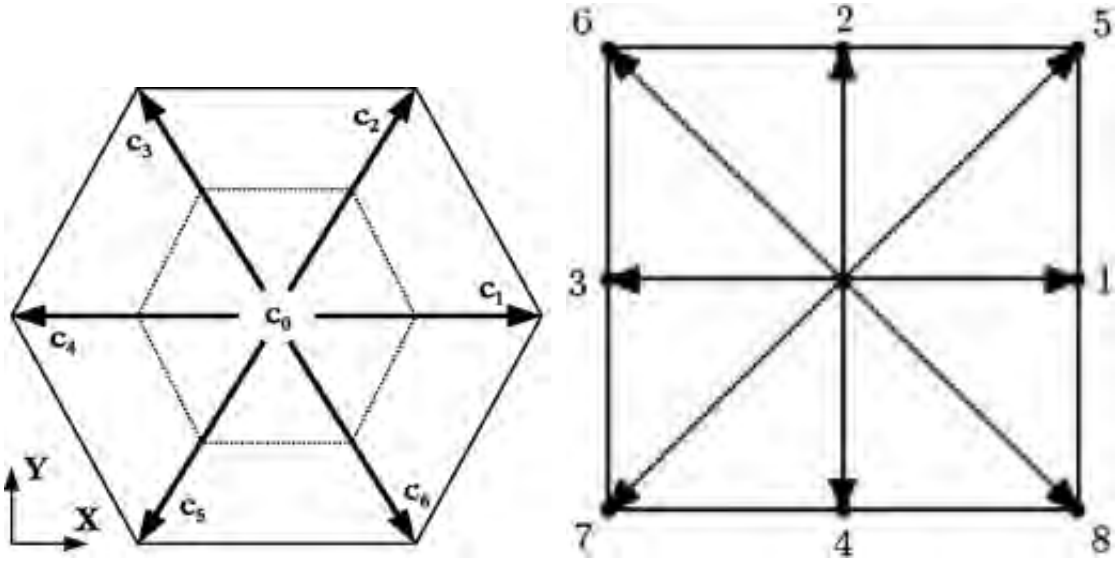

(a) D2Q7 (b) D2Q9

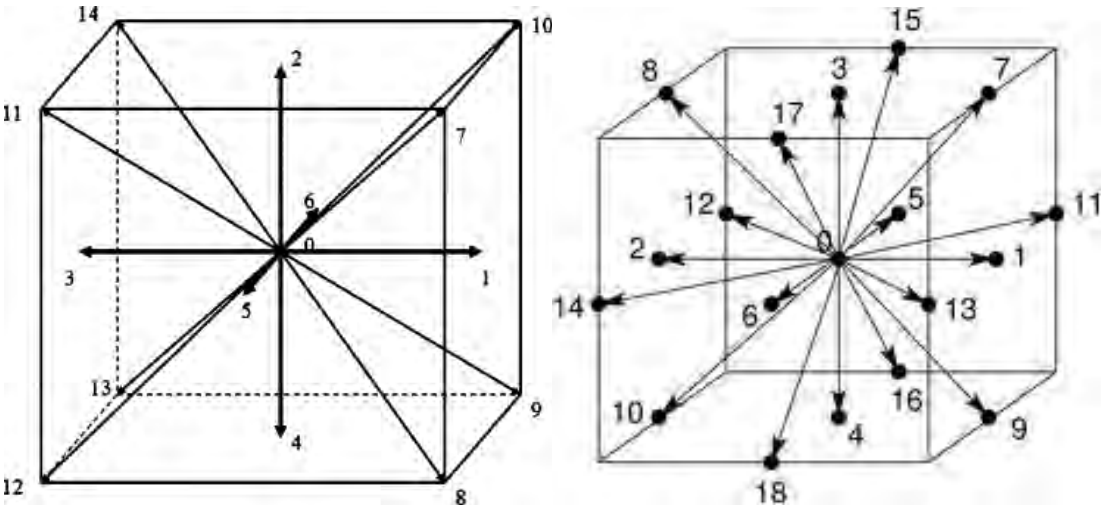

(c) D3Q15 (d) D3Q19

Figure 4.1: Commonly Used Lattices

simulations can be performed. This makes it an ideal choice for modelling flow over superhydrophobic surfaces as it is intrinsically a mesoscopic method. This allows it to model the fluid as a continuum but unlike the standard Navier-Stokes solvers, have better control of the micro scale physics involved.

Before proceeding, the important concept of a lattice needs to be presented. A lattice is a set of sites that are connected by links which form a discrete and regular space. In square lattices, the length of the links is Δx for links to nearest neighbours, $\sqrt{2}\Delta x$ for links to diagonal neighbours in an orthogonal lattice, or $\sqrt{3}\Delta x$ for longer links. The unit vector $\mathbf{e}$ is used to locate the surrounding nodes with the x,y and z values of $\mathbf{e}$ being either 0 or ± 1. Lattices are named based on both their dimensionality (d) and the number of links to neighbouring sites (ℓ) in the form DdQ(ℓ+1). Some common lattices can be seen in Figure 4.1 with (a) showing a hexagonal two-dimensional 6-speed lattice, (b) showing a square two-dimensional 9-speed lattice, (c) showing a square three-dimensional 15-speed lattice and (d) showing a square three-dimensional 19-speed lattice.

4.1 Background

The origins of the lattice Boltzmann method can be traced back to the cellular automata methods first conceived by Ulam and von Neumann in the 1940's. These methods consist of a dynamic system that is discretised in both space and time. The simulation occurs on a regular lattice of cells, each of which can take on one of a number of finite states and are updated synchronously according to a set of evolution rules. These rules are based on both the state of the cell being acted on and it's neighbouring cells. One of the best known implementations of cellular automata is "Conway's Game of Life", devised by John Conway [27] in 1970. This is a model in which cells take initial boolean values of either true (alive) or false (dead) and as the system evolves, the cells transition between alive and dead based on the states of their neighbours.

Another notable cellular automata model is that of the lattice gas cellular automata (LGCA). The original lattice gas model, known as the HPP model, was developed by Hardy, Pomeau and de Pazzis [53] in 1973 but it was not fully capable of modelling fluid flow as it did not correctly recover the Navier-Stokes

equations. However, an updated version by Frisch, Hasslacher and Pomeau [44], referred to as the FHP model, was able to do so. The FHP model was based on a D2Q7 lattice (see Fig 4.1a) in which all lattice nodes were spaced equidistantly ($\Delta x = 1$ lattice unit (lu)) and the particles could only move at one speed (1 lattice unit per time step (lu/ts)). At each node $\mathbf{x}$ there were up to 6 particles that could move along the links between nodes. Boolean variables contained the state of each link indicating whether or not a particle was traversing the link. The evolution of this system proceeded in a two stage process. The first step, where the particles travel along the links, is known as the transport or streaming step. Once the particles arrive at the next lattice node, they then undergo a collision step which determines which link they will travel on in the next time step.

The lattice gas cellular automata can be expressed mathematically as

$$N_i(x + e_i\delta x, t + \delta t) - N_i(x, t) = \Omega_i \tag{4.1}$$

where $N_i = 1$ if a particle is moving in the e_i direction, or $N_i = 0$ if it is not. Ω_i is known as the collision operator and controls the speed of the changes throughout the collision. By implementing a sufficiently complex collision operator, LCGA was used to simulate quite complex systems including artificial life [27], multiphase flows [114], porous media flows [136, 137], relativistic flows [4], chemical reactions [34], and quantum mechanics [12].

LGCA does still contain some major drawbacks, most noticeably a high degree of statistical noise, an exponential complexity when extending to three-dimensional systems, and a lack of Galilean invariance. Galilean invariance states that the laws of motion are the same in all inertial frames. An example of this can be thought of as an aeroplane flying through the air. Either the plane can be considered to be stationary with the fluid moving past it, or alternatively, the fluid can be considered to be stationary with the plane moving through it. Either way, the lift and drag on the plane should be the same. With the lattice gas cellular automata this was not the case.

In order to overcome these issues with the LCGA the lattice Boltzmann method was devised.

4.2 Theory of the Lattice Boltzmann Method

The major numerical difference between the lattice gas cellular automata and the lattice Boltzmann method is that the boolean variables indicating whether a particle is traversing a link or not are replaced by a particle density distribution $f(x, p, t)$. Instead of just a boolean value being used, the distribution gives the probability of finding a particle at position x with momentum p at time t. If this distribution function (neglecting the momentum) is substituted into the LGCA Equation (Equation 4.1), an evolution equation for the lattice Boltzmann model is formed.

$$f_i(x + e_i\delta x, t + \delta t) - f_i(x, t) = \Omega_i \tag{4.2}$$

Instead of dealing with boolean values the lattice Boltzmann model uses real-valued variables allowing macroscopic values of the flow being studied to be found by taking moments of the distribution function. For instance, the density and velocity of the fluid being simulated can be calculated by taking the zeroth and first moments respectively, as shown in Equation 4.3.

$$\rho(x, t) = \sum_{i=0}^{n} f_i(x, t) \qquad \mathbf{u}(x, t) = \frac{1}{\rho} \sum_{i=0}^{n} f_i(x, t) \cdot \mathbf{e}_i \tag{4.3}$$

This also necessitates that the lattice Boltzmann collision operator be different to that of the LGCA operator. Higuera *et. al.* [60] proposed a linear collision operator centred around a local equilibrium solution. One of the most common linear collision operators in use today is the BGK model, initially proposed by Bhatnager, Gross and Krook [9] in 1954 and first implemented by Koelmann [73] and Qian *et. al.* [103], and is shown in Equation 4.4[1].

$$\Omega_i(f(x, t)) = \frac{1}{\tau}[f_i^{eq}(x, t) - f_i(x, t)] \tag{4.4}$$

[1] A derivation of this Equation can be seen in Appendix C.1

Table 4.1: Parameters of commonly used lattices.

Lattice	Parameters
D2Q7	$\mathbf{e}_i = \begin{cases} (0,0) & \text{i = 0} \\ (\pm 1, 0), (\pm 1/2, \pm\sqrt{3}/2) & \text{i = 1, 2, 3, 4, 5, 6} \end{cases}$ $w_i = \begin{cases} 1/2 & \text{i = 0} \\ 1/12 & \text{i = 1, 2, 3, 4, 5, 6} \end{cases}$ $c_s^2 = 1/4$
D2Q9	$\mathbf{e}_i = \begin{cases} (0,0) & \text{i = 0} \\ (\pm 1, 0), (0, \pm 1) & \text{i = 1, 2, 3, 4} \\ (\pm 1, \pm 1) & \text{i = 5, 6, 7, 8} \end{cases}$ $w_i = \begin{cases} 4/9 & \text{i = 0} \\ 1/9 & \text{i = 1, 2, 3, 4} \\ 1/36 & \text{i = 5, 6, 7, 8} \end{cases}$ $c_s^2 = 1/3$
D3Q15	$\mathbf{e}_i = \begin{cases} (0,0,0) & \text{i = 0} \\ (\pm 1, 0, 0), (0, \pm 1, 0), (0, 0, \pm 1) & \text{i = 1, 2, ..., 6} \\ (\pm 1, \pm 1, \pm 1) & \text{i = 7, 8, ..., 14} \end{cases}$ $w_i = \begin{cases} 4/9 & \text{i = 0} \\ 1/9 & \text{i = 1, 2, 3, 4} \\ 1/36 & \text{i = 7, 8, ..., 14} \end{cases}$ $c_s^2 = 1/3$
D3Q19	$\mathbf{e}_i = \begin{cases} (0,0,0) & \text{i = 0} \\ (\pm 1, 0, 0), (0, \pm 1, 0), (0, 0, \pm 1) & \text{i = 1, 2, ..., 6} \\ (\pm 1, \pm 1, 0), (\pm 1, 0, \pm 1), (0, \pm 1, \pm 1) & \text{i = 7, 8, ..., 18} \end{cases}$ $w_i = \begin{cases} 1/3 & \text{i = 0} \\ 1/18 & \text{i = 1, 2, 3, 4} \\ 1/36 & \text{i = 7, 8, ..., 18} \end{cases}$ $c_s^2 = 1/3$

By combining Equations 4.2 and 4.4, and adding a term to incorporate additional forces onto the right hand side, the complete BGK lattice Boltzmann equation (also known as the LBGK equation) is generated and is shown as Equation 4.5).

$$f_i(x + e_i, t + \delta t) - f_i(x, t) = \frac{1}{\tau}[f_i^{eq}(x, t) - f_i(x, t)] + \mathbf{F}_i(x, t) \tag{4.5}$$

The addition of the force term can be used to incorporate external forces, be they chemical, gravity, pressure, electro-magnetic or some combination of these or others. Although there are numbers of methods of incorporating these forces, in this work they have been added as can be seen in Equation 4.6.

$$f_i(x + e_i, t + \delta t) - f_i(x, t) = \frac{1}{\tau}[f_i^{eq}(x, t) - f_i(x, t)] + w_i \rho F_\alpha e_i / c^2 \tag{4.6}$$

This has the effect of increasing the population density in the direction that the force (F) is acting, and decreasing the population density in the opposite direction whilst keeping the total density constant.

4.2.1 Equilibrium Distribution Function

The equilibrium distribution function f_i^{eq} plays a major role in the collision operator and therefore deserves some attention. It's basis is in the continuum Maxwell-Boltzmann distribution function, shown in Equation 4.7, with R being an ideal gas constant; d being the dimensionality being considered; ρ, $\mathbf{u}$ and T being the macroscopic density, velocity and temperature respectively; and $\mathbf{e}$ being a directional vector as was the case in the LGCA models. The equilibrium distribution function used in this work is appropriate for isothermal incompressible flows, however variations to model temperature dependant, or compressible flows are possible.

$$f^{eq} = \frac{\rho}{(2\pi RT)^{d/2}} \exp\left(-\frac{(\mathbf{e} - \mathbf{u})^2}{2RT}\right) \tag{4.7}$$

By performing a Taylor series expansion for low Mach number ($M = \frac{\mathbf{u}}{c_s} \ll 1$ where c_s is the speed of sound) Equation 4.7 can be written as

$$f = \frac{\rho}{(2\pi RT)^{d/2}} \exp\left(-\frac{(\mathbf{e}\cdot\mathbf{e})}{2RT}\right) \exp\left(\frac{(\mathbf{e}\cdot\mathbf{u})}{2RT} - \frac{(\mathbf{u}\cdot\mathbf{u})}{2RT}\right) \tag{4.8}$$

$$\begin{aligned} &= \frac{\rho}{(2\pi RT)^{d/2}} \exp\left(-\frac{(\mathbf{e}\cdot\mathbf{e})}{2RT}\right) \\ &\quad \times \left[1 + \frac{\mathbf{e}\cdot\mathbf{u}}{RT} + \frac{(\mathbf{e}\cdot\mathbf{u})^2}{2\left(RT\right)^2} - \frac{\mathbf{u}^2}{2RT}\right] + O\left(\mathbf{u}^3\right) \end{aligned} \tag{4.9}$$

As was discussed in Section 2.1.2, fluid motion is governed by three key conservation equations, namely mass, momentum and energy. These conservation laws act as constraints on the collision operator and therefore act directly on the equilibrium distribution function. In order to meet these conservation requirements, and to achieve the lattice symmetry required by the Navier-Stokes equation, moments of the equilibrium distribution function need to be exactly recover the following:

$$\sum_i f_i^{eq} = \rho \tag{4.10}$$

$$\sum_i f_i^{eq} \left(e_{i\alpha} - u_\alpha\right) = \rho u_\alpha \tag{4.11}$$

$$\sum_i f_i^{eq} \left(e_{i\alpha} - u_\alpha\right)\left(e_{i\beta} - u_\beta\right) = \rho c_s^2 \delta_{\alpha\beta} \tag{4.12}$$

$$\sum_i f_i^{eq} \left(e_{i\alpha} - u_\alpha\right)\left(e_{i\beta} - u_\beta\right)\left(e_{i\gamma} - u_\gamma\right) = 0 \tag{4.13}$$

These equations can be thought of as the lattice Boltzmann equivalent conservation equations with mass being conserved in Equation 4.10, momentum being conserved in Equation 4.11, and energy being conserved in Equation 4.12 and 4.13. These constraint mean that the values of the equilibrium distribution function exactly equal the d-dimensional Maxwell-Boltzmann equation up to fourth order.

If the first term of Equation 4.9 is replaced with w_i with values for selected lattice geometries given in Table 4.1[1], and with the substitution of

[1]The substitution of w_i is a simplification. A full derivation and procedure by which the w_i values are calculated can be found in the work of He and Luo [55]

$RT = c_s^2 = 1/3$, the equilibrium distribution function to be used is obtained and shown in Equation 4.14.

$$f_i^{eq} = w_i \rho \left[1 + 3\frac{\mathbf{e}_i \cdot \mathbf{u}}{c^2} + \frac{9}{2}\frac{(\mathbf{e}_i \cdot \mathbf{u})^2}{c^4} - \frac{3}{2}\frac{\mathbf{u}^2}{c^2} \right] \tag{4.14}$$

If this is combined with the momentum flux tensor, shown in of Equation 4.15, the Navier-Stokes equation can be recovered.

$$\Pi_{\alpha\beta} = \sum_i \left(\mathbf{e}_i\right)_\alpha \left(\mathbf{e}_i\right)_\beta \left[f_i^{eq} + \left(1 - \frac{1}{2\tau}\right) f_i^{(1)} \right] \tag{4.15}$$

$$\Pi_{\alpha\beta}^{(0)} = \sum_i \left(\mathbf{e}_i\right)_\alpha \left(\mathbf{e}_i\right)_\beta f_i^{eq} = p\delta_{\alpha\beta} + \rho u_\alpha u_\beta \tag{4.16}$$

$$\Pi_{\alpha\beta}^{(1)} = \left(1 - \frac{1}{2\tau}\right) \sum_i \left(\mathbf{e}_i\right)_\alpha \left(\mathbf{e}_i\right)_\beta f_i^{eq} = \nu \left(\nabla_\alpha \left(\rho \mathbf{u}_\beta\right) + \nabla_\beta \left(\rho \mathbf{u}_\alpha\right) \right) \tag{4.17}$$

where $p = \rho/3$ is the pressure giving a constant sound speed $c_s = 1/\sqrt{3}$ and the kinematic viscosity is given by

$$\nu = c_s^2 \left(\tau - \frac{1}{2}\right) \delta t \tag{4.18}$$

resulting in a momentum equation of

$$\rho \left(\frac{\partial \mathbf{u}_\alpha}{\partial t} + \nabla_\beta \cdot \mathbf{u}_\alpha \mathbf{u}_\beta \right) = -\nabla_\alpha p + \nu \nabla_\beta \cdot \left(\nabla_\alpha \rho \mathbf{u}_\beta + \nabla_\beta \rho \mathbf{u}_\alpha \right) \tag{4.19}$$

which is equivalent to that shown previously in Section 2.1.2.4. A more detailed de-revision of this can be found in the seminal work of Chen & Doolen [22].

4.2.2 Equations of State

The concept introduced in the previous section of the pressure being directly related to the density occurs due to the lattice Boltzmann method obeying an

equation of state. If the fluid being simulated is modelled as an ideal fluid, the equation of state used is

$$pV = mRT \tag{4.20}$$

With the knowledge that the speed of sound is proportional to the temperature (T) and the gas constant (R), taking the volume (V) of a cell to be 1, and replacing the mass (m) with the cell density (ρ), the ideal gas equation can be rearranged as shown in Equation 4.21 to show that the pressure is directly proportional to the fluid density. This means that the time consuming pressure-velocity coupling that occurs in standard CFD solvers does not need to be done in the lattice Boltzmann method.

$$p = \frac{mRT}{V} = \frac{RT}{V}\rho = \frac{1/3}{1}\rho = \rho/3 \tag{4.21}$$

For simulations where fluids are not to be modelled as ideal gases, for instance in situations involving multiple phases or components alternative equations of state can be used. This will be expanded on in Section 4.7.

4.3 Operation of the Lattice Boltzmann Method

As was the case with the LGCA, the lattice Boltzmann model runs with two operations per iteration, *streaming* and *collision*.

$$\underbrace{f_i(x + e_i, t + \delta t) - f_i(x, t)}_{Streaming} = \underbrace{\frac{1}{\tau}[f_i^{eq}(x, t) - f_i(x, t)] + \mathbf{F}_i(x, t)}_{Collision} \tag{4.22}$$

The first "streams" the particle distributions to the neighbouring nodes, and the second step, known as the "collision", acts to relax the density populations at each lattice cell back towards their equilibrium values. The name of this second step appears to have carried over from the early cellular automata models, as unlike the CA models, particles in the lattice Boltzmann method do not collide per se. The collision step is also the time that interactions between the fluid and any walls within the domain occur, as will now be discussed.

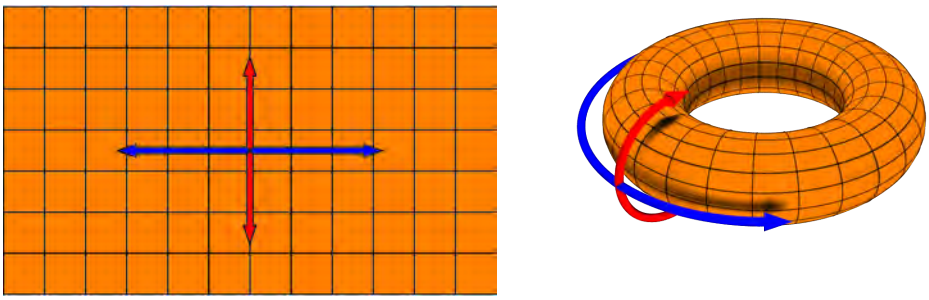

Figure 4.2: Domain that is periodic in two dimensions.

4.3.1 Boundary Conditions

Boundary conditions play a large role in the accuracy of any CFD solution as they affect the behaviour of the fluid within the domain. Like all types of CFD, the lattice Boltzmann method has a number of different boundary conditions types that can be implemented.

4.3.1.1 Periodic Boundaries

Periodic boundary conditions are the easiest boundary conditions to implement and are ideal when surface effects are negligible. They act by connecting the open edges of the domain, redirecting the fluid that is flowing out of one side back into the other side. In this way, they are able to isolate the bulk of the fluid from the actual boundaries of the system. For example, a domain that is periodic in two dimensions can be thought of as a torus, as shown in Figure 4.2.

4.3.1.2 Walls

Although there are several problems that can be studied using only periodic conditions, most real world problems contain at least one solid boundary. To reproduce this in the lattice Boltzmann method walls are implemented using a bounce-back method. The basic idea behind the bounce back scheme is quite simple and states that when an incoming particle reaches a wall node it is reflected back into the fluid. Depending on how it is reflected, the boundary can be set as a no-slip wall, a partial slip wall or a free slip wall. For a no-slip wall, the particle

is reflected back in the direction from which it arrived. Summing the particle momentum both before and after the collision shows that the momentum and hence the velocity at the wall is equal to zero, as it should be for a no-slip condition. To instead create a free-slip wall, the incoming particles are reflected back out into the fluid with their velocity component normal to the wall reversed, but their parallel component unchanged. The free-slip condition can also be thought of as a symmetry condition. It is also possible to reflect part of the particle density in each direction to create a partial slip wall. This is further illustrated in Figure 4.3.

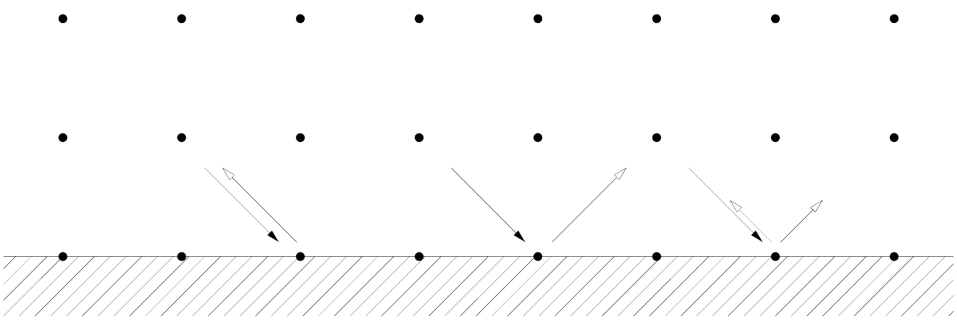

Figure 4.3: Wall type boundary conditions. The black headed arrow is the incoming population and the open headed arrow is the out going population. From left to right : No Slip Wall, Free Slip Wall, Partial Slip Wall.

As was discussed in Section 2.1.1, when fluid flows over a surface, a boundary layer forms that exerts a force on both the fluid and the wall. This force acts to retard the motion of the fluid and is known as drag. The total amount of drag acting on the wall is found by an application of Newtons second law, $\mathbf{F} = m\mathbf{a} = \frac{\Delta \mathbf{P}}{\delta t}$, where $\Delta \mathbf{P}$ in this case is a change in momentum. When a fluid particle collides with a no slip wall it is reflected back in the direction opposite to that in which it arrived. This can be viewed as an elastic collision meaning that both the wall and the particle (p) experience the same magnitude of force (in opposite directions). As the collision occurs in a single time step (δt), and using the density as the particle mass, the force acting on the wall due to the change of momentum of the fluid particle can be found. This is shown mathematically in Equation 4.23.

$$\begin{aligned}\mathbf{F}_p &= \frac{\Delta \mathbf{P}_p}{\delta t} \\ &= \frac{\rho \mathbf{v}_{out} - \rho \mathbf{v}_{in}}{\delta t}\end{aligned}$$

Given that

$$\mathbf{v}_{in} = -\mathbf{v}_{out} \tag{4.23}$$

$$\begin{aligned}\mathbf{F}_p &= 2\rho \mathbf{v}_{p,out}/\delta t \\ \mathbf{F}_{wall} &= -\mathbf{F}_p \\ &= -2\rho \mathbf{v}_{p,out}/\delta t\end{aligned}$$

This gives the momentum transfer and hence drag on each wall node. The total drag on the wall is then found by summing the drag at each wall node in the domain.

$$\text{Total Drag} = \sum^{\text{All Wall Nodes}} \mathbf{F}_{wall}$$

Some flow scenarios require fluid to enter or exit the computational domain. This is achieved by using boundary conditions known as inlets and outlets, or collectively as openings. The lattice Boltzmann method has a number of different ways of implementing these boundaries including velocity openings [77], pressure opening [152], porous plugs and zero-gradients [121].

Of these, only the velocity and pressure conditions have been used in this work, and only in the validation process. As such, they will not be further discussed here, however details of them are available in the above references.

4.3.2 Unit Conversion

Unlike most other CFD solvers, the lattice Boltzmann method uses its own system of units, with lengths measured in lattice units, and time measured in time steps. Simulations of physical systems are of little use unless they are able to replicate both the geometry and scale of the physical system in question, and as such, a way of converting between physical units and lattice Boltzmann units needs to

be used. This process is achieved by the use of a non-dimensional intermediate step. For the lattice Boltzmann simulation to accurately reproduce the physical system the non-dimensional values for both the physical and numerical systems need to be the same.

To illustrate this, an example of flow of sea water through a smooth pipe is used. The characteristics of the flow are dependent on a number of variables including the pipe diameter (ϕ), the speed of the flow (U), and the density (ρ) and viscosity (μ) of the water. In standard SI units, these can be measured in meters (m), meters per second (m/s), kilograms per cubic meter (kg/m^3), and meters squared per second (m^2/s) respectively. Converting each of these parameters into lattice Boltzmann units directly would not necessarily ensure that the simulated system and the physical system were equivalent. However, by using the physical parameters to create a non-dimensional number, an equivalent set of lattice Boltzmann parameters can be found. In the pipe flow case, the logical non-dimensional number to use is a Reynolds number based on pipe diameter, $Re_\phi = \frac{\rho U \phi}{\mu}$. For a 10 mm diameter pipe and a flow velocity of 0.01 m/s, this corresponds to a Reynolds number of ≈ 95, as shown in Equation 4.24.

$$\begin{aligned} Re_\phi &= \frac{\rho U \phi}{\mu} \\ &= \frac{1025 \times 0.01 \times 0.01}{1.88 \times 10^{-3}} \\ &= 94.9 \end{aligned} \tag{4.24}$$

For the lattice Boltzmann simulation to correctly reproduce the behaviour of the flow, the Reynolds number of the simulation needs to also be ≈ 95. If a domain chosen with a channel diameter of 40 lattice units, along with a relaxation factor of $\tau = 0.6$, which as Equation 4.18 showed gives a kinematic viscosity of 0.033 ls^2/ts, and using the standard lattice Boltzmann convention of modelling fluids with a density of $\rho = 1$, the velocity of the flow required to give an equivalent Reynolds number to the the physical system can be found, as shown in Equation 4.25.

$$\begin{aligned} U &= \frac{Re_\phi \, \nu}{\phi} \qquad \text{where } \nu = \frac{\mu}{\rho} \\ &= \frac{94.9 \times 0.033}{40} \\ &= 0.0783 \; lu/ts \end{aligned} \tag{4.25}$$

The specific values of the LBM parameters, can be almost anything as long as two constraints are met. Latt [76] states that the parameters should be equivalent to the physical system, and that they should be chosen in such a way that the system reaches the required accuracy. In practice, this second constraint means that the relationship between the choice of resolution of the system and the selected time step need to be balanced. This will be expanded on further when stability and accuracy of the lattice Boltzmann method are discussed in Section 4.4.1.

Although a velocity conversion has been shown here, other quantities can also be converted between physical and lattice Boltzmann units in the same way. Forces and drag can be converted by the use of drag co-efficients, and surface tension and buoyancy terms can be converted through the intermediate calculation of the Eötvös number and the Weber number.

4.3.3 Validation

Having introduced the method and some basic boundary conditions and units, a test case can be run to validate the implementation of this into code in a laminar flow environment. An ideal benchmark to use for this validation is the Poiseuille flow as it is possible to analytically calculate the solution to the flow which can then be compared to the simulation result [57].

The simulation domain is the same as that presented above, with a channel of height 40 (half channel height of $\delta = 20$) with walls on the top and bottom boundaries and periodic conditions on the sides. A relaxation factor of $\tau = 0.6$ was used, with a driving force of $F = 1.29 \times 10^{-5}$. This resulted in an average velocity of 0.0816 lu/ts and a Reynolds number of $Re_\phi = 95.6$. The velocity at any point in a Poiseuille flow can be found analytically using Equation 4.26.

$$\frac{u(y)}{U_0} = 1 - \left(\frac{y - \delta}{\delta}\right)^2 \tag{4.26}$$

where $\frac{u(y)}{U_0}$ is the normalised velocity with respect to the channel centreline velocity. A plot of the velocities from the discrete cells in the simulation is compared with the analytical results for the channel in Figure 4.4. As can be seen, the points from lattice Boltzmann method lie on the analytical results, to

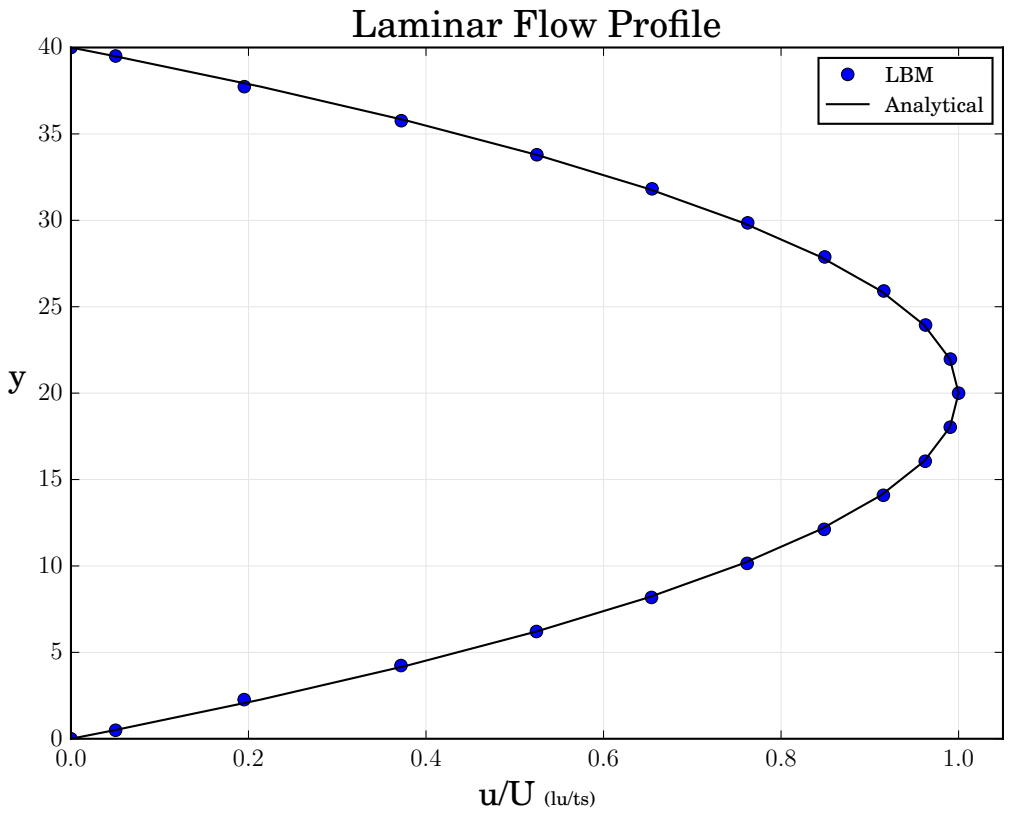

Figure 4.4: Simulation vs Analytical Result of a Poiseuille flow at $Re_\phi = 100$. The flow is stationary at the channel walls at $y = 0$ and $y = 40$ while the maximum velocity occurs at the channel centreline at $y = 20$. The velocity profile is parabolic as would be expected for a Poiseuille flow.

an accuracy of better than 95%, indicating that the lattice Boltzmann method can accurately reproduce hydrodynamic flow.

Having compared the implemented code with analytical results, and showing the validity of the code, the method can now be extended by adding the complexity of turbulence.

4.4 Turbulence

Turbulence is a common feature in both nature and commercial applications, and as a result of this, there has been significant work done to extend the lattice Boltzmann method so that it can correctly account for this physical phenomenon. In this section, methods of implementing turbulence into the LBM will be introduced and discussed.

4.4.1 Turbulence and the lattice Boltzmann method

There are two different ways in which turbulence can be implemented into a lattice Boltzmann solver. In a similar technique to the standard Navier-Stokes solvers, dedicated turbulence models can be added. These act to model the small eddies and simulate the large eddies. Turbulence models such as the k-ϵ and k-ω have been shown to work by Teixeira [123] while others like the eddy-viscosity, and Smagorinsky LES have been implemented by Hou *et. al.* [62]. These models are added by either adding additional terms to the collision operator term (Equation 4.4) in the case of the k-ϵ and eddy-viscosity, or modifying the relaxation time on a cell by cell basis for the Smagorinsky model. These types of models are intended to allow high Reynolds number flows to be simulated in large domains over large geometries.

The alternative to turbulence models is to simulate the entirety of the flow including the sub-grid eddies. To achieve this, the grid needs to be refined to the point that the eddies are no longer sub-grid and can be completely modelled. This is the realm of Direct Numerical Simulations (DNS) which although accurate, are also very computationally expensive. It can be shown that in a DNS, the ratio of the smallest to the largest scales in the flow is proportional to $Re^{-3/4}$. With increasing Reynolds number, the separation between the scales therefore increases, proportionally increasing the computational cost. It can also be shown that the total number of points required to model a turbulent simulation scales as $Re^{9/4}$, meaning that in order to model flow around an average sized cargo ship where the Reynolds number can be up to 10^9, a total of 3×10^{22} points would be needed!

Much of the computational expense of the DNS method, indeed sometimes up to 90%, is attributed to the pressure-velocity coupling calculations. A benefit of the lattice Boltzmann method is that it does not need to perform these expensive calculations as the pressure and velocity are linked via the equation of state as was discussed in Section 4.2.2. With the pressure being linked to the density by $p = \rho c_s^2 = \rho/3$, the lattice Boltzmann method is capable of performing similar simulations to a DNS for a reduced computational cost. This was shown to be a valid approach by Bespalko, Pollard and Uddin [8] and is the method implemented in this work.

As was discussed in Section 4.2.1, in order for the lattice Boltzmann method to recover the Navier-Stokes equations, the viscosity needed to be related to the relaxation time by the equation

$$\nu = c_s^2(\tau - \frac{1}{2})\delta t \tag{4.27}$$

From this it can be seen that for a fixed value of δt[1], in order to reduce the viscosity and correspondingly increase the Reynolds number, the relaxation value τ needs to be reduced; however, τ is limited to a minimum value $> \frac{1}{2}$ otherwise we reach the physically impossible scenario of having a negative viscosity. The low relaxation value also corresponds to a low coefficient of numerical diffusion, leading to instability in the model. In practice, lowering the relaxation value below about 0.51 leads to levels of instability so high that the model fails unless other methods of stabilisation are added.

4.4.1.1 Channel Dimensions

In similar circumstances to the direct numerical simulation methods, a drawback to modelling turbulence with the lattice Boltzmann method comes in the size of the domain required to model high Reynolds number flows. In the case of channel flow, for a selected relaxation value and corresponding viscosity, the Reynolds number becomes only a function of the channel height δ and the fluid velocity U shown in Equation 4.28

$$Re_\phi = \frac{U\delta}{\nu} \tag{4.28}$$

[1]Although δt is strictly a variable, in order to maintain stability it is prefereable to keep it of the order of $\delta x/\delta t^2 \approx 1$. This will be further discussed in Section 4.5

Table 4.2: Reynolds Numbers vs Channel Dimensions for $\tau = 0.51$

Re_ϕ	Height	Length	Width	Number of Cells
10	0.22	0.35	0.10	$0.01^\star$
100	2.22	3.49	1.05	$8.12^\star$
1000	22	35	10	8123
10000	222	349	105	8.123×10^6
100000	2222	3491	1047	8.123×10^9

* These values are the numerically required sizes to capture turbulent motion in a channel; however, in reality, a channel height of at least 10 cells would be needed to reproduce an adequate velocity profile. With $\tau < 0.51$ the system would be extremely unstable and would probably fail.

With the fluid velocity being limited to a maximum of $\approx 0.15\ lu/ts$ due to the low Mach number dependence ($Ma = \frac{u_{max}}{c_s} \ll 1$), this means that at high speeds, the Reynolds number is directly proportional to the channel height.

Jiminez and Moin [71] found that the minimum sized domain capable of capturing turbulence is $\pi\delta \times \delta \times 0.3\pi\delta$ in the streamwise, wall normal and spanwise directions respectively and where δ is the half height of the channel. Table 4.2 shows the required channel dimensions required to attain selected Reynolds numbers. From this, it can be clearly seen that trying to model flows with Reynolds numbers up to and exceeding 100000 becomes very computationally expensive[1].

As is the convention in boundary layer studies, instead of using a Reynolds number based on length or channel diameter, a Reynolds number based on wall friction velocity is used instead. This gives a better indication of the near wall effects due to viscosity and velocity. The typically used velocity scale in the near wall region is known as the friction or shear velocity and is defined as

$$u^\star = \sqrt{\frac{\tau_w}{\rho}} \tag{4.29}$$

[1]See note of hardware used in Appendix B.

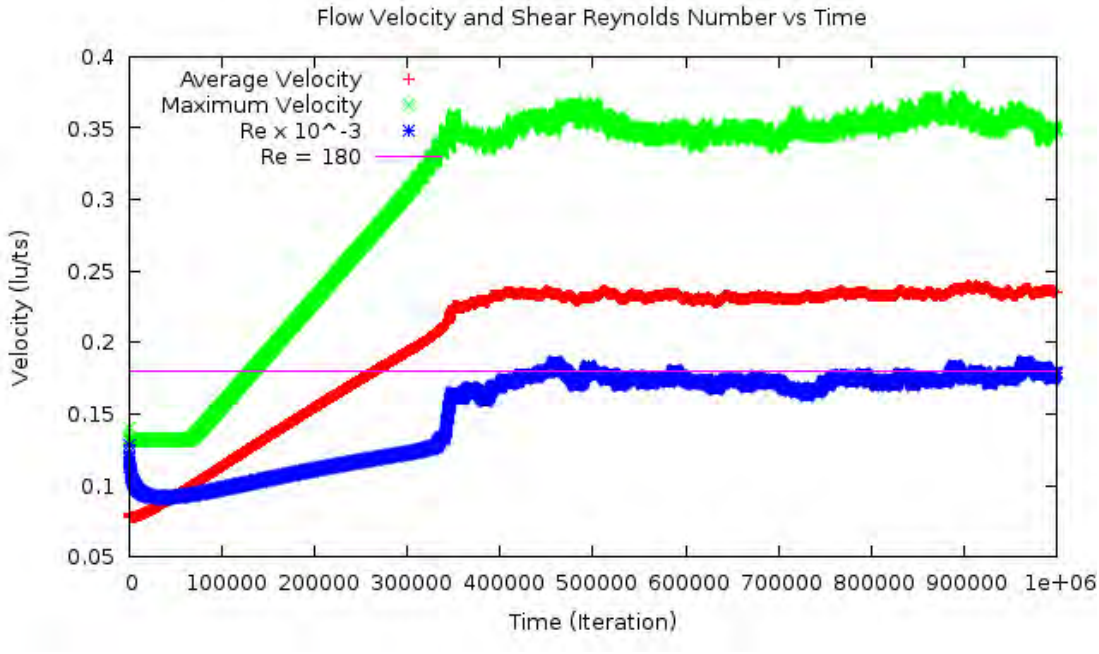

Figure 4.5: Plot of friction Reynolds number (Re_τ) (blue), Average Velocity (red) and Maximum Velocity (green) against iteration number for a channel flow at a nominal value of $Re_\tau = 180$. The point at which the flow trips into turbulent flow can be seen by the sharp rise in Re_τ at iteration $\approx$ 330000.

Combining the friction velocity and the channel half height gives the friction Reynolds number

$$Re_\tau = \frac{u^\star \delta}{\nu} \tag{4.30}$$

In practice, maintaining this friction Reynolds number is achieved by applying a body force to the fluid, as will be further discussed later in this work.

4.4.2 Validation

Three validation cases have been conducted to ensure the accuracy of the methods implemented to this point. The first of these is a turbulent channel flow which is used to ensure that the velocities and turbulent motion being simulated are correct. Two additional validation tests have also been conducted to ensure that the walls within the domain are operating correctly and accurately measuring the force being applied to the walls. These tests feature flow over a cube and flow over a foil.

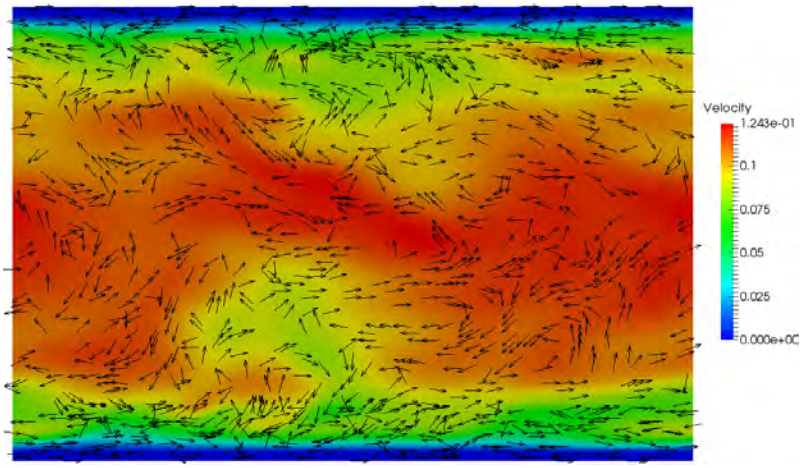

Figure 4.6: Section through the centre of the domain showing both the velocity and vorticity of the flow at $Re_\tau = 180$. The colour contours indicate the velocity while the arrows indicate the vorticity.

4.4.2.1 Turbulent Channel Flow

To ensure the code is capable of correctly simulating turbulence, a simulation was undertaken and compared to the the seminal work of Moser *et. al.* [90] who in 1999 performed a detailed DNS study of turbulent channel flow.

The simulation domain had dimensions of $124 \times 80 \times 40$ lattice units length, height and width respectively conforming to the $\pi\delta \times \delta \times 0.3\pi\delta$ required as previously mentioned. Unlike the simulation performed by Moser where the mesh was refined in the near wall region, a uniform mesh was used throughout the entire domain. This was done because the standard implementation of the lattice Boltzmann method only supports a uniform mesh size.

The flow was first initialised with a uniform velocity in the streamwise direction. Onto this, a three dimensional random velocity perturbation was then added and smoothed to minimise instabilities in flow in the same manner as that of Zecevic [148]. In order to maintain the flow velocity throughout the course of the simulation, a body force was imparted to the fluid, the magnitude of which was sized to ensure a friction Reynolds number of ≈ 180.

Even with the initial velocity perturbations, the flow still needed to iterate for some time before it tripped into fully turbulent flow. This can be seen in Figure 4.5 with the onset of turbulence being indicated by the sharp rise in the

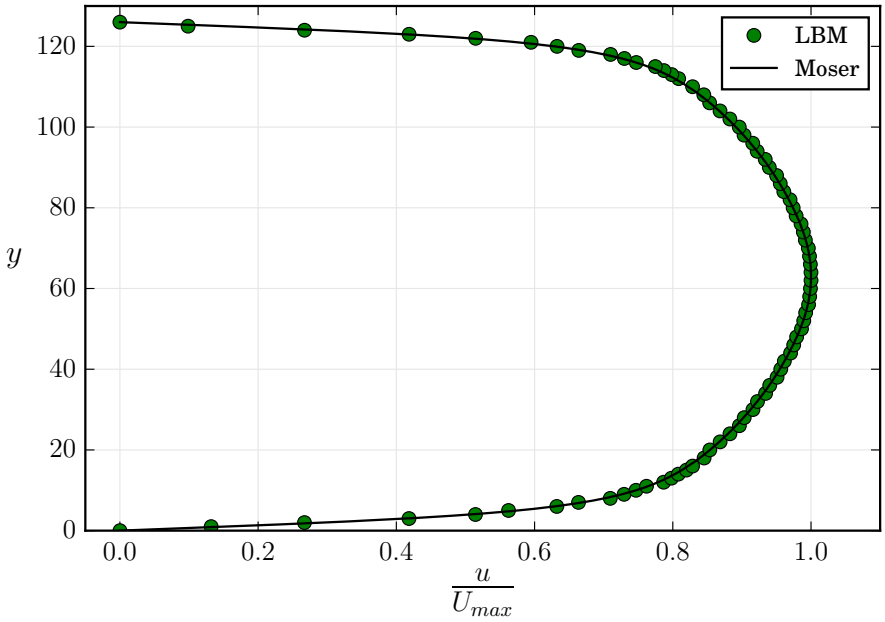

Figure 4.7: Averaged velocity profile after 1000 eddy turn over times at $Re_\tau \approx 180$. The solid black line shows the results of Moser *et. al.* while the dots represent the points generated by the LBM code.

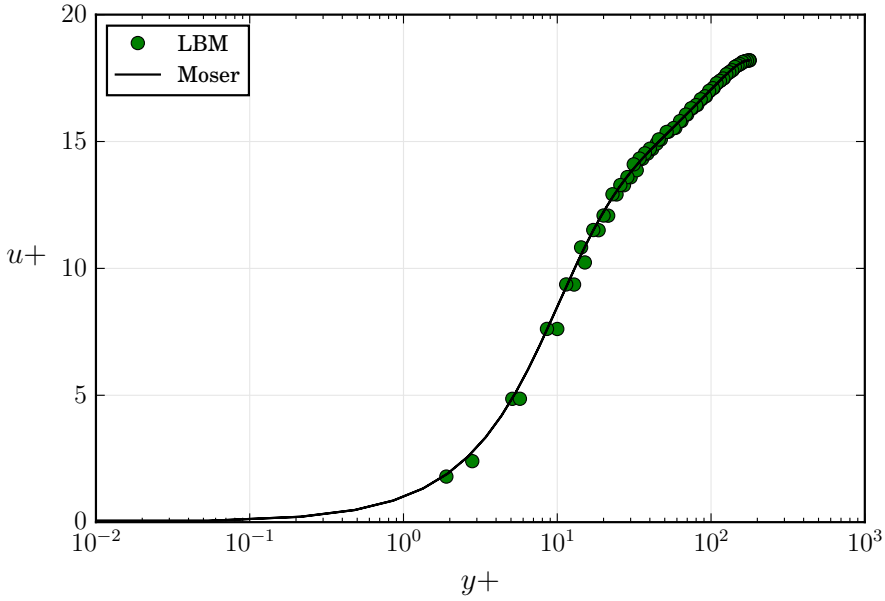

Figure 4.8: Comparison of the lattice Boltzmann method and DNS results of Moser *et. al.* at $Re_\tau \approx 180$. The line shows the DNS results while the points show the results of the lattice Boltzmann code.

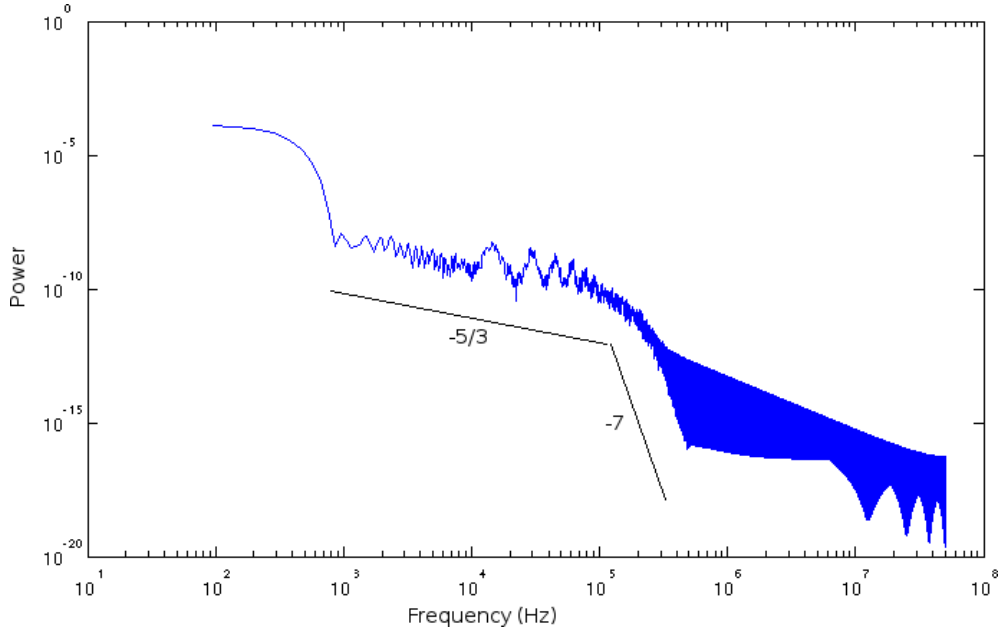

Figure 4.9: Power spectral density of velocity measurements

Reynolds shear number at ≈ 330000. An image of the flow at this point showing both velocity and vorticity can be seen in Figure 4.6. After the flow had become fully turbulent a velocity profile was measured and averaged over a period of 1000 eddy turn over times (t_{eddy}), where an eddy turnover time is defined as $t_{eddy} = \frac{\delta}{u_{max}}$.

This velocity profile was non-dimensionalised against u^+ and y^+ and compared to the results of the work by Moser *et. al.* As can be seen in Figures 4.7 and 4.8, there is a good level of correlation between the results, particularly in the log-law region.

Having verified the velocity profile was correct, a brief frequency analysis of the results was also performed. This was achieved by taking a fast Fourier transform (FFT) of the fluctuating velocity from a single point in the centre of the channel. The velocity at this point was recorded for 1048578 timesteps (2×10^{20}) at an evenly spaced sampling rate of 1×10^8 Hz.

As can be seen in Figure 4.9, comparison between the FFT result and the $-5/3$ and -7 slopes expected for turbulent flow decay are accurate to within 5%, indicating the accuracy of the simulation in modelling turbulent flow.

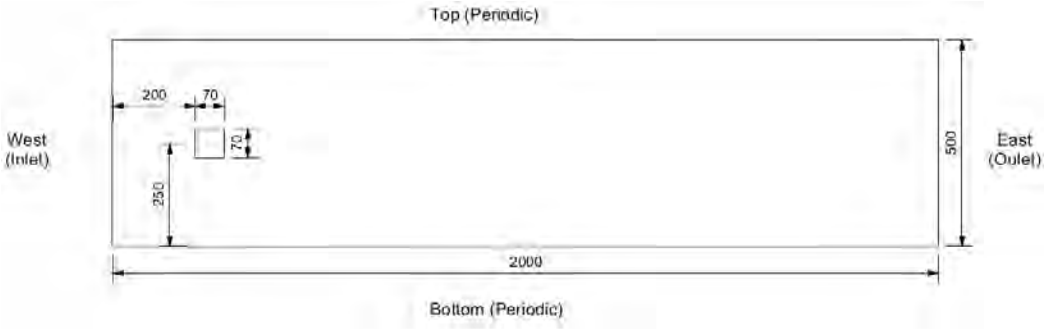

Figure 4.10: Geometry of the domain for flow around a cube validation case.

4.4.2.2 Turbulent Flow Past a Cube

With the code shown to produce accurate results of turbulent channel flow, the introduction of a cube into the simulation allows the measurement of drag to be better validated. As has been shown both experimentally [61] and by simulations [115], the co efficient of drag of a cube in flow with Reynolds numbers greater than 10^3 is $C_d = 1.05$.

The domain geometry required to test the code for this validation case entailed a rectangular box $200 \times 50 \times 50$ length, width, height respectively. With a δx value of 0.1, this resulted in a domain of 2000 lattice units $\times$ 500 lattice units $\times$ 500 lattice units. The top, bottom, front and back walls were initialised as periodic boundary condition while the west and east boundaries were set as a velocity inlet and pressure outlet respectively. A cube of length 7 (70 lu) cube was positioned 200 lattice units downstream of the inlet as can be seen in Figure 4.10.

With the inlet velocity set to 0.1 lu/ts, a relaxation factor of $\tau = 0.6$ and using a timestep of $\delta t = 0.01$ to keep the $\frac{\delta x^2}{\delta t}$ ratio equal to 1, the Reynolds number of the flow was calculated as

$$\begin{aligned} Re &= \frac{UL}{\nu} \\ &= \frac{0.1 \times 70}{3.33 \times 10^{-4}} \\ &\approx 21000 \end{aligned} \tag{4.31}$$

The simulation was iterated until the drag fluctuations were within 1% of the mean value. At this point, the free stream velocity and combined drag from each

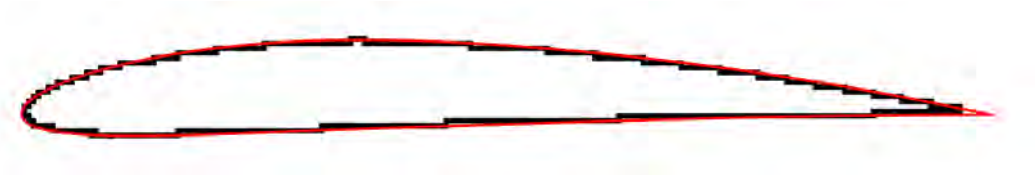

Figure 4.11: NACA 4410 Profile. The red line is the actual profile of the foil and the black lines represents the shape of the foil tested.

face of the cube were recorded and used to find the drag co-efficient as can be seen in Equation 4.32.

$$\begin{aligned} C_d &= \frac{D}{\frac{1}{2}\rho A U^2} \\ &= \frac{26.5933}{0.5 \times 1 \times 4900 \times 0.1027^2} \\ &= 1.0294 \end{aligned} \tag{4.32}$$

With the simulation value of $C_d = 1.0294$ being with 2% of the quoted value of $C_d = 1.05$, it is clear that the measurement and calculation of drag is operating correctly.

4.4.2.3 Turbulent Flow Over a Foil

A final validation case of flow over a NACA 4410 foil was also performed to ensure that forces perpendicular to the direction of fluid flow were also being accurately calculated. By measuring the lift and drag of a foil and comparing them with known values, the accuracy of the code can be shown.

With the implemented code limited to square edged geometries the cross sectional profile of the NACA 4410 was unable to be simulated without some simplification. An approximation to this profile was therefore used as can be seen in Figure 4.11. The computational domain was again similar to that used in the cube validation case being 2000 lattice units long × 500 lattice units wide × 500 lattice units high. The foil of chord length 200 lu was positioned 200 lattice units downstream of the velocity inlet. The top, bottom, front and back walls were all set as periodic boundary conditions, and the east wall was again a pressure outlet.

Table 4.3: NACA 4410 Results.

	Expected	Simulation
Re	25000	26143
C_d	0.029	0.032
C_l	0.286	0.341
Lift / Drag	9.862	10.656

Comparison of lift and drag for the expected values and simulated values of the NACA 4410 foil at an angle of attack of 0°.

Table 4.4: NACA 4410 at $\alpha = 0.2°$ Results.

	Simulation	Expected
Re	26143	26000
C_d	0.032	0.026
C_l	0.341	0.341
Lift / Drag	10.656	13.267

Comparison of lift and drag for the simulated values and expected values of the NACA 4410 foil at an angle of attack of 0.2°.

The inlet velocity was set at 0.1 lu/ts and a relaxation value of 0.524 was used. Combined with a δx value of 0.1 and a time step of $\delta t = 0.01$, this corresponds to a dynamic viscosity of $\nu = 8 \times 10^{-5}$ leading to a nominal Reynolds number of $Re = 25000$.

The simulation was run until it reached a steady state at which time the forces and fluid velocity were extracted, an image of which can be seen in Figure 4.12. The values were non-dimensionalised and compared to expected values generated by the XFoil software package [36], results of which are shown in Table 4.3.

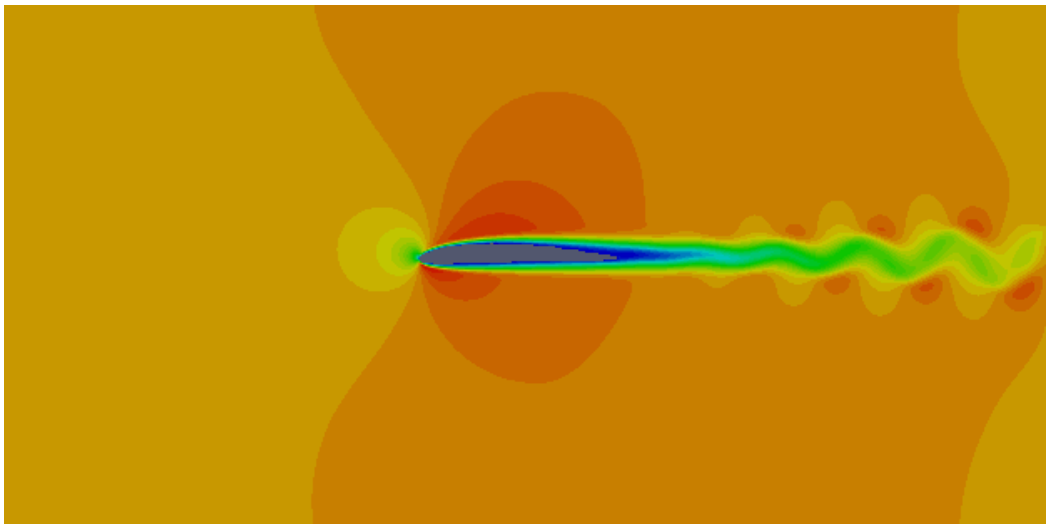

Figure 4.12: Velocity contours of the flow around the NACA 4410 foil.

From these results it can be seen that the drag co-efficient of the simulated foil is 10% higher than the expected value. This is not surprising as the square edged geometry is not as streamlined as the actual NACA 4410 profile. However, of more interest is the fact that the lift co-efficient is almost 20% higher than the expected value, leading to a lift on drag ratio for the simulated foil being about 8% higher than would otherwise be expected.

A reason for this may be due to the distance of the foil from the top and bottom boundaries. With these being periodic, the domain can be thought of as being replicated both above and below creating an infinite series of "virtual foils" identical to the one simulated both above and below the domain akin to the flow over the middle airfoil of a triplane. The value of the lift co-efficient of the simulated foil is consistent with it having an angle of attack (α) of 0.2°, an angle which could easily be created by the "virtual foils" above and below. Table 4.4 shows a comparison of the simulation results with the expected results for the foil at the 0.2° angle of attack. This shows that the simulated foil has a 20% higher drag, and hence a 20% lower lift on drag ratio, a value which can easily be attributed to the squared edged geometry.

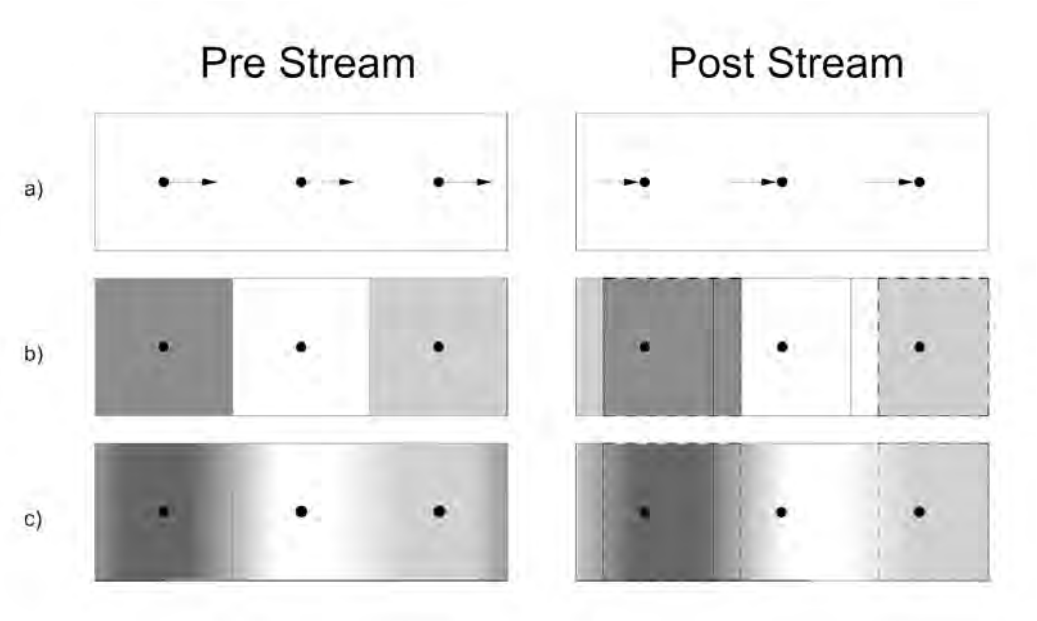

Figure 4.13: Illustration of fractional propagation in one-dimension. The shading indicates different population densities.
(a) Unmodified streaming method without finite volumes.
(b) Qian's method of fractional propagation where density populations in finite volumes are considered to be uniform.
(c) Zhang's method of fractional propagation where density populations in finite volumes are considered to vary linearly.

4.5 Fractional Propagation

As was seen in Section 4.4, modelling high Reynolds number flows requires very large domains and very low relaxation values leading to highly unstable models. One way of overcoming these issues is to incorporate fractional propagation. This is a method that was first proposed by Qian *et. al.* [102] in 1997 and later refined in 2001 by Zhang *et. al.* [149]. It works by effectively creating a finite volume around each lattice node. For each time step, only a fraction of the density population is allowed to cross the volume boundary between neighbouring cells while the remainder stays in the original cell. The fraction is represented by the parameter "p" and can be varied between $0 < p \leqslant 1$. Incorporating this into the lattice Boltzmann method is achieved by changing only the streaming equations and can be seen in Equations 4.33 and 4.34.

$$\begin{aligned} f_i(x, t+\delta t) = p\left[f_i'(x - e_i\delta t, t) + \frac{(1-p)}{2}\delta f_i'(x - e_i\delta t, t)\right] \\ + (1-p)\left[f_i'(x,t) - \frac{p}{2}\delta f_i'(x,t)\right] \end{aligned} \tag{4.33}$$

$$\delta f_i' = f_i'(x + e_i\delta t, t) - f'(x,t) \tag{4.34}$$

Zhang's addition of Equation 4.34 adds a piecewise linear correction term to the original equation (4.33) proposed by Qian. As the population densities only propagate a fraction of the distance between nodes, they cannot reach the neighbouring node within a single iteration. This means that the value of the population density at the lattice node itself must be interpolated from the values at the surrounding nodes. Qian's method uses first-order interpolation and assumes the population density in each finite volume is uniform throughout that volume. The correction term proposed by Zhang allows second order interpolation which treats the population densities as being linearly distributed throughout the volume. Using second order interpolation allows fractional propagation method to exactly recover the Navier-Stokes equations. This can be better illustrated with a one dimensional example, as can be seen in Figure 4.13.

$$f_i(x, t+\delta t) = p\left[f_i'(x - e_i\delta t, t) + \frac{(1-p)}{2}(f_i'(x,t) - f_i'(x - e_i\delta t, t))\right] + (1-p)\left[f_i'(x,t) - \frac{p}{2}(f_i'(x + e_i\delta t, t) - f_i'(x,t))\right] \tag{4.35}$$

Combining Equations 4.33 and 4.34 into Equation 4.35 gives the complete form of the updated streaming equation in which f_i is the post streamed value, and f_i' is the post collision value of the distribution functions. If parameter p is set to a value of 1, the equation takes the same form as the original streaming equations shown in Equation 4.2. When a Chapman-Enskog expansion is undertaken using these updated equations, it is found that the parameter p also needs to be included in the viscosity equation (Equation 4.36).

$$\nu = c_s^2\left(\tau - \frac{1}{2}\right)\delta t \times p \tag{4.36}$$

This shows that as the parameter p is always between $0 < p \leqslant 1$, the viscosity is reduced linearly by the value of p. This reduction in the viscosity means that a higher Reynolds number can be achieved for the same velocity and domain size. Recalling from Section 4.4.1 that the maximum attainable Reynolds number was limited by domain size, this reduction to the viscosity helps allieviate this problem somewhat, however does not entirely eradicate it. Revisiting Table 4.2, and now also including a value of $p = 0.1$, Table 4.5 shows that the required channel heights have been lowered by an order of magnitude which correspondingly decreases the overall sizes of the models by three orders of magnitude.

As well as allowing simulation of higher Reynolds numbers, fractional propagation is also able to increase the stability of the lattice Boltzmann method. Work by Cao *et. al.* [19] has shown that the standard lattice Boltzmann model marginally satisfies the Courant-Freidrichs-Lewy (CFL) condition ($\delta t|\mathbf{e}_i|/\delta x \leq 1$) which is an indicator of stability. When the fractional propagation parameter is introduced into this, as shown in Equation 4.37, it linearly reduces the left hand side of this equation, further assisting the method to meet the CFL condition and hence adding to the overall stability.

$$p \times \delta t|\mathbf{e}_i|/\delta x \leq 1 \tag{4.37}$$

Table 4.5: Reynolds Numbers vs Channel Dimensions for $\tau = 0.51$ and $p = 0.1$

Re_ϕ	Height	Length	Width	Number of Cells
10	0.02	0.03	0.01	$0.00^\star$
100	0.22	0.35	0.10	$0.01^\star$
1000	2	3	1	$8^\star$
10000	22	35	10	8123
100000	222	349	105	8.123×10^6

* These values are the numerically required sizes to capture turbulent motion in a channel; however, in reality, a channel height of at least 10 cells would be needed to reproduce an adequate velocity profile.

As well as allowing increased Reynolds numbers to be modelled, and higher levels of stability, the incorporation of fractional propagation and the introduction of the finite volume method it brings can also be used in other areas of the simulation. As will be shown in Section 4.6, a volumetric approach can also give significant benefits to mesh refinement.

Amid all the benefits, there is a detriment to using fractional propagation. As the density populations only progress a fraction (p) of the distance between nodes, the time it takes them to reach the neighbouring node is therefore $\frac{1}{p}$. So instead of each iteration corresponding to a timestep δt, each iteration is only equal to an effective timestep of $\delta t_e = \frac{1}{p}\delta t$. This means that the total simulation time is also linearly increased by this factor of $\frac{1}{p}$ before it reaches the same point as a simulation not using fractional propagation. However, as the number of cells in the domain varies cubically with the channel height and the increase in timesteps varies linearly, a reduction in the total number of cells still provides a significant overall increase in the efficiency of the simulation. Additionally, due to the ever increasing availability of computational processing power, this increase of runtime can be minimised to an extent and is therefore not as significant an issue as it has previously been.

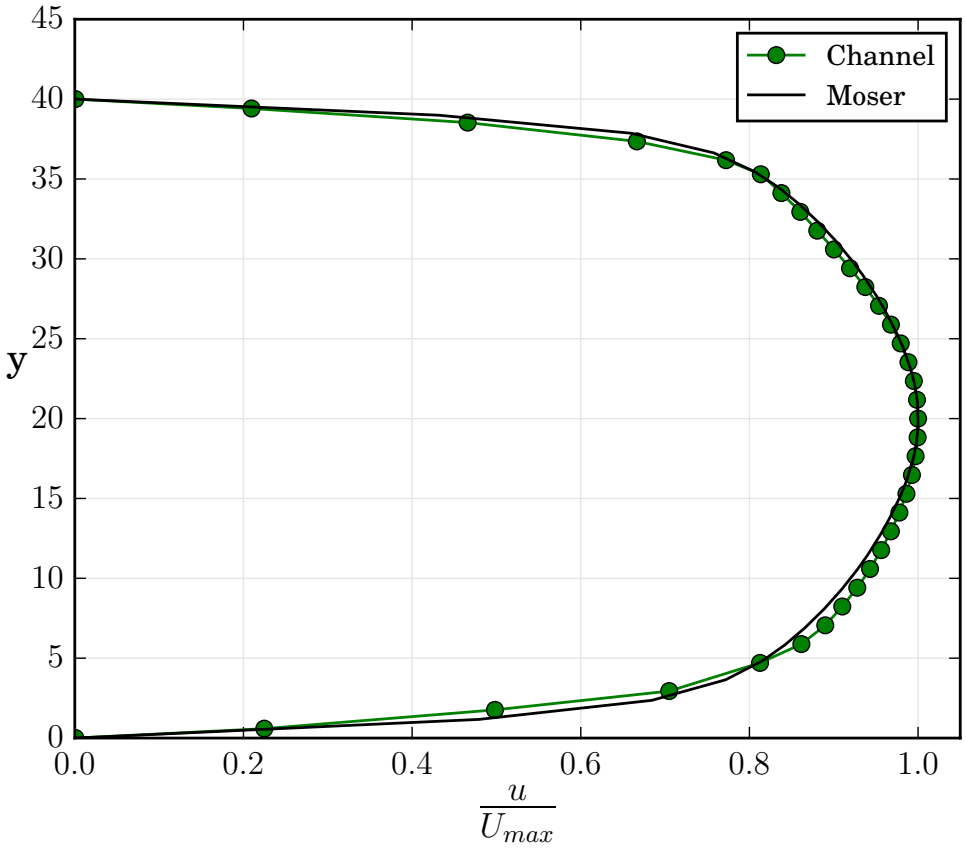

Figure 4.14: Velocity Profile using Fractional Propagation. A fully developed turbulent profile has been recovered from a domain of half-height $\delta = 20$ by using a fractional propagational parameter of $p = 0.05$. Compared to the turbulent profile at $Re_\tau = 180$ published by Moser the profile appears relatively accurate.

Validation

The validation of turbulent flow in Section 4.4 was achieved in a domain that was $124 \times 80 \times 40$ lattice units length, height and width respectively. In order to confirm the accuracy of the implementation of the fractional propagation, the same case has been simulated on a significantly smaller domain.

Whereas the domain in Section 4.4 had a half channel height of $\delta = 40$, a domain with half channel height $\delta = 20$ has now been used. In order to lower the viscosity and hence maintain a practical velocity, the fractional propagation parameter was lowered to $p = 0.05$. Combined with a relaxation value $\tau = 0.51$, this resulted in a turbulent channel flow with $U = 0.135\ lu/ts$ corresponding to a Reynolds number of $Re_\phi = 16265$ (which was equivalent in this case to $Re_\tau \approx 180$).

The velocity profile taken from this simulation can be seen in Figure 4.14 and is again compared to the fully turbulent flow profile published by Moser. The near wall regions again show some deviation from that expected, however the central region is remarkably close to the DNS results which were performed in a significantly larger domain.

4.6 Mesh Refinement

The standard BGK lattice Boltzmann model leads to a lattice that is uniformly spaced in the x, y and z directions. This means when studying channel flow, the spacing of the mesh in the middle of the channel is the same as the spacing at the wall. In order to capture more detail of the boundary layer, a high resolution mesh needs to be used close to the walls, this then means that the mesh in the middle of the channel is accordingly of a higher resolution than necessary. A way to circumvent this issue is using a method of mesh refinement. There are various techniques of mesh refinement available within the lattice Boltzmann framework including finite difference schemes (Mei [87]), finite volume schemes (Nannelli [92], Chen [21]), interpolation supplemented schemes (He [56]), locally embedded uniform gridding (Filippova [42, 42], Rohde [109]), and multi-block methods (Yu [146, 147]).

The method implemented in this work combines elements of Rohde's method using the locally embedded uniform grid, with the multiblock method by Yu. A brief overview of both these methods is now presented.

4.6.1 Locally Embedded Uniform Grid

The locally embedded uniform grid technique works in the way it sounds, with refined mesh areas embedded into the existing uniform mesh. This is illustrated in Figure 4.15.

Each embedded mesh has different time and length scales as a function of the level of refinement n, as shown in Equations 4.38 and 4.39 where the subscripts c and f correspond to the coarse and fine meshes respectively.

$$\delta_{x,c} = n\delta_{x,f} \tag{4.38}$$

$$\delta_{t,c} = n\delta_{t,f} \tag{4.39}$$

This is done to keep an equal fluid velocity $\mathbf{u}_i$ in both meshes. Another consequence of having different time and length scales is that the Reynolds number in each mesh differs. In order to keep it constant across the refined meshes, the viscosity, and hence relaxation value for each mesh needs to be scaled as well. This scaling equation can be seen in Equation 4.40 with the full derivation shown in Appendix C.

$$\tau_c = (\tau_f - \frac{1}{2})/n + \frac{1}{2} \tag{4.40}$$

The method operates by performing collision and streaming steps individually on the different meshed regions, and transports the density populations between the regions at the refinement interface. This concept had been previously proposed by Fillipova and Hanel [42], and implemented by Dupuis and Chopard [38], however had the issue that the non-equilibrium density populations did not scale correctly between the coarse and fine mesh regions leading to non conservation of both mass and momentum. To overcome this, both first and second order interpolations in both time and space were required to meet the conservation laws and to keep second order accuracy for the simulation.

Rohde [109] instead proposed that by using a volumetric form, similar to that implemented with the fractional propagation, the non-equilibrium components do

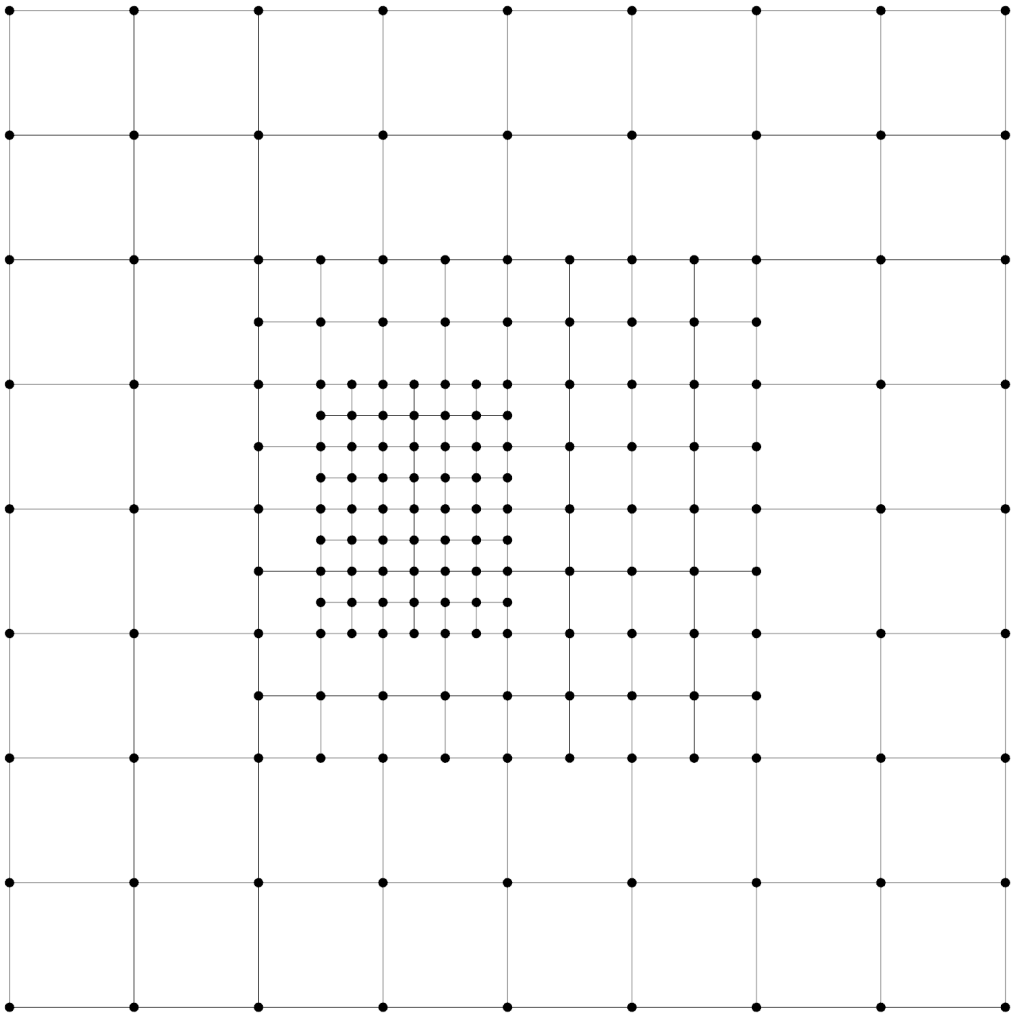

Figure 4.15: Example of locally embedded uniform grids. As can be seen, multiple grids can be embedded inside each other.

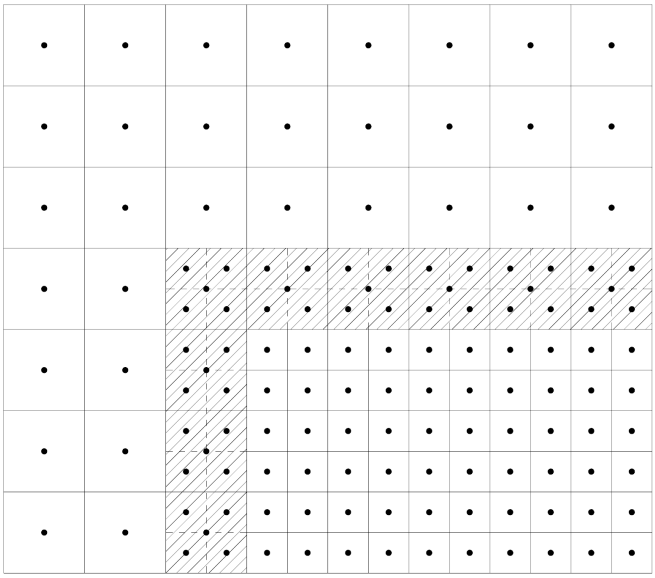

Figure 4.16: Volumetric locally embedded uniform grids. The interface between the coarse and fine grids is indicated by the hatching. In this area, both the coarse and fine cells coexist.

not need to be scaled and mass and momentum are both conserved. An example of a locally embedded volume can be seen in Figure 4.16.

The method proceeds by first performing the collision step on both the coarse and fine nodes. The density populations in the interfacial cells of the coarse mesh are then redistributed into the corresponding cells of the fine mesh so that the population density in each of the fine mesh cells is equal to that of the original coarse cell $(f_i)_c = (f_i)_f$. This redistribution process is often referred to as "exploding". Both the fine and coarse grids are then streamed as per normal.

If identical test particles[1] are placed in both the coarse and fine meshes, for a single time step it would be expected that both particles travel the same distance. In order for this to occur, the fine mesh needs to undergo $n-1$ more collisions and streaming processes. Although the additional streaming stages occur as normal

[1]A test particle is an idealized model of an object whose physical properties (usually mass, charge, or size) are assumed to be negligible except for the property being studied, which is considered to be insufficient to alter the behaviour of the rest of the system

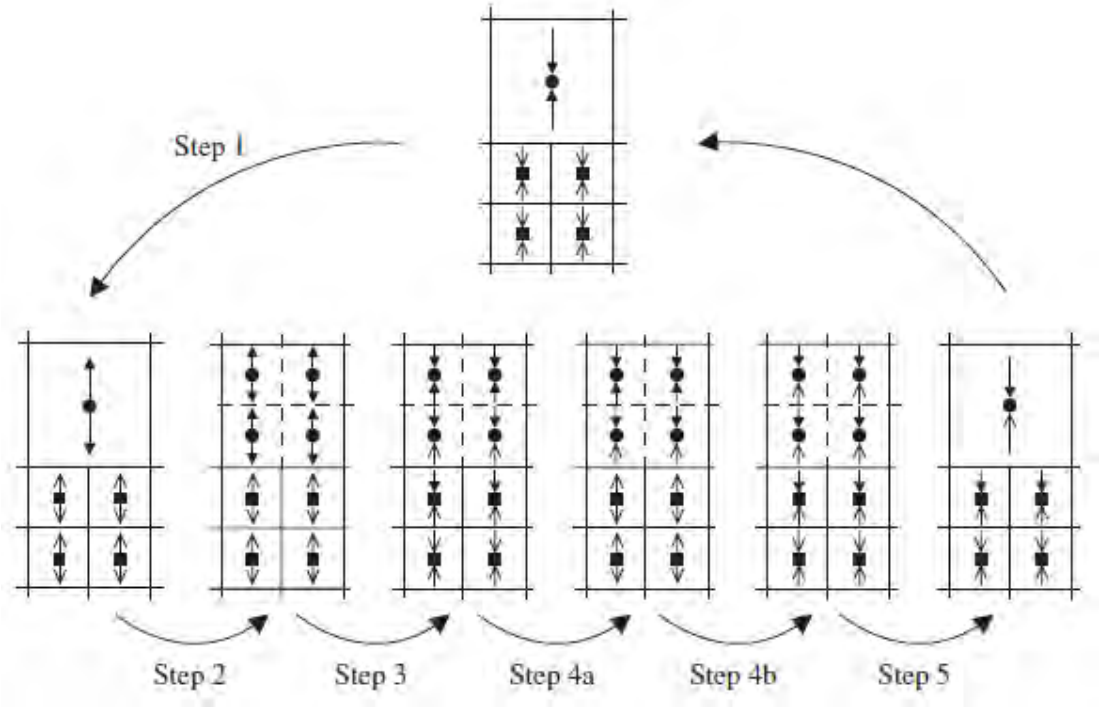

Figure 4.17: Schematic of locally embedded uniform grid operation. The circles (•) denote the centres of the cells in the coarse grid, the squares (■) denote the centre of the cells in the fine grid. The open arrow heads (⋀ and ⋁) correspond to particle densities originating from the fine grid, the closed arrow heads (▲ and ▼) to particle densities that originate from coarse grid cells. Particle distributions after a propagation step are represented by arrows pointing *towards* the cell centre, particle distributions after a collision step are denoted by arrows pointing *from* the cell centre. Figure taken from work by Rohde [109].

Step 1: Collision on coarse and fine meshes.
Step 2: Redistribution of density populations from coarse grid to fine grid.
Step 3: Streaming process on coarse and fine grid.
Step 4: Collision and streaming on fine grid.
Step 5: Redistribution of density populations from fine grid to coarse grid.

across all the fine cells, the collisions are limited to only occur in regions of the fine mesh not including the interface cells. This is because the cell values in the interfacial region have already undergone a collision based on the length scale of the coarse mesh.

Having performed the $n-1$ additional collisions and streaming processes on the fine mesh, the values are then redistributed back into the coarse mesh by averaging the values of the fine cells within each coarse cell in a process often referred to as "coalescing".

The operation of the locally embedded uniform grid method is illustrated in Figure 4.17 which has been adapted from the work of Rohde [109].

4.6.2 Multi Block Mesh Refinement

The multi block method of mesh refinement differs from the locally embedded method in that the meshes reside in different lattices. Although the mesh within each lattice is still uniform (i.e. $\Delta x = \Delta y = \Delta z$), each different lattice can have a different mesh size, as is illustrated in Figures 4.18 and 4.19. Whereas in the embedded grids, where the density populations only need to be redistributed locally, the multi block method requires that the density populations be transferred between lattices. This dividing of the domain into smaller blocks can be beneficial for several reasons. Lin and Lai [81] used this technique to significantly speed up overall simulation time by first running the model using only coarse mesh blocks to quickly initialise and allow the boundary information to propagate throughout the domain. Mesh blocks in key areas of the domain were then converted to higher resolution meshes and run concurrently with the coarse grid to resolve the details in their simulations. Another benefit of the multiple block approach is that each block can be treated as a separate computational entity. This means that when the simulation is being performed in a parallel processing environment, higher resolution lattice blocks can have additional processing nodes assigned to them, better balancing the load across all available processors.

As with the embedded version, the differences in the mesh refinement level mean that the time and length scales, and hence the viscosity and relaxation

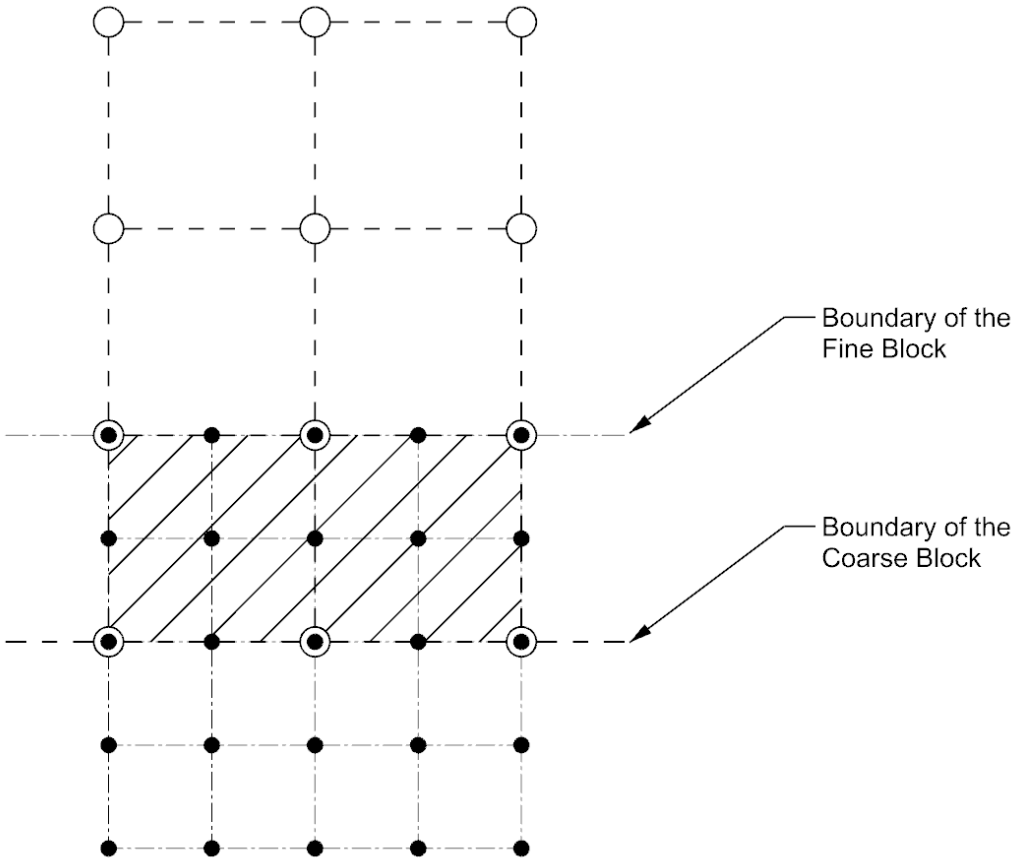

Figure 4.18: Interface between two block using the multiblock method. The • indicate the nodes of the fine mesh lattice, while the ◯ indicate the nodes of the coarse mesh lattice. The lattices overlap by one cell width of the coarse lattice.

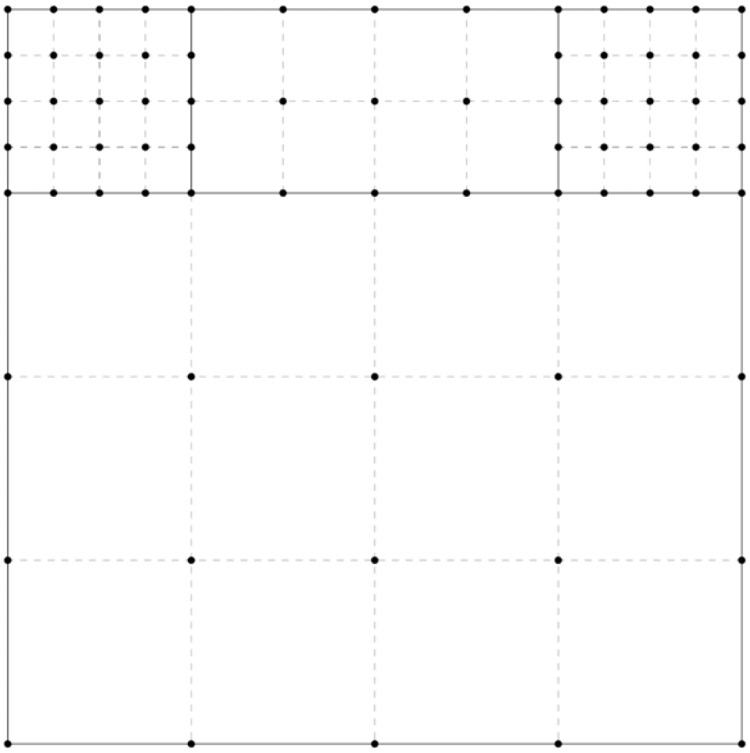

Figure 4.19: Multiblock mesh refinement example. The solid lines show the boundaries of each lattice block, and the • indicates the resolution of each of the lattices. This style of blocking layout is commonly used for modelling lid driven cavity flows.

factors within each lattice need to vary. The scaling ratios are the same as was previously shown in Equations 4.38 to 4.40.

The operation of the multi block method is similar to the locally embedded uniform grid in that lattice blocks with higher levels of refinement undergo additional collision and streaming steps. The major difference however is that the density population values for the interfacial boundary nodes in the fine block need to be interpolated from the surrounding nodes of the coarse block, necessitating that the edges of the adjoining lattices are overlapped. To avoid any asymmetry in the interpolations, a spatial symmetric cubic spline interpolation is required. Further to this, as the fine lattice performs two collisions and streaming steps for every iteration, a temporal interpolation is required for the nodes on the boundary of the fine lattice block. Yu was able to accomplish this temporal interpolation

by using a three-point Lagrangian. If the system is to be three-dimensional, the symmetric cubic spline interpolation instead needs to be replaced by a bicubic surface interpolation.

4.6.3 Combined Mesh Refinement Method

The mesh refinement method implemented in this work combines features from the two methods just described. The domain is broken up into separate lattices as per the multi block method, but due to the lattices already being in volumetric form from the fractional propagation, the redistribution mechanism from the locally embedded grid system has also been used. This gives the advantage that there is no need to perform multiple interpolations in both time and space, leading to reduced runtime while still remaining second order accurate. It also means the workload can be shared more easily leading to improved computational efficiency as was previously mentioned.

Both the embedded grid method and multi block methods utilise different time and length scales in the different mesh resolution areas, and the combined method is no different. It uses the same equations as previously defined in Equations 4.38 to 4.40 for time, length, and viscosity scaling.

As was shown in Section 4.5, for fractional propagation to work, interpolation both forwards and backwards in space is required to find the density populations at the nodes. This means that when implementing mesh refinement, an additional layer of cells needs to be overlapped as compared with the embedded grid model, so that both lattices have the information they require. Figure 4.20 shows that passing the data between the lattices can be done asymmetrically in that the coarse grid requires all the values from the fine grid to accurately resolve the density populations, whereas the fine grid does not need the top row of the overlapped cells. This is because the values in the final row of overlapped cells is only ever used for the interpolation in the fractional propagation step, and therefore do not undergo a collision step in the alternate lattice. The order of operation in this combined method is similar to that of the embedded grid and is shown schematically in Figure 4.21.

A summary of the mesh refinement methods can be seen in Table 4.6.

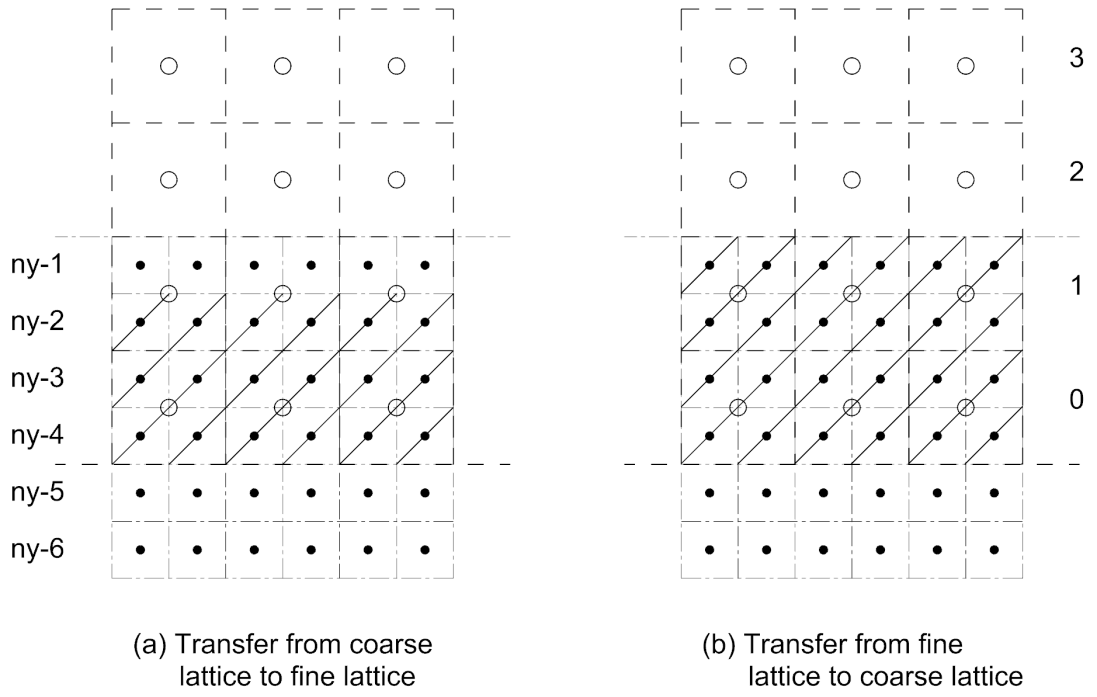

Figure 4.20: Combined Method Interface and Transfer. The • indicates the cells of the fine lattice block and the ◯ indicates the cells of the coarse lattice block. (a) shows the cells that need data to be redistributed from the coarse lattice to the fine lattice. (b) shows that cells that need data to be redistributedfrom the fine lattice to the coarse lattice. The labelling system of cells in the vertical direction is also shown.

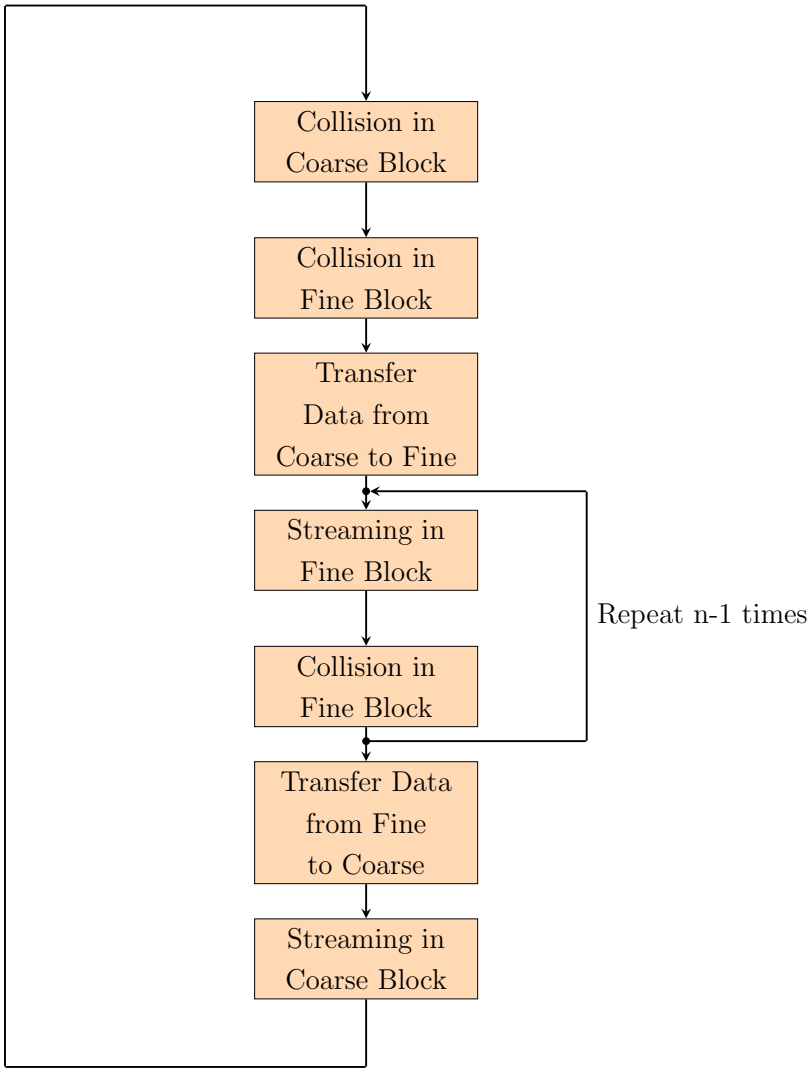

Figure 4.21: Combined mesh refinement method order of operation schematic. n referes to the difference in refinement level between the lattices.

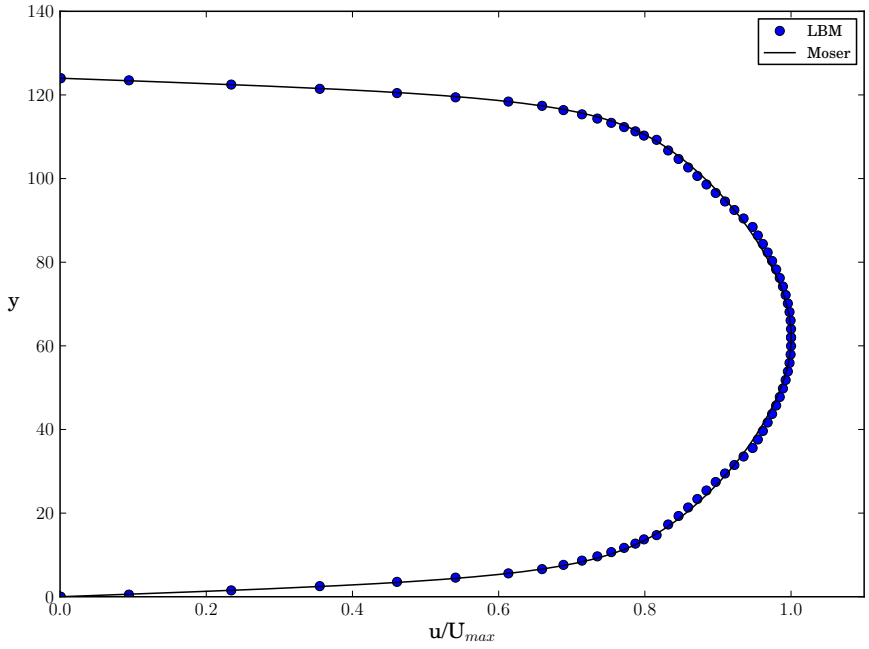

Figure 4.22: Turbulent flow velocity profile in refined mesh.

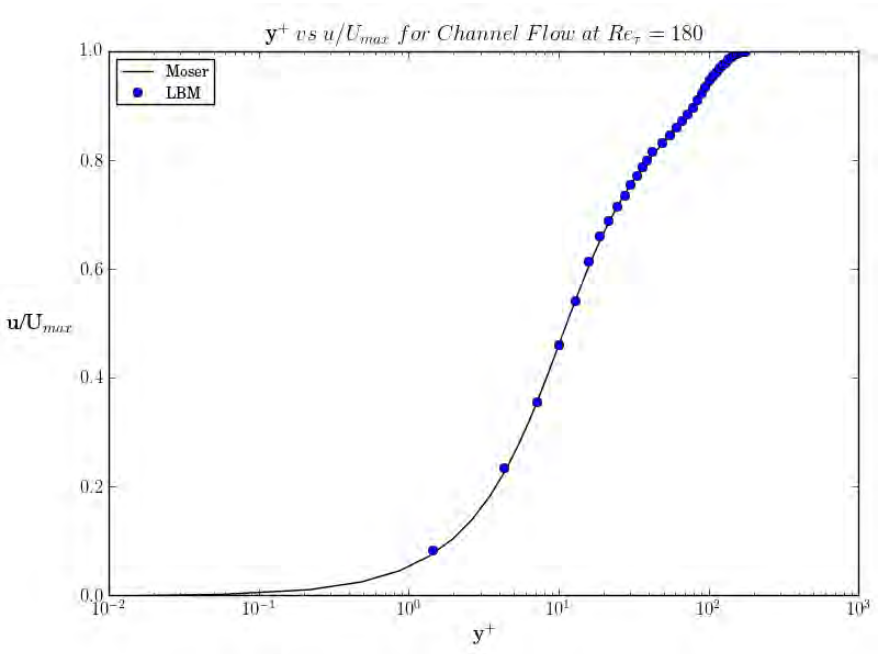

Figure 4.23: y^+ vs u/U_{max} for turbulent channel flow at $Re_\tau = 180$ with the refined mesh.

Table 4.6: Mesh Refinement Methods Summary.

	Locally Embedded Grid Method	Locally Embedded Volume Method	Multiblock Method	Combined Method
Required Overlapped Lattices	×	✓	✓	✓
Requires Spatial Interpolation	✓	×	✓	×
Required Temporal Interpolation	✓	×	✓	×
Easy load sharing / parallelisation	×	×	✓	✓

4.6.4 Validation

To validate the implementation of the mesh refinement a Poiseuille flow has again been simulated. Similar to the validation study of the unrefined lattice, a Reynolds number of $Re_\phi = 100$ has been used, this time with a channel of height 88 lu. The refinement layers near the walls are each 14 lu high and the central lattice is 30 lu high. Where previously the accuracy of the lattice Boltzmann solver was to within 5% of the analytical values, the use of the mesh refinement allows the LBM to be accurate to within 0.2%. A picture of both the simulation domain showing the areas of mesh refinement, and a comparison between the lattice Boltzmann results and the analytical result for the Poiseuille flow can be seen in Figure 4.24.

A similar validation study has also been performed for turbulent flow. A domain of dimensions $200 \times 124 \times 60$ lu length, height and width respectively was refined with 19 cells in the near wall regions. The flow was again applied with a body force to maintain a friction Reynolds number of ≈ 180. A plot of the velocity profile against the velocities shown by Moser is again used to confirm that the mesh refinement method operates correctly. As can be seen in Figure 4.22,

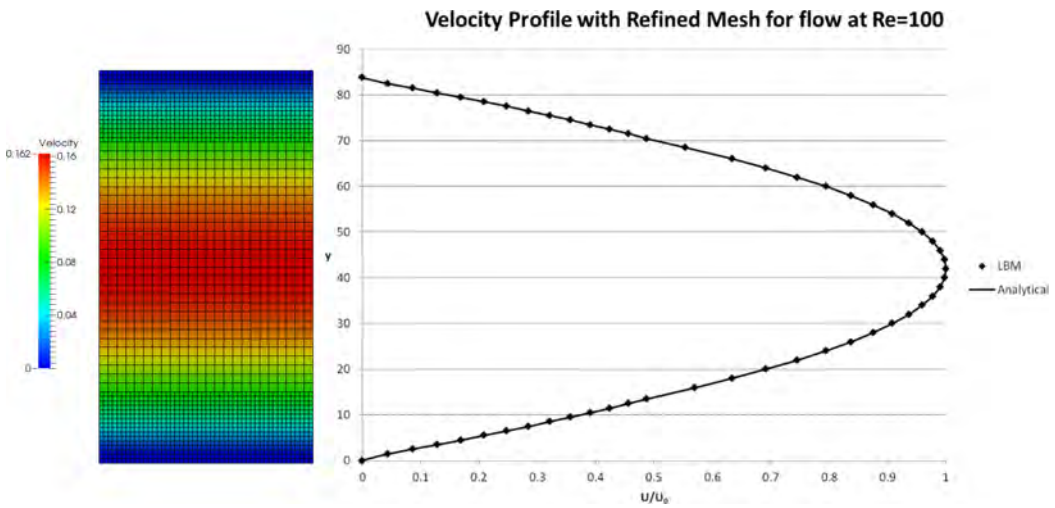

Figure 4.24: Laminar flow velocity profile with the refined mesh. The refinement can be seen in the image on the left, and the velocity profile compared to the analytical results on the right.

the method of refining the mesh has increased the accuracy of the results of the lattice Boltzmann method, particularly in the near wall regions. This is further illustrated in Figure 4.23 which shows all of the points generated by the lattice Boltzmann method lying on the line given by Moser.

4.7 Multiphase Flows

4.7.1 Background and Theory

Significant research on multiphase flows has been conducted by the lattice Boltzmann community and as such, a number of different methods of implementing them have been developed. These include the colour-fluid method [50, 82], free energy method [17, 122], and the phase-field method [65] which is implemented in this work.

As with the standard lattice Boltzmann model, the fluid motion is governed by the Navier Stokes equations; however, in order to simulate the multiple phases and the interactions between them, the Cahn-Hillard equation, shown in Equation 4.41, is also implemented. The use of a convection-diffusion equation such as the Cahn-Hillard equation in the phase-field method, as

opposed to an advection equation as is commonly used in standard level-set and volume-of-fluid (VOF) models, allows further physical phenomena to be more accurately captured. Specifically, a convection-diffusion equation enables the discontinuous pressure across a curved interface to be correctly resolved.

$$\partial\phi + (\mathbf{u} \cdot \nabla)\phi = M\nabla^2\mu \tag{4.41}$$

In this equation, the phase concentration is described by ϕ and is allowed to vary smoothly between $-1 \leq \phi \leq 1$ across the interface. As is common, $\mathbf{u}$ is the fluid velocity, M represents a mobility parameter, and μ is the chemical potential between the phases.

The implemented method was proposed by Huang, Shu and Chu [65] and assumes a square gradient interfacial energy density. The mechanics of this assumption are that instead of a sharp boundary between the phases, the quantities vary smoothly within a very thin interfacial region. This means that the behaviour of the fluid at any location is dependant not just on its properties, but also on its surrounding properties [48]. The square gradient interfacial energy density can be expressed as

$$E(\phi, \nabla\phi) = \int_V (\Psi(\phi) + (\kappa/2)|\nabla\phi|^2)dV + \int_S \varphi(\phi_S)dS \tag{4.42}$$

where the $\Psi(\phi)$ term gives the bulk free energy density, the $(\kappa/2)|\nabla\phi|^2$ contributes the interfacial energy density, V is the volume over which the equation is integrated, $\varphi(\phi_S)$ is the surface energy due to the fluid being in contact with solid boundaries, and S is the surface area of the fluid in contact with the solid boundary. The bulk free energy term can be defined in a number of ways and in this work, is implemented as the commonly used double well form, shown in Equation 4.43.

$$\Psi(\phi) = a(\phi + 1)^2(\phi - 1)^2 \tag{4.43}$$

The values of a and κ in these equations are constants and are related to the surface tension (σ) and the interface width (W) as given by Equation 4.44. The interface width constant relates to the number of cells used to transition from one phase to the other.

$$a = (3\sigma)/(4W) \qquad \kappa = 3\sigma W/8 \tag{4.44}$$

The chemical potential μ is also a function of both a and κ and can be found by taking the variation of the free energy with respect to the concentration, as is detailed in Equation 4.45.

$$\mu = \delta E/\delta\phi = \Psi'(\phi) - \kappa\nabla^2 = 4a\phi(\phi^2 - 1) - \kappa\nabla^2\phi \tag{4.45}$$

4.7.2 Implementation

With the introduction of multiple phases into the simulation, additional terms need to be added to the lattice Boltzmann evolution equations. These terms allow the inclusion of the interaction forces acting between the phases and apply a force to the fluid as a result of these interactions. In the case of the governing LBGK equation, with the added interaction term can be written as

$$\begin{aligned} f_i(x + e_i, t + \delta t) - f_i(x, t) = \\ \frac{1}{\tau_f}[f_i^{eq}(x, t) - f_i(x, t)] + w_i\rho F_\alpha e_i\frac{1}{c_s} + \delta t w_i e_i \left(\mu\nabla\phi\right)/c_s^2 \end{aligned} \tag{4.46}$$

The added term is applied during the collision step meaning the fractional propagation scheme described in Section 4.5 can still be used with this equation during the streaming step. In order to propagate the phase information throughout the domain, an equation of the same form as Equation 4.5 is again used, and is shown in Equation 4.47 with the phase population densities in each direction indicated by g_i.

$$g_i(x + e_i, t + \delta t) - g_i(x, t) = \frac{1}{\tau_g}[g_i^{eq}(x, t) - g_i(x, t)] \tag{4.47}$$

As with the fluid density, this equation can also be extended with a fractional propagation parameter q. Work by Huang, Zheng, Lu and Shu [63] showed that in order to correctly model the interface between the fluids, the Cahn-Hillard equation for the phase field does not need to be modelled to the same extent as the Navier Stokes equations for the fluid field. In a similar manner, the fractional propagation parameters for the fluid field and the phase field are not required to be the same and accordingly in this work they differ. The instabilities in the fluid field, both due to the low viscosity and the added forces from the multiphase model necessitates a low value of p to increase the level of stability. The phase

field fractional parameter q can be set closer to 1 so that the interface between the fluids can be resolved and updated more quickly.

As well as changes to the evolution equations, the equilibrium equations need to be modified for the fluid population density, and defined in the case of the phase populations density. These equations can be seen in Equations 4.48 and 4.49. It can be seen from an examination of these equations that in regions occupied by a single phase where there is zero chemical potential, these equilibrium distribution functions return the same result as the original.

$$f_i^{eq} = w_i \left[A_i + \rho \left(\frac{\mathbf{e}_i \cdot \mathbf{u}}{c_s^2} + \frac{(\mathbf{e}_i \cdot \mathbf{u})^2}{2c_s^4} - \frac{\mathbf{u}^2}{c_s^2} \right) \right]$$
$$\text{where} \tag{4.48}$$
$$A_i = \begin{cases} \left(\rho c_s^2 + \phi\mu\right)/c_s^2 & \text{, if } i > 0. \\ w_0^{-1}\left[\rho - (1 - w_0)\left(\left(\rho c_s^2 + \phi\mu\right)/c_s^2\right)\right] & \text{, if i=0.} \end{cases}$$

$$g_i^{eq} = w_i \left(B_i + \phi \mathbf{e}_i \mathbf{u} / c_s^2 \right)$$
$$\text{where} \tag{4.49}$$
$$B_i = \begin{cases} \overline{M}\mu/c_s^2 & \text{, } if\ i > 0. \\ w_0^{-1}\left[\phi - (1 - w_0)\left(\overline{M}\mu/c_s^2\right)\right] & \text{, } if\ i{=}0. \end{cases}$$

In Equation 4.49, $\overline{M}$ is a mobility parameter which has been left constant throughout this work. Further details on this parameter are available in work by Huang [63].

As was discussed in Section 4.2.1 the equilibrium distribution function has some requirements it needs to meet in order for the Navier-Stokes equations to be recoverable. This is also true of the phase population density equilibrium equation, the conditions for which are given below

$$\sum_i g_i^{eq} = \phi \tag{4.50}$$

$$\sum_i g_i^{eq} e_{i\alpha} = \phi u_\alpha \tag{4.51}$$

$$\sum_i g_i^{eq} e_{i\alpha} e_{i\beta} = \overline{M}\mu\delta_{\alpha\beta} \tag{4.52}$$

An additional constraint of the fluid equilibrium distribution function is also required and shown in Equation 4.53

$$\sum_i f_i^{eq} e_{i\alpha} e_{i\beta} = \rho u_\alpha u_\beta + \left(\rho c_s^2 + \phi\mu\right)\delta_{\alpha\beta} \tag{4.53}$$

He and Doolan [54] state that in order to maintain Galilean invariance this constraint needs to be $\sum_i f_i^{eq}\mathbf{e}_\alpha\mathbf{e}_\alpha = \rho RT\mathbf{I} + \rho\mathbf{uu}$ which can be achieved by incorporating a forcing term into the f^{eq} equation. With the forcing term added as shown in Equation 4.46, this multiphase method is able to maintain Galilean invariance. Further details of this can be seen in the work of Huang, Shu & Chew [64] and Zheng, Shu & Chew [151].

As previously mentioned, use of the square gradient interfacial energy density technique means that the properties at any location are dependant on their surroundings. A method of calculating first and second order gradients is required to implement the multiphase equations in a discrete system. This has been achieved by using the stencils published by Pooley and Furtado [99] which are shown in Equations 4.54, 4.55 and 4.56. Pooley and Furtado showed that the use of these stencils gives a substantial reduction in spurious velocities, which are a common feature in the simulation of multiphase flows.

$$\frac{\partial\phi}{\partial x} = \frac{1}{12}(4\phi_{i+1,j} + \phi_{i+1,j-1} + \phi_{i+1,j+1} - 4\phi_{i-1,j} - \phi_{i-1,j-1} - \phi_{i-1,j+1}) \tag{4.54}$$

$$\frac{\partial\phi}{\partial y} = \frac{1}{12}(4\phi_{i,j+1} + \phi_{i+1,j+1} + \phi_{i-1,j+1} - 4\phi_{i,j-1} - \phi_{i+1,j-1} - \phi_{i-1,j-1}) \tag{4.55}$$

$$\begin{aligned}\nabla^2\phi = \frac{1}{6}(&4\phi_{i+1,j} + 4\phi_{i,j+1} + 4\phi_{i-1,j} + 4\phi_{i,j-1} \\ &+ \phi_{i+1,j+1} + \phi_{i+1,j-1} + \phi_{i-1,j+1} + \phi_{i-1,j-1} - 20\phi_{i,j})\end{aligned} \tag{4.56}$$

When implemented, the multiphase method just described is capable of modelling multiple fluids; however, it does not have the capability to model fluids of differing densities. Methods of achieving density differences, and more importantly high ratio density differences such as is seen between the density of

air and water, have been proposed most notably by Imamuro *et. al.* [66] and Lee [79]; however, due to the increased complexity of implementation, a density difference method has not been used in this work. Instead, a pseudo density difference has been implemented by controlling the forces applied on a phase by phase basis. To model buoyancy, the nominally lighter of the two fluids has been given a force in the vertical direction whenever it is below the global free surface height. Conversely, any regions of the heavier fluid above the global free surface height are given a downward force component.

Additionally, without incorporating a density difference, there is also no viscosity difference between the fluids. This has been addressed at least in the laminar and transitional regime simulations by lowering the relaxation value τ for the phase representing air so that at least some viscosity difference exists between the fluids. At higher Reynolds numbers this was not possible as the relataxtion value τ was already at its limit of stability, as discussed in Section 4.4.1. In this regime, the inertial effects of the flow dominate the viscous effects meaning that lack of a viscosity ratio is less of a problem.

4.7.3 Boundary Conditions

Implementation of a fluid-solid interaction requires additional functionality from the basic walls previously detailed in Section 4.3.1. The wetting phenomenon, discussed in Section 2.1.5 also needs to be implemented and controlled. If the surface energy, previously shown in Equation 4.42, is assumed to be linearly related to the phase concentration at the wall, it can be represented by

$$\varphi(\phi_s) = -\omega\phi_s \tag{4.57}$$

where ω is a parameter controlling the concentration and is a function of the contact angle of the surface. This can be implemented by creating a boundary condition specified as

$$\kappa\hat{\mathbf{n}} \cdot (\nabla\phi)_S = -\omega \tag{4.58}$$

where $\hat{\mathbf{n}}$ is a unit vector pointing from the wall into the fluid. Following the same approach of Briant [16] and De Gennes [32] allows the surface tensions to be written as

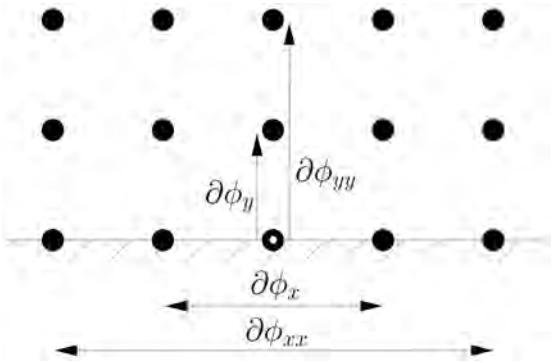

Figure 4.25: Boundary conditions at a wall.

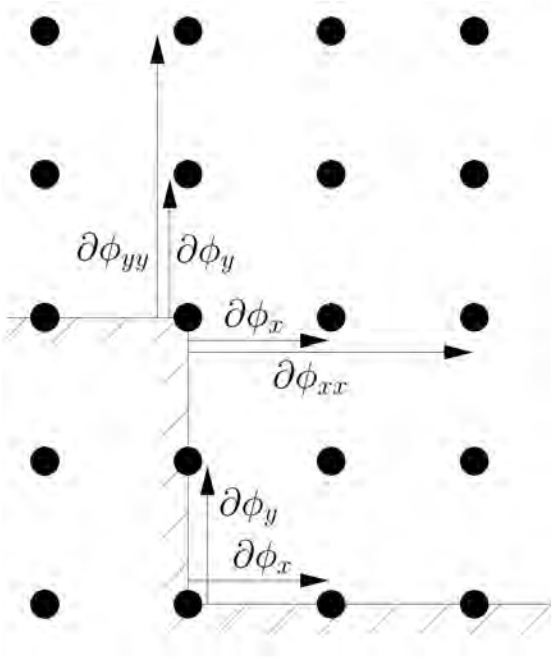

Figure 4.26: Boundary condition at a corner.

$$\sigma_{sg} = -\omega\phi + \frac{\sigma}{2} - \frac{\sigma}{2}(1-\bar{\omega})^{3/2} \tag{4.59}$$

$$\sigma_{sl} = -\omega\phi + \frac{\sigma}{2} - \frac{\sigma}{2}(1+\bar{\omega})^{3/2} \tag{4.60}$$

where again, σ_{sg} is the surface tension between the solid and the gas, σ_{sl} is the surface tension between the solid and the liquid, and σ is the surface tension between the liquid and the gas. Substituting these values into Youngs equation (Equation 2.12) gives

$$\cos\theta_w = \frac{1}{2}\left[(1+\bar{\omega})^{\frac{3}{2}} - (1-\bar{\omega})^{\frac{3}{2}}\right] \tag{4.61}$$

where $\bar{\omega} = \omega/(\sqrt{2\kappa a})$. This equation allows calculation of the wetting angle for a known value of ω, however a more helpful formulation of this allows calculation of ω for a specified contact angle θ_w. This can be found in the range of $0 < \theta_w < \pi$ by Equation 4.62 which was published by Papatzacos [95].

$$\omega = 2sgn\left(\frac{\pi}{2} - \theta_w\right)\left[\cos\left(\frac{\alpha}{3}\right)\left[1 - \cos\left(\frac{\alpha}{3}\right)\right]\right]^{\frac{1}{2}} \tag{4.62}$$

where $\alpha = \arccos(\sin^2\theta_w)$ and $sgn(x)$ gives the sign of x (positive or negative).

Implementation of this theory is achieved by forcing the concentration gradient at the wall to be

$$\partial\phi_\perp = -\omega/\kappa \tag{4.63}$$

along with calculating the first and second order derivatives to correctly compute both $\nabla\phi$ and $\nabla^2\phi$ which are required in Equations 4.45 and 4.46 respectively. The equations to compute the required wall derivatives are:

$$\partial_x\phi|_{i,j} \approx (\phi_{i+1,j} - \phi_{i-1,j})/(2\delta_x) \tag{4.64}$$

$$\partial_y\phi|_{i,j} = -\omega/\kappa \tag{4.65}$$

$$\partial_{xx}\phi|_{i,j} \approx (\phi_{i+1,j} - 2\phi_{i,j} + \phi_{i-1,j})/\delta_x^2 \tag{4.66}$$

$$\partial_{yy}\phi|_{i,j} \approx (6\omega\delta_x/\kappa + \phi_{i,j+2} + 4\phi_{i,j+1} - 5\phi_{i,j})/(4\delta_x^2) \tag{4.67}$$

$$\nabla^2\phi = \partial_{xx}\phi + \partial_{yy}\phi + \partial_{zz}\phi \tag{4.68}$$

In three dimensions, the derivatives in the z-axis are similar to those on the other non-wall normal axis, which in this case is the x-axis. Combinations of

these can then be constructed along the wall. This is shown diagramatically in Figures 4.25 and 4.26.

An important feature of wall bounded flows is the way in which the wall interacts with the fluid. This is critical in multiphase flows as differences in the surface tension between the fluids and the surface give rise to different physical wetting properties of the wall. The formula for the internal contact angle was devised by Young and can be seen as Equation 4.69 where the σ terms represent the surface tension at the solid-gas interface, the solid-liquid interface, and the gas-liquid interface respectively.

$$\cos\theta = \frac{\sigma_{sg} - \sigma_{sl}}{\sigma_{gl}} \tag{4.69}$$

In order to confirm accuracy of the simulations in this area, three simulations were conducted with differing wall wetting parameters corresponding to contact angles of 45°, 90° and 110°. The test domain was a box measuring 60 lattice units on each edge. The top and bottom surfaces were set as no-slip walls whilst the remaining surfaces were set as periodic boundaries. A spherical droplet of water with a radius of 20 lattice units was initially placed above the wall and then was allowed to drop onto the surface. After landing on the wall, the droplet underwent some transient oscillatory behaviour as it moved towards an equilibrium state. After reaching this steady state, a slice was taken through the centre of each droplet. As the interface spreads across a number of cells, as was discussed in Section 4.7.1, an iso-surface of $\phi = 0$ was created to improve the accuracy of the contact angle measurements. The measured contact angles were found to be within 3% of the desired angles indicating that the code performs accurately for multiphase boundary interactions. Results of this test can be seen in Figure 4.27.

4.7.4 Surface Tension and Buoyancy

At small scales, the forces resulting from surface tension can dominate fluid behaviour. A prime example of this is shown in the way that insects and other small creatures are able to use surface tension to balance the gravitational forces being applied to them and walk on water. With this in mind, controlling the strength and influence of the surface tension in these simulations is paramount.

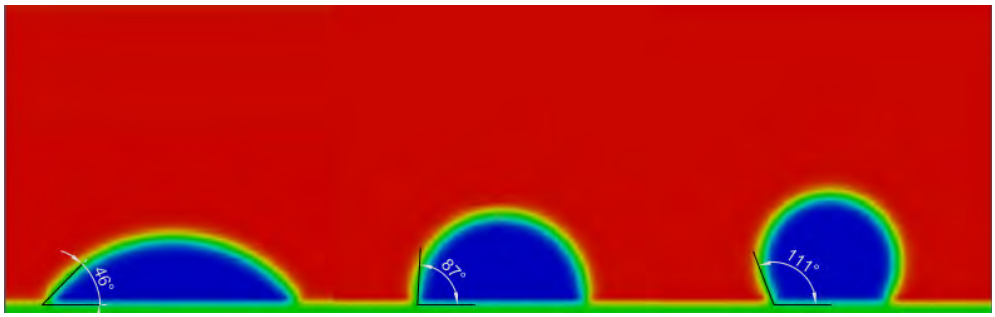

Figure 4.27: Droplets on hydrophillic, regular and hydrophobic surfaces exhibiting nominal internal contact angles of 45°, 90° and 110°. Measured contact angles are within 3% of the nominal values.

The surface tension parameter (σ) is found using the same method as all other variables in the lattice Boltzmann method, namely through the intermediate of a non-dimensional number. The relevant non-dimensional numbers used to find the surface tension and the gravitational acceleration (which is applied as a body force and gives bubbles their buoyancy) are the Eötvös number (Eo), and the Weber number (We), which are defined in Equations 4.70 and 4.71 respectively.

$$Eo = \frac{\Delta\rho \; g \; L^2}{\sigma} \tag{4.70}$$

$$We = \frac{\rho \; U^2 \; L}{\sigma} \tag{4.71}$$

Confirming the value of the surface tension can be achieved used the procedure outlined by Jain, Tentner and Rizwan-uddin [68]. With the Young-Laplace equation, shown as Equation 4.72, the surface tension can be calculated by taking measurements of both the radius and the pressure within a droplet or bubble.

$$\Delta P = \frac{\sigma}{R} \tag{4.72}$$

Finding the internal pressure can be accomplished by using an equation of state. He and Doolen [54] showed that for a single component multiphase system (of which this implementation is an example of) the equation of state is

$$P = \rho RT + \frac{GRT}{2} \left[\psi \left(\phi\right)\right]^2 \tag{4.73}$$

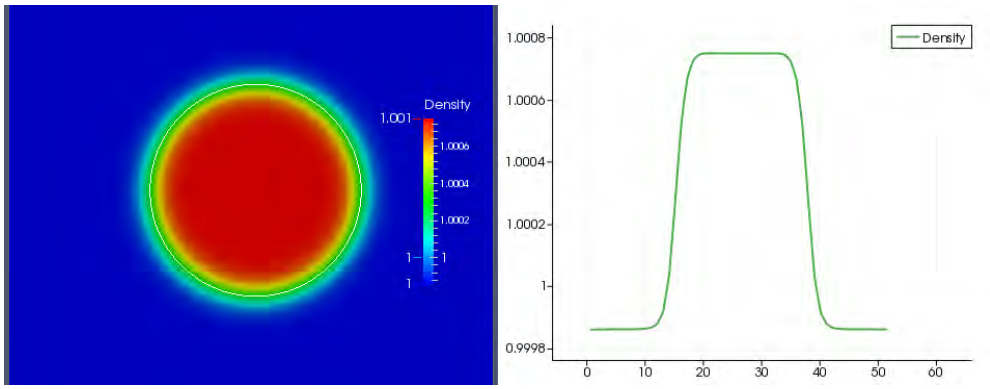

Figure 4.28: Surface Tension Measurement. Left: Contours of phase concentration of phases representing air (red) and water (blue). The highlighted isocurve at $\phi = 0$ is used to measure the radii of the bubble. Right: A plot of density taken along a slice through the middle of the bubble.

where G represents the interaction strength, $\psi(\phi)$ represents the interaction potential as a function of the phase density, and $RT = \frac{1}{3}$ as discussed in Section 4.2.1. In this work, the interaction strength is directly proportional to the mobility parameter $\overline{M}$, and the interaction potential is calculated via the stencils presented in Equations 4.54, 4.55 and 4.56.

The process of measuring the surface tension involves initialising a circular droplet of fluid in a two dimensional periodic domain. As the simulation progresses, the droplet shrinks in size due to the effect of surface tension until the inward component of the force on the surface is counter-acted by the internal pressure. When the solution reaches this steady state, by measuring the radii of the droplet and the pressure difference between the inside and outside of the droplet the Young-Laplace equation is used to calculate the actual surface tension.

A series of simulations was performed to ensure the surface tension was accurate using the method just described. The procedure was applied to bubbles of varying size for a fixed value of σ, the results of which were plotted with a line fitted to them so that they could then be used as a calibration factor. Figure 4.28 shows one of these measurement taking place.

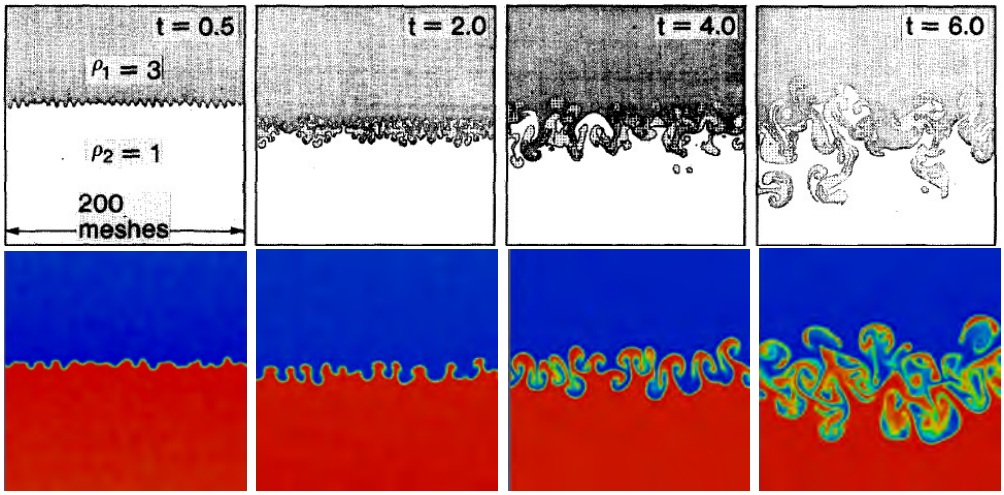

Figure 4.29: Top Row - Results of Youngs [144].
Bottom Row - corresponding plots generated
by the lattice Boltzmann code.[3]

4.7.5 Rayleigh-Taylor Instabilities

Finally, as a way of combining both the turbulence modelling and the multiphase components of the code, a simulation of Rayleigh-Taylor instability was undertaken. As shown by Youngs [144, 145], these instabilities, formed when a heavy density fluid is accelerated into an immiscible fluid of lighter density, exhibit turbulent flow characteristics. Similar to the previous tests, the domain used for this case was a channel with periodic boundary conditions on the sides and no-slip walls on the top and bottom.

The code used to perform these simulations does not have a method of providing a numerical density difference implemented, as the additional complexity of implementing this outweighs the benefits of doing so. However, a pseudo density difference has still been achieved by applying different body forces to the different fluids.

The fluid in the bottom half of the domain, having an initial concentration of $\phi = 1$ was given a body force acting upwards. The force was then continually applied to all cells with a concentration greater than 0. The fluid with a phase concentration less than 0 was given a body force acting downwards that was three times the magnitude of that of the upward force. These initial conditions actually correspond to a meta-stable state, and without some form of perturbation,

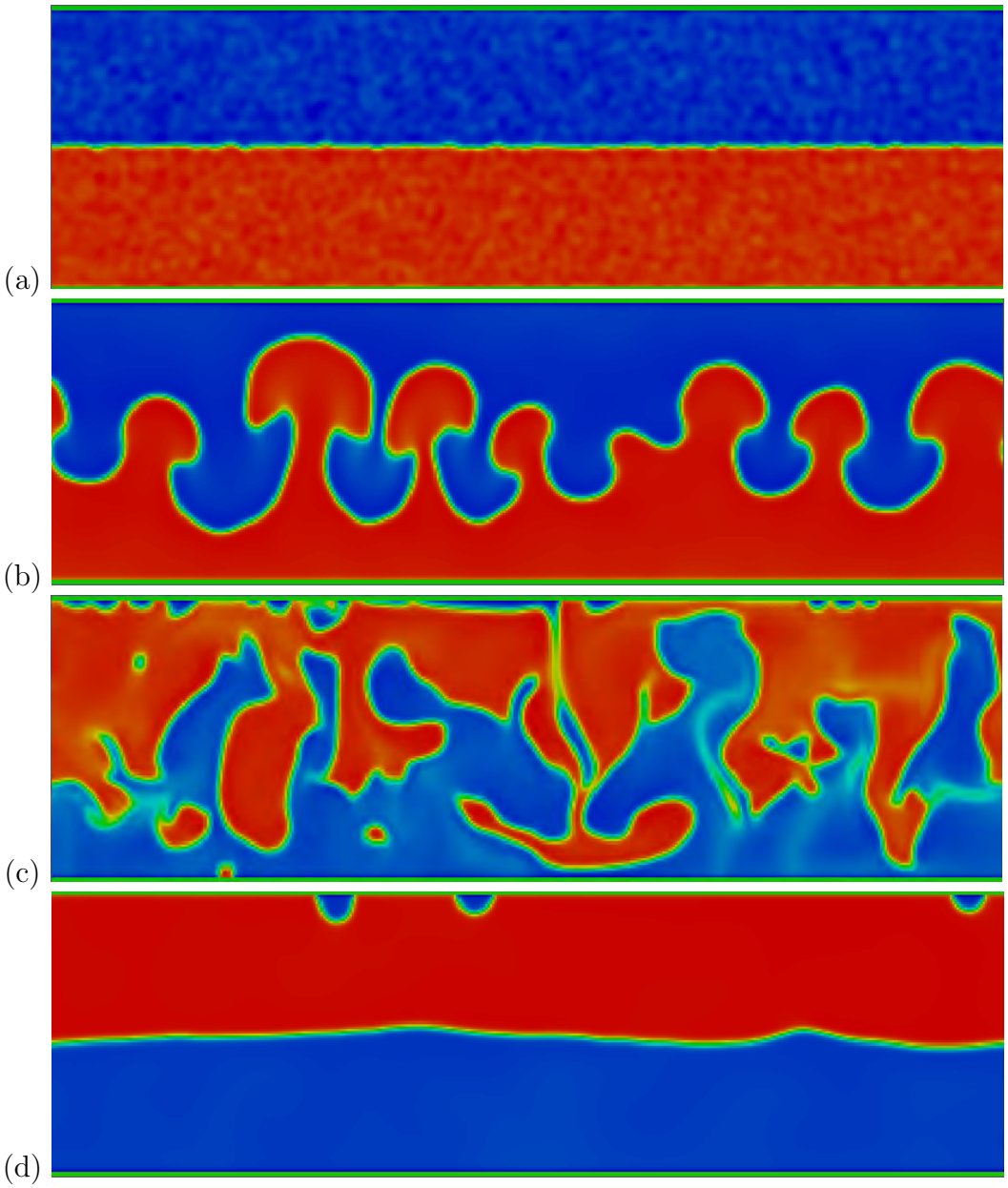

Figure 4.30: Time series images of simulation of Rayleigh-Taylor instabilities.
(a) initial condition with perturbation.
(b) Rayleigh-Taylor instabilities.
(c) turbulent mixing.
(d) phase segregation

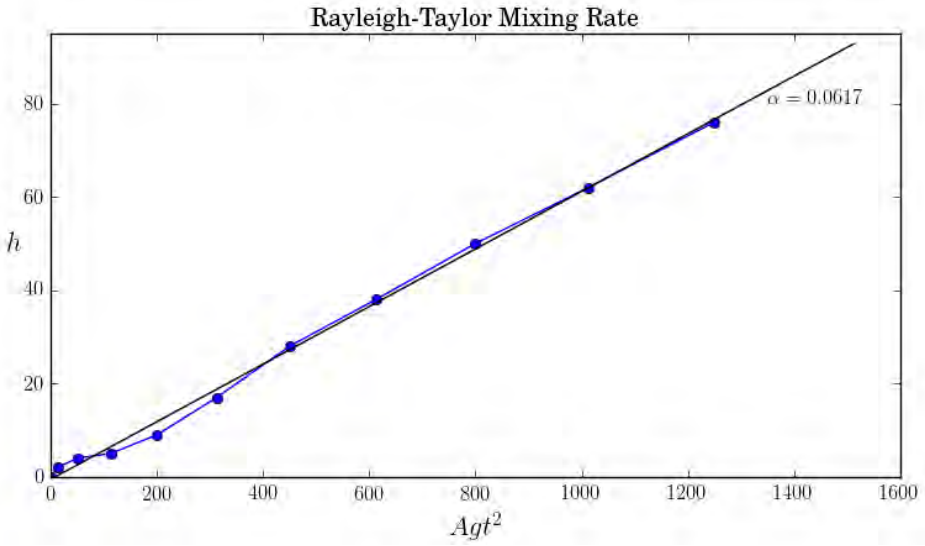

Figure 4.31: Calculation of the Rayleigh-Taylor mixing co-efficient. By plotting the bubble penetration height against the Agt^2 term, the RT mixing co-effieient α is measured by finding the gradient of the line.

the fluids will stay in their initial locations. In order to start the turbulent mixing, a random velocity perturbation similar to that described in the turbulent validations previously performed was introduced.

Visual inspection of Figure 4.29 shows that the results of the current work and those of Youngs are qualitatively similar. If the simulation is allowed to run until it reaches a stable state, a number of different phenomena can be seen throughout the course of the computations. Figure 4.30 shows Rayleigh-Taylor instabilities early in the simulations, followed by a turbulent mixing phase. Finally, the fluids undergo spinodal decomposition, a process which is consistent with the Cahn-Hillard equation.

The Rayleigh-Taylor instability simulation has also been validated in the same method as that of Read & Youngs [104, 144]. This involves measuring a dimensionless mixing co-efficient α which is defined as

$$h = \alpha A g t^2 \tag{4.74}$$

where h is the height of the bubble penetration above the initial free surface, A is the Atwood number (shown in Equation 4.75), g is the gravitational acceleration,

and t is the simulation time. Although the densities of both fluids in this simulation were the same, the application of different forces to them gives them effective densities of $\rho_1 = 1$ and $\rho_2 = 3$ respectively. This results in an Atwood number of

$$\begin{aligned} A &= \frac{(\rho_2 - \rho_1)}{(\rho_2 + \rho_1)} \\ &= \frac{(3-1)}{(3+1)} \\ &= 0.5 \end{aligned} \tag{4.75}$$

Combining this with a gravitation acceleration of 0.01 lu/ts^2, the resulting bubble penetration heights can be plotted against the Agt^2 term with the gradient of the line being equal to the mixing co-efficient α. Figure 4.31 shows this plot which gives an α value of 0.0617. Experiments have shown that the mixing co-efficient should be in the range of 0.05 $\rightarrow$ 0.077 indicating that the Rayleigh-Taylor instability simulation is operating correctly.

4.7.6 Super Hydrophobic Validation

With the goal of this research being to investigate turbulent flow over hydrophobic surfaces, confirming that this method is able to accurately do so is paramount. As has been previously discussed in Chapter 2, there has been minimal work looking at turbulent flow over these surfaces, however there has been significant work done in the laminar regime. As such, confirming that the code can accurately reproduce these laminar flow results would go a long way towards confirming it's viability for use in this research.

A series of experiments were performed by Shin [41] as part of an undergraduate project investigating the use of super-hydrophobic surfaces for heat transfer and heat insulation. Shin's experiment used a channel of $1.75mm \times 50\mu m \times 100\mu m$ length, width and height respectively with 25 identical micro features of $40\mu m$ each separated by $30\mu m$ ridges. Due to the size of the experiment, only very low Reynolds numbers flow could be studied. Although Shin performed tests at a range of flow rates, only one has been replicated in this work, namely the case corresponding to a Reynolds number of $Re_\phi = 1$.

Using air and water as the working fluids, and with an inlet velocity of $0.011m/s$ (corresponding to a flow rate of $6\mu L/min$), relevant non-dimensional numbers for the experiment can be calculated.

The Reynolds number for the physical experiment (designated by subscript $phys$) is based on the channel height, fluid velocity and kinematic viscosity of water and is shown in Equation 4.76.

$$Re_{\phi,phys} = \frac{U\phi}{\nu} = \frac{0.011 \times 100 \times 10^{-6}}{1.004 \times 10^{-6}} = 1.096 \tag{4.76}$$

Likewise, the Weber and Eötvös numbers were also calculated, and can be seen in Equations 4.77 and 4.78.

$$We_{phys} = \frac{\rho U^2 \phi}{\sigma} = \frac{1000 \times 0.011^2 \times 100 \times 10^{-6}}{7.2 \times 10^{-2}} = 1.677 \times 10^{-4} \tag{4.77}$$

$$Eo_{phys} = \frac{\Delta\rho g \phi^2}{\sigma} = \frac{1000 \times 9.81 \times (100 \times 10^{-6})^2}{1.004 \times 10^{-6}} = 1.363 \times 10^{-3} \tag{4.78}$$

Corresponding values for the lattice Boltzmann simulation (designated by subscript lbm) were then found by iteratively solving the three non-dimensional equations. The resulting values can be seen in Equations 4.79, 4.80 and 4.81. (δx and δt were both set to 1.)

$$Re_{\phi,lbm} = \frac{3.272 \times 10^{-4} \times 100}{0.02987} = 1.096 = Re_{\phi,phys} \tag{4.79}$$

$$We_{lbm} = \frac{1 \times (3.272 \times 10^{-4})^2 \times 100}{6.42 \times 10^{-2}} = 1.674 \times 10^{-4} \approx We_{phys} \tag{4.80}$$

$$Eo_{lbm} = \frac{1 \times 8.72 \times 10^{-9} \times 100^2}{6.42 \times 10^{-2}} = 1.363 \times 10^{-3} = Eo_{phys} \tag{4.81}$$

This resulted in a set of multiphase parameters as shown in Table 4.7.

Using these values, the simulation was initially run with no fluid flow until it reached a steady state to be consistent with the initial state of the experiment. The inlet velocity was then set to 3.272×10^{-4} and allowed to iterate until a steady state was again reached.

(a) Free surface at start of the experiment.

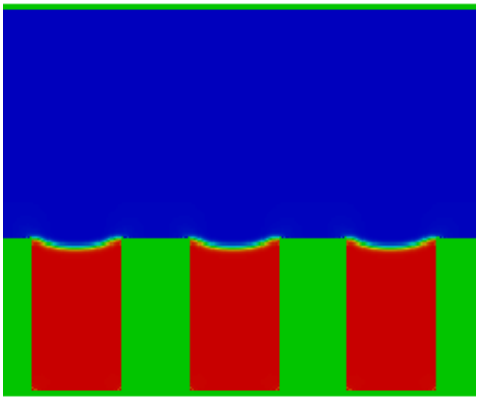

(b) Free surface at start of the simulation.

(c) Free surface at steady state in the experiment.

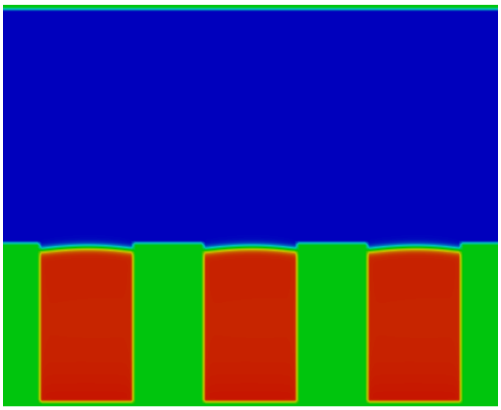

(d) Free surface at steady state in the simulation.

Figure 4.32: Comparison of experimental and simulated free surface location for a hydrophobic surface. Experimental images are from an undergraduate project by Shin [41].

Table 4.7: Multiphase Parameter Summary.

Parameter	Symbol	Physical	LBM
Velocity	U	0.011	3.272×10^{-4}
Density	ρ	1000	1
Surface Tension	σ	0.072	0.064
Channel Height	ϕ	100×10^{-6}	100
Density Difference Ratio	$\Delta\rho$	1000	1
Kinematic Viscosity	ν	1.004×10^{-4}	0.02987
Gravity	g	9.81	8.72×10^{-9}
Relaxation	τ	-	0.5896

Shin provided images taken under a microscope showing the location of the free surface both before starting the experiment and after the experiment reached a steady state. These can be directly compared to the corresponding images taken from the simulations, and are shown in Figure 4.32. As is immediately obvious, the simulations have replicated the free surface locations quite accurately.

Although Shin was predominantly interested in heat transfer effects, he did measure and publish a percentage difference in pressure drop between the micro-featured channel shown and the theoretical pressure drop in an unfeatured plain channel. Shin found that the super-hydrophobic surface reduced the pressure drop through the channel by 17.83%. Instead of measuring the pressure drop across the channel, the simulation instead measured the drag force on the walls of the super-hydrophobic and an unfeatured channel with the same dimensions and parameters. The super-hydrophobic channel exhibited 13.4% less drag than the unfeatured channel, a result that indicates that the simulation may be slightly under-estimating the drag reduction measured.

Based on the accuracy of the free-surface location, and the relative accuracy of the pressure drop / drag measurements, it appears that this implementation of the lattice Boltzmann method is capable of studying flow over super-hydrophobic surfaces.

4.8 Implementation

With the theory explained and validated, a few comments will now be made about the actual implementation of the code. Further details can be seen in Appendix B.

This implementation of a lattice Boltzmann code was written in version 11 of C++. This allowed the use of some of the newer features, especially the lambda functions that allow a programmer to write cleaner and more efficient code. The production version of the code was compiled using the Portland Group compiler (PGI) with optimisation flags specific to the architecture of the hardware on which the code was run, to maximise performance, and minimise simulations run times.

4.8.1 Measurements

To investigate drag reduction it is first essential that the drag force acting on a surface can be accurately measured. As was discussed in Chapter 2 drag, or more properly from a naval architecture perspective, resistance, is composed of shear drag and pressure or form drag.

The typical technique of measuring drag in the lattice Boltzmann method was described in Section 4.3.1.2 however in most cases this only gives the total drag on an object, and not the component values. This issue is alleviated in this work by virtue of only using walls aligned with the lattice, meaning that any walls perpendicular to the free stream are contributing to the pressure drag and walls parallel to the free stream contribute to the shear drag.

As an aside, a more general method of determining the drag components is to measure the shear drag independently. From basic fluid dynamics, the value of shear stress on a surface force can be found by

$$\tau_w = -\mu \frac{\partial U}{\partial y} \tag{4.82}$$

where μ is the dynamic viscosity and $\frac{\partial U}{\partial y}$ can be found by explicitly measuring the velocities in cells between the wall and the centre of the channel. The dynamic viscosity is trivial to calculate given the relation $\nu = \frac{\mu}{\rho}$. In practise this is achieved

by measuring the the density of the fluid in each cell and multiplying by the global kinematic viscosity to give the local dynamic viscosity.

By integrating this shear stress over the area of the boundary, the shear drag on the wall can be found, as shown in Equation 4.83

$$\text{Drag}_{Shear} = \int -\mu \frac{\partial U}{\partial y} dA \tag{4.83}$$

The pressure drag component can also be found by subtracting the shear drag component from the total drag found by the momentum transfer method

$$\begin{aligned} \text{Drag}_{Total} &= \text{Drag}_{Shear} + \text{Drag}_{Pressure} \\ \therefore \text{Drag}_{Pressure} &= \text{Drag}_{Total} - \text{Drag}_{Shear} \end{aligned} \tag{4.84}$$

This process can be validated by measuring the drag on the wall of a smooth channel. Given that the total drag is due only to the shear drag component, both the standard lattice Boltzmann method of calculating drag, and the method just presented should both give the same result. This has been achieved by using the same Poiseuille flow simulation as was presented in Section 4.3.3. As is shown in Figure 4.33, the shear force acting on the wall should be equal to the force being applied to the fluid between the wall and the centre of the channel. Based on the applied force of $F = 1.29 \times 10^{-5}$ and the channel height of 40 lu, Equation 4.85 gives the expected shear force on the wall per unit area[1].

$$\begin{aligned} \tau_{w,Expected} &= F\delta \\ &= 1.29 \times 10^{-5} \times 21 \\ &= 2.709 \times 10^{-4}\ lu^2/ts^2 \end{aligned} \tag{4.85}$$

Taking a vertical section through the channel and extracting the velocities at each point between the wall and the channel centreline allows the calculation of $\frac{\partial U}{\partial y}$ and is shown in Table 4.8. These values are measured across the width of the boundary layer (or in this case the half channel height) to give the value of $\frac{\partial U}{\partial y}$ used to find the shear force on the wall, as shown in Equation 4.86. With the relaxation value for the simulation set at $\tau = 0.6$ and the density set at $\rho = 1$, this corresponds to a dynamic viscosity of $\mu = 0.0\dot{3}\ lu^2/ts$.

[1]The value of $\delta = 21$ is due to the fact that for 20 lattice cells there are 21 nodes at which the force is applied.

Table 4.8: Wall shear drag calculation using $\tau_w = -\mu \frac{\partial U}{\partial y}$

$U \quad (\times 10^{-2})$ (lu/ts)	y (lu)	$\frac{\partial U}{\partial y} \quad (\times 10^{-2})$ $(\frac{1}{ts})$
12.3344	20	0.6167
12.3021	19	0.6475
12.2054	18	0.6781
12.0441	17	0.7085
11.8184	16	0.7387
11.5281	15	0.7685
11.1734	14	0.7981
10.7541	13	0.8272
10.2704	12	0.8559
9.7221	11	0.8838
9.1093	10	0.9109
8.4321	9	0.9369
7.6903	8	0.9613
6.8841	7	0.9834
6.0133	6	1.0022
5.0781	5	1.0156
4.0784	4	1.0196
3.0141	3	1.0047
1.8853	2	0.9427
0.6921	1	0.6921
0	0	0

$\tau_w = -\mu \frac{\partial U}{\partial y} \Rightarrow$	$\frac{\partial U}{\partial y}$	8.0916×10^{-3}
	μ	$0.0\dot{3}$
	τ_w	-2.6972×10^{-4}

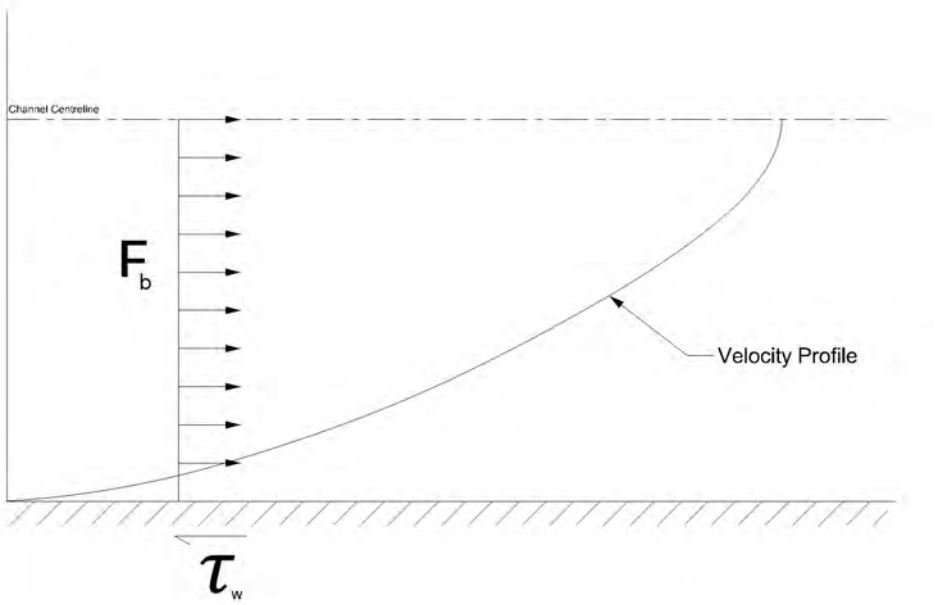

Figure 4.33: Forces involved in Poiseuille flow. The shear force at any point on the wall (τ_w) should be equal to the sum of the body forces ($\mathbf{F}_b$) being applied to the fluid between the wall and the centre of the channel at the same streamwise location. The velocity profile at this location allows calculation of $\frac{\partial U}{\partial y}$.

$$\begin{aligned} \tau_w &= -\mu \frac{\partial U}{\partial y} \\ &= -0.0\dot{3} \times 8.0916 \times 10^{-3} \\ &= -2.6972 \times 10^{-4}\ lu^2/ts^2 \end{aligned} \tag{4.86}$$

Comparing this with the expected wall shear of $2.709 \times 10^{-4}\ lu^2/ts^2$ shows that measuring the shear drag in this manner appears to be an accurate alternative to the momentum exchange method. The error between the two methods is 0.435%, a value which is easily attributed to numerical round off within the comparison calculations.

4.8.2 Parallelisation

Due to the local nature of the governing equations, and the fact that each node only ever needs to communicate with its closest neighbours, the lattice Boltzmann

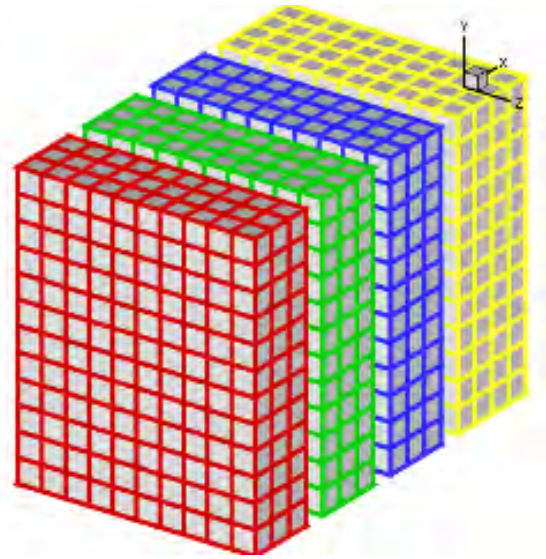

Figure 4.34: "Book" style domain decomposition.

method is highly parallelisable. This means the domain can be decomposed across a large number of processing cores to increase the computational efficiency and minimise the overall run time of the simulation. Ideally, a domain should be decomposed in a way that gives the lowest surface area to volume ratio, so that the information required to be passed to neighbours can be kept to a minimum while the number of local nodes is maximised. This also needs to be balanced against the concept of load-sharing, where each processing node has a roughly equivalent amount of work to do. To achieve this, the decomposition method utilised was that of the "book" approach, where slices are taken through the domain on the Y-Z axis. An example of this can be seen in Figure 4.34. In order to ensure each processor received a similar amount of work, the slices are all made to be the same thickness.

A study was undertaken to find the optimum number of processing cores on which to run the simulations. This was done by first calculating the speedup factor of various numbers of processors. The speedup factor can be defined as

$$S_p = \frac{T_1}{T_p} \tag{4.87}$$

where S is the speedup factor, p is the number of processors, and T is the time taken to execute the program on 1 and p processors respectively. As the

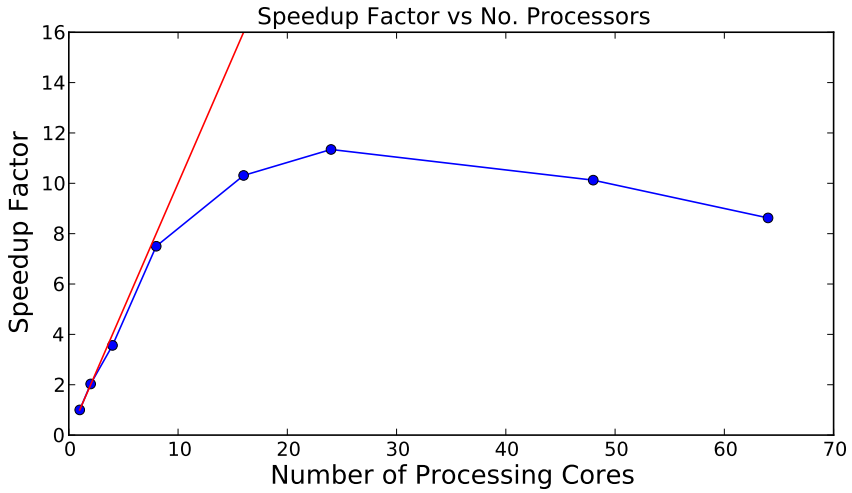

Figure 4.35: Speedup factor with varying number of processors. The red line indicates a linear speedup. As can be seen, for a small number or processors the speedup follows this quite closely.

number of iterations completed is inversely proportional to the runtime, this can be re-written as

$$S_p = \frac{I_p}{I_1} \tag{4.88}$$

with I being the number of completed iterations within a given time period.

The speedup factors were found by running a series of identical simulations for a 24 hour period on differing numbers of processors. The number of iterations each simulation completed was then recorded and normalised against the number achieved by a single core, as can be seen in Table 4.9. As the code only reports every 1000 iterations[1] the values can be up to 999 iterations more than shown in Table 4.9. Calculating the worst case scenario, which occurs when the single processor value is 32999 and the remainder of the results are unchanged shows that for the 24 processor case the speedup factor is lowered by $\approx 3\%$ to 11.0.

Shown graphically, in Figure 4.35, it is clear to see that running on 24 processing cores gives the fastest result. From this graph, it is also clear that for low numbers of processors, the speedup factor lies on or near the linear speedup

[1]The code can be set to report more frequently however CPU cycles spent outputting result data are CPU cycles not being used for computation. By keeping the reporting to the bare minimum the overall efficiency can be increased.

Table 4.9: Results of processor scaling test

Procs	Iteration	Speedup Factor (S_p)	Time/Iter (sec)	Normalised Time/Iter (%)	Worst Case Speedup Factor
1	32000	1.000	2.700	100.00%	1.000
2	65000	2.031	1.329	49.23%	1.970
4	114000	3.562	0.758	28.07%	3.455
8	240000	7.500	0.360	13.33%	9.273
16	330000	10.312	0.262	9.70%	10.000
24	363000	11.344	0.238	8.82%	11.000
48	324000	10.125	0.267	9.88%	9.818
64	276000	8.625	0.313	11.59%	8.364

line. At higher numbers of processors, the speedup decreases again, largely as a result of the extra inter-processor communication required due to the increased surface area to volume ratio of the sub domains.

In practice, the simulations were run on a combination of 16 or 24 processing cores. The hardware being used had either 48 or 64 processing cores per machine meaning that for the expense of 1 unit of speedup (10 down from 11), and extra simulation could be run on a 48 core machine. i.e. three 16 core jobs are run instead of two 24 core jobs. The reduction in efficiency of the reduced number of processing cores for the simulation is far outweighed by running an extra simulation simultaneously. Similarly, on machines with 64 processing cores, to make full use of the resources running four simulations each with 16 cores has a higher overall efficiency than running two simulations each with 24 cores and one with 16 cores.

Details about the hardware these simulations were run on can be found in Appendix B.

Chapter 5

Computational Setup

With both the theory and implementation of the lattice Boltzmann method covered, it can now be used for the purpose it was intended, namely to simulate flow over super hydrophobic surfaces. The set up of the simulation can be divided into two areas, the geometrical and the physical. The geometrical set up consists of the size and shape of the domain and the grooves and posts it contains. The physics setup deals with the fluid properties, including but not limited to velocities, applied body forces, viscosity and buoyancy. Both of these areas are further described below.

5.1 Geometrical Setup

5.1.1 Channel

Each of the super hydrophobic geometries tested in this work have their basis in a simple channel flow domain. This basis geometry, as can be seen in Figure 5.1, consisted of a rectangular box with walls on the top and bottom and open ends and sides. Both the ends and sides were set as periodic boundary conditions meaning the simulation was effectively flow between infinite flat plates. The walls themselves were set as no-slip walls and were implemented as was described in Section 4.3.1. Although this domain does not correspond exactly to the case of flow over the bottom of a ship, as it would if only a single wall were used, the study of flow between infinite parallel plates allows for higher Reynolds number flows to be simulated for the same sized domain as the turbulence can be generated

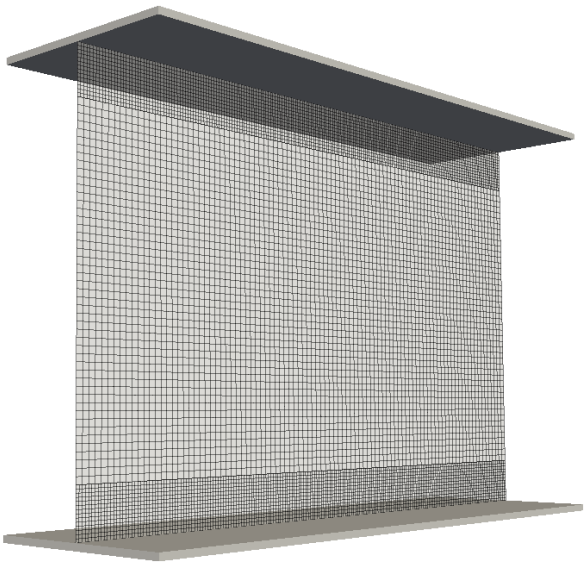

Figure 5.1: Channel Geometry

and contained within the domain as opposed to having a slip wall with would not generate any form of turbulence.

The coordinate system used in the domain was oriented so that the nominal direction of fluid flow was aligned with the positive x-axis. The y-axis origin was at the top of the domain and was positive in the downwards direction, and the z-axis was the span-wise direction, positive as per a right-handed coordinate system.

The total height of the channel was set at 128 lattice units, but with two cells at both the top and bottom used in the implementation of the wall[1], this left an effective channel height of 124 lu, which can also be expressed as a half channel height (δ) of 62 lu. In order to conform to the minimum size required to fully capture the turbulent motions in the flow, the domain needed to be a minimum of 197.9 lu in the streamwise direction, and 59.3 lu in the spanwise direction, as was discussed in Section 4.4.1.1. These values have then been rounded up to be 200 lu and 60 lu respectively.

[1]Due to the implementation of the periodic boundary conditions, in order to isolate the top and bottom boundaries from each other a set of solid nodes was needed. Without this the multiphase model included the opposite wall in it's phase gradient calculation.

Figure 5.1 also shows the mesh refinement with a refined layer adjacent to both the top and bottom walls. As was discussed in Section 2.1.1, the log-law region begins at a y^+ of ≈ 30. Below this, in the buffer layer and viscous sub-layer the viscous effects are highly significant, so in order to both capture these near wall effect, and more importantly, accurately measure the drag force on the wall, a refined mesh was implemented. Refining the mesh in the near wall region also allows a greater number of surface features to be modelled without having to enlargen the whole domain. The refined mesh extended 14 lattice units from the wall, a value which corresponds to a minimum of $y^+ \approx 40$ from the wall in the turbulent flow cases. Table 5.1 indicates the location of the grid refinement transition, and the cell sizes in dimensionless wall units for the range of wall shear Reynolds numbers investigated.

The mesh was kept identical throughout all simulations. This was done for two reasons, the first being to maintain consistency between tests. Secondly, and more importantly, although the height of the refinement layer could have been reduced to keep the same transition point for the mesh with the higher Reynolds numbers, the refined mesh is also required to accurately model the multiphase interface. With this interface moving more at the higher Reynolds numbers, the extra height of the refined mesh in these situations is advantageous.

This meshing strategy has been achieved by using 3 lattices, as was described in Section 4.6. The top and bottom lattice blocks have usable dimensions of $L \times H \times W = 200 \times 14 \times 60$, and an additional 5 cells of height where two cells were used in the wall implementation and three cells are used in the transfer overlap with the adjoining lattice. The central lattice block has dimensions of $L \times H \times\ W = 100 \times 46 \times 30$, again with additional cells in the y-axis so that two cells can be overlapped at both the top and bottom of the central lattice block. These lattices combine to form a domain with two 228,000 cell lattices and one 150,000 cell lattice giving a total of 606,000 cells. With the repeated streaming and collision operations needed in the refined regions, in each single iteration, a total of 1,062,000 lattice updates are performed[1].

[1] A lattice update refers to a single set of streaming and collision processes performed on a lattice cell.

Table 5.1: y^+ values for selected wall shear Reynolds numbers. These values were based on $y = 14$, and $\delta = 62$. The Fine and Coarse values give the y^+ range that a single fine and coarse cell cover respectively. The first cell height is half the height of the fine cell size due to the half-way bounce back boundary condition.

Re_τ	y^+ Transition	Δy^+ Fine	Δy^+ Coarse	y^+ First Cell
10	2.258	0.161	0.323	0.081
50	11.290	0.806	1.613	0.403
100	22.581	1.613	3.226	0.806
180	40.645	2.903	5.806	1.452
395	88.065	6.290	12.581	3.145
590	128.710	9.194	18.387	4.597

5.1.2 Spanwise Grooves

As discussed in Section 2.2, a typical structured super hydrophobic surface has micro structures that can consist of "posts", "ridges", "grooves" and / or "gaps". These features can be of a range of sizes, however in this work, barring a small variation study in Chapter 8, have been kept at a constant size of 10 μm. Although most of the work detailed in Chapter 2 used larger features than this, the majority of them have been targeted at laminar flow. Reducing the spacing between the features means the free-surface is more supported and therefore has a higher chance of producing drag reduction in the turbulent flow. Various combinations of geometry have been produced using this sizing, the first to be discussed being a span-wise grooved surface, shown in Figure 5.2.

This geometry contains a series of equally spaced spanwise ridges and grooves along the top wall of the domain. The depth and width of the grooves are 14 μm and 10 μm respectively with a resolution of 1 lu per μm. The ridges and grooves are rectangular in shape with square edged corners. The bottom wall of the domain is unchanged from the original smooth channel.

The height of the channel between the bottom wall and the top of the ridges has been kept the same as the original channel tested at 124 lu. The extra height

Figure 5.2: Span-wise Geometry

of the grooves is then added above this by increasing the height of top lattice block from 19 to 33 lattice units. This also results in the refined mesh covering the entirety of the micro structured surface.

Dealing just with the top wall, as was reported in Section 2.2.2, many researchers have made the assumption that the free-surface interface in the "gaps" experiences minimal out-of-plane deflection, and can therefore be treated as if it were a free-slip wall. Taking this assumption as correct, a reduction in wetted surface area of the surface can easily be found. For the span-wise case, the effective wetted surface area of this geometry relative to the channel is 50%.

The domain has been oriented this way because if super hydrophobic surfaces were applied to boats or ships, the surface would be at the top of the water column, not on the bottom as others have modelled it. This has the effect that buoyancy forces bring air bubbles towards the surface, rather than take them away meaning that any air bubbles that are removed from the surface are directed back towards the surface, with the aim that they might rejoin the air still on the surface.

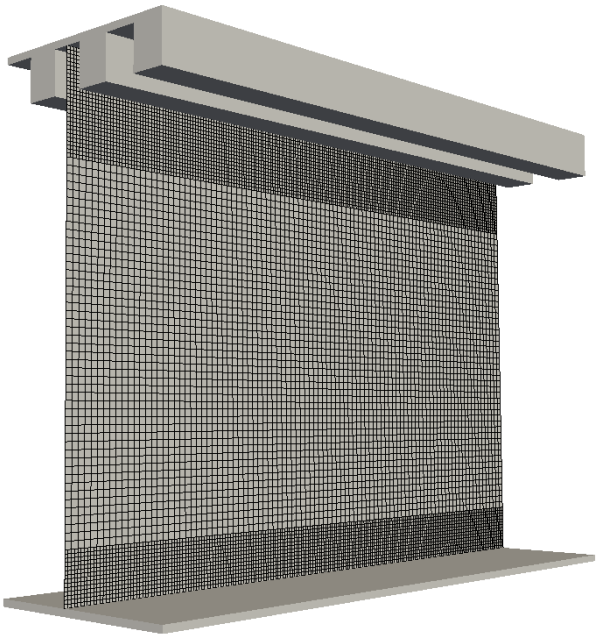

Figure 5.3: Stream-wise Geometry

5.1.3 Streamwise Grooves

The next geometry to be investigated contains stream-wise grooves and is shown in Figure 5.3. These grooves are aligned with the nominal direction of the flow and are again sized with both the width of ridges and the gaps at 10 μm and a height of 14 μm with a resolution of 1 lu per μm. The distance between the top of the ridges and the bottom wall has again been kept at 124 lu, and the wetted surface area relative to the channel is again 50%.

5.1.4 Aligned Posts

The aligned posts geometry is a combination of the span-wise and stream-wise geometries and can be seen in Figure 5.4. This combination results in posts being created instead of ridges as were seen in the previous geometries. The posts are $10\mu m \times 10\mu m$ square blocks and again are a height of 14 μm. This corresponds to a reduction in wetted surface area relative to the channel of 75%.

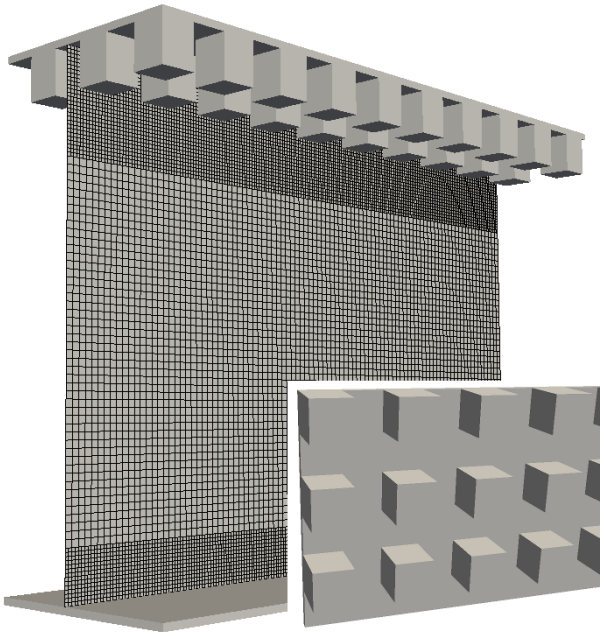

Figure 5.4: Aligned posts geometry. The inset image shows the posts aligned in both the stream-wise and span-wise directions.

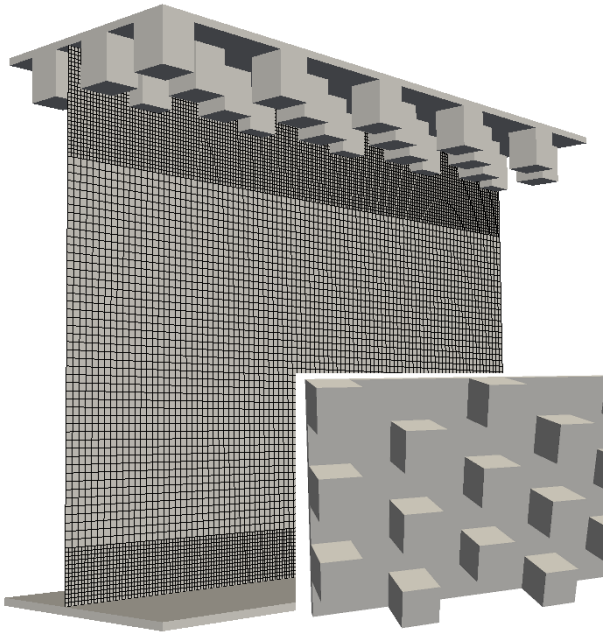

Figure 5.5: Offset posts geometry. The inset image shows the posts aligned in span-wise direction but offset in the stream-wise direction.

5.1.5 Offset Posts

The final geometry to be tested, shown in Figure 5.5, again uses posts instead of grooves and ridges however instead of the posts being aligned in both the span-wise and stream-wise directions, they are offset in the span-wise direction to stop the formation of the stream-wise grooves. This has been trialled in an attempt to minimise the "fetch" that the water has as it interacts with the air trapped on the surface. As with the aligned post geometry, the offset posts have a reduction in wetted surface area relative to the channel of 75%.

The offset post geometry, although still structured, is the closest of the tested geometries to the randomly structured surfaces that are increasingly finding favour. As opposed to structured surfaces, which need to be manufactured using either photo lithography, or other micro fabrication techniques, random post geometries can be created chemically and sprayed onto surfaces, allowing large areas to be coated.

5.2 Physical Setup

The lattice Boltzmann method differs from most CFD solvers in that it uses its own system of units. In order to give it the correct inputs, the physical units must first be non-dimensionalised then converted into lattice Boltzmann units, as was discussed in Section 4.3.2. These can then be used to control the velocity of the flow, the viscosity of the fluids, the resolution of the mesh and the multiphase specific parameters such as surface tension, contact angle and buoyancy forces.

5.2.1 Length, Time and Viscosity

Before non-dimensionalisation can occur, the characteristic variable of length and time must first be defined. The characteristic length in the simulation was set at 10μm, to match the typical sizing of the geometric features. With a resolution of 10 lattice units per characteristic length unit, this corresponds to a lattice unit length of $\delta_x = 0.1$. To maintain stability, a characteristic time step of $\delta_t = 0.01$ was also chosen.

As was earlier discussed in Chapter 4, the viscosity of fluids in the simulation is a key area of control within the lattice Boltzmann method. The best way

to achieve the high Reynolds numbers required is to minimise the viscosity; however, as the viscosity is proportional to both the relaxation factor and the fractional propagation parameter, decreasing the viscosity directly impacts both the stability and runtime of the simulation. In this work, both the relaxation factor and the fraction propagation parameters were kept constant at 0.52 and 0.1 respectively. These values result in a value of viscosity of 6.667×10^{-4} lu^2 [1].

5.2.2 Reynolds Numbers and Applied Forces

Probably the most important physical variable in these simulations was the shear velocity Reynolds number (Re_τ), shown again in Equation 5.1. This is a Reynolds number based on the wall shear velocity and is a commonly used non-dimensional number in bounded turbulent flow analysis

$$Re_\tau = \frac{u^* \delta}{\nu} \tag{5.1}$$

where u^* is the wall shear velocity ($u^* = \sqrt{\frac{\tau_w}{\rho}}$), δ is the half-channel height and ν is the fluid kinematic viscosity.

Six values of Re_τ have been tested ranging from laminar flow at $Re_\tau = 10$ up to fully turbulent flow at $Re_\tau = 590$. These values were chosen so as to align with the turbulent channel flow data made available by Moser *et. al.* This adds an additional level of validation and allows further comparisons to be made between the surfaces tested here and some verified data. Increasing the shear velocity Reynolds number is achieved by increasing the wall shear stress, which in turn is achieved by increasing the body force driving the fluid. With the wall shear stress being equal to the applied force times the half channel height ($\tau_w = F\delta$), Equation 5.1 can be re-arranged to provide the force required to drive the flow as a function of the requested Reynolds number, as shown in Equation 5.2 [2].

$$F = \frac{\rho(Re_\tau \nu)^2}{\delta^3} \tag{5.2}$$

Using values from this equation as an initial approximation, simulation on the smooth channel were run and the applied forces adjusted so as to get within

[1] The reported viscosity is for the refined mesh lattices. As was discussed in Section 4.6, the viscosity in the coarse lattice is half that of the refined lattices.

[2] This re-arrangement can be seen in Appendix C

Table 5.2: Applied forces at the different nominal Reynolds numbers and their corresponding actual Reynolds numbers in the smooth channel geometry.

Nom Re_τ	F_x	Actual Re_τ
10	$3.39E-10$	13.416
50	$7.63E-09$	53.876
100	$2.88E-08$	107.401
180	$4.64E-08$	182.704
395	$2.48E-07$	394.794
590	$6.84E-07$	584.229

10% of the nominal Reynolds numbers[1]. These values can be seen in Table 5.2. Each of the other geometries was then tested using the same applied forces as had been used in the smooth channel tests. The forces were only applied in the stream-wise direction and only within the confines of the channel, meaning that the fluid in the gaps and grooves does not have a force applied to it. This concept is similar to a lid driven cavity flow, and is more akin to the actual conditions that the surfaces would experience if they were to be applied to a ship. If the forces were also applied to fluid within the grooves, the upwind side of the micro features would exhibit a higher force than it actually should due to the force of the fluid within the groove being directly applied to it.

5.2.3 Initial Velocities

Another key physical feature is the initialisation of the velocity field within the domain. In each case, the fluid in the channel (again excluding any fluid in the gaps or grooves) was given a stream-wise velocity ten times that of the expected shear velocity. A rough guide is that the shear velocity is approximately $1/10th$ of the average flow velocity. By making use of this approximation, the simulation could be initialised in the general region where it was expected to become stable, and so decrease the amount of required run time for the system to stabilise. On

[1]With the exception of the $Re_\tau = 10$ case.

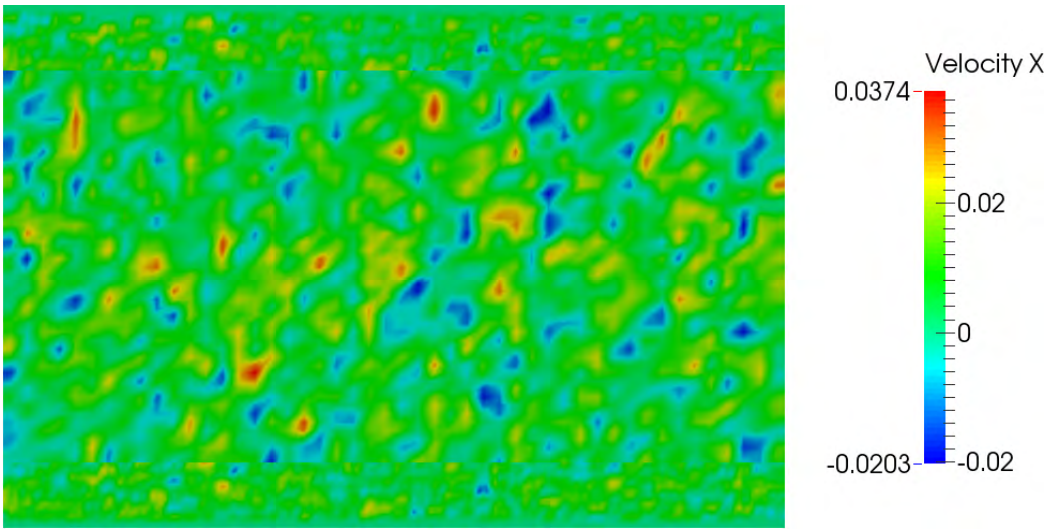

Figure 5.6: Initial velocity field in the stream-wise direction for the smooth channel case at $Re_\tau = 180$ with the random perturbation.

top of this uniform velocity, a random perturbation was super-imposed to assist in the flow tripping from laminar to turbulent. This perturbation could be up to 5% of the initial velocity, and was applied independently in the stream-wise, span-wise, and wall normal directions. After the perturbation had been applied, the velocity field underwent a smoothing operation to avoid discontinuities in neighbouring cells that would otherwise cause the simulation to fail. An example of the initial velocity field for the smooth channel at $Re_\tau = 180$ can be seen in Figure 5.6.

5.2.4 Multiphase Parameters

With the multiphase features of the simulation being of critical importance to the results, control of the specific parameters is paramount. The multiphase parameters were found in the same manner an that done in Section 4.7.6 with the Reynolds number, Weber number and Eötvös numbers all found and matched for the physical and non-dimensional systems. For the simulations, a value for the surface tension of $\sigma = 3.35 \times 10^{-5}\ lu^3/ts$ was used. This was combined with a gravitational acceleration of $4.52 \times 10^{-9}\ lt/ts^2$ resulting in a similar physical behaviour would be expected for air and water (albeit without the physical density difference).

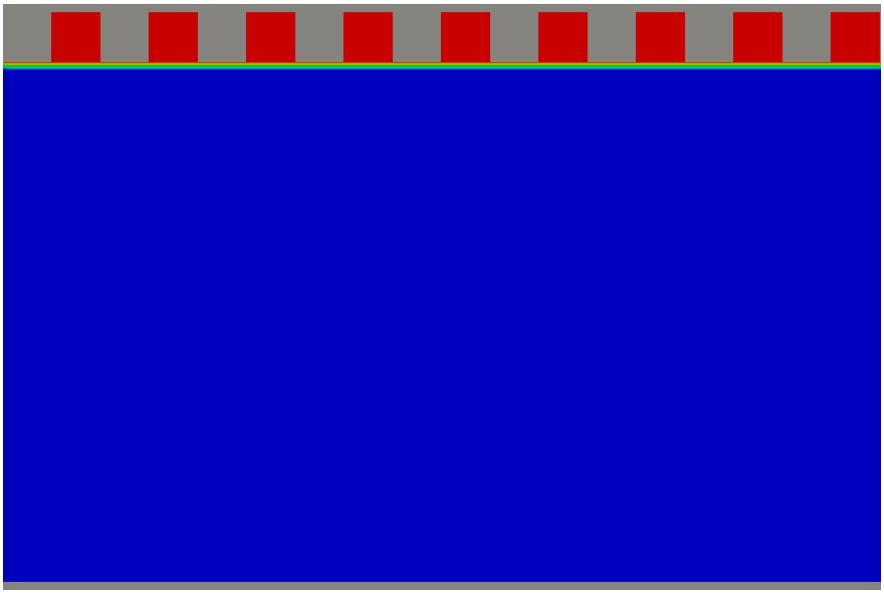

Figure 5.7: Initial phase concentrations in the spanwise hydrophobic geometry. The blue regions indicates water and the red regions indicate air. The green indicates the interface between the fluids. After the flow had become fully turbulent, the concentrations were again reset to this state.

Although the surface being modelled is super-hydrophobic, and therefore has an internal contact angle $> 150°$, the specified contact angle used is only $110°$. This has been done as the high contact angle exhibited by super hydrophobic surfaces is caused by the combination of the hydrophobic surface and the surface roughness.

5.3 Simulations

A series of simulations were conducted using the geometries and physics just described. The channel geometry was run only with a single phase fluid, as without the micro features, super hydrophobicity is impossible. Each of the other geometries described in Section 5.1 was tested in two conditions; firstly as a roughened wall with a single phase fluid (hereafter referred to as rough), and then as a super hydrophobic wall with two phases of fluid corresponding to air and water (hereafter referred to as hydrophobic). By testing in this way,

a comparison between a smooth channel, a wetted rough surface and a super hydrophobic surface could be made.

Each of the transitional and turbulent simulations were run for at least 1000 eddy turnover times, where $t_{eddy} = \frac{\delta}{u_{max}}$. The laminar flow cases were run until they reached convergence with average flow velocity fluctuations not exceeding 5%. In the case of the multiphase simulations, the domains were initialised with the phase representing water in the channel section of the domain, and the phase representing air in the grooves and gaps above the channel, as can be seen in Figure 5.7. The simulation was then run for about one and a half million iterations in order to fully develop the velocity field and turbulent structures. After this had occurred, the phases were reset to their original locations and concentrations, and results began to be sampled.

Sets of averaged data were sampled every 100 iterations (on the order of a turnover time for the high Reynolds number flows), with values taken for shear drag, pressure drag, velocity, mass and phase concentration for both the channel as a whole, and the individual walls. Full sets of data which could be transformed into images were also taken every 10000 iterations.

As was discussed in Section 4.7.2, the code is not capable of providing either a significant density or viscosity ratio between the fluids. This means that there should be no appreciable difference between the value of drag measured on the rough or hydrophobic surface. Indeed, when the drag values for the hydrophobic surface from the "air" and "water" are combined, the results are almost the same as those of the rough surface in which only "water" is modelled, as can be seen in Figure 5.8. Notwithstanding this, if the drag from the "air" phase is neglected, as would be more in keeping with the case in reality with the density and viscosity of the air being 1000 times smaller than that of the water, combined with the velocities in the air gaps being an order of magnitude lower than they are in the water, an indication of the relative merit of the hydrophobic surface can be assessed. The simulations also give an indication of how the deformation of the free-surface can affect the flow over the surfaces, and hence affect the drag results.

The assumption of the air having minimal effect of the simulation is consistent with the assumptions made in simulations that represent the hydrophobic surface as a series of alternating slip and no slip walls, as were presented in Chapter 2. In these cases, not only do they neglect the entirety of the drag from the air, but

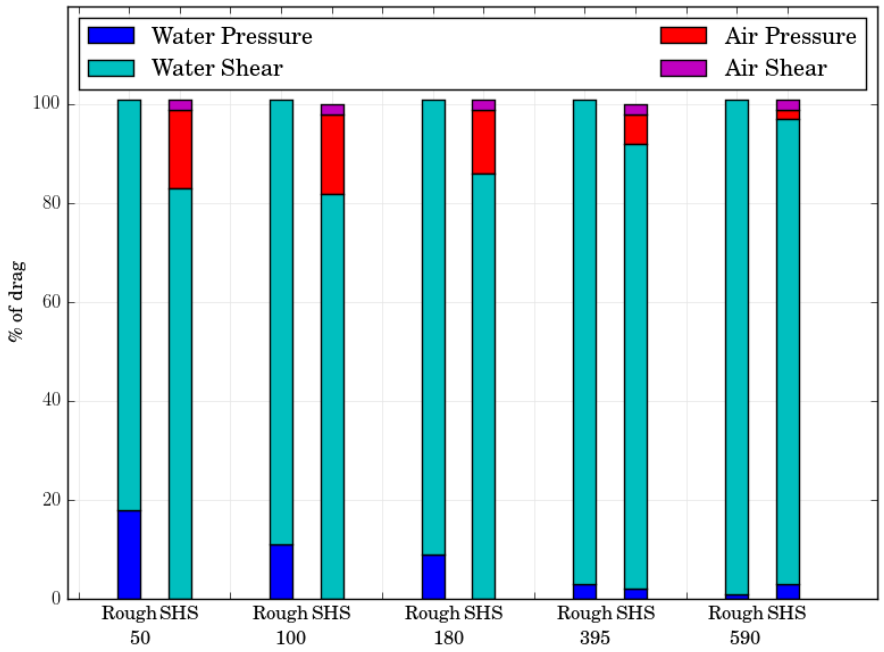

Figure 5.8: Comparison of the air and water drag components on the rough and hydrophobic spanwise grooved surfaces. Due to the lack of a density or viscosity difference between the air and water phases the total drag due to both fluids is almost identical. If the air drag was neglected, as could be the case if it were modelled with a lower density and viscosity, it can be seen that there would be a noticeable reduction in the total drag acting on the hydrophobic surface.

they also neglect the pressure drag of the water, or the drag due to the water impacting on surfaces perpendicular to the direction of the flow. This means the results presented in Chapters 6, 7, and 8 give what is in effect a best case scenario for the drag reduction by the hydrophobic surface. Even so, these results are backed up and further reinforced by the velocity profile analysis presented in Chapter 9.

Chapter 6

Computational Results 1: Grooved Geometries

The results of the simulations will be presented with the grooved surfaces reported on here, and the post surfaces in the following chapters. As is common practice in the field of fluid mechanics, the results are non-dimensional with co-efficients of drag, friction and pressure used to denote the forces, and wall shear Reynolds number being used to non-dimensionalise the flow velocity. This is especially useful in this work as although the body forces applied to the fluid were the same for each Reynolds number tested, the average fluid velocities in the different cases varied by up to as much as 20% in the laminar regime and 5% in the turbulent regime.

Figure 6.1 shows the drag co-efficient of the smooth channel plotted against the wall shear Reynolds number. Immediately obvious from this plot is the resemblance that it has with a Moody friction plot, with a linear relationship in the laminar region ($Re_\tau < 100$), and a downward trending curve in the turbulent region ($Re_\tau > 180$). This is not surprising as in both cases the plots are comparing wall friction with Reynolds number. The Moody friction plot is comparing the friction factor of a pipe with a diameter based Reynolds number, as opposed to the drag co-efficient and wall shear Reynolds number shown here, however non-dimensionally, both of these are equivalent.

Using the smooth channel as a baseline to compare with, results of the specific geometries can now be presented. Each geometry will have results shown at $Re_\tau = 50$, 180 and 590, corresponding to a laminar, transitional and fully

Table 6.1: Comparison of Re_τ values for each of the tested geometries.

Nominal	Channel	Rough Spanwise	SHS Spanwise	Rough Streamwise	SHS Streamwise	Rough Aligned Posts	SHS Aligned Posts	Rough Offset Posts	SHS Offset Posts
10	13.42	10.17	9.33	9.99	9.24	8.42	8.49	7.97	4.57
50	53.88	40.96	22.01	44.42	39.30	39.98	22.24	35.68	22.49
100	107.40	83.00	41.59	99.68	81.70	80.16	38.20	71.76	43.55
180	182.70	138.61	87.65	160.71	133.04	120.41	67.65	87.79	66.31
395	394.79	258.16	272.55	316.63	272.03	211.93	176.18	150.62	169.90
590	564.23	351.18	368.61	462.76	309.93	298.06	295.93	204.58	203.92

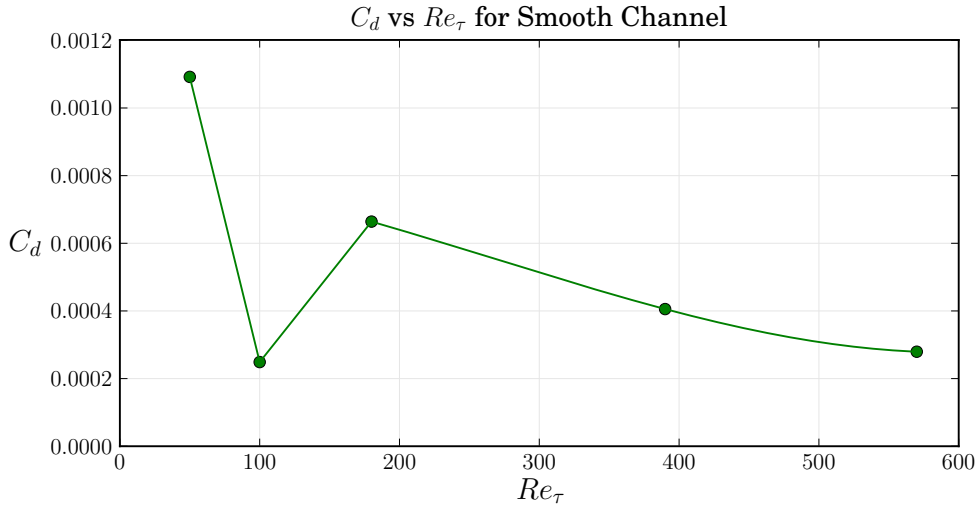

Figure 6.1: Co-efficient of drag (C_d) vs Re_τ for the smooth channel. Note the resembalance to a Moody friction factor plot.

turbulent flow case. Although $Re_\tau = 180$ should be fully turbulent, and indeed it is in the smooth channel geometry, with the reduced velocities in the rough and hydrophobic cases, the corresponding wall shear Reynolds numbers also appear to have decreased. Table 6.1 shows the measured wall shear Reynolds numbers for each of the simulations. As the force driving the flow in each of the different Reynolds number cases has remained the same, results will still be presented at their nominal Reynolds number as opposed to the measured Reynolds number.

As a brief aside, although it appears useful to compare the drag results of the rough and hydrophobic surfaces with those of the smooth channel it does not actually tell the full story. Compared with the size of the micro features being studied, the smoothness of the boundary in the smooth channel makes it almost an atomically smooth surface, a scenario that is hard to achieve in a laboratory and an impossibility on the hull of a ship. Values of surface roughness on newly painted ships tend to be in the order of $30\mu m$, or 3 times bigger than the surface features being investigated here. When calculating the drag on a ship, as was discussed in Section 2.1.1, the total drag coefficient is found by the equation

$$C_{d,Total} = (1 + k)C_{d,f} + C_{d,r} + c_a \tag{6.1}$$

where $C_{d,Total}$ is the coefficient of total drag, $(1 + k)$ is a form-factor co-efficient and is related to the shape of the vessel, $C_{d,f}$ is a frictional drag co-efficient,

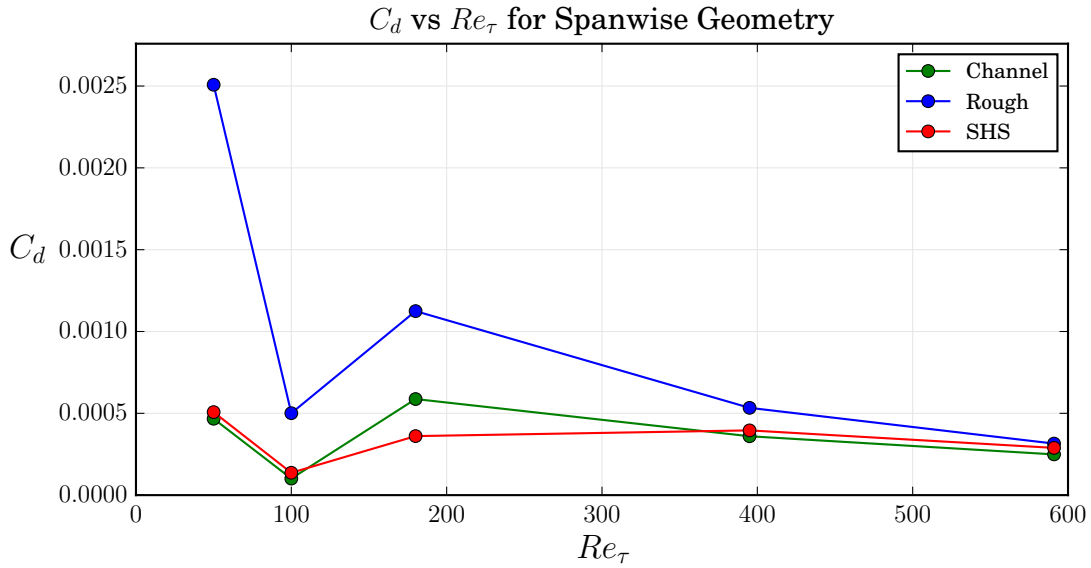

(a) Coefficient of drag (C_d).

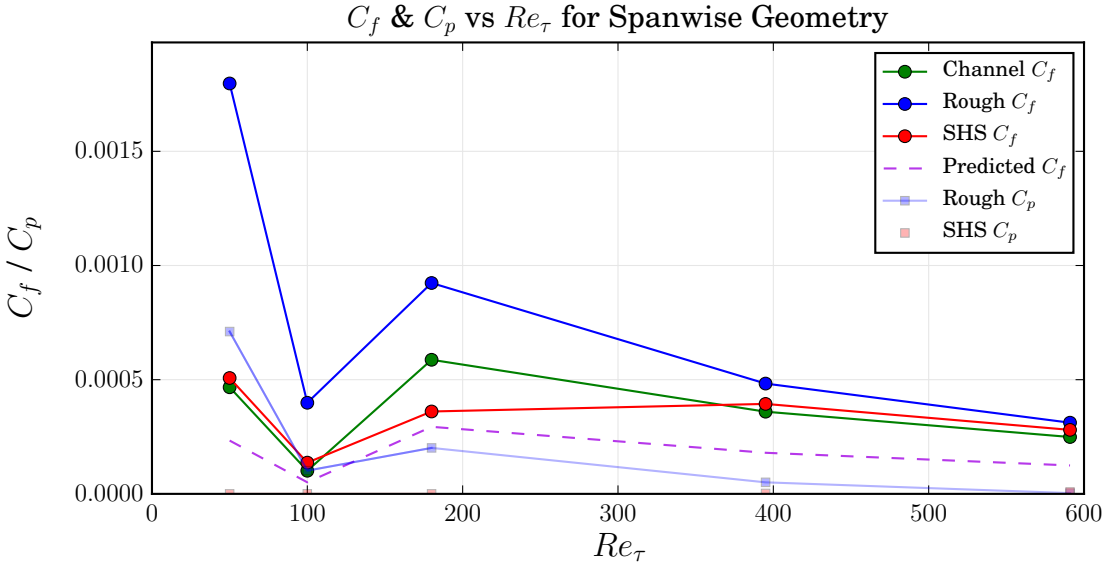

(b) Co-efficients of friction (C_f) and pressure (C_p).

Figure 6.2: Drag co-efficients vs Reynolds number for spanwise geometry and smooth channel.

$C_{d,r}$ is a residuary drag coefficient and is composed of the pressure drag and wave making drag of a vessel and c_a is a correlation allowance. The correlation allowance is introduced to account for the surface roughness on a ship, both due to natural surface roughness, and other imperfections such as weld lines or minor plate deformations. A typical value for the correlation allowance is $c_a = 0.0004$ however for smaller boats, it can be as much as double this value. With the drag co-efficient of the smooth channel being in a range between $C_d = 3 \times 10^{-4}$ and 11×10^{-4}, an additional $c_a = 4 \times 10^{-4}$ (or somewhere between 36% and 133%) is a significant increase, and shows that although the smooth channel results presented in this work may appear to have lower drag values than the micro-featured surfaces, in practice this is unlikely to be the case.

6.1 Spanwise Grooves

As was discussed in Chapter 2 there have been many studies, both experimental and numerical, into turbulent flow over roughened surfaces. Under the right conditions it has been shown that roughness from spanwise riblets or grooves can be used to control a turbulent boundary layer and minimise the drag of an object.

The drag from the spanwise grooved surface is composed of both frictional drag and pressure drag due to the geometrical features being transverse to the direction of flow. Figure 6.2a shows the drag co-efficient of the three surfaces (hydrophobic, rough and smooth), and the break down of the total drag into its components. The frictional and pressure drag components have been measured by the method described in Section 4.8.1 and been non-dimensionalised to yield C_f and C_p.

6.1.1 Laminar and Transitional Regimes

Figure 6.2 illustrates that in the laminar and transitional flow regimes, the drag reduction effect of the hydrophobic surface as compared to the rough surface is significant with a reduction in total drag of between 76% at $Re_\tau = 50$ decreasing to 72% at $Re_\tau = 100$ & 180. While quite similar to the smooth channel at both low and high Reynolds numbers, there is a distinct difference at $Re_\tau = 180$ where the hydrophobic surface approaches roughly half the value of the smooth channel.

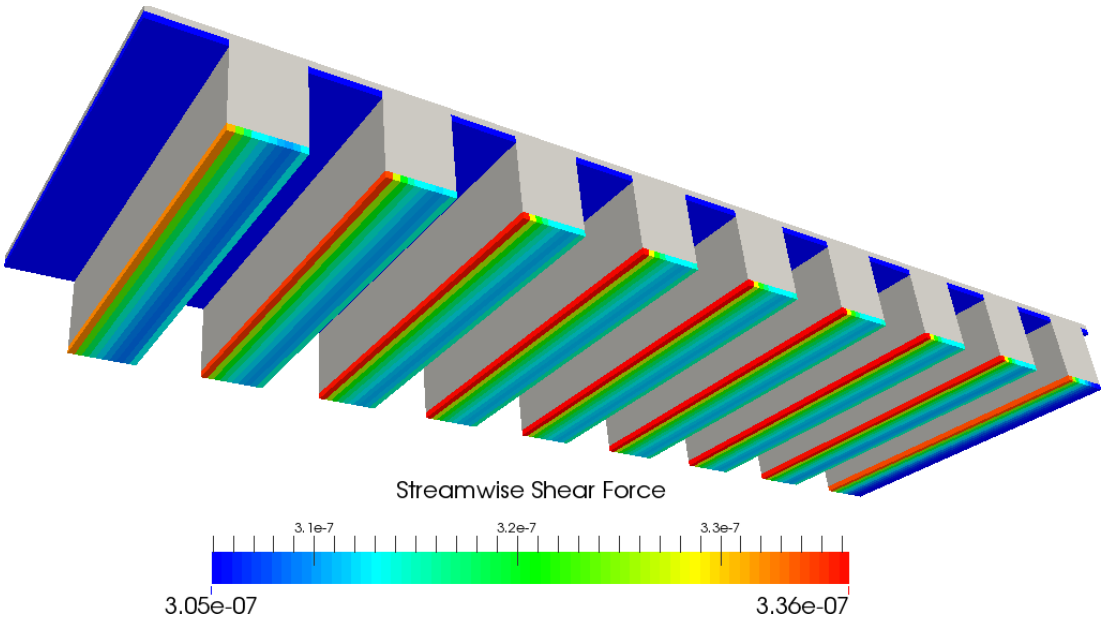

(a) Rough Geometry

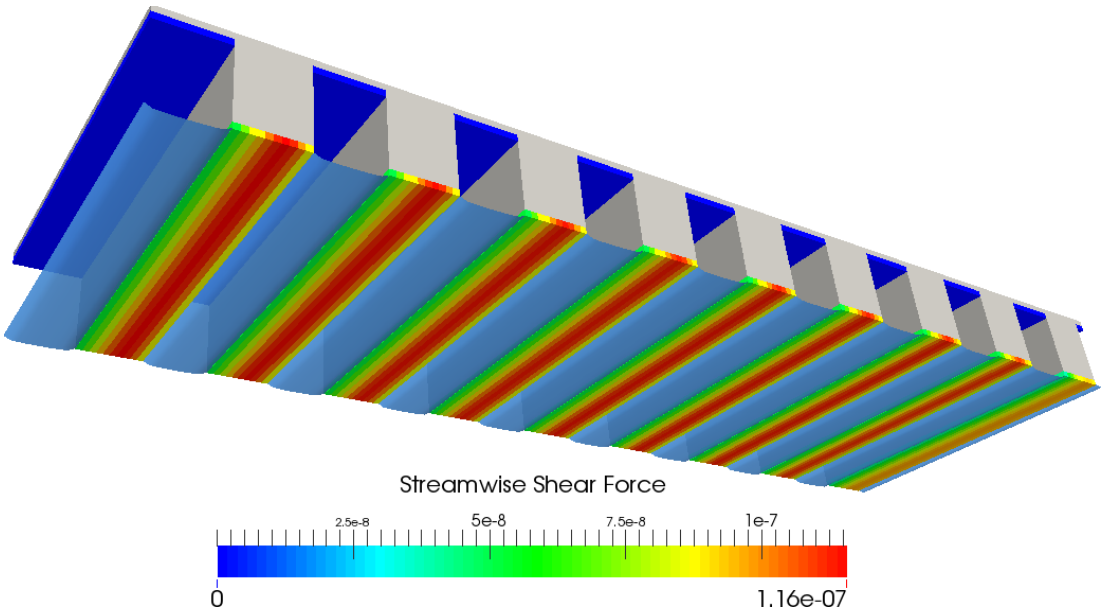

(b) Hydrophobic Geometry.
The air-water interface is indicated by the translucent blue surface.

Figure 6.3: Time-averaged shear force and free-surface on spanwise geometry at $Re_\tau = 50$. Note the differences in shear drag distribution between the two surfaces.

Conversely, the drag on the rough surface is significantly higher than that of both the hydrophobic surface or the smooth channel throughout the laminar flow regime.

The difference between the frictional drag components of the rough and hydrophobic surfaces at these low speeds can be better understood by viewing the shear forces acting on the wall. Figure 6.3 shows that the shear stresses act predominantly on the top face of the ridges. Looking first at the distribution on the rough surface, it can be seen that the maximum shear stress occurs at the leading edge of the ridge. This differs with the distribution on the hydrophobic surface which instead has its minimum shear stress at the leading edge, and progressively increases to a maximum in the middle of the ridge. The reason for the distributions appearing this way can be explained by looking at near wall velocity vectors, shown in Figure 6.4.

Examination of these near wall vectors immediately shows that the flow over the surfaces is quite different. In the case of the rough surface, the fluid flows almost parallel to the surface. Due to the depth of the grooves, both clockwise and counter-clockwise eddies are created. Conversely, the flow over the hydrophobic surface does not run parallel to the surface, but instead appears to be deflected downwards by the air-water interface. This downward deflection causes an eddy to form in the water adjacent to the interface. The flow of the water on the lower side of the interface then causes the air within the cavity to rotate in the opposite direction to that which was seen in the rough surface case. With frictional drag only being related to the component of the velocity flowing parallel to the surface, the act of deflecting the water minimises this component of the velocity, and hence reduces the frictional drag.

These velocity vectors also illustrate the difference in the pressure drag between the two surfaces. The air-water interface on the hydrophobic surface insulates the leading edges of the ridges from any perpendicular flow in the streamwise direction, resulting in zero pressure drag. With the near parallel flow past the rough surface, the leading edges of the ridges are exposed to a streamwise velocity component, and hence have a non-zero pressure drag.

Similar analysis has been performed with the transitional flow case to see the differences between flow over the rough and hydrophobic surfaces. As was the case with the laminar flow, Figure 6.5 shows an eddy is present below the

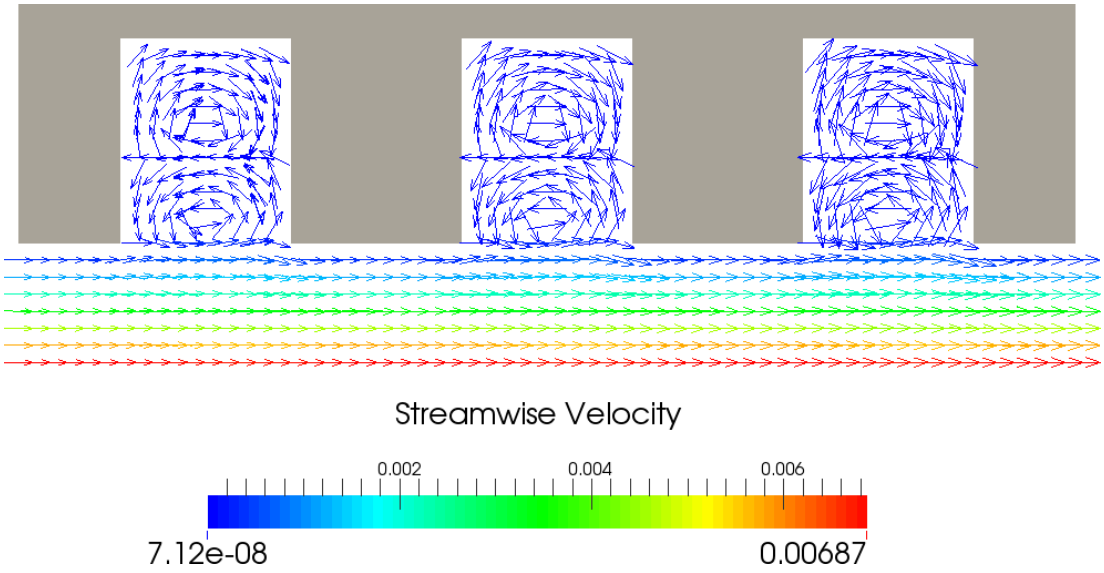

(a) Rough Geometry

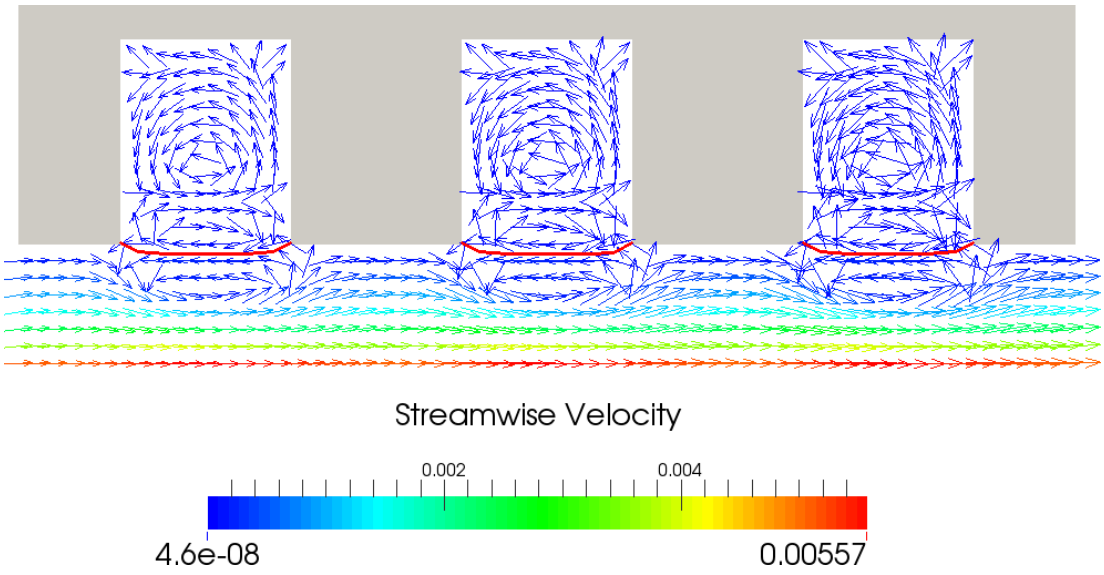

(b) Hydrophobic Geometry.
The red lines indicate the location of the air-water interface.

Figure 6.4: Time-averaged velocity vectors and free-surface profile on the spanwise geometry at $Re_\tau = 50$. Both the rough and hydrophobic geometries exhibit flows commonly seen in high aspect ratio lid-driven cavity flows. Note the presence of the counter-clockwise vortex below the free-surface in the hydrophobic case.

air-water interface, albeit flatter and smaller in the higher speed flow than it was at low speed. The free surface is once again deflecting the water away from the surface leading to a reduced frictional drag component and a zero pressure drag component in the streamwise direction. Rotational direction of the flow within the grooves remains opposite between the cases as was also shown in the laminar flow regime.

6.1.2 Turbulent Regime

Figure 6.2 also shows that at high Reynolds numbers, the hydrophobic surface drag values again are quite close to those of the smooth channel. In this regime, the rough surface exhibits drag values closer to those of both the smooth and hydrophobic surfaces, and at $Re_\tau = 590$, the drag co-efficients of all three surfaces are almost identical. The similarity between the rough and the hydrophobic surfaces can again be explained by examining images of the velocity vectors in the near wall region.

Figure 6.6 shows that at high Reynolds numbers, the location of the free surface has moved into the groove. With the air-water interface no longer in a position to deflect the water away from the surface, the flow in the near wall region of the hydrophobic surface much more closely resembles that over the rough surface, with flow parallel to the surface being much more prevalent that in the lower Reynolds number cases.

An image of the shear force acting on the surface in the high Reynolds number flow is provided in Figure 6.7, which by visual inspection also confirms that shear drag over the two surfaces appears to be quite similar.

With the results indicating that the location of the air-water interface has a large influence on the drag on the surface, further investigation into what causes the free-surface to move needs to be undertaken. If the assumption is made that pressure acting normal to the air-water interface is the same as that measured on the tops of the ridges, then a force balance between the pressure force trying to move the free-surface into the grooves and the surface tension overcoming this force can be set up. The Young-Laplace equation, $\Delta P = \sigma(\frac{1}{R_x} + \frac{1}{R_y})$ gives the pressure difference that can be supported by an interface with surface tension σ and radii R_x and R_y. In the case of the spanwise geometry, the curvature of the

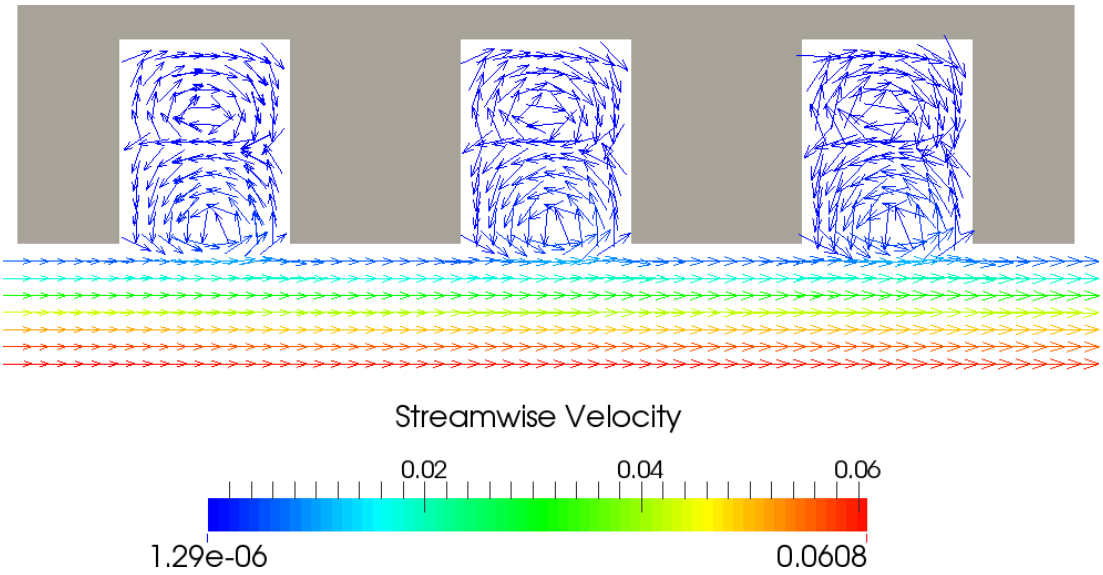

(a) Rough Geometry

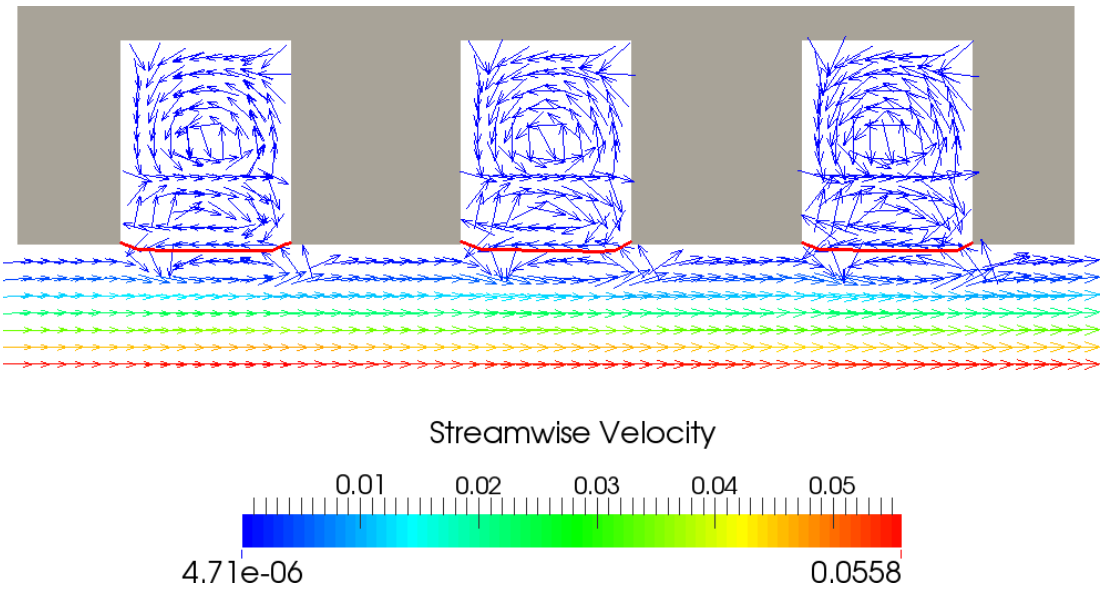

(b) Hydrophobic Geometry.

The red lines indicate the location of the air-water interface. The vectors above this line are indicating the velocity of the air.

Figure 6.5: Time-averaged velocity vectors and free-surface profile on the spanwise geometry at $Re_\tau = 180$. Again note the presence of the counter-clockwise vortex below the free-surface in the hydrophobic case; however, with the increased velocity, the vortex is smaller and flatter.

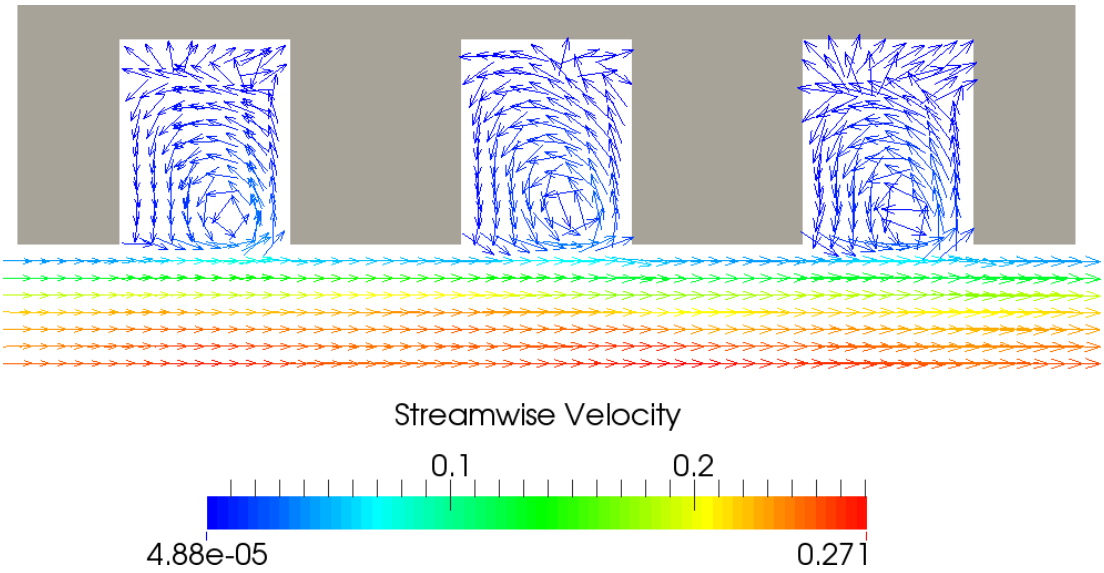

(a) Rough Geometry

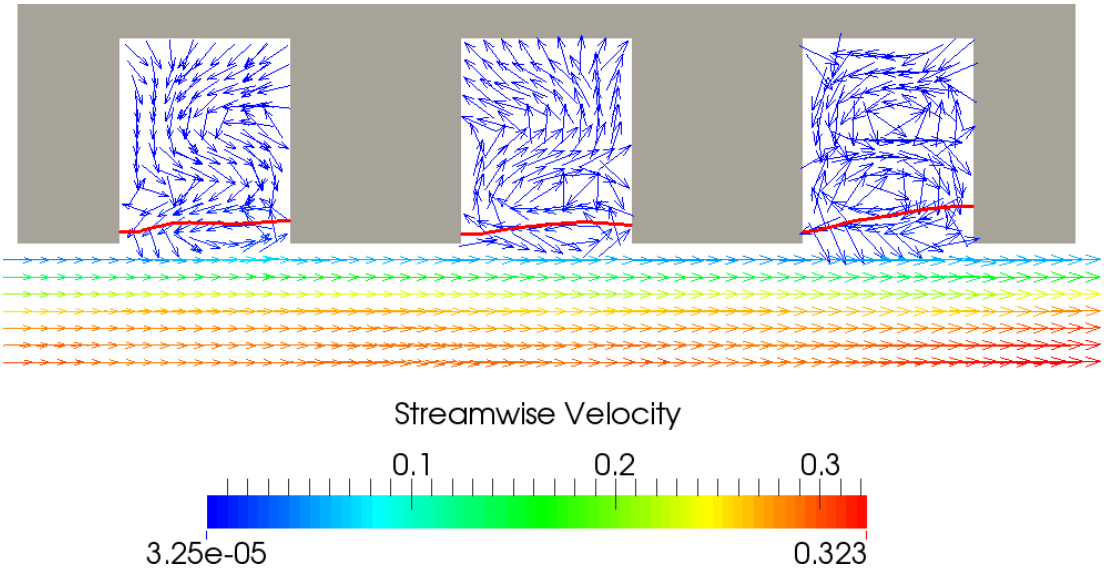

(b) Hydrophobic Geometry.
The red lines indicate the location of the air-water interface.

Figure 6.6: Time-averaged velocity vectors and free-surface profile on the spanwise geometry at $Re_\tau = 590$. At the higher speed the rough surface displays a more common lid-driven cavity flow. No consistent result can be inferred from the vectors deep within the grooves for the hydrophobic surface.

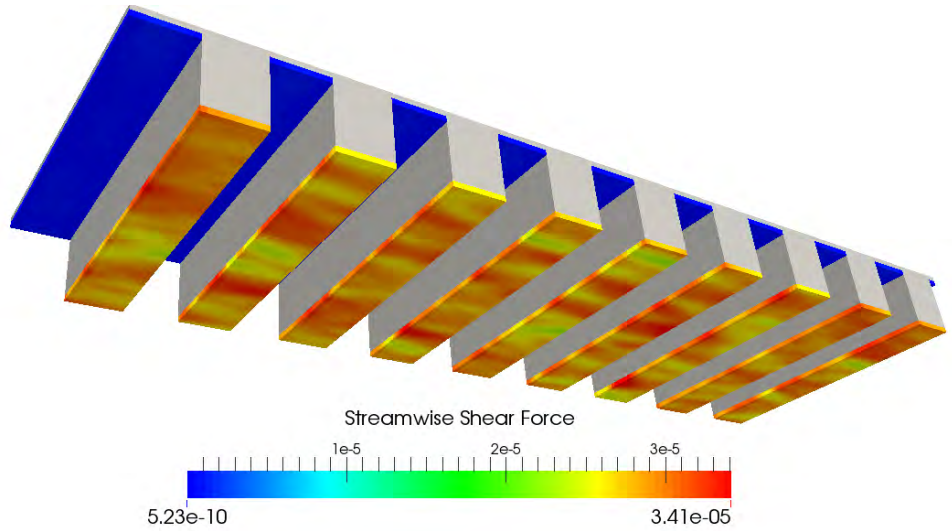

(a) Rough Geometry

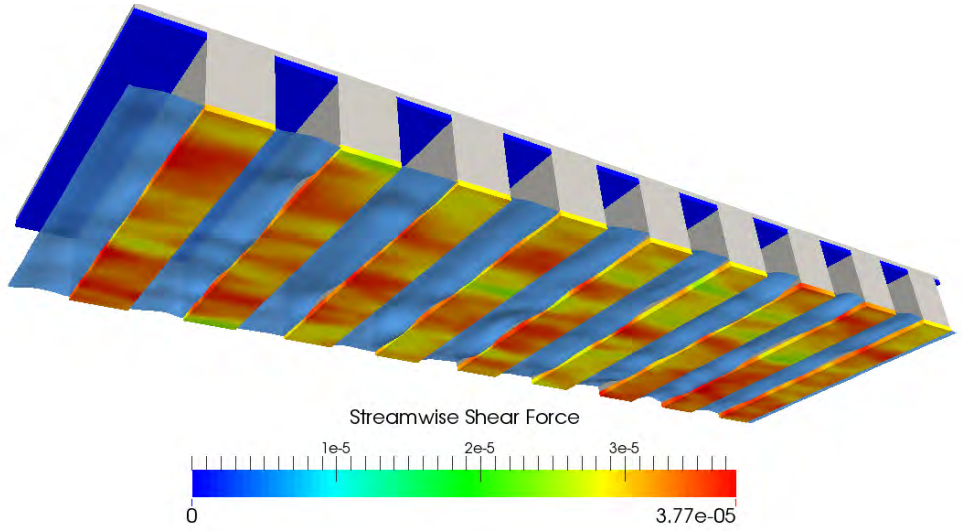

(b) Hydrophobic Geometry.
The air-water interface is indicated by the translucent blue surface.

Figure 6.7: Time-averaged shear force and free-surface profile on spanwise geometry at $Re_\tau = 590$. The streaky nature of the results is due to the images being sampled only every 10000 iterations and the difference in shear across the domain due to turbulence.

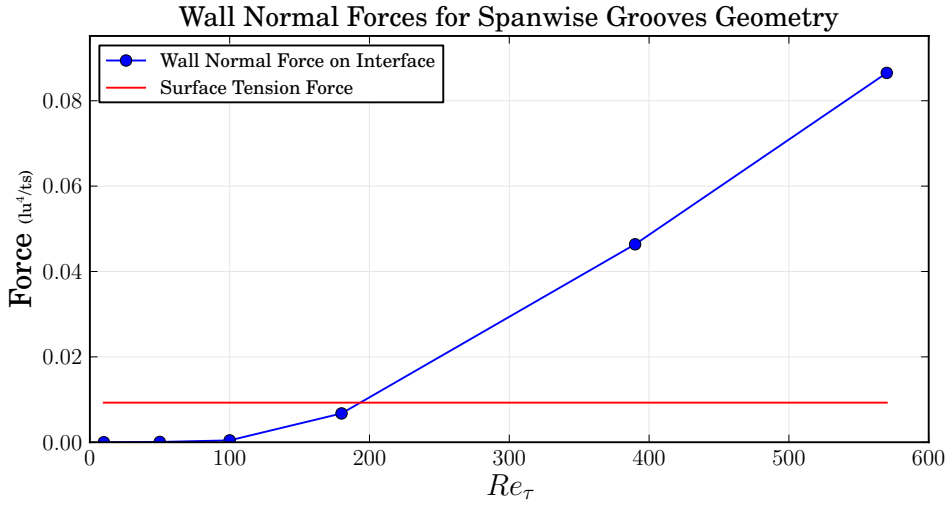

Figure 6.8: Vertical forces on the spanwise geometry compared to surface tension force. At Reynolds numbers above ≈ 200, the normal force on the free-surface is greater than the supporting surface tension force.

interface is only one dimensional, allowing the R_y term to be ignored. With a contact angle of 110° and a spacing between the ridges of $10\mu m$, the radius of curvature of the surface is approximately 13 lattice units. Making the assumption that the pressure in the groove and in the channel are equal[1], the ΔP term gives the force that the interface should be able to hold.

Substituting in for σ and R_x gives the force that each cell supporting the interface can hold. In the spanwise geometry, (and as it turns out, each of the other geometries) there are N=1200 cells along the edges of the ridges and posts. As was discussed in Section 4.7.1, modelling the transition from the air phase to the water phase occurs over three discrete cells, meaning that the total number of cells supporting the free-surface is 3600. The total force capable of being sustained can be found by multiplying the force per cell by the total number of cells.

[1]In reality, Bernoulli's principal would indicate that due to the difference in velocity between the fluids, the pressure in the groove should be slightly higher than that in the channel.

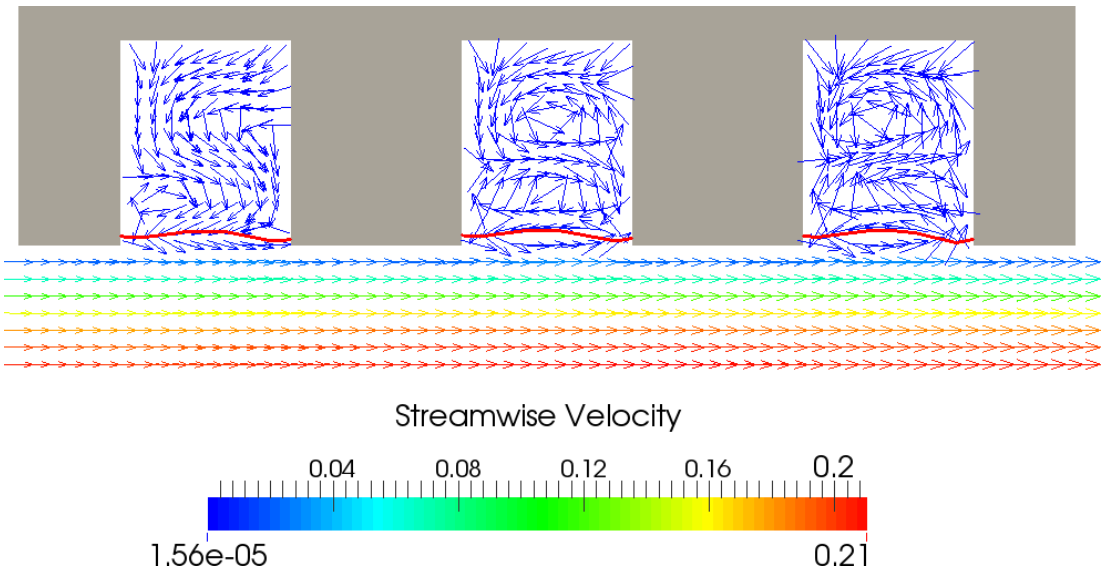

Figure 6.9: Time averaged velocity vectors and free-surface profile on the spanwise geometry at $Re_\tau = 395$. The red line shows the air-water interface has been moved into the grooves as was predicted.

$$\begin{aligned} \Delta P &= \sigma \times \left(\frac{1}{R_x}\right) \\ &= 3.35 \times 10^{-5} \times \frac{1}{13.16} \\ &= 2.55 \times 10^{-6}\ lu^2/ts^2 \\ F_y &= \Delta P \times N \\ &= 2.52 \times 10^{-6} \times 3600 \\ &= 9.18 \times 10^{-3}\ lu^4/ts^2 \end{aligned} \tag{6.2}$$

A plot comparing the force in the wall normal direction against the surface tension force can be seen in Figure 6.8. This plot predicts that at Reynolds numbers below $Re_\tau \approx 190$, the pressure forces acting on the surface should not cause substantial movement or deflection. As has been shown in this section, this appears to be the case, with the free-surface in the $Re_\tau = 180$ case seemingly unaffected. Figure 6.8 also suggests that at the $Re_\tau = 395$ case, the surface tension force will be insufficient to support the interface, and it will be distorted or displaced into the groove. Figure 6.9 shows the free surface location and velocity vectors for the $Re_\tau = 395$ case which confirms this prediction.

6.1.3 Summary

Table 6.2 gives the numerical values of the drag reduction of the rough and super hydrophobic surfaces as a percentage of the smooth channel, where a positive value is an increase in drag, and a negative value is a decrease in drag. In laminar flow, the super hydrophobic surface exhibits levels of drag similar to those of the smooth featureless surface. Through the transition at $Re_\tau = 180$, a significant reduction of drag on the hydrophobic surface is observed. At higher Reynolds numbers, The drag is again consistent with that of the smooth wall. At low speeds, the rough surface has significantly higher levels of drag than the smooth wall; however, once the flow becomes turbulent, the differences in drag values between the surfaces reduce

The drag reduction effect of the super hydrophobic surface as compared to the rough surface at the low speeds is due to the air-water interface deflecting the water away from the surface. At higher speeds, where this effect is less

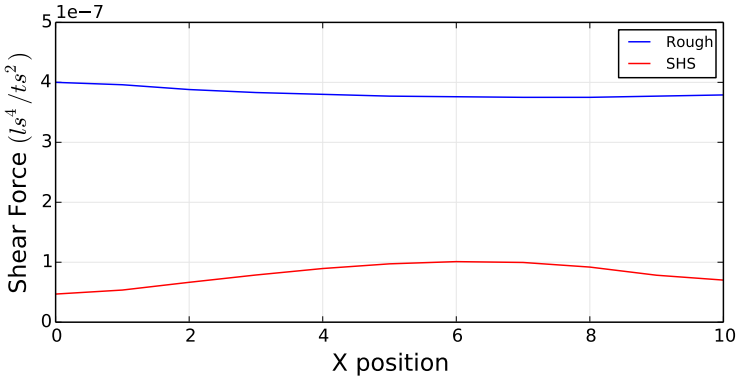

(a) Shear distribution at $Re_\tau = 50$

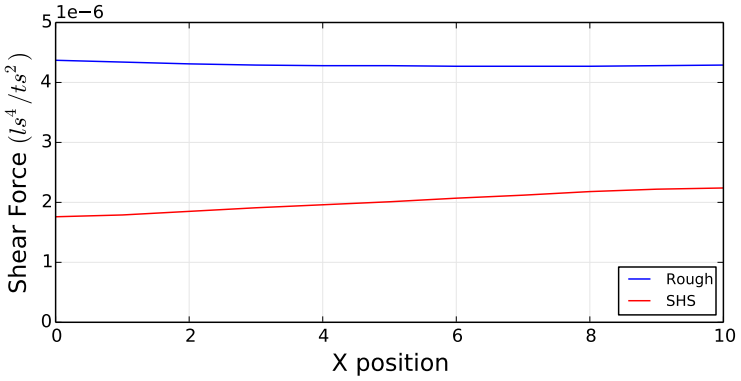

(b) Shear distribution at $Re_\tau = 180$

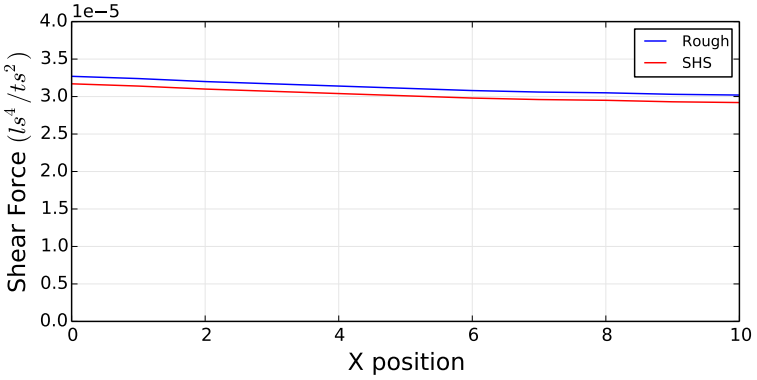

(c) Shear distribution at $Re_\tau = 590$

Figure 6.10: Shear force distribution on tops of the ridges in the spanwise geometry. In laminar and transitional flow the shear force on the hydrophobic surface is significantly less than that on the rough surface. Additionally, the maximum value occurs further downstream on the post. The rough surface exhibits its highest shear at the leading edge. In turbulent flow at $Re_\tau = 590$ there is minimal difference between the shear force distributions.

Table 6.2: Summary of drag reduction of rough and hydrophobic channels as a percentage of drag on the smooth channel. +ve values indicate an increase in drag and −ve values indicate a reduction in drag.

Re_τ	Rough	SHS
50	+ 437.3	+ 8.69
100	+ 394.5	+ 35.08
180	+ 91.53	−38.56
395	+ 48.25	+ 9.96
590	+ 26.51	+ 15.96

pronounced, the behaviour of the hydrophobic surface approaches that of the fully wetted rough surface, and no appreciable drag reduction is observed as compared to the smooth wall.

The distribution of shear drag over the ridges can also be better visualised by inspecting Figure 6.10. These plots show the shear force as a function of the X-position on the tops of the ridges and clearly show that in the laminar and transitional flows the shear force on the tops of the ridges of the hydrophobic surface is substantially lower than on the corresponding ridges of the rough surface. Not only is the shear force reduced, but the maximum value of shear is located further downstream on the post, as was shown in the shear contour images previously.

This page is intentionally left blank.

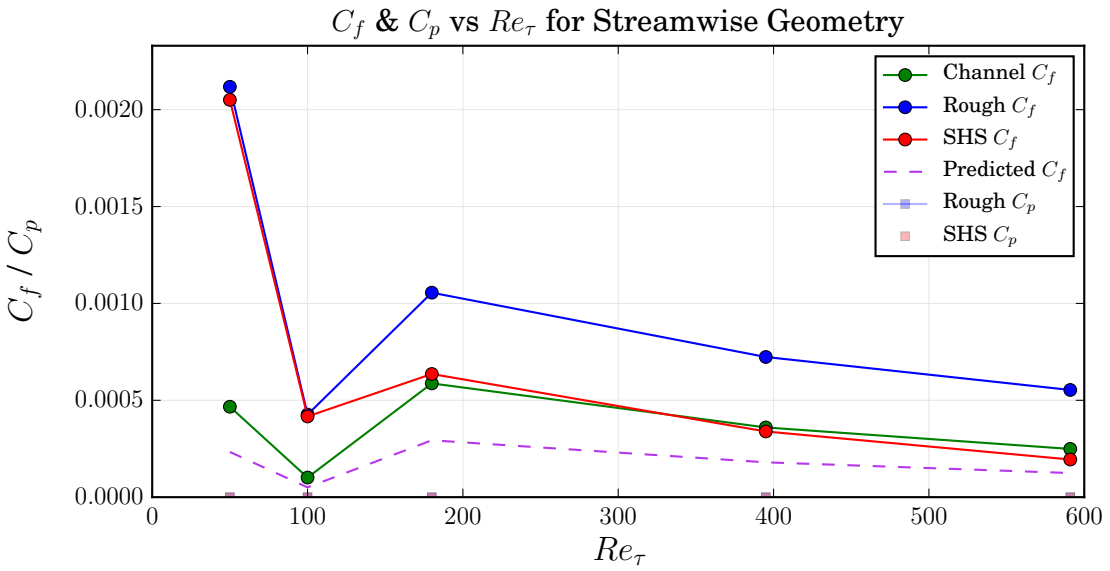

Figure 6.11: Components of drag for Streamwise Geometry and smooth channel.

6.2 Streamwise Grooves

Streamwise grooves, like their spanwise counterparts, have been a subject of intense research in an effort to modify and control the turbulent boundary layer. It has been shown that the streamwise ridges tend to prevent the formation of hairpin vortices, an action which results in a reduction of drag as previously discussed. Unlike the spanwise geometry, the streamwise grooves only have a frictional drag component since there are no surfaces perpendicular to the streamwise flow. Figure 6.11 shows the friction drag co-efficients for the smooth channel, the rough surface and the hydrophobic surface.

Unlike the spanwise grooved geometry, where at high Reynolds numbers the drag co-efficients of the rough and hydrophobic surfaces tended to converge, as seen in Figure 6.11 this is not the case. Instead, after the onset of turbulence, the hydrophobic surface exhibits significantly less drag than the rough surface, and slightly less drag than the smooth channel giving some credence to the results earlier shown by Park *et. al.* [96] who showed drag reductions in the order of 70% for a streamwise grooved surface at $Re_\tau = 250$. The streamwise grooves on the rough surface give similar results as those of the hydrophobic surface at low

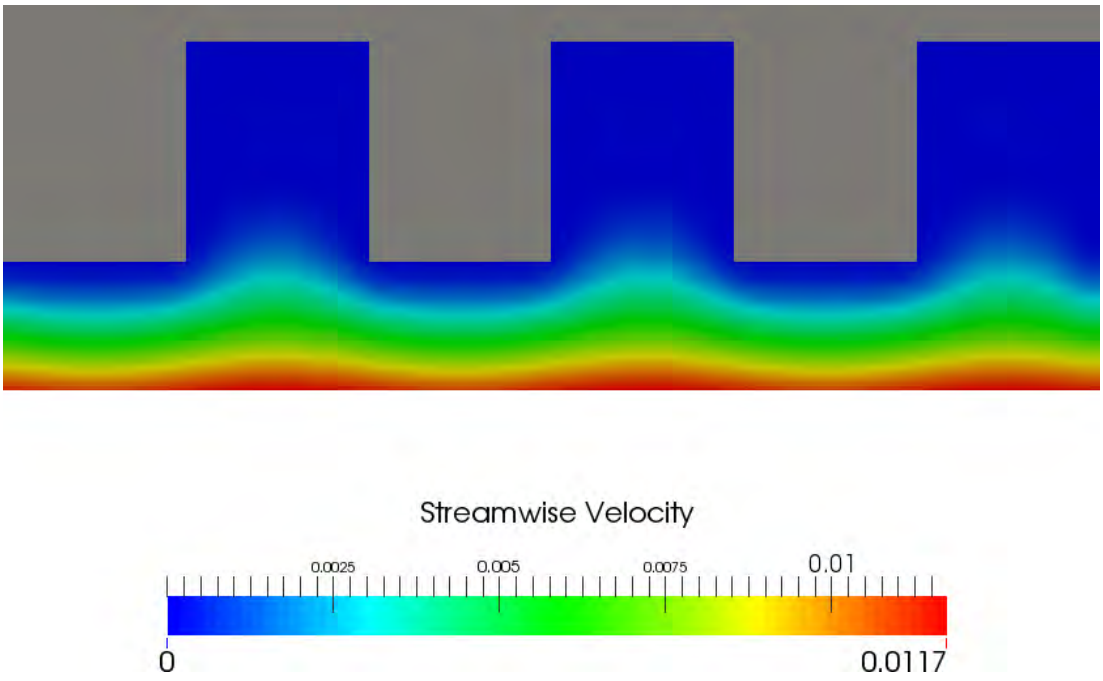

(a) Rough Geometry

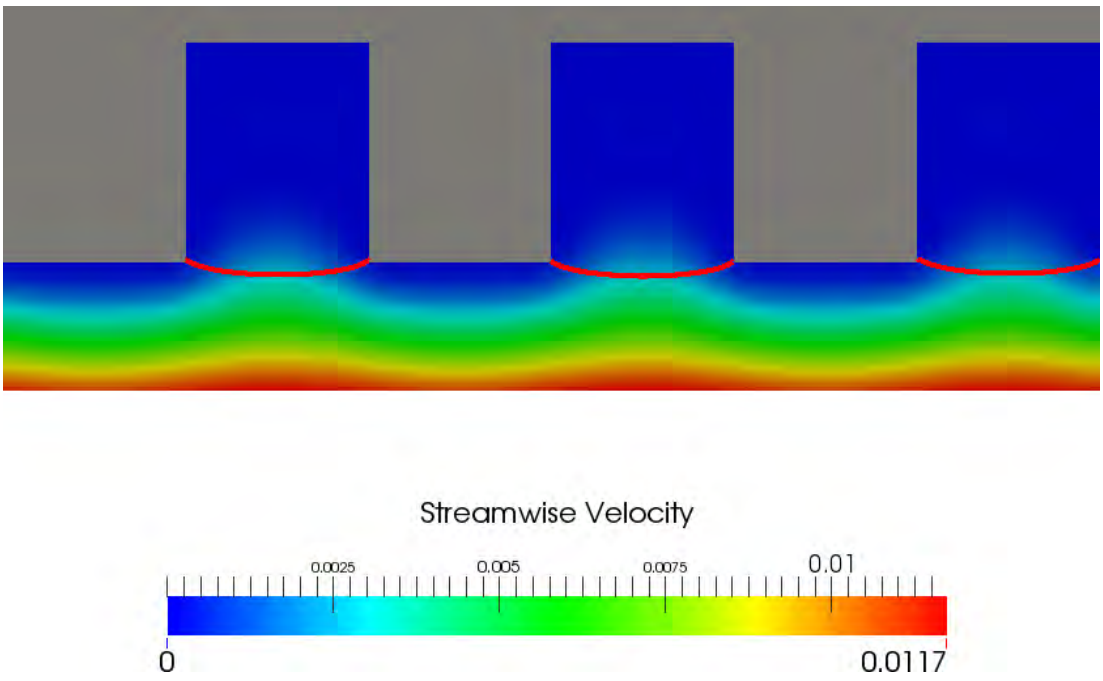

(b) Hydrophobic Geometry.
The red lines indicate the location of the air-water interface.

Figure 6.12: Time-averaged velocity contours and free-surface profile on the streamwise geometry at $Re_\tau = 50$.

Reynolds numbers but then are consistently about double the drag of the smooth channel across the transitional and turbulent flow regimes.

In the spanwise geometry, the location of the air-water interface was shown to be the main reason for the reduction in drag. The analysis of the force balance between the wall normal and the surface tensions forces also quite accurately predicted when the stability of the free-surface would no longer be able to be maintained. Performing this same analysis with the streamwise geometry reveals similar results, as Figure 6.13 shows, since with the streamwise geometry, the wall normal forces acting on the free-surface exceed the supporting force provided by the surface tension above $Re_\tau \approx 410$.

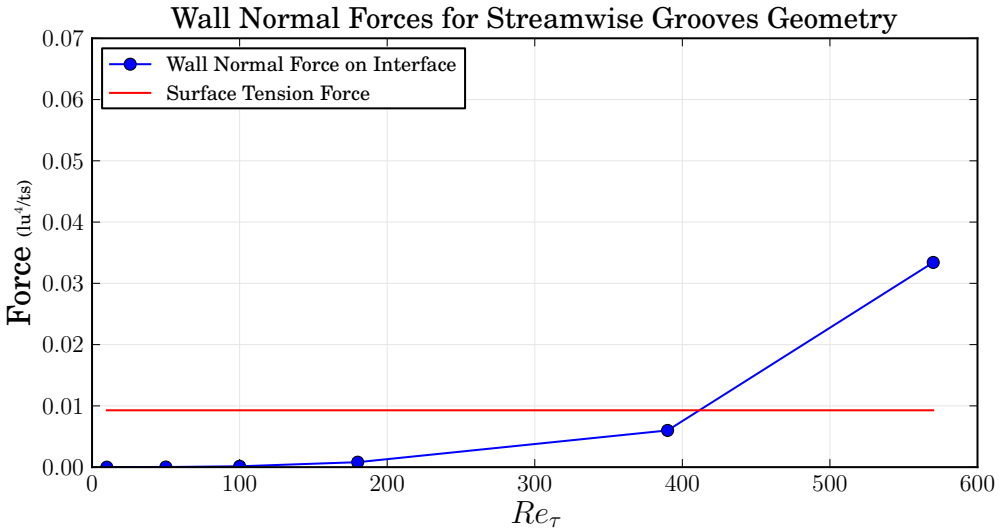

Figure 6.13: Vertical forces on the streamwise geometry compared to surface tension force. The surface tension force can withstand the wall normal forces up to ≈ 410 before the interface becomes unstable.

6.2.1 Laminar and Transitional Regimes

Based on Figure 6.11 both the streamwise rough and hydrophobic surfaces have similar drag coefficients to each other, both significantly higher that of the smooth surface. The reason for this appears to be due to the freedom of movement of the fluid within the grooves in the streamwise direction. Figure 6.12 shows that although the ridges have hard edged corners on them, the velocity contours curve

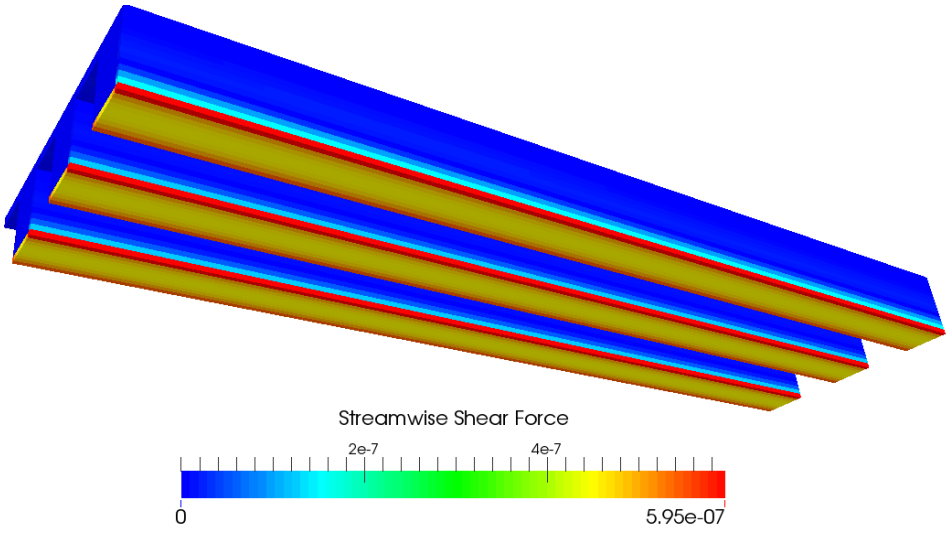

(a) Rough Geometry

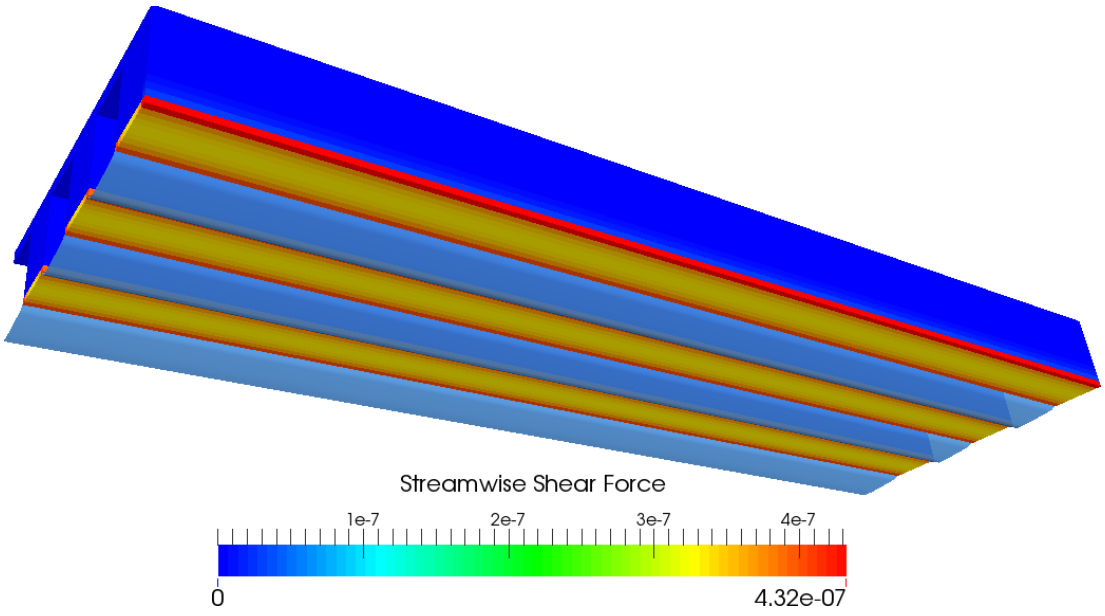

(b) Hydrophobic Geometry.

The air-water interface is indicated by the translucent blue surface.

Figure 6.14: Time-averaged shear force and free-surface profile on the streamwise geometry at $Re_\tau = 50$. Note the shear forces acting on the sides of the rough ridges, a feature which is not exhibited by the hydrophobic surface.

smoothly in and out of the grooves. This means that there is high velocity fluid in close proximity with the corners, leading to a corresponding increase in the wall shear on the corners of the ridges, as is illustrated in Figure 6.14. Comparing the top and bottom walls of the domain indicates that although the centre of the ridges have a similar drag to the bottom wall, the shear force at the edges increases by approximately 28%. This additional contribution elevates the shear force acting on the micro featured surface above that of the wall of the smooth channel.

As was also noticeable in the plot of drag co-efficients (Figure 6.11), the rough surface has a slightly higher drag than that of the hydrophobic in the laminar regime. This is explained by the shear forces acting on the sides of the ridges as well as the top, as is visible in Figure 6.14a. By visual inspection, the shear forces acting on the sides of the ridges extend two to three cells into the groove. Calculating the increased drag above that of the hydrophobic surface based on the extra two to three cells would result in an additional 3% drag on the rough surface. The actual measured drag increase on the rough surface is 3.29%, again indicating that the minimisation of the wetted surface area is key to reducing the drag at low speeds.

In the transitional range between $Re_\tau = 100$ and $Re_\tau = 180$, the drag co-efficients of the micro featured surfaces diverge with values for the hydrophobic surface approaching those of the smooth channel. The difference between the hydrophobic and rough surface values at $Re_\tau = 180$ is due to both the wetted walls of the rough surface contributing a significant amount of frictional drag, as can be seen in Figure 6.15, and the free-surface minimising the fluid velocity within the grooves, which can be seen in Figure 6.16. Also noticeable in this figure is that the free-surface still appears to be stable and symmetrical. This implies that the surface tension force is still able to withstand the vertical forces applied to the interface by the turbulent flow in the water.

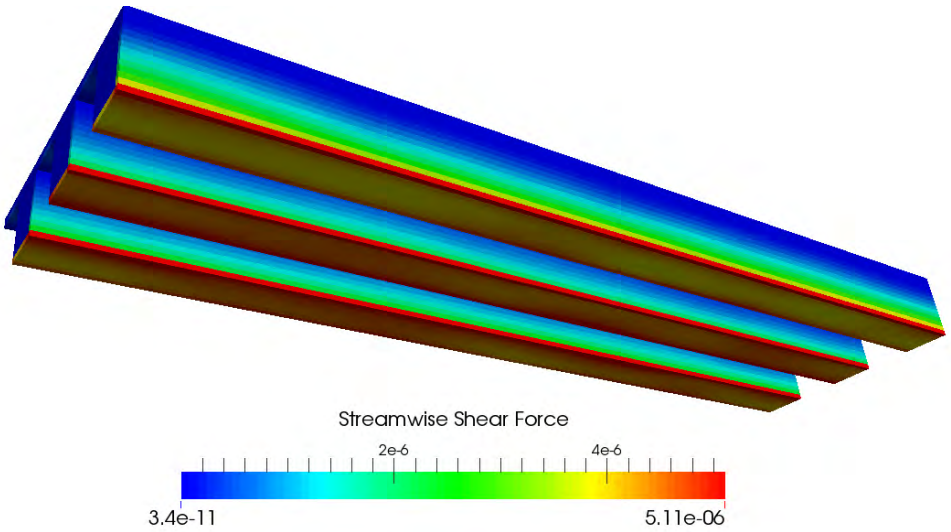

(a) Rough Geometry

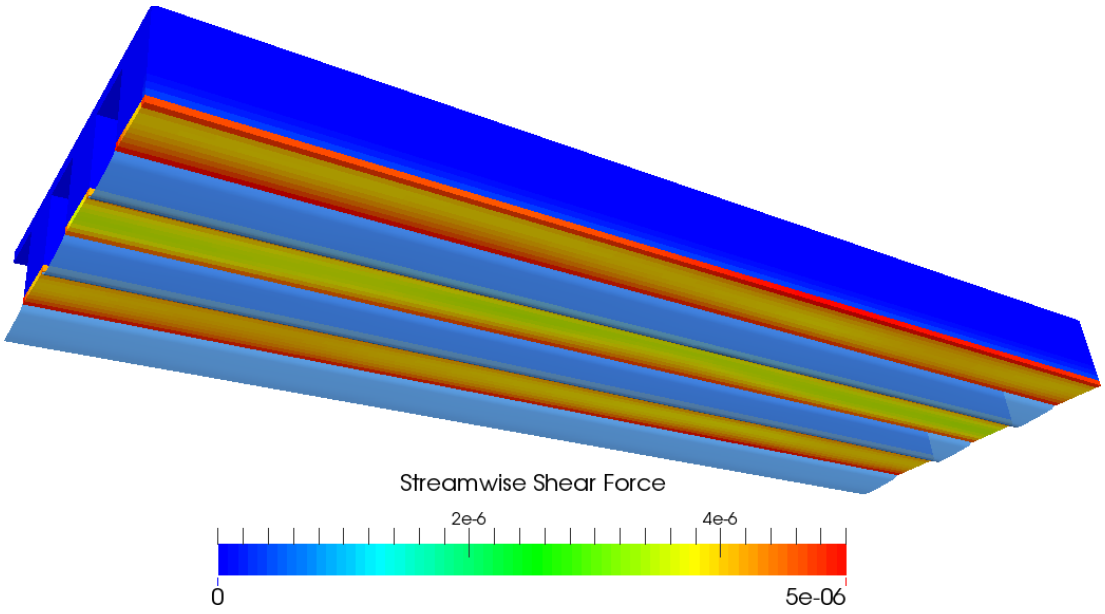

(b) Hydrophobic Geometry.
The air-water interface is indicated by the translucent blue surface.

Figure 6.15: Time averaged shear force and free-surface on the streamwise grooves surface at $Re_\tau = 180$. The difference between the shear forces acting on the sides of the ridges of the rough and hydrophobic surfaces is much more visible at the higher Reynolds number.

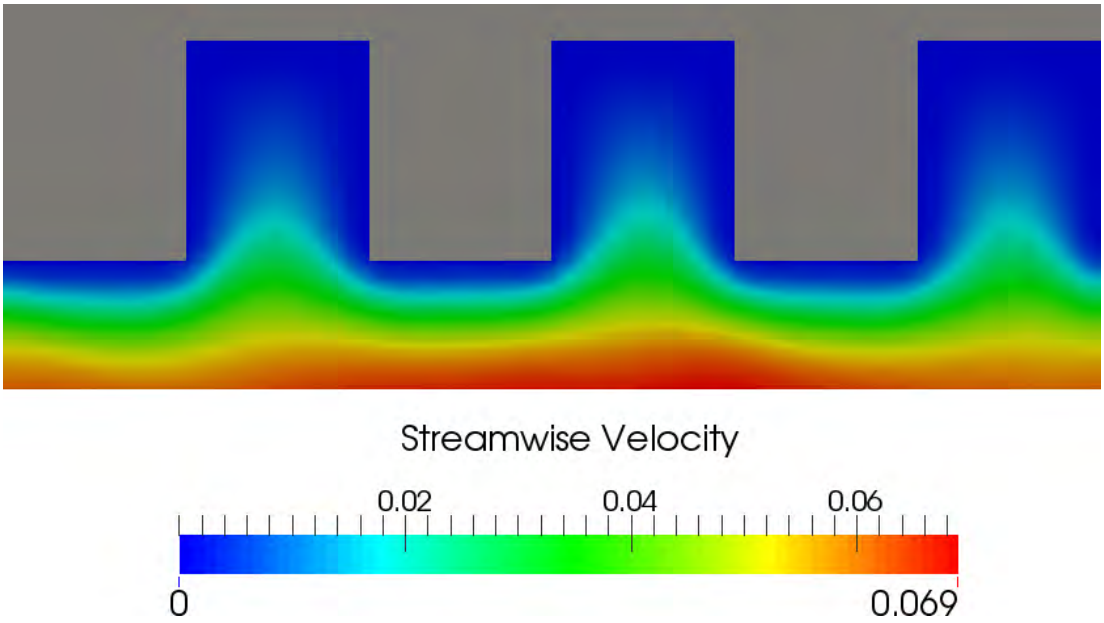

(a) Rough Geometry

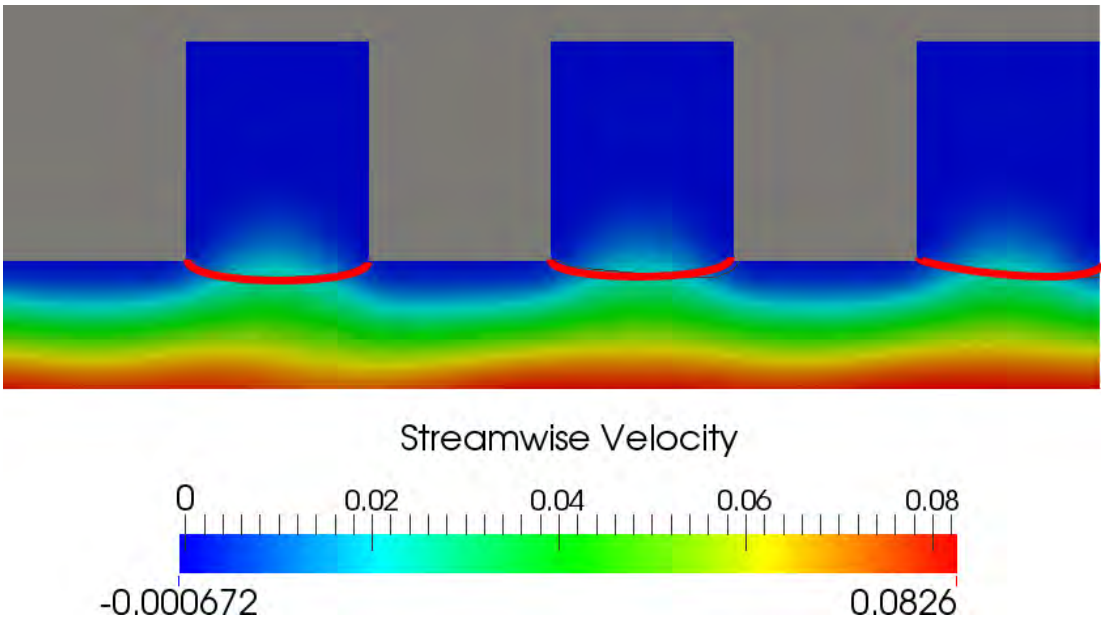

(b) Hydrophobic Geometry.
The red lines indicate the location of the air-water interface.

Figure 6.16: Time averaged velocity contours and free-surface on the streamwise grooves geometry at $Re_\tau = 180$. As can be seen, the presence of the free-surface has led to a lower velocity within the grooves.

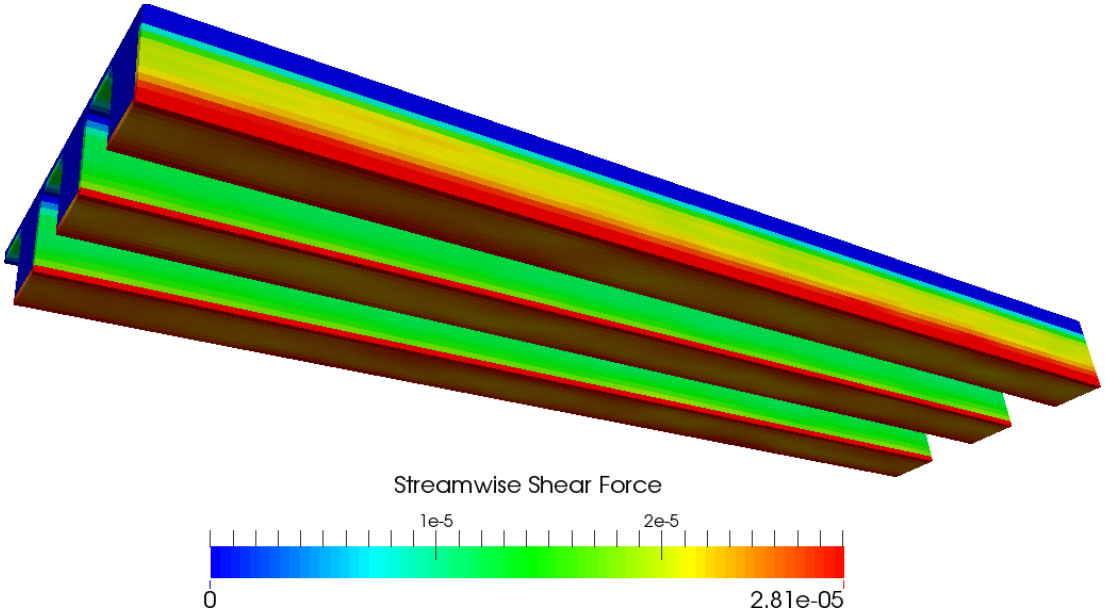

(a) Rough Geometry

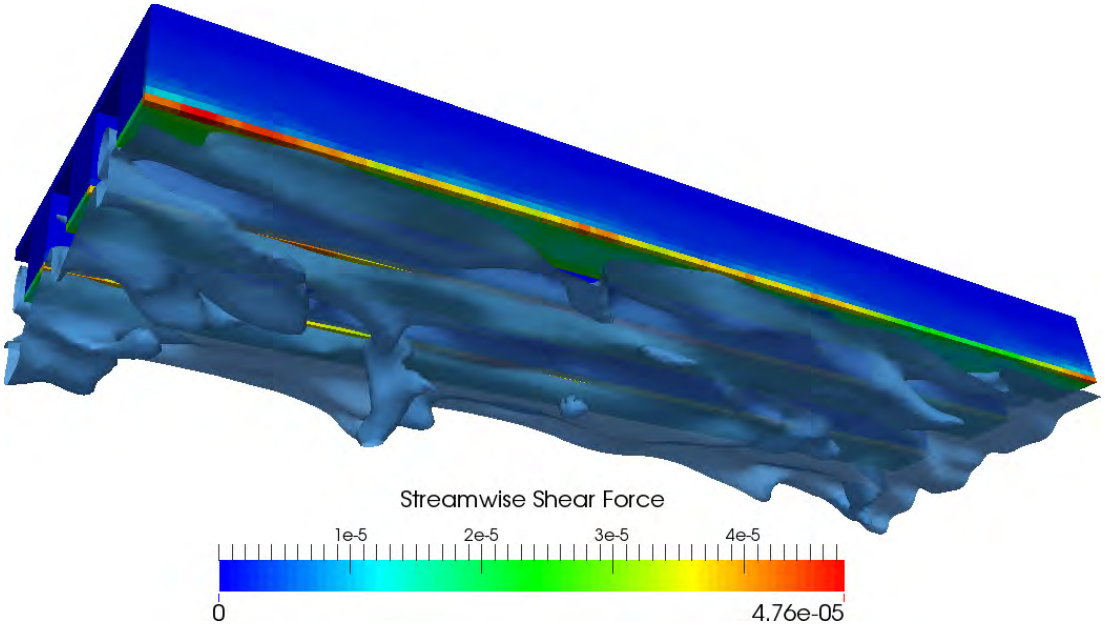

(b) Hydrophobic Geometry.
The air-water interface is indicated by the translucent blue surface.

Figure 6.17: Time averaged shear force and instantaneous free-surface on the streamwise grooved surface at $Re_\tau = 590$. The air has moved from within the grooves and is now covering most of the surface. The shear force distribution is again clearly different between the rough and hydrophobic surfaces.

6.2.2 Turbulent Regime

At high Reynolds numbers, the hydrophobic surface matches or out performs the smooth surface and has almost 65% less drag than the rough surface. Once again, this drag reduction can be attributed to the presence and influence of the air water interface. Figure 6.17b shows the location of the air-water interface at $Re_\tau = 590$. The combination of the high velocity flow and the increased pressure force distorting the free-surface has caused the air to move out of the grooves and instead cover large portions of the ridges. With the ridges covered in this way, the hydrophobic surface has a reduction in wetted surface area as compared to the rough surface. This minimisation of wetted surface results in the hydrophobic surface having on average 59% less area experiencing a streamwise shear force than the rough surface, corresponding to the 65% reduction in drag.

Figure 6.18 again shows velocity contours in the streamwise direction. Unlike previous velocity contour images for the streamwise geometry, a significant difference can be seen in the velocity of the fluid within the grooves between the two surfaces. The velocity within the grooves of the rough surface is up to 20% greater than of the grooves of the hydrophobic surface. This is also confirmed by looking at the shear force distribution in Figure 6.17, with the majority of the force acting on the tops of the ridges on the hydrophobic geometry. This is contrasted by the shear forces acting on both the sides of the ridges, and the top wall of the domain on the rough surface.

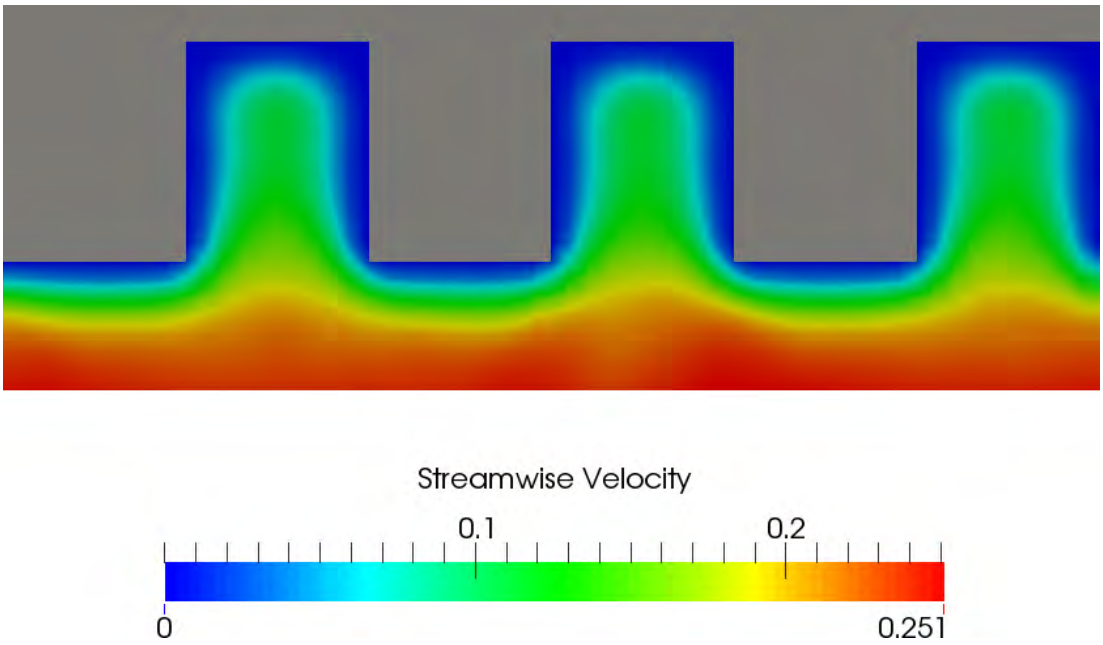

(a) Rough Geometry

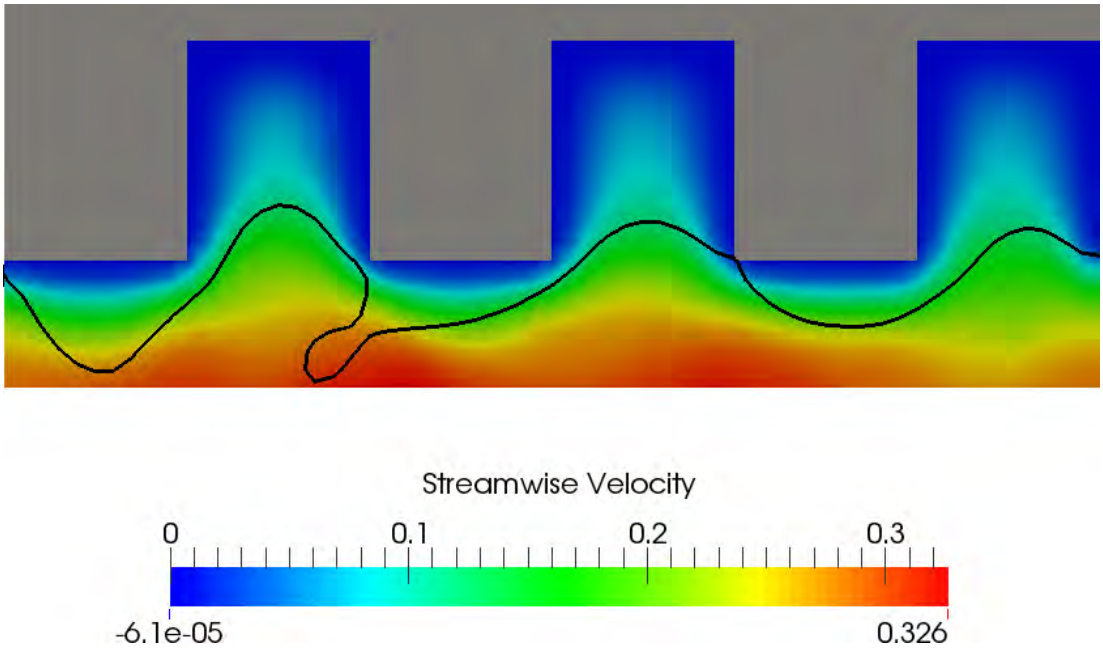

(b) Hydrophobic Geometry.
The black line indicates the location of the air-water interface.

Figure 6.18: Time-Averaged Velocity contours over the Streamwise Geometry at $Re_\tau = 590$.

Table 6.3: Summary of drag reduction of rough and hydrophobic channels as a percentage of drag on the smooth channel. +ve values indicates an increase in drag and −ve values indicate a decrease in drag.

Re_τ	Rough	SHS
50	+ 353.7	+ 339.3
100	+ 321.1	+ 311.6
180	+ 79.75	+ 8.27
395	+ 101.1	− 5.76
590	+ 122.2	− 21.9

6.2.3 Summary

The results have shown that the streamwise grooved super hydrophobic surface is able to reduce the the drag on the surface throughout the turbulent flow regime. As can be seen in Table 6.2, as the Reynolds number increases, the drag reduction effect also increases to a maximum of almost a 22% reduction at $Re_\tau = 590$. This effect occurs at higher Reynolds numbers because as the wall normal forces increase, the air that was contained within the grooves is forced out and instead covers both the tops of the ridges as well as the bottom of the grooves leading to a large decrease in wetted surface area. This decrease in wetted area is then responsible for the reduction in drag.

Compared to the low Reynolds number drag being over four times greater than the smooth channel, some amount of drag reduction in the transitional and turbulent flows appears to be evidenced. Based on the increased surface area of the rough surface over the smooth channel, a drag increase of roughly 250% would be expected (the rough surface has 2.5 times the surface area of the smooth channel). With the drag measured at in the transitional and turbulent regimes being less than half the expected value, the drag reduction appears to occurs as the reduced velocity of the fluid within the grooves leads to a lower overall shear force acting on the surface.

This page is intentionally left blank.

Chapter 7

Computational Results 2: Post Geometries

Compared with the grooved surfaces discussed in the previous chapter, the surfaces featuring posts have a planform wetted surface area that is 50% smaller. If the assumption continues to hold true that the drag is proportional to the wetted surface area, these surfaces should be able to offer up to double the drag reduction than has been shown for the grooved surfaces.

This chapter will detail the results of the aligned and offset post geometries which have post height, post width, and gap spacing equal to that of the grooves and ridges in Chapter 6. The analysis procedure will be the same, with results presented for laminar, transitional and turbulent flow of both the wetted rough surface and the un-wetted hydrophobic surface; both of which will again be compared to the smooth channel.

7.1 Aligned Posts

Plots of the drag co-efficients for the aligned post geometry can be seen in Figure 7.1. Interestingly, the pressure drag component is significantly higher on the post geometries than it was in the grooved geometries, as can be seen in both Figure 7.1b and Table 7.1.

As shown in the table, the streamwise pressure force made up 15.42% of the total drag force acting on the spanwise grooved geometry. In the aligned post case,

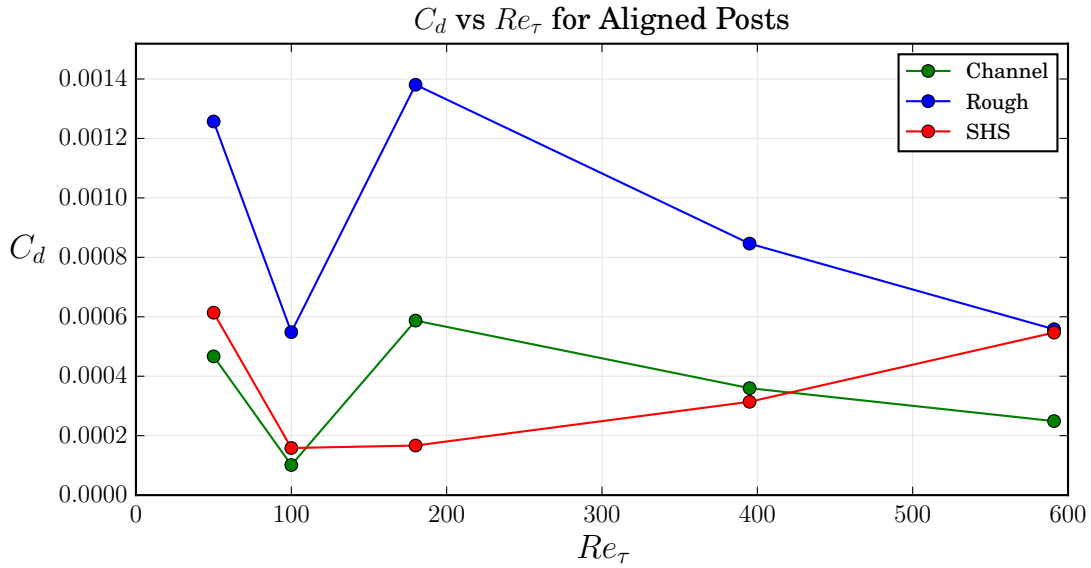

(a) Coefficient of drag (C_d).

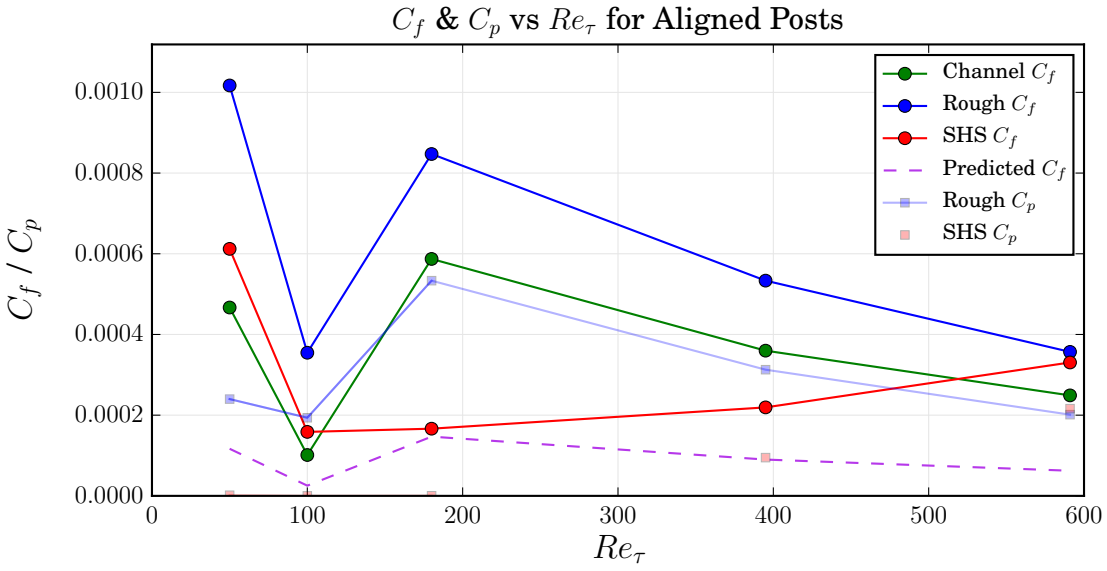

(b) Co-efficients of friction (C_f) and pressure (C_p).

Figure 7.1: Drag co-efficients vs Reynolds number for aligned post geometry and smooth channel.

Table 7.1: Force components as a percentage of the total drag of the rough surface. The streamwise grooves have been omitted as they have no pressure force component.

	Spanwise Grooves		Aligned Posts		Offset Posts	
Re_τ	Pressure	Friction	Pressure	Friction	Pressure	Friction
50	28.34	71.66	19.08	80.92	34.90	65.10
100	20.32	79.68	35.31	64.69	46.62	53.38
180	17.89	82.11	38.63	61.37	47.54	52.46
390	9.47	90.53	36.96	63.04	46.59	53.41
570	1.07	98.93	36.06	63.94	36.07	63.93
Average	15.42	84.58	33.21	66.79	42.34	57.66

where compared to the spanwise grooves the exposed frontal area was halved, the pressure drag component actually doubled to 33.21%.

The other notable feature of the plot in Figure 7.1 is the convergence in the drags of the rough and hydrophobic surfaces at $Re_\tau = 590$. This again is similar behaviour to that observed with the spanwise geometry.

7.1.1 Laminar and Transitional Regimes

The laminar flow results are similar to those seen in the spanwise geometry, with the drag co-efficients for the hydrophobic surface being similar to those of the smooth channel. As was the case previously, this is again due to the reduced wetted surface area in contact with the fluid flowing through the channel, combined with the low velocity of fluid moving between the posts. In the case of the hydrophobic surface, the air-water interface again insulates the posts leading to a further reduction in drag as compared with the rough surface. This is illustrated in Figure 7.2. Also visible in this figure is the shear distribution on the tops of the posts. On the hydrophobic surface, this distribution resembles that of the streamwise grooves with the highest shear occurring along the edges of the posts. This is again a result of the air within the gaps being free to move

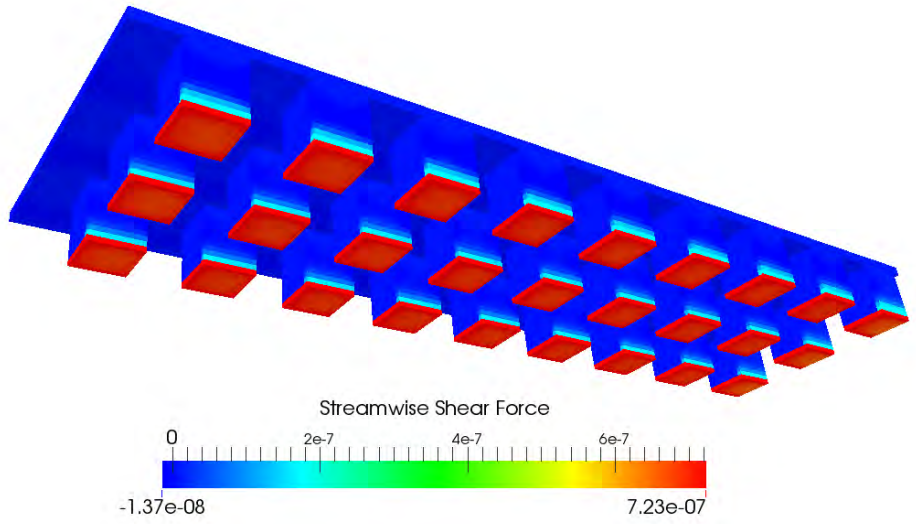

(a) Rough Geometry

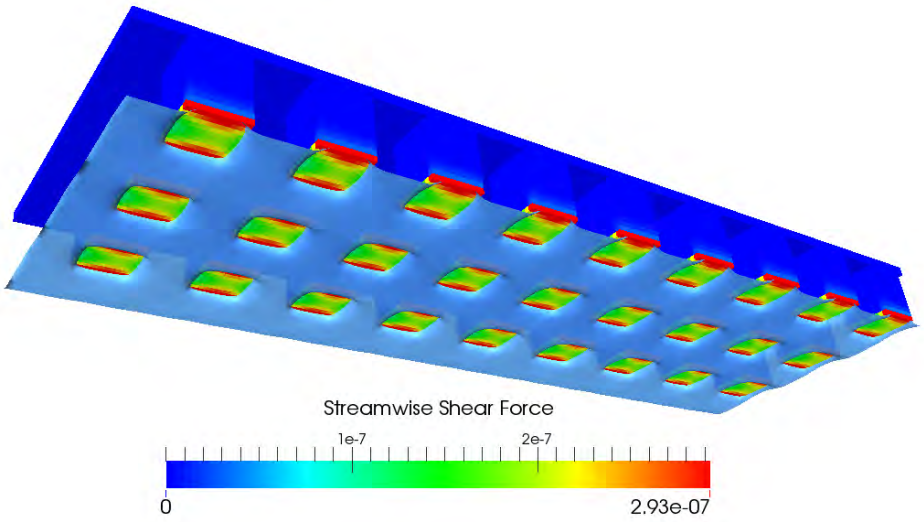

(b) Hydrophobic Geometry.
The air-water interface is indicated by the translucent blue surface.

Figure 7.2: Time averaged shear force and free-surface on the aligned post surface at $Re_\tau = 50$. The difference in the distribution of shear force can be clearly seen, both on the tops and sides of the posts.

in the streamwise direction; however, a difference in this scenario is that the free surface is also deflecting the flow of the water away from the tops of the post, as was seen in the spanwise geometry analysis in Section 6.1.

The insulation effect due to the free-surface and flow fields around the posts can be seen by looking at the velocity vectors in the streamwise direction in Figure 7.3. As was the case with the spanwise geometry, it is clear as to why the rough surface has a higher value for both the shear and pressure forces, as the free-surface acts to divert the flow away from the surface in the hydrophobic case. However, unlike the spanwise geometry where the flow within the grooves resembled that of a lid driven cavity flow, the fluid between the posts looks quite different. In the case of the rough surface, there is a small eddy behind the top of each post and a net flow towards the surface. Conversely, the hydrophobic surface again shows an eddy below the air-water interface, and a net flow between the posts towards the centre on the channel. The eddy below the interface is significantly smaller and weaker than it was at the same Reynolds number in the spanwise grooves geometry, this being a result of the three dimensional curvature of the free-surface stopping the reinforcement of the eddy that was taking place in the two dimensional spanwise groove case. The net flow, both towards and away from the surface, is also a feature of the three dimensionality of the micro features. As the velocity vectors are only being shown on the X-Y plane, there is no indication of the spanwise flow. The vectors themselves are also not being length scaled by value due to the difference in magnitude between the highest and lowest velocities. These factors make the flow towards the wall at the bottom of the gaps look stronger than it really is. Figure 7.4 shows an instantaneous set of three-dimensional streamlines flowing between and around the posts and gives some idea of the spanwise flow in areas of the domain..

The plot showing co-efficients of frictional and pressure drag verses Reynolds number (Figure 7.1b) also showed that throughout the transition between laminar and fully turbulent flow the hydrophobic surface has a substantially lower drag than either the smooth channel or rough surface. The reason for this is similar to that of the streamwise geometry at high Reynolds numbers, with the free-surface moving from between the posts, and instead forming waves which propagate over the surface. These waves then wet and un-wet the tops of the posts causing the overall wetted surface area to be decreased. Figure 7.6 shows the average shear

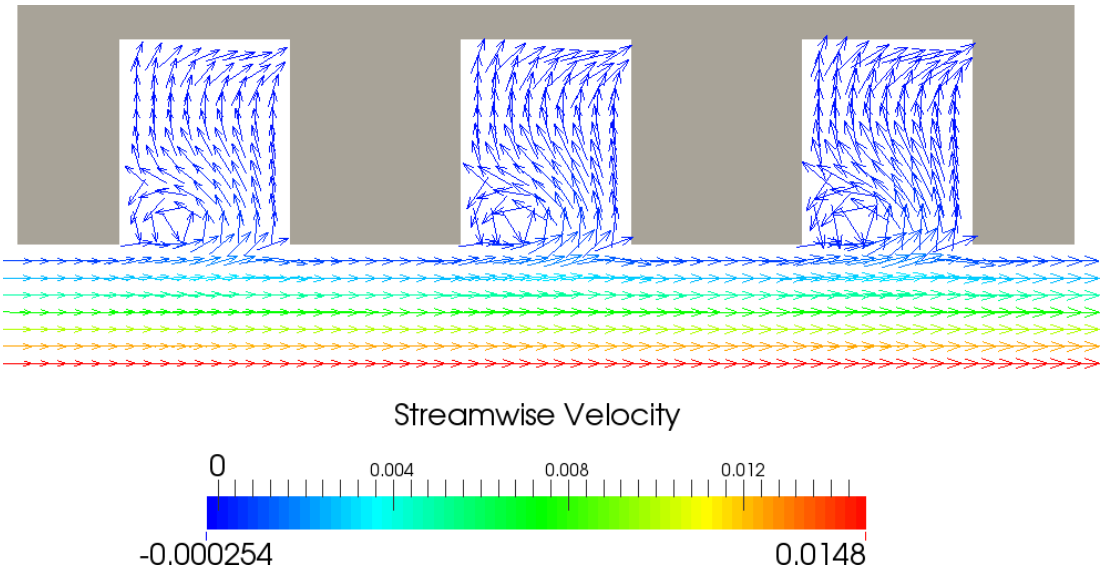

(a) Rough Geometry

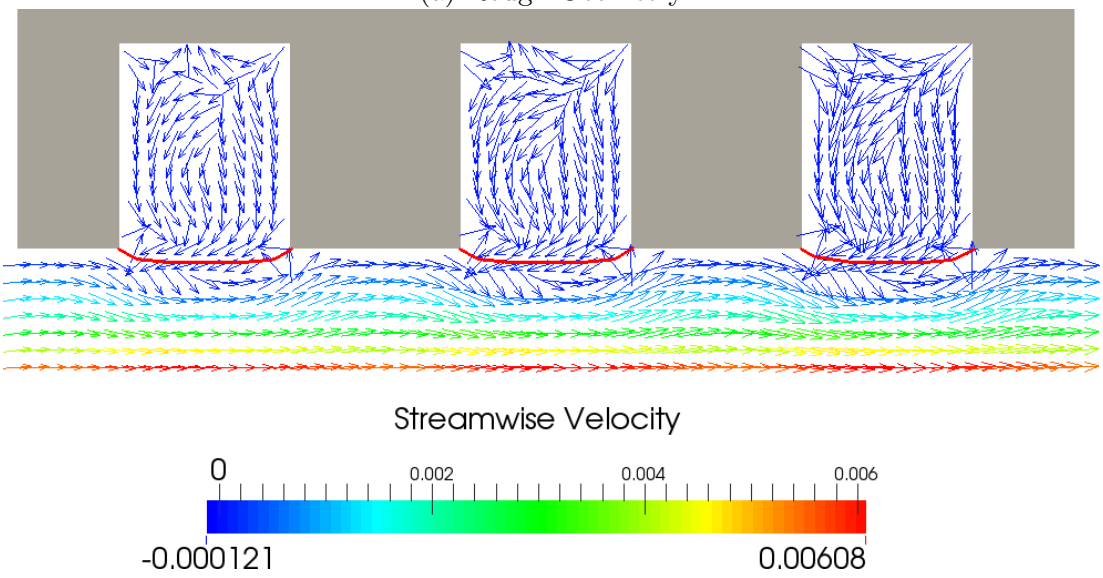

(b) Hydrophobic Geometry.
The air-water interface is indicated by the red line.

Figure 7.3: Time averaged velocity vectors and free-surface on the aligned post surface at $Re_\tau = 50$. Note the reduced size of the eddy below the free-surface that was observed in the spanwise grooves geometry. Also missing is the typical lid-driven cavity flow structure. Both of these are due to the three-dimensional nature of the flow around the posts.

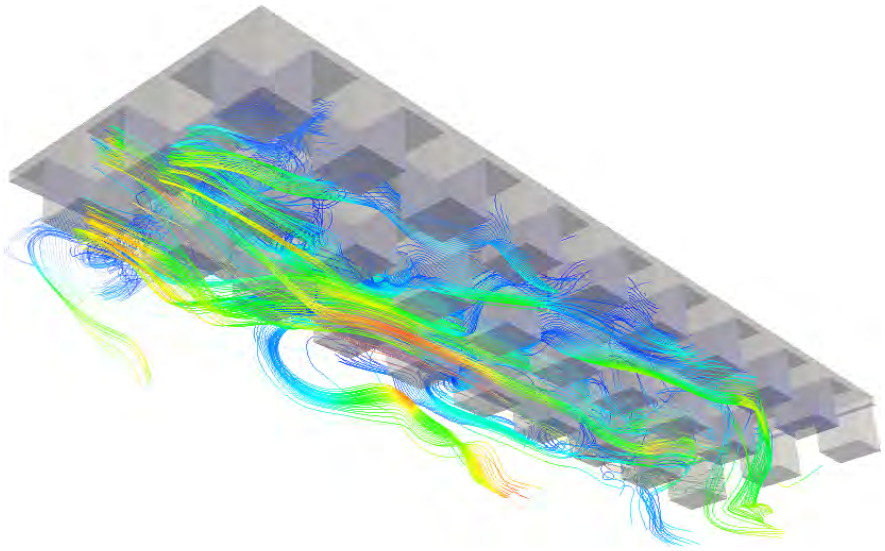

(a) Isometric view.

(b) Side view.

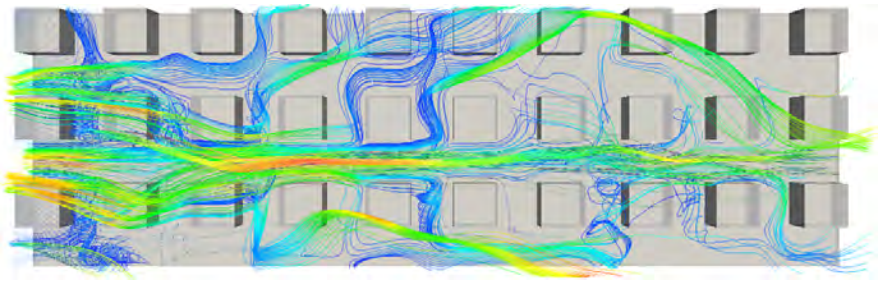

(c) Top view.

Figure 7.4: Three-dimensional streamlines flowing between and around the posts at $Re_\tau = 180$ for the rough surface. The side view shows the vortices that form behind the posts, while the top view gives an indication of both the streamwise and spanwise flow between the posts.

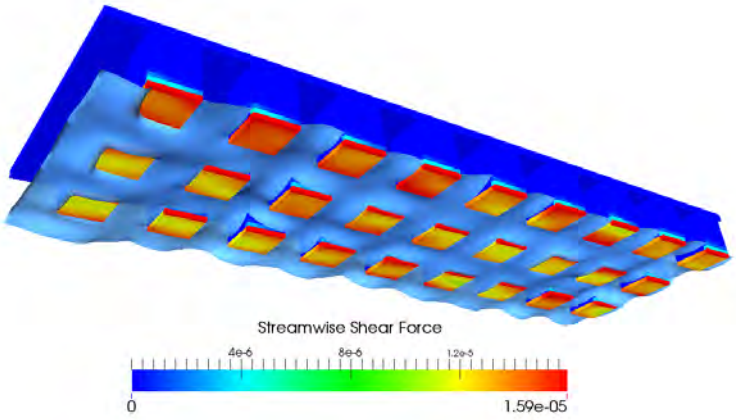

(a) Hydrophobic surface at $Re_\tau = 395$

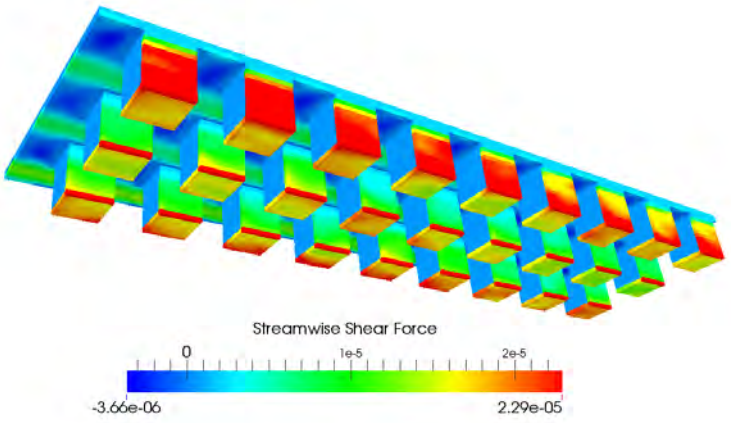

(b) Rough surface at $Re_\tau = 590$

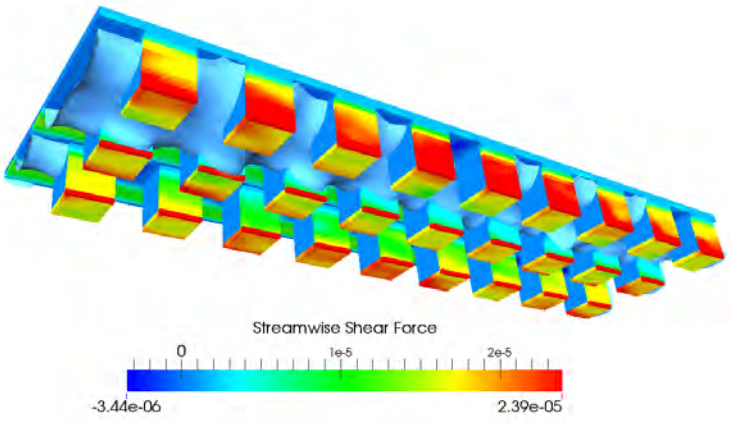

(c) Hydrophobic surface at $Re_\tau = 590$

Figure 7.5: Time averaged shear force and instantaneous free-surface location for the rough and hydrophobic surfaces at turbulent Reynolds numbers. The translucent blue surface indicates the location of the free surface.

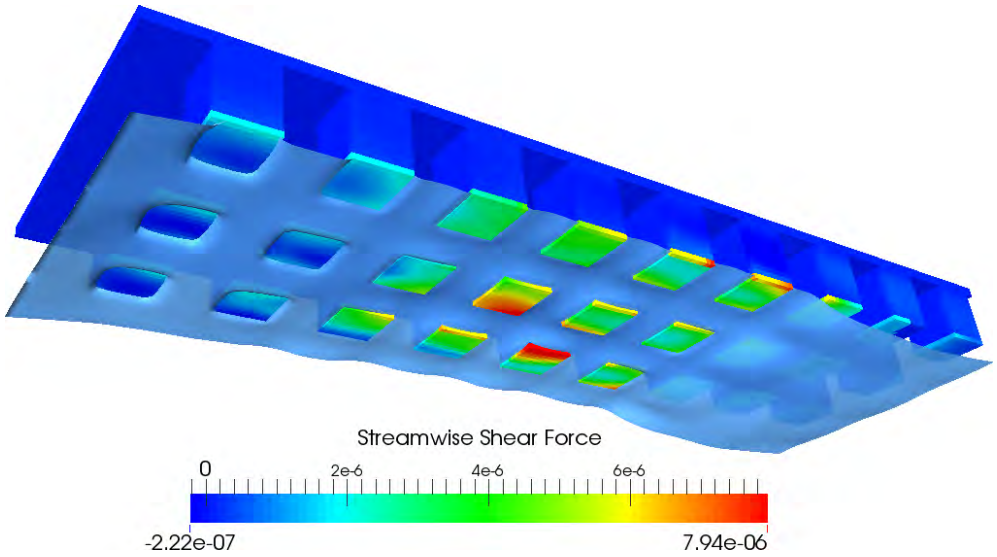

Figure 7.6: Time averaged shear force on the hydrophobic aligned posts surface at $Re_\tau = 180$. The air-water interface is indicated by the translucent blue surface.

force acting on the hydrophobic surface with an instantaneous position of the air-water interface superimposed on top. At this timestep, almost a third of the surface is clear of the water as the wave passes over it. This causes a significant reduction in wetted surface area leading to the low drag value.

7.1.2 Turbulent Regime

Very different results for the hydrophobic surface are seen at the two different turbulent Reynolds numbers tested. At the lower value, $Re_\tau = 395$, the frictional drag shows a substantial reduction as compared with the smooth surface. Combined with a small pressure force component, the total drag of the hydrophobic surface is slightly lower than that of the smooth channel, and significantly lower than that of the rough surface.

This is vastly contrast however with the results of the hydrophobic surface at the high Reynolds number. At $Re_\tau = 590$, the drag of the hydrophobic surface is nearly identical to that of the rough surface and almost double that of the smooth channel. This increased drag can be explained by comparisons of the air-water interface at the two different Reynolds numbers, shown in the shear

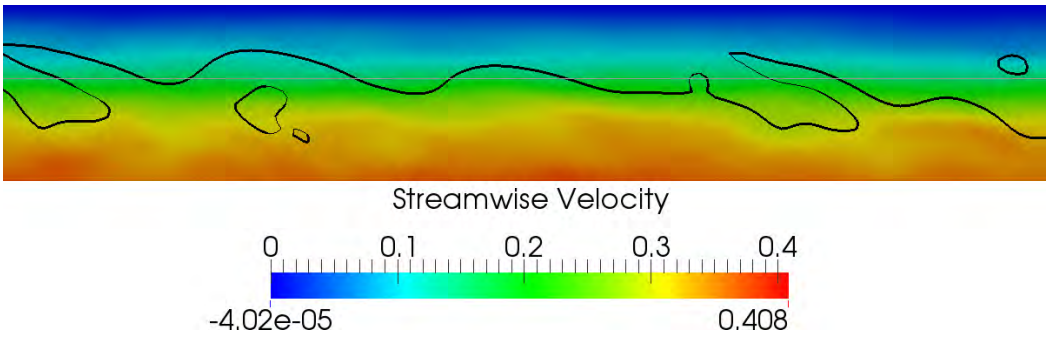

Figure 7.7: The black line shows the location of the free surface at $Re_\tau = 590$. Droplets and bubbles are both visible in this image.

force images in Figure 7.5. At $Re_\tau = 395$, the air is insulating the posts from the water leading to the reduced drag as has been the case in earlier simulations. However, at $Re_\tau = 590$, the air layer has been removed, and the posts are exposed to both shear forces and pressure forces in much the same way as the rough surface. The comparison between the rough and hydrophobic surfaces, seen as Figures 7.5b and 7.5c show that the shear stress distributions on the surface are almost identical.

Figure 7.7 shows the location of the free-surface for a single timestep soon after the phases were reset. The slice is taken down the centre of the domain between the posts and shows the level to which the free-surface has been distorted, with waves, bubbles and droplets all visible. Although the multiphase method implemented in the lattice Boltzmann code conserves the mass of both phases, when the free surface becomes this distorted a high level of numerical condensation occurs. This results in the air being converted into water, and the surface becoming fully wetted, as was seen in Figure 7.5c. Fortunately, the result of this process is remarkably similar to the dissolution of air into the water as was mentioned in Chapter 2.

As was the case in the laminar and transitional regime, the rough surface has a higher drag than either the smooth channel or the hydrophobic surface for both of the tested turbulent Reynolds numbers. This is due to both the increased surface area with the sides of the posts exposed, and the increased pressure drag force that was highlighted in Table 7.1.

7.1.3 Summary

The aligned posts have been shown to give significant reduction for transitional flows with up to 71% less resistance at $Re_\tau = 180$. Once the flow becomes turbulent, although initially a drag reduction is still observed, at high Reynolds numbers this effect disappears as the air layer on the surface is depleted. After this occurs, the hydrophobic surface performs near identically to the rough surface.

Table 7.2: Summary of drag reduction of rough and hydrophobic surfaces as a percentage of drag on the smooth channel. +ve values indicate an increase in drag and −ve values indicate a reduction in drag.

Re_τ	Rough	SHS
50	+ 169.3	+ 31.47
100	+ 441.6	+ 56.59
180	+ 135.1	− 71.59
395	+ 135.1	− 12.73
590	+ 124.1	+ 119.6

By again plotting the values of the shear force distributions on the top of the posts for the rough and hydrophobic surfaces, the differences in shear can easily be seen. As shown in Figure 7.8, at $Re_\tau = 180$ the hydrophobic surface experiences less shear force, with the maximum values being found along the sides of the post where the higher velocities are. As was the case with the spanwise geometry discussed previously, the maximum shear value occurs at the leading edge of the rough surface, and about 60% of the post length downstream on the hydrophobic surface. When the air layer has been removed at high Reynolds numbers, the shear forces of the tops of both the rough and hydrophobic posts become almost the same.

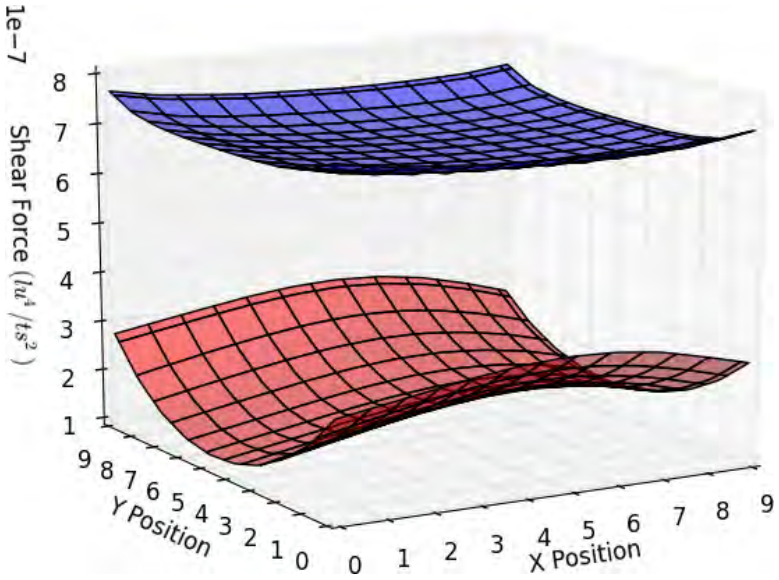

(a) Shear distribution at $Re_\tau = 180$.
(Blue = Rough Surface, Red = SHS)

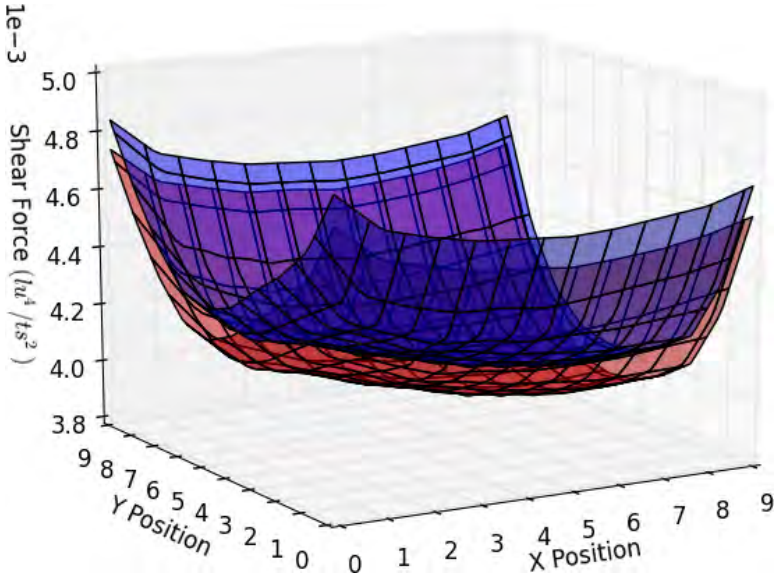

(b) Shear distribution on the top of a post at $Re_\tau = 590$.
(Blue = Rough Surface, Red = SHS)

Figure 7.8: Shear force distribution on tops of the posts in the aligned post geometry. In the hydrophobic $Re_\tau = 180$ case, the shear force acting on the posts is highest along the sides, and reaches a maximum value about 60% of the way along the post, similar to what was shown earlier in the spanwise geometry case. The rough surface posts also have their maximum shear force values occurring along the edges, but with the highest value occurring at the leading edge of the post. In the $Re_\tau = 590$ case, when the air layer has been depleted, the distributions are very similar.

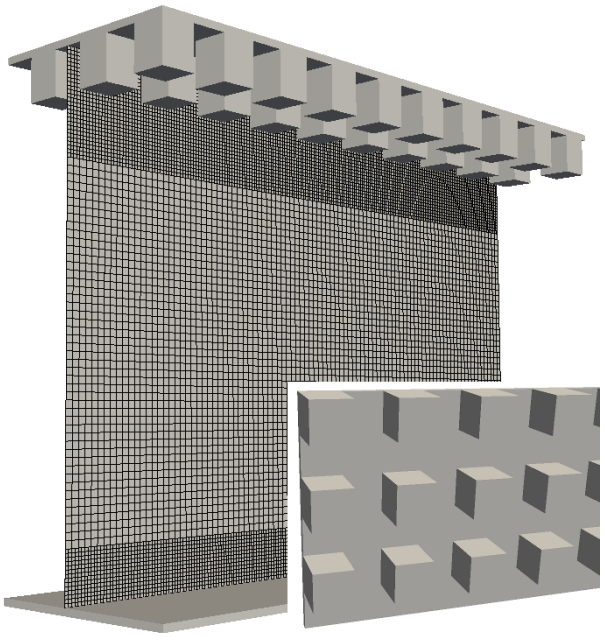

(a) Aligned posts geometry. The inset image shows the posts aligned in both the stream-wise and span-wise directions.

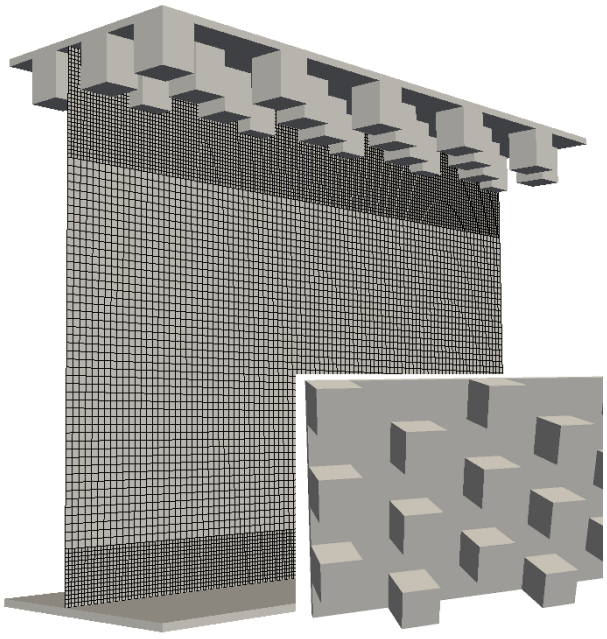

(b) Offset posts geometry. The inset image shows the posts aligned in span-wise direction but offset in the stream-wise direction.

Figure 7.9: Comparison of aligned and offset posts geometries.

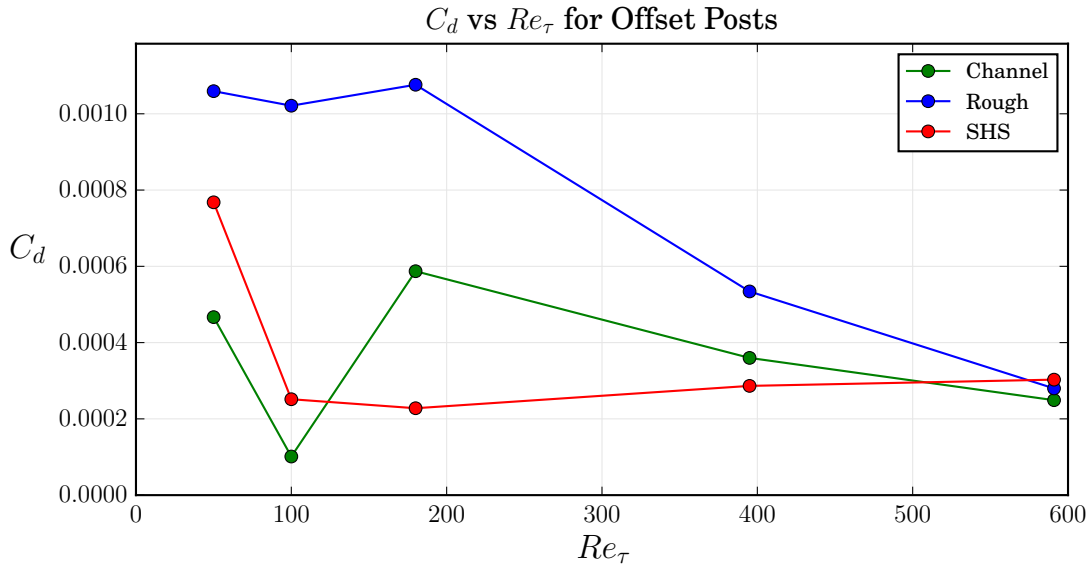

(a) Coefficient of drag (C_d).

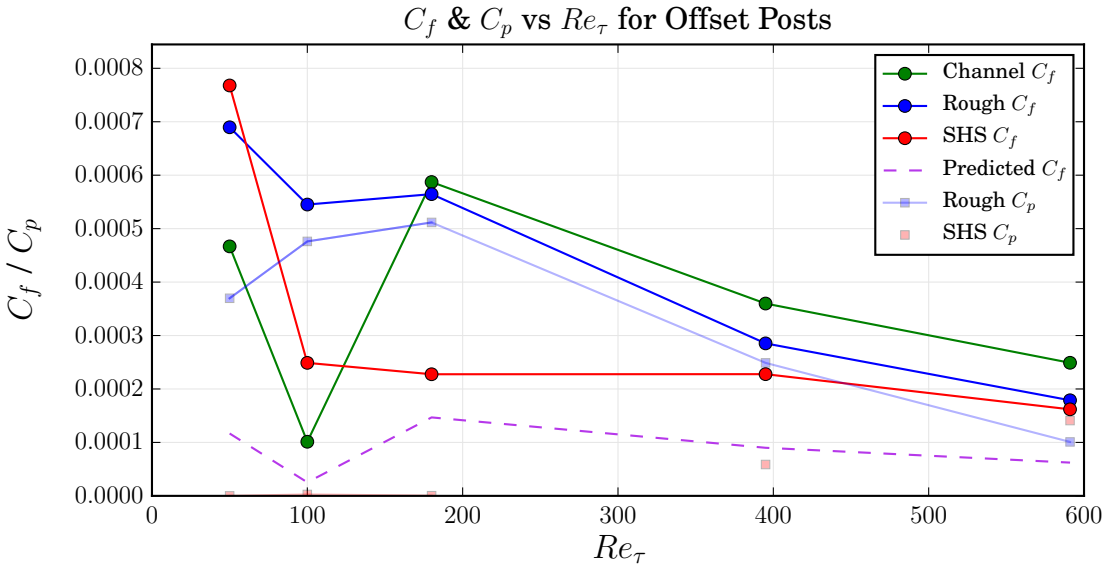

(b) Co-efficients of friction (C_f) and pressure (C_p).

Figure 7.10: Drag co-efficients vs Reynolds number for offset post geometry and smooth channel.

7.2 Offset Posts

The offset posts geometry differs slightly to that of the aligned posts as the streamwise grooves running between the lines of posts have been blocked, as can be seen in Figure 7.9. Even with the streamwise grooves obstructed, the drag co-efficient results, shown in Figures 7.10a and 7.10b are quite similar to those seen previously in the aligned post geometry with the hydrophobic surface providing a reduction in drag through the transitional and low turbulent number cases before being near identical to the rough surface at $Re_\tau = 590$.

With the posts offset, the exposed frontal area is equal to that of the spanwise geometry; however, as was previously shown in Table 7.1, the average pressure force component makes up 42.34% of the total drag of the surface. This is almost three times higher in the case of the offset posts than it was in the case of the spanwise grooves. Even more interesting results can be seen if a comparison is made between the magnitudes of the pressure forces instead of just the component percentages of drag, as shown in Table 7.3.

Table 7.3: Summary of pressure forces acting in the streamwise direction on each geometry. (Units are all lu^4/ts^2)

	Spanwise		Aligned Posts		Offset Posts	
Re	Rough	SHS	Rough	SHS	Rough	SHS
50	9.10×10^{-4}	0.0	9.91×10^{-4}	1.74×10^{-6}	9.43×10^{-4}	0.0
100	2.40×10^{-3}	0.0	4.97×10^{-3}	0.0	6.44×10^{-3}	2.80×10^{-5}
180	5.71×10^{-3}	0.0	1.25×10^{-2}	1.25×10^{-5}	9.71×10^{-3}	8.83×10^{-6}
390	9.51×10^{-3}	4.63×10^{-4}	3.59×10^{-2}	1.85×10^{-2}	2.76×10^{-2}	1.00×10^{-2}
570	1.82×10^{-3}	5.71×10^{-3}	6.82×10^{-2}	7.80×10^{-2}	3.30×10^{-2}	4.92×10^{-2}

This shows that in turbulent flow, the pressure force acting on the aligned posts geometry is almost double that of the offset posts, which is in turn almost an order of magnitude higher than that of the spanwise geometry. The reason that the offset post pressure force is lower than that of the aligned posts can be

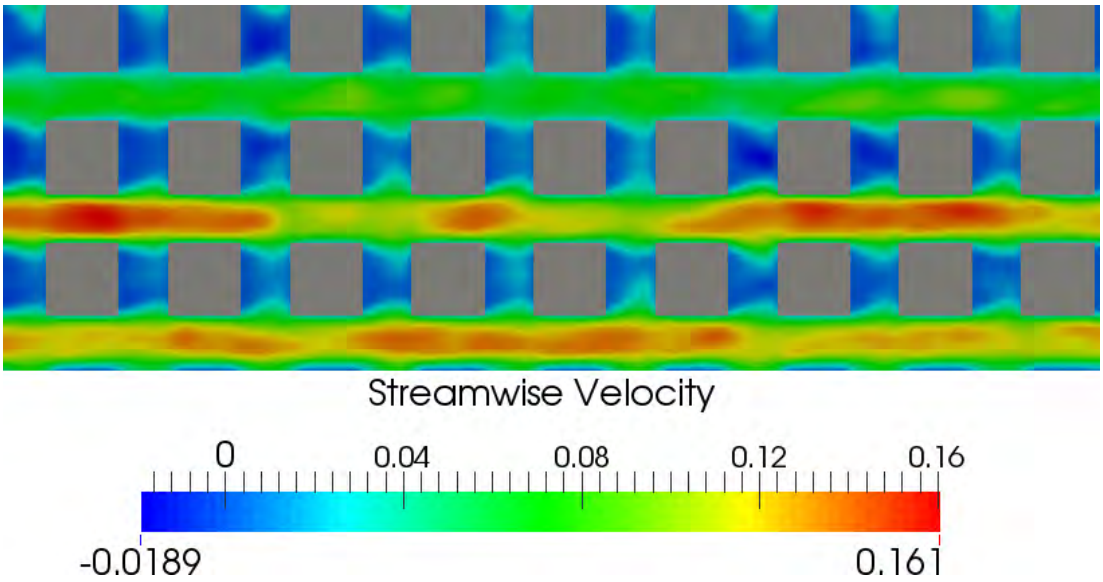

(a) Aligned post geometry.

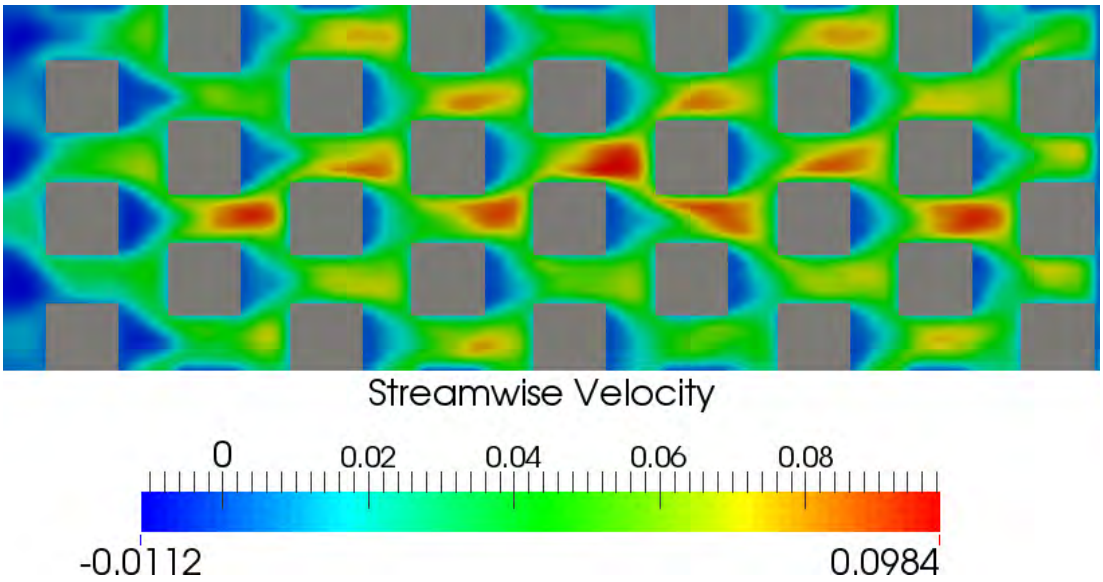

(b) Offset posts geometry.

Figure 7.11: Streamwise velocity contours through mid-height of posts. It can be seen that the velocity between the offset posts is substantially lower than it is between the aligned posts, resulting in less drag acting on the posts.

seen by looking at the velocity of the fluid between the posts. Figure 7.11 shows a horizontal slice through the middle of the posts. From this, it can be seen that the maximum velocity in the case of the aligned posts is 63% higher than it is in the offset posts geometry. Similarly, the average velocity between the aligned posts is 83% higher than it is between the offset posts. This indicates that the presence of the posts blocking the streamwise pathways significantly slows the fluid velocity between the posts. This reduction in velocity leads to a both a reduced pressure force and reduced shear force acting on the posts in turbulent flow. At lower speeds, the differences in velocity in the flow between the posts is minimal.

7.2.1 Laminar and Transitional Regimes

The drag reductions in the laminar regime for the hydrophobic surface are similar to what has been seen in the other geometries. As was the case with the aligned posts, a substantial drag reduction has been measured at $Re_\tau = 180$ of 61%. Counterpoint to this is the rough surface, which has a completely different drag profile to what has been seen in the results thus far. The marked reduction in drag between $Re_\tau = 50$ and $Re_\tau = 100$ has not occurred as seen in the other geometries tested. This appears to be largely due to an increased pressure force acting on the posts, as the frictional drag has decreased in similar fashion to that already shown.

As can be seen in Figure 7.13, the distribution of shear on the hydrophobic posts is similar to that seen in the aligned posts cases, with the highest shear stresses occurring along the sides of the top of the posts. This is also the case with the rough surface posts with their distribution similar to that previously observed with the maximum shear occurring at the leading edge, along with some evidence of shear forces on the side walls of the post.

The velocity vectors showing the flow over the surfaces, illustrated in Figure 7.12, again show the air-water interface deflecting the water away from the surface in the hydrophobic case, while in the rough case, the velocity component across the top of the post is relatively undisturbed. This again accounts for some of the increase in drag between the rough and hydrophobic surface in the low speed cases.

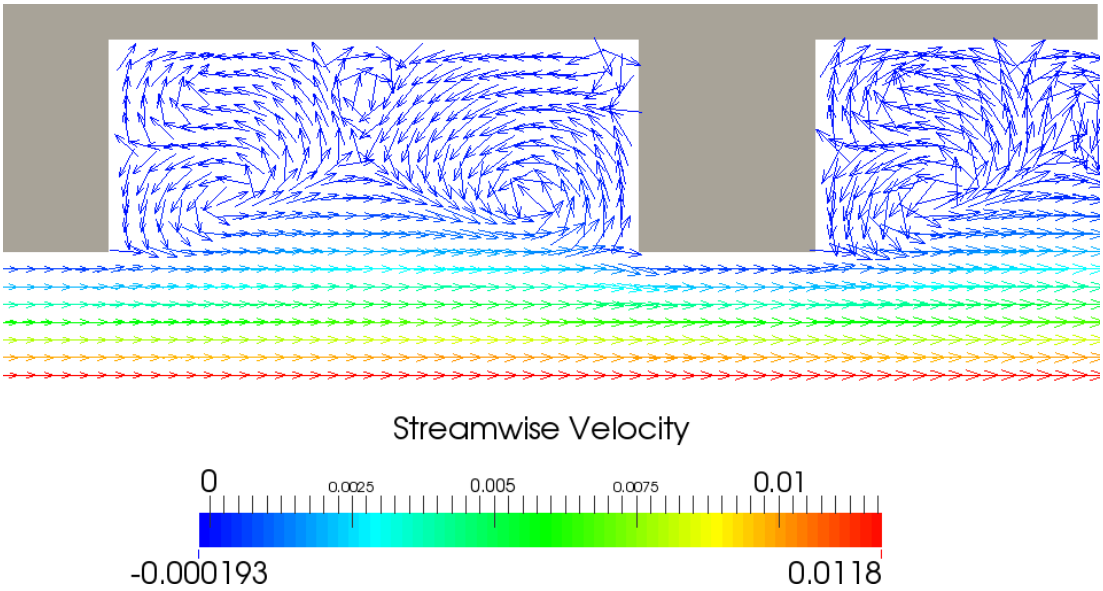

(a) Rough Geometry

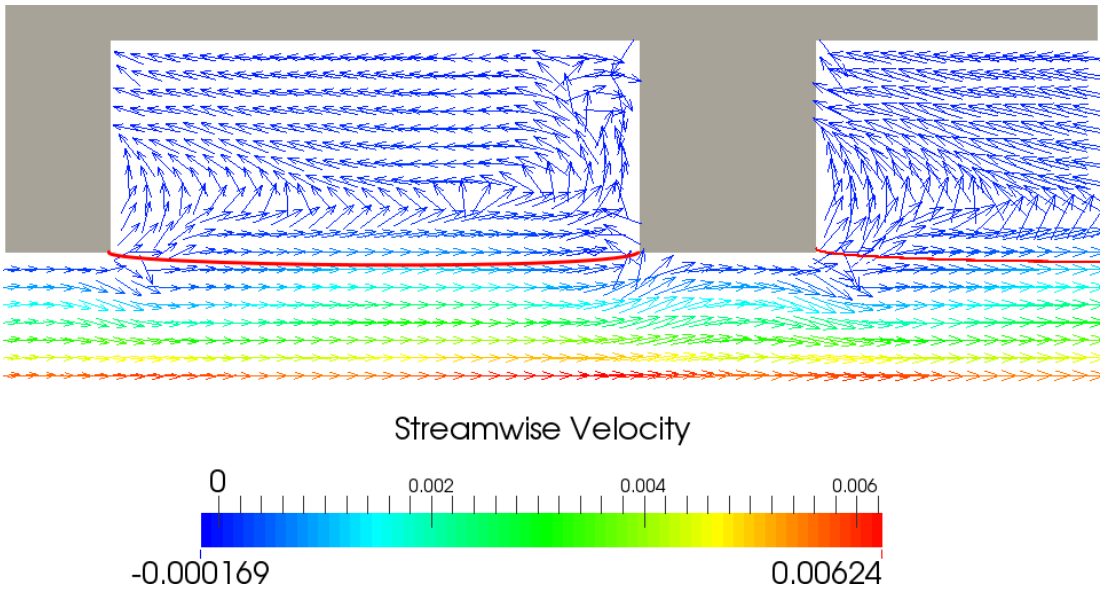

(b) Hydrophobic Geometry.
The air-water interface is indicated by the red line.

Figure 7.12: Velocity vectors and free-surface profile for the offset post surface at $Re_\tau = 50$. The presence of the free-surface minimises the vortices within the gaps between the posts.

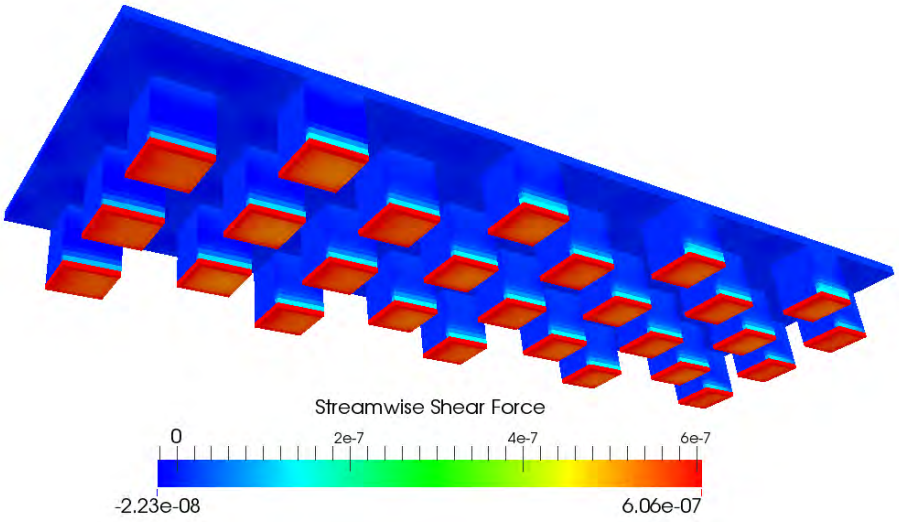

(a) Rough Geometry

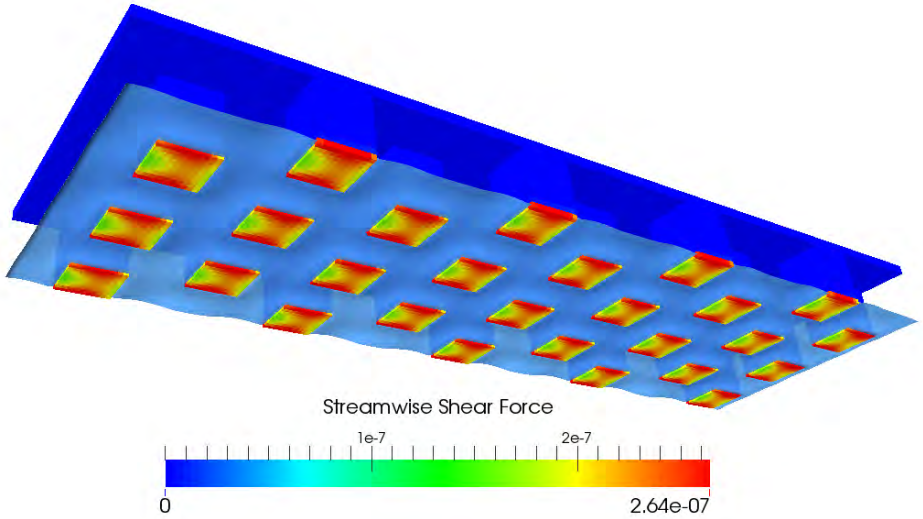

(b) Hydrophobic Geometry.
The air-water interface is indicated by the translucent blue surface.

Figure 7.13: Shear force and free-surface for the offset posts surface at $Re_\tau = 50$. The distribution of shear force is again similar to what was seen in the aligned posts case discussed previously.

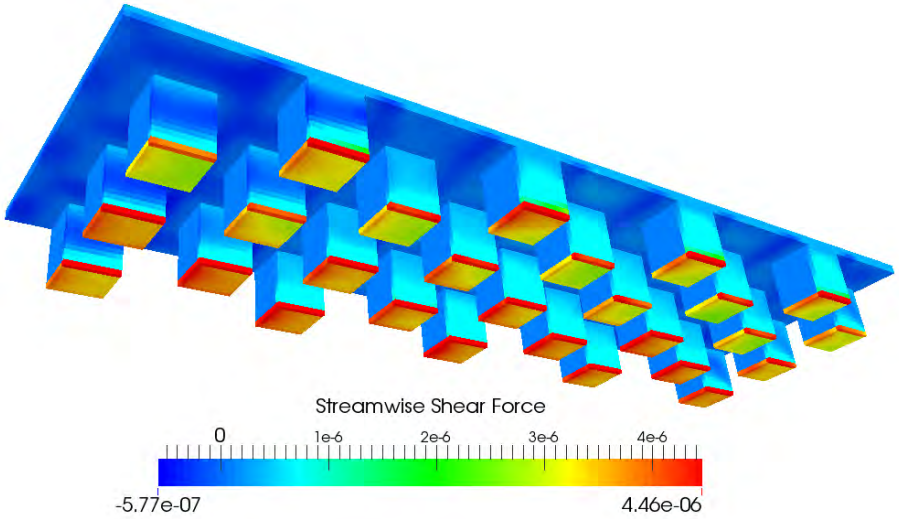

(a) Rough Geometry

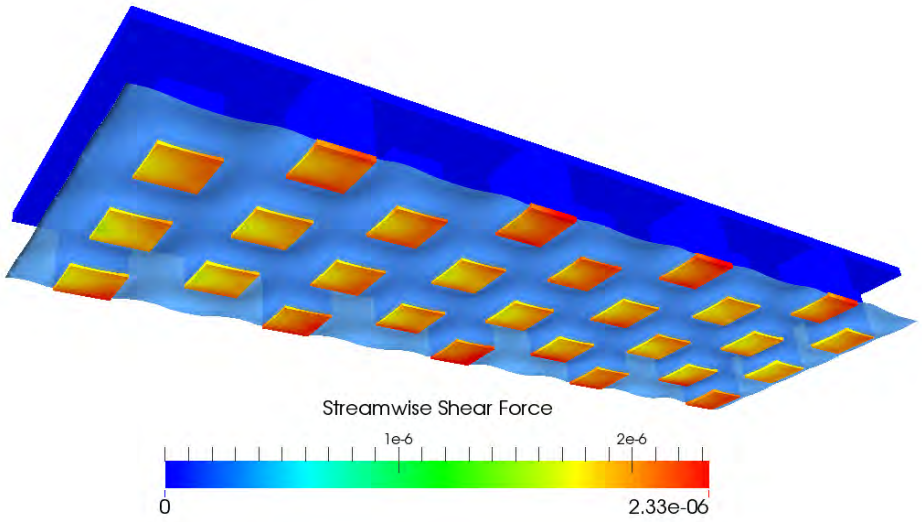

(b) Hydrophobic Geometry.
The air-water interface is indicated by the translucent blue surface.

Figure 7.14: Shear force and free-surface for the offset posts surface at $Re_\tau = 395$. It can be seen by the distribution of the shear forces that the free-surface is insulating the posts reducing the area on which the shear forces act.

7.2.2 Turbulent Regime

The turbulent flow results also mimic those of previously discussed geometries with the flow over the hydrophobic surface at $Re_\tau = 395$ having both reduced levels of frictional and pressure drag. This can again be related to the effect of the free-surface in insulating the sides of the posts from the water, and deflecting the flow over the tops of the posts, as can be seen in Figure 7.14. A similar result to the aligned posts geometry is also seen in the $Re_\tau = 590$ case with the air having been removed from the surface, which can be seen in Figure 7.15. With the air removed from the surface the hydrophobic surface again becomes effectively the same as the rough surface, so it is expected that their drag values would be similar. This is further confirmed by the drag distributions on the posts, as can be seen in Figure 7.15.

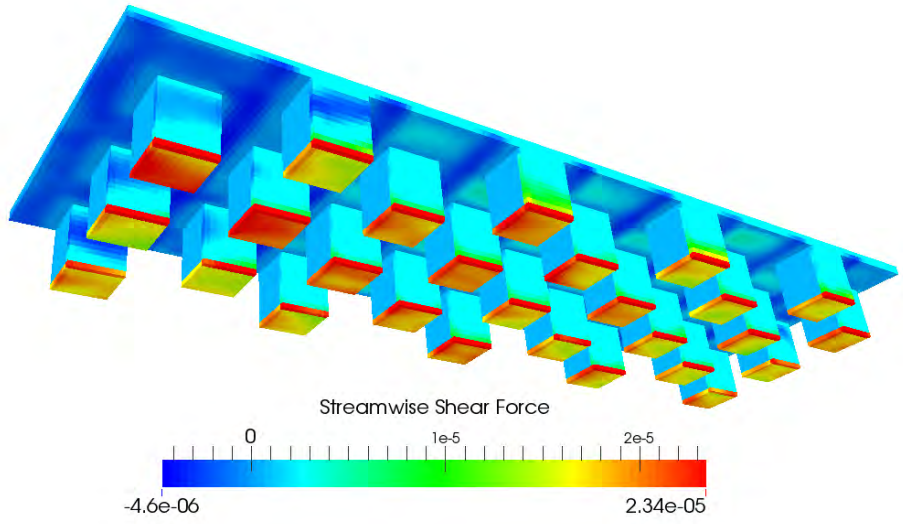

(a) Rough Geometry

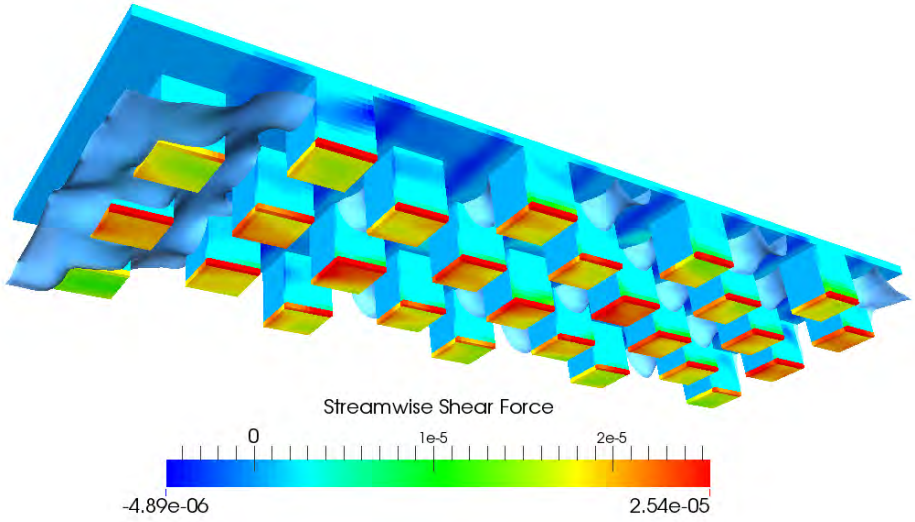

(b) Hydrophobic Geometry.
The air-water interface is indicated by the translucent blue surface.

Figure 7.15: Shear force and free-surface for the offset posts surface at $Re_\tau = 590$. With the air layer mostly removed, the shear force distribution on both the rough and hydrophobic surfaces are very similar.

7.2.3 Summary

The offset posts hydrophobic geometry gives no drag reductions in laminar flow however a large drag reduction of over 60% is observed through the transitional and low turbulent flow regimes. This appears due to the offset posts geometry reducing the velocity of the flow between the posts leading to both lower shear drag and pressure drag. At the highest Reynolds number tested there is again minimal difference between the rough and hydrophobic surfaces as the layer of air on the surface is removed meaning the two surfaces are almost identical.

Table 7.4: Summary of drag reduction of rough and hydrophobic surfaces as a percentage of drag on the smooth channel. +ve values indicate an increase in drag and −ve values indicate a reduction in drag.

Re_τ	Rough	SHS
50	+ 126.9	+ 64.49
100	+ 908.6	+ 148.4
180	+ 83.27	− 61.19
395	+ 48.43	− 20.39
590	+ 12.36	+ 21.62

This page is intentionally left blank.

Chapter 8

Computational Results 3: Post Size Variation

With the previous results showing that a reduction in the wetted surface area of the posts and ridges corresponded to a reduction in drag in flows between $Re_\tau \approx 180$ and $Re_\tau \approx 395$, a brief study has been undertaken to further decrease the wetted surface area. This has been done by simulating flow over two additional geometries which have had the sizes of the posts and gaps between the posts modified.

As is illustrated in Figure 8.1, these additional surfaces are based on the aligned post geometry described previously in Section 5.1.4; however, unlike the previous geometries where the sizes of the posts, ridges, grooves and gaps were kept constant at 10 μm, these surfaces instead have 20 μm gaps between the posts. The size of the posts themselves have also been varied with a 5 μm square post being trialled on one of the surfaces to further minimise the wetted area. With the size of the gaps between the posts increasing, it was necessary to increase the height of the posts to keep the post height/gap ratio constant. This was done to ensure the air-water interface did not touch the top wall of the domain for the slightly deformed interface curvatures exhibited in the previous results at Reynolds numbers between $Re_\tau = 100$ and $Re_\tau = 395$. This increase of the post heights resulted in the posts being 28 μm high, again at a resolution of 1 lu per μm. Although the post height has been increased, the distance between the tops of the posts and the opposite wall of the domain has been kept constant

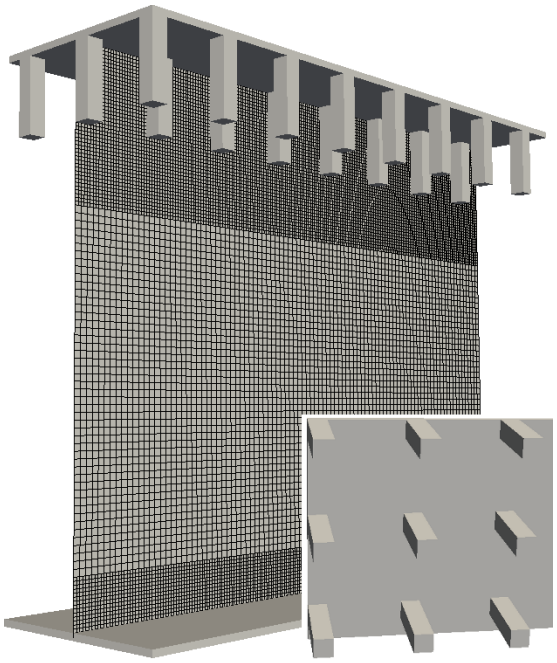

(a) 5/20 aligned posts geometry. $5\mu m$ square posts with $20\mu m$ gaps between them.

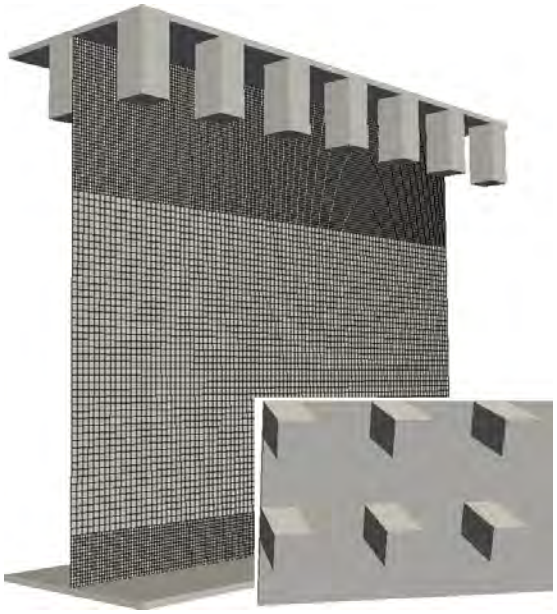

(b) 10/20 aligned posts geometry. $10\mu m$ square posts with $20\mu m$ gaps between them.

Figure 8.1: Additional aligned post geometries.

at 124 lu as was the case in the other tested geometries to maintain consistency between the simulations.

The wetted surface area of these geometries relative to the smooth channel have been calculated in the same manner as was done in the previous chapters and were found to be a 96% reduction in wetted surface area for the 5 μm post geometry, and a 89% reduction for the 10 μm. As a naming convention for these additional geometries, the surface with 10 μm posts with 20 μm gaps is referred to as the 10/20 aligned posts geometry, and the surface with 5 μm posts with 20 μm gaps is referred to as the 5/20 aligned posts geometry.

8.1 10/20 Aligned Posts

8.1.1 Laminar and Transitional Regimes

In a similar manner to that done with the previously tested geometries, plots of the drag co-efficients for the total drag and the frictional and pressure drag components have been generated for the varied post / gap size geometries, and can be seen in Figure 8.2. The first thing that is immediately noticed when looking at the drag coefficient plot shown in Figure 8.2a is that at $Re_\tau = 100$ the drag of the rough surface has increased from its value at $Re_\tau = 50$. This increase has not been exhibited by any of the other surfaces, so an investigation of the cause for it needs to be undertaken. From Figure 8.2b it can be seen that the increase in drag appears to be due entirely to an increase in frictional drag, as the pressure drag exhibited by the surface has decreased in a similar manner to that which has been reported in the previous results.

The explanation for this increase in frictional drag appears similar to the reason for the decrease in frictional drag shown with the offset posts; that is, it is due to the velocity of the fluid flowing through the gaps between the posts. With the increased spacing between the posts, there is less to retard the flow, leading to higher velocities and correspondingly higher shear forces. This can be clearly seen in Figure 8.3 which shows the difference in streamwise velocities in a slice parallel to the wall through the mid height of the posts.

In the transitional regime at $Re_\tau = 180$, the rough surface exhibits a

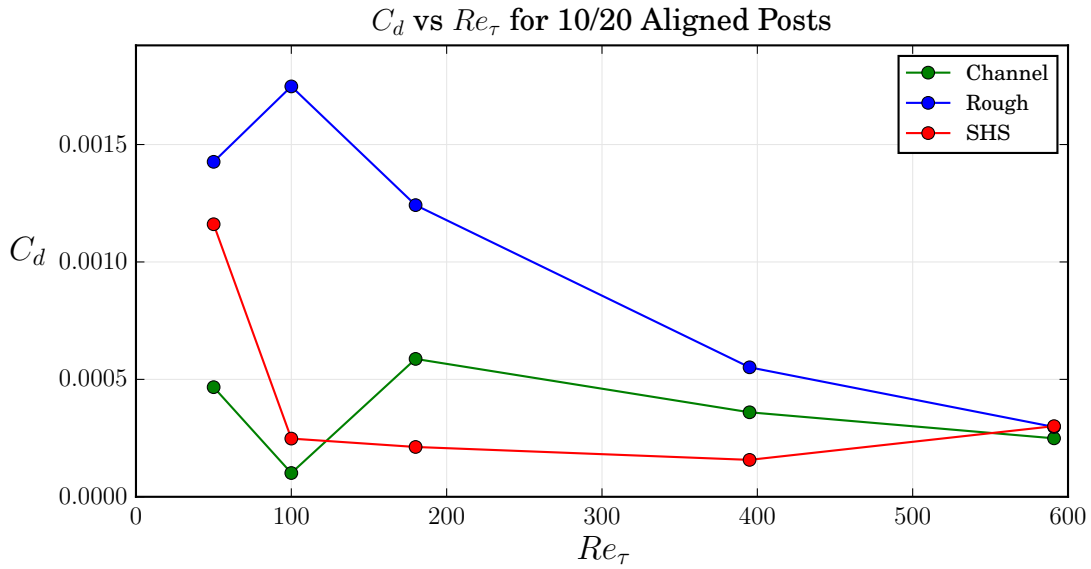

(a) Coefficient of drag (C_d).

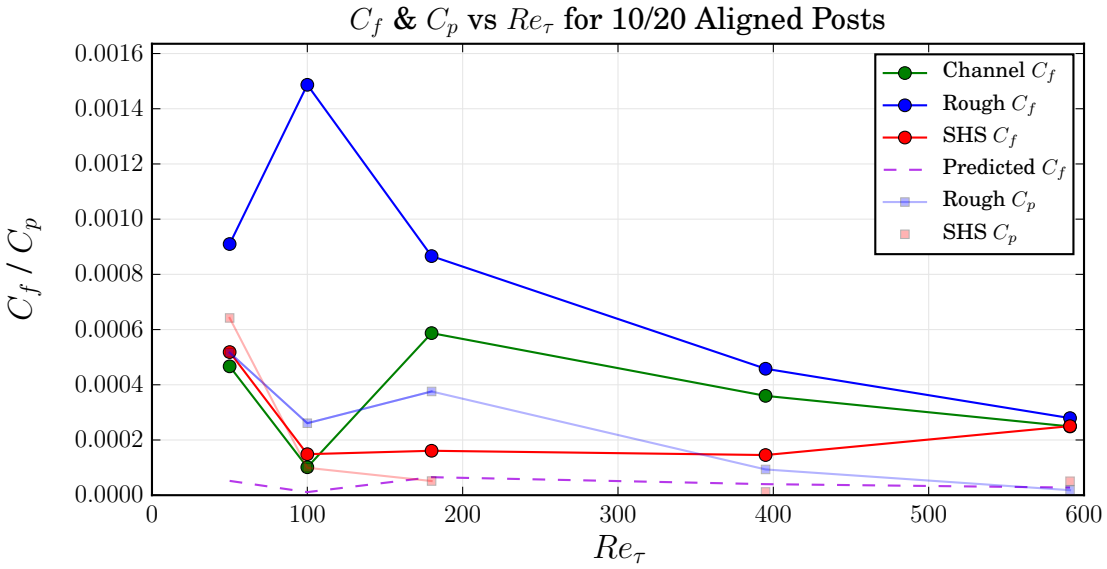

(b) Co-efficients of friction (C_f) and pressure (C_p).

Figure 8.2: Co-efficients of friction and pressure vs Reynolds number for 10/20 aligned posts geometry

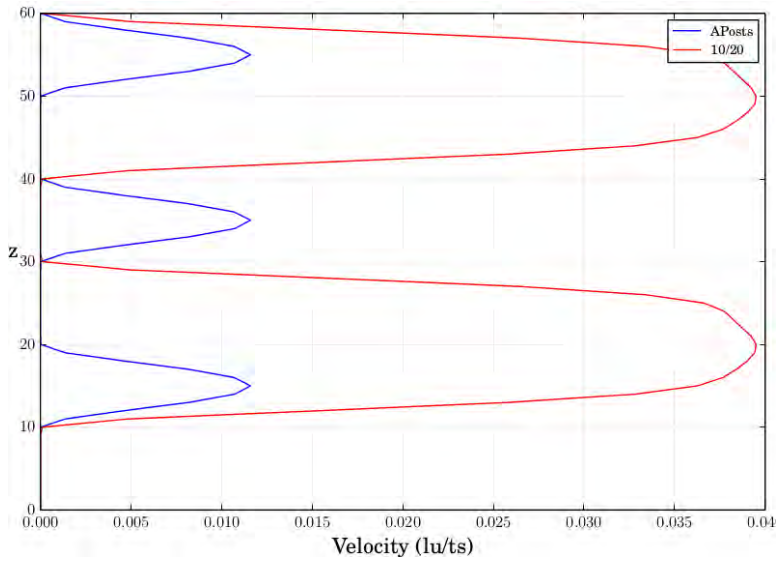

Figure 8.3: Comparison of velocity in the streamwise direction for the aligned post and 10/20 post geometries for the rough surface at $Re_\tau = 100$. The regions of zero velocity correspond to the locations of the posts. It can be seen that the velocity in the 10/20 posts geometry is significantly higher due to the increased spacing between the posts leading to an increased shear force.

significantly higher drag than either the smooth surface or the hydrophobic surface. Conversely, at both this and the next Reynolds number tested, the hydrophobic surface shows drag reductions of up to 63%, which as Figure 8.4 shows is due to the air layer stopping the water from interacting with the posts. This causes a reduction in pressure drag, and minimises the wetted area leading to a lowering of the shear drag. As can be clearly seen in the figure, although the maximum shear force on the hydrophobic surface is slightly higher than the maximum occurring on the rough surface, the distribution of shear forces on the rough surface covers significantly more area, leading to a substantially higher overall drag. The distribution on the tops of the posts is again similar to that seen in previously tested geometries, with the hydrophobic posts having the maximum shear force occurring on the sides of the posts, whereas on the rough surface this occurs at the leading edge of the posts.

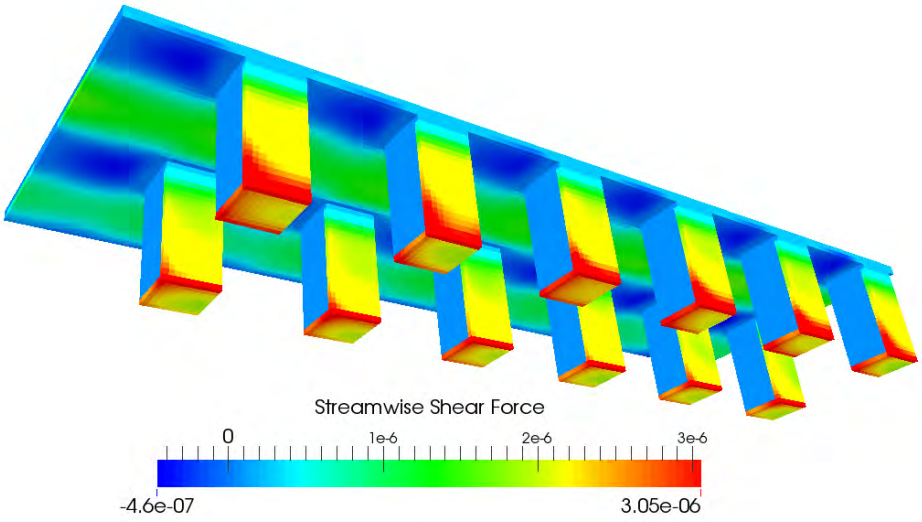

(a) Rough Geometry

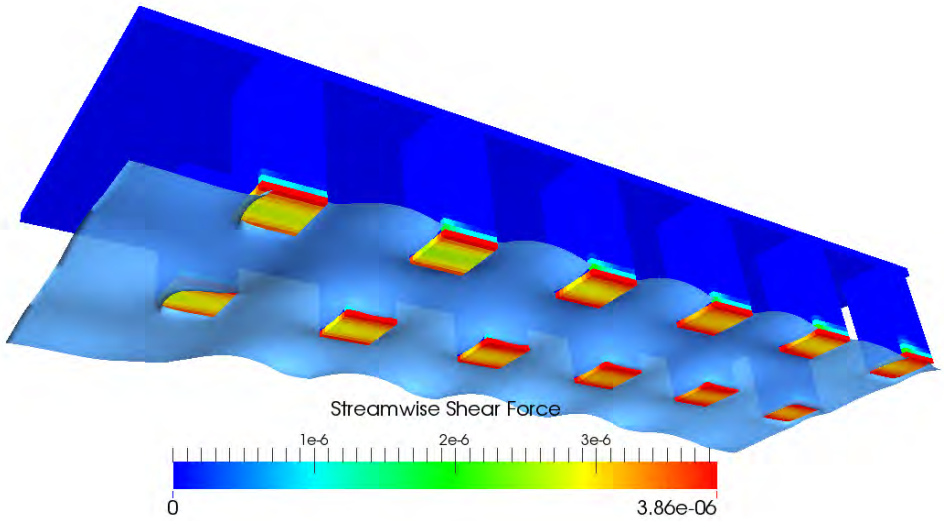

(b) Hydrophobic Geometry.
The air-water interface is indicated by the translucent blue surface.

Figure 8.4: Shear force and free-surface for offset post surface at $Re_\tau = 180$. The deflection of the free surface is visibly greater with the increased post spacing than it was with the earlier geometries at the same Reynolds number.

8.1.2 Turbulent Regime

At low turbulent Reynolds numbers, the hydrophobic surface outperforms both the rough and smooth surfaces with a reduction in drag of 56% of the smooth channel surface, and 83% of the rough surface channel at $Re_\tau = 395$. At this Reynolds number, the pressure drag on the hydrophobic surface is still minimal, accounting for only 2.5% of the total drag, meaning that the bulk of the drag is due to friction.

The rough surface again exhibits more drag than the smooth surface and is significantly higher the drag of the hydrophobic surface. This result is also slightly lower than it should be, as with no body forces being applied to the fluid between the posts, the shear forces are lower than they would otherwise be; an issue that will be further discussed in Section 10.4.

At the maximum Reynolds number tested of $Re_\tau = 590$, the drag of both the rough and hydrophobic surfaces again converge. As was the case in the earlier tested post geometries, this is again due to the layer of air against the hydrophobic surface being depleted. Without the air to insulate the posts, the hydrophobic surface becomes almost identical to the rough surface, and the results are accordingly similar.

By undertaking the vertical force analysis shown in earlier chapters and displayed in Figure 8.5, it is clear that the surface is unable to support the air-water interface at high Reynolds numbers. As was visible in Figure 8.4, at $Re_\tau = 180$ the interface was already experiencing deformation as was predicted by the analysis.

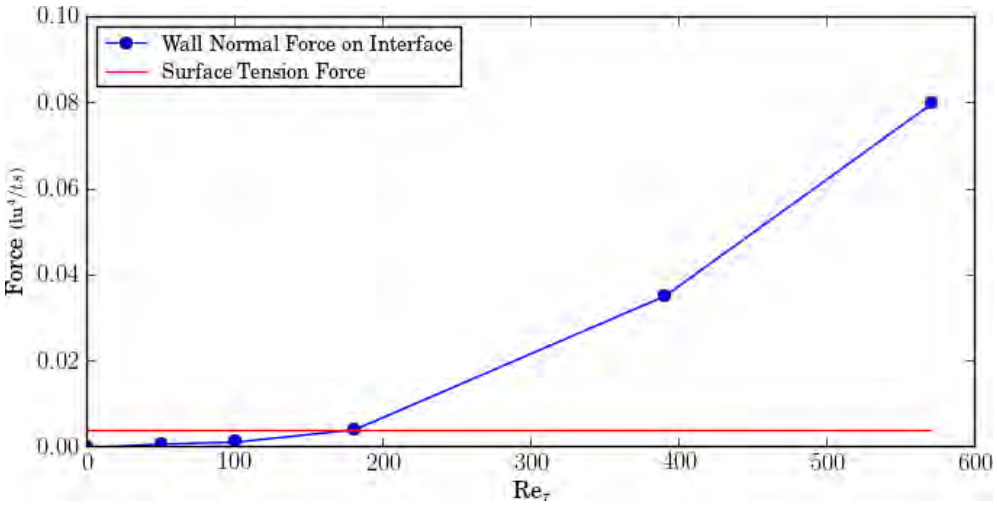

Figure 8.5: Vertical forces on the 10/20 posts. This indicates that at Reynolds numbers above $Re_\tau = 180$ the free surface is likely to deform and potentially allow the air layer to be removed. The results at $Re_\tau = 590$ confirm this prediction with the drag of the rough and hydrophobic surfaces alomst identical.

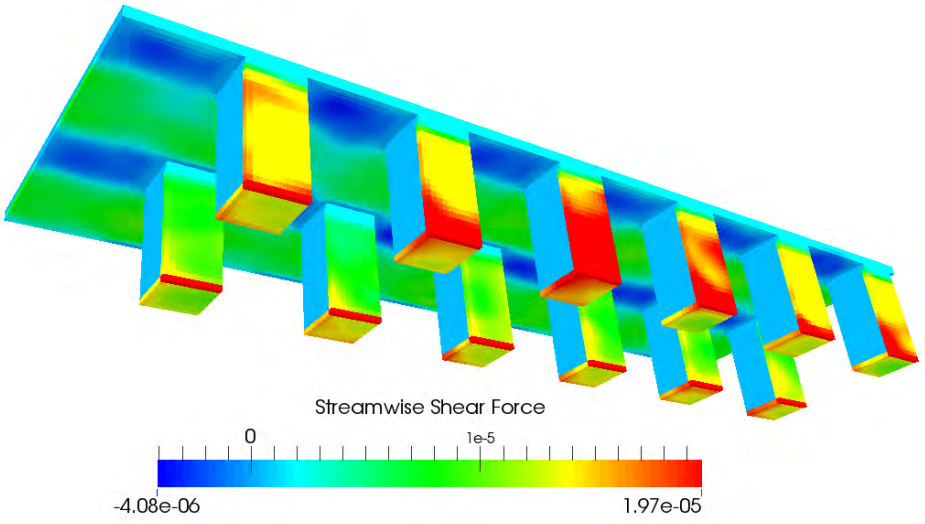

(a) Rough Geometry

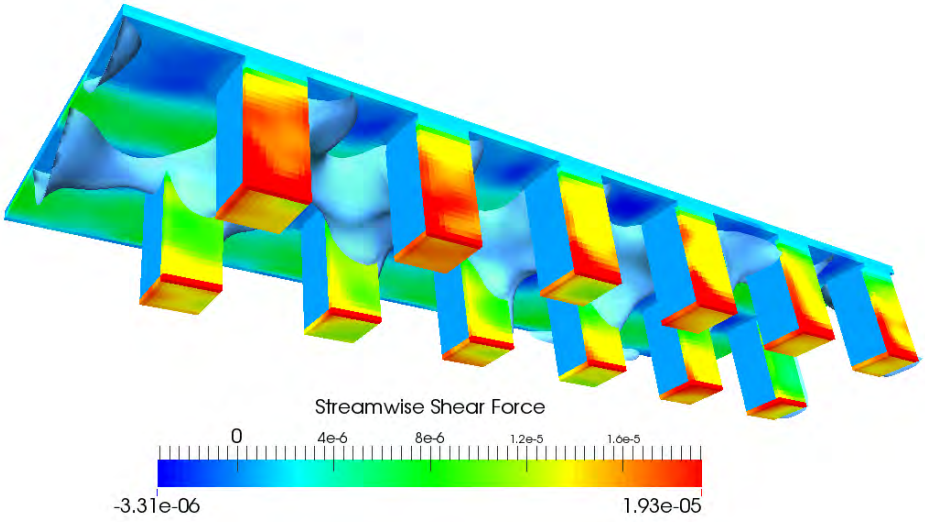

(b) Hydrophobic Geometry.
The air-water interface is indicated by the translucent blue surface.

Figure 8.6: Shear force and free-surface for 10/20 aligned post surface at $Re_\tau = 590$. As was the case with the previous posts geometries, the air layer has again been removed causing the surfaces to act very similarly.

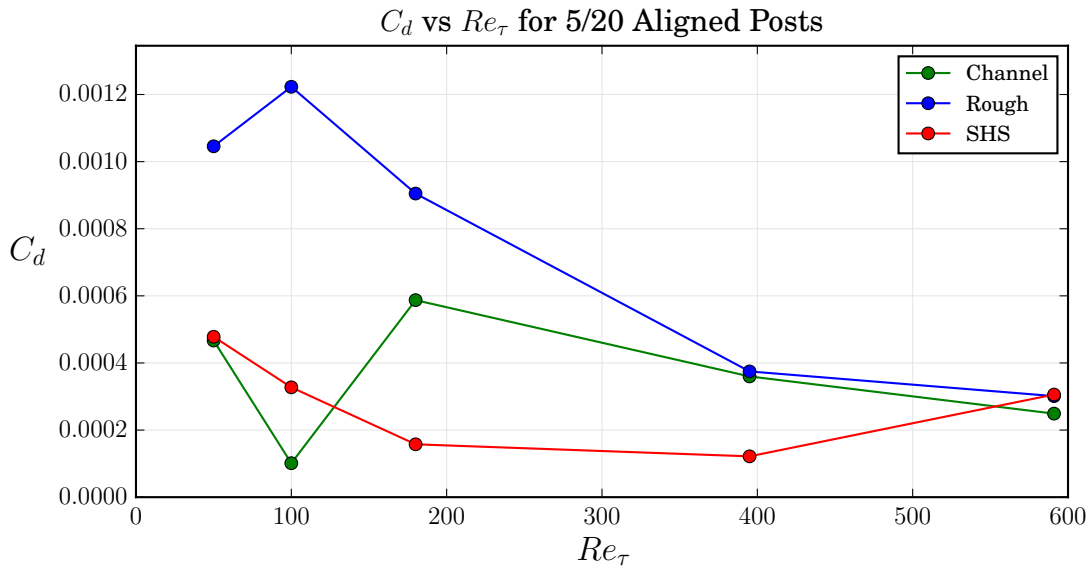

(a) Coefficient of drag (C_d).

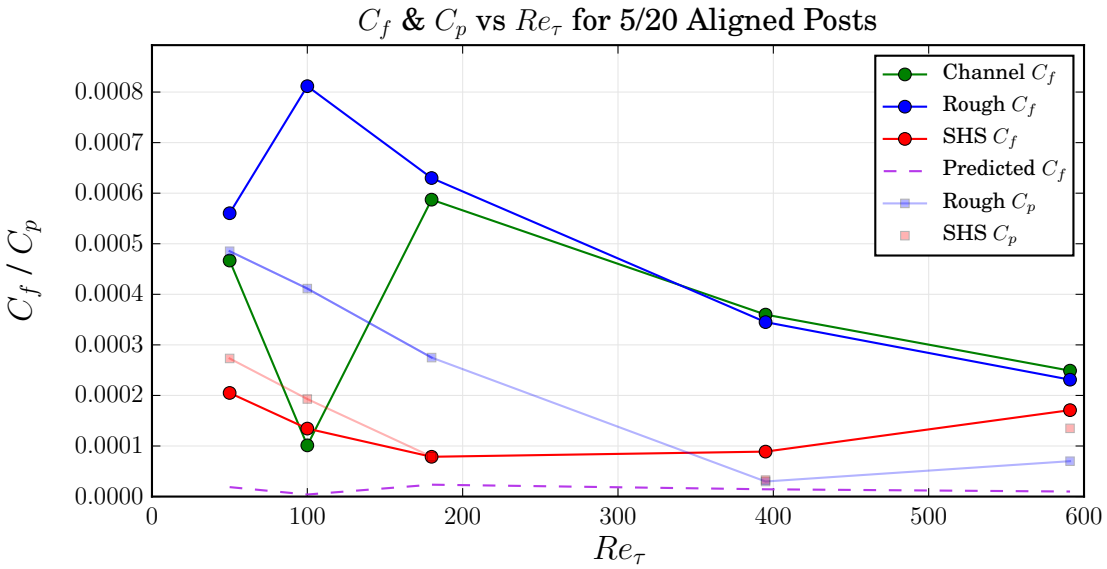

(b) Co-efficients of friction (C_f) and pressure (C_p).

Figure 8.7: Co-efficients of friction and pressure vs Reynolds number for 5/20 aligned posts geometry

8.2 5/20 Aligned Posts

8.2.1 Laminar and Transitional Regimes

The results shown in Figure 8.7 for the 5/20 surface are again similar to those already seen and have most in common with the 10/20 surface just shown. The rough surface has increased in drag between $Re_\tau = 50$ and $Re_\tau = 100$, again due to the expanded gaps between the posts allowing higher velocity flow closer to the surface. Interestingly, as was also the case in the 10/20 rough geometry, while the frictional drag has increased, the pressure drag co-efficient has dropped between $Re_\tau = 50$ and $Re_\tau = 100$. Both the increased friction and the decreased pressure can be better explained by looking at the velocity vectors of the flow over the surface in Figure 8.8. This show that at the lower Reynolds number, the fluid forms vortices in the gaps between the posts. This results in the fluid being directed towards the fronts of the posts, increasing the pressure forces whilst minimising the streamwise component of the velocity flowing past the posts, leading to a decrease in shear drag. At $Re_\tau = 100$, the fluid instead flows across the tops of the posts, reversing the situation with higher shear forces and lower pressure drags due to reduced impact between the fluid and the wall. The hydrophobic surface follows the same trend as has previously been seen with total drag decreasing throughout the laminar and transitional regimes with a significant drag reduction of 63% over the smooth surface observed at $Re_\tau = 180$.

The shear distribution, shown as Figure 8.9, is also similar to that which has previously been shown with the air-water interface, again minimising the shear on the sides of the posts and the top of the channel as compared with the rough surface.

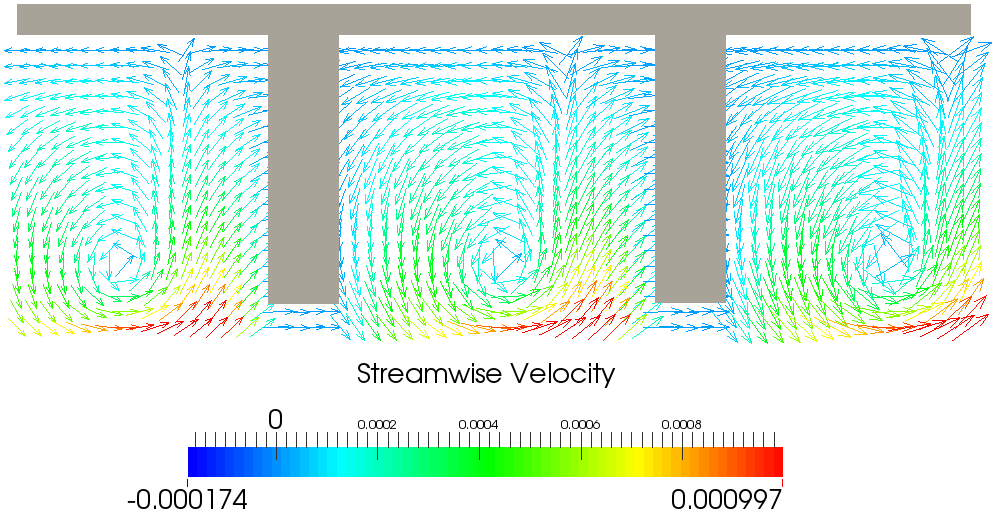

(a) $Re_\tau = 50$

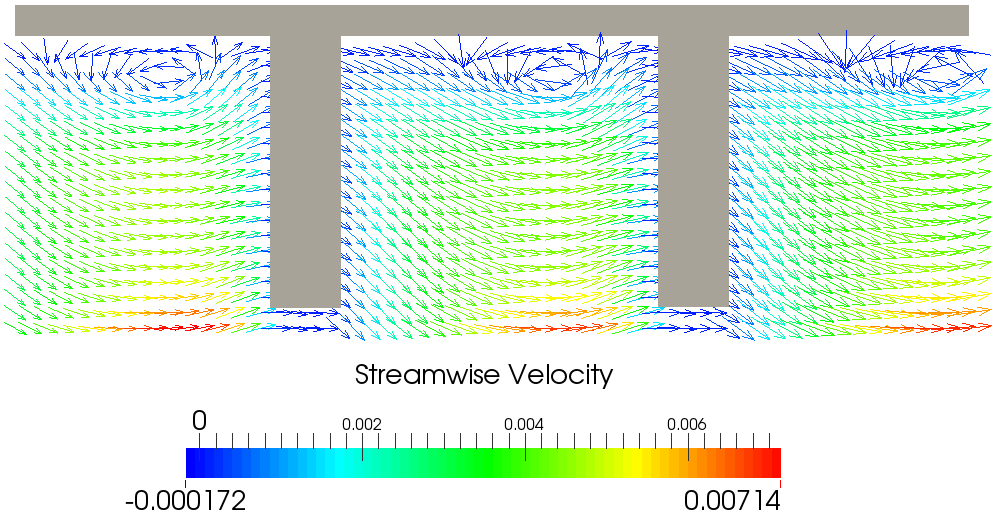

(b) $Re_\tau = 100$

Figure 8.8: Velocity vectors in streamwise direction for rough 5/20 geometry. The $Re_\tau = 50$ case exhibits large vortices in the gaps between posts, whereas the $Re_\tau = 100$ case has small vortices against the top wall and relatively straight flow past the posts leading to a decrease in pressure drag but an increase in frictional drag in the streamwise direction. The vortices against the wall in the $Re_\tau = 100$ case are again a feature of the three-dimensional flow around the posts.

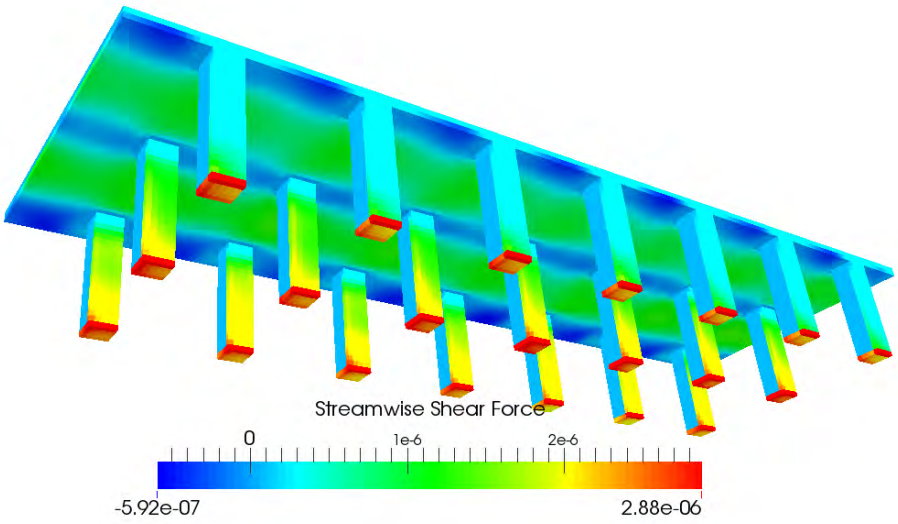

(a) Rough Geometry

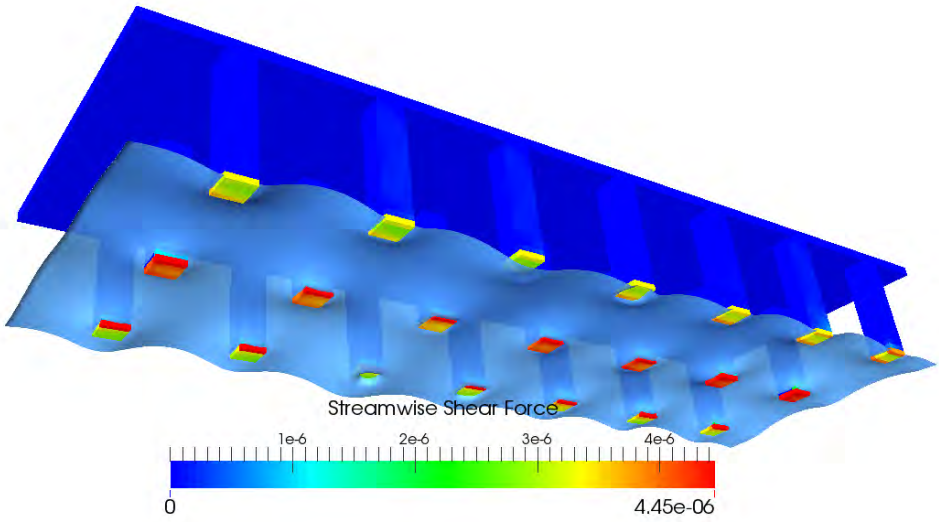

(b) Hydrophobic Geometry.
The air-water interface is indicated by the translucent blue surface.

Figure 8.9: Shear force on 5/20 aligned post surface at $Re_\tau = 180$.

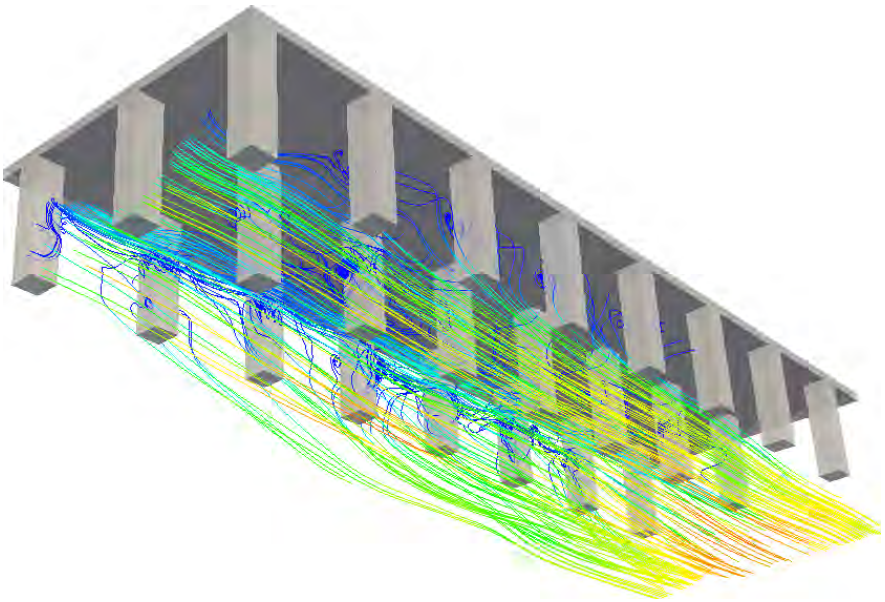

(a) Isometric view.

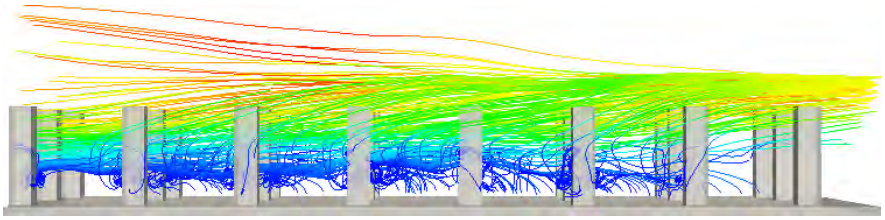

(b) Side view.

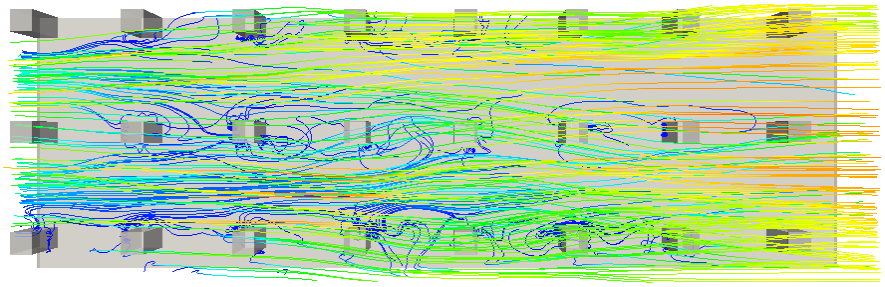

(c) Top view.

Figure 8.10: Three-dimensional streamlines flowing between and around the posts at $Re_\tau = 180$ for the rough surface. The side view shows the vortices that form behind the posts, while the top view gives an indication of both the streamwise and spanwise flow between the posts.

8.2.2 Turbulent Regime

The turbulent flow results of the hydrophobic 5/20 posts surface conform to the pattern shown by all of the other surfaces, with a reduction in drag exhibited at between $Re_\tau = 180$ and $Re_\tau = 395$, followed by a convergence with the rough surface result at $Re_\tau = 590$. As was the case with the other post geometries, the convergence is due to the depletion of the air layer surrounding the posts, a process which begins to occur when the vertical forces acting on the interface are greater than the surface tension supporting the interface can withstand.

The drag values for the rough surface converge with the smooth channel results at $Re_\tau = 395$ and are also relatively close at $Re_\tau = 590$, however as will be further discussed in Chapter 10, appear to be artificially low compared to the values they should take.

A further key point to note is the minimal spanwise flow that occurs on the geometries with the increased posts spacing. Figure 8.10 shows streamlines of the flow over and around the 5/20 geometry for the rough surface. In contrast to the streamlines showed in Section 7.1, there is significantly less flow in the spanwise direction observed with the increased post spacing.

8.3 Summary

The additional geometries tested have again shown substantial reductions in drag in both the laminar and low Reynolds number turbulent flows compared to the rough surface. As was the case with the posts in the previous chapter, at the highest tested Reynolds number, the air layer against the surface was depleted, causing the surface to act almost identically to the rough surface.

The results of the rough surface were also similar to previous tests with the notable exception of the $Re_\tau = 100$ case. For both the additional geometries tested, a large increase in the drag co-efficient was exhibited at $Re_\tau = 100$. This was shown to be due to the increased spacing size between the posts reducing the retardation of the fluid velocity, corresponding to increased shear and pressure forces.

The drag reduction values for both of the additional surfaces can be seen in Table 8.1.

Table 8.1: Summary of drag reduction of rough and hydrophobic channels as a percentage of drag on the smooth channel for the 10/20 posts and 5/20 posts surfaces. +ve values indicates an increase in drag and −ve values indicate a reduction in drag.

10/20 Posts

Re_τ	Rough	SHS
50	+ 124.01	+ 2.42
100	+ 1107.94	+ 223.34
180	+ 54.10	− 73.16
395	+ 4.14	− 73.16
590	+ 20.95	+ 22.81

5/20 Posts

Re_τ	Rough	SHS
50	+ 205.57	+ 148.62
100	+ 1625.92	+ 144.83
180	+ 111.51	− 63.86
395	+ 53.22	− 56.31
590	+ 19.42	+ 20.82

Chapter 9

Computation Results 4: Velocity Profile Analysis

In order to further validate and add credence to the results presented thus far, some additional analysis of the simulations conducted in Chapters 6 and 7 has been undertaken. This analysis centres on the flow profiles through the channel, and the additional data and results that can be extracted from these profiles.

9.1 Theory

As was discussed in Chapter 2 the study of how fluid flows has been keenly researched over a long period of time. Some of the major advancements were made by Osborne Reynolds, after whom the Reynolds number was named. His studies lead to the concepts of laminar and turbulent flows, and the differences between them. These differences are clear when looking at the profile of the velocity of fluid flowing between parallel plates, as is shown in Figure 9.1, with the laminar profile being parabolic, and the turbulent profile taking more of a power series shape.

These profiles are well known however are not always observed. In cases with asymmetric roughness on the walls, as researched by Hanjalić and Launder [52], the peak of the velocity profile moves away from the roughened surface and towards the smoother surface, as can be seen in Figure 9.2. This is due to the

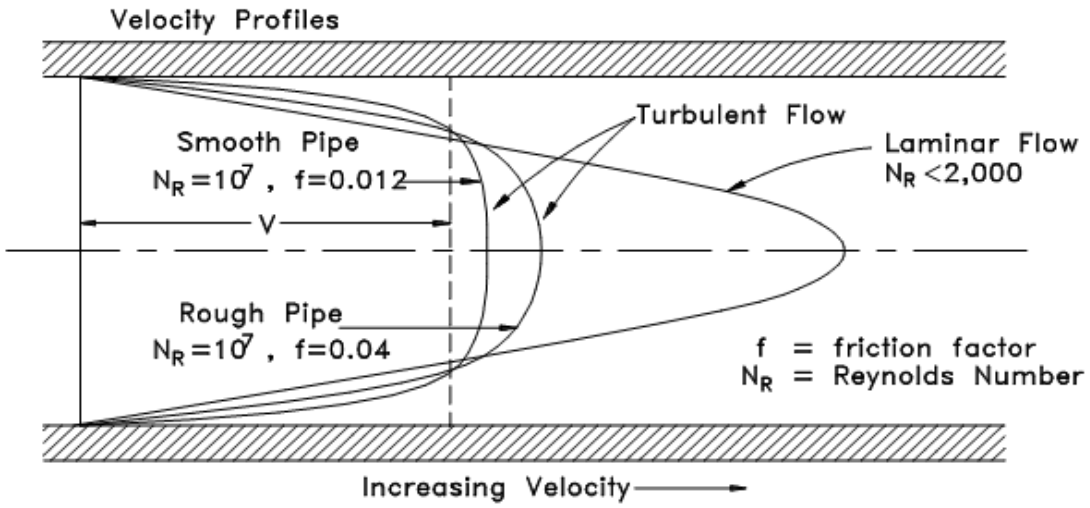

Figure 9.1: Velocity profiles for laminar and tubulent flow in rough and smooth pipes. [51]

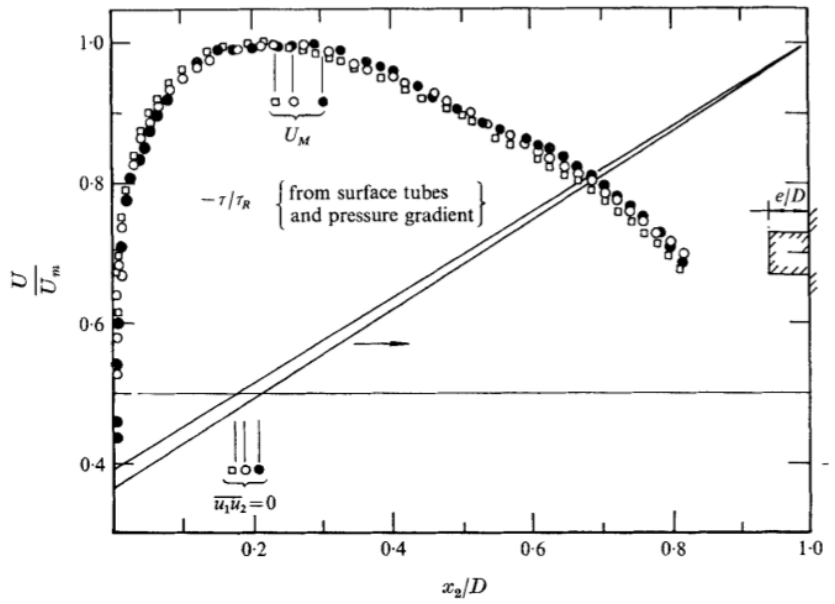

Figure 9.2: Velocity profiles for fully turbulent flow in an asymmetric channel. The right hand side of the channel was roughened causing the U_{max} point to move towards the smoother wall.

•, $Re = 18700$; ∘, $Re = 36400$; □, $Re = 56000$. [52]

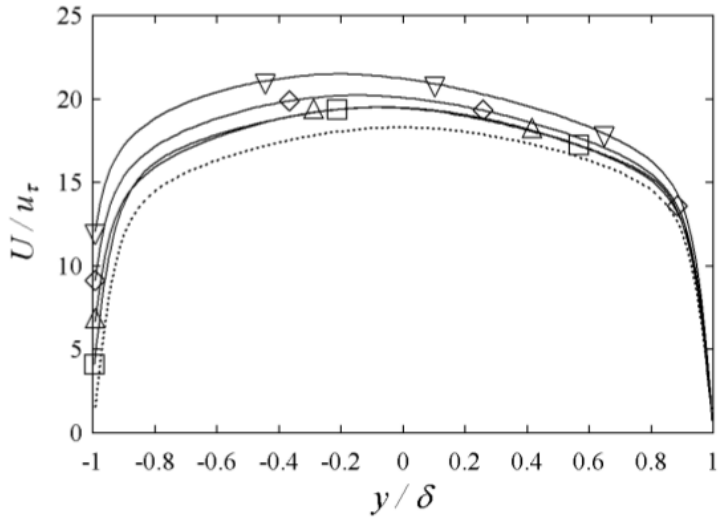

Figure 9.3: Velocity profiles for fully turbulent flow in a channel where the left wall features alternating slip / no slip boundaries. The different lines represent different ratios of slip / no-slip area with the the line marked by $\bigtriangledown$ having the greatest ratio. The dotted line indicates the velocity profile for a typical channel. In each case it can again be seen that the peak of the velcocity profile has moved towards the side of the channel with the lower drag. [83]

rough side having a higher drag and hence causing the fluid to slow more than it does on the smooth side of the channel.

A similar result was also shown by Martell [83] in his DNS analysis of super hydrophobic surfaces. By modelling the surface as alternating slip and no-slip boundaries, Martell reduced the drag on one wall of the channel, leading to the peak velocity of the flow moving away from the smooth side of the channel and towards the side of the channel with a slip boundary condition. This is illustrated in Figure 9.3.

9.2 Results

The velocity profiles extracted from the simulations in this work show a similar pattern. As was discussed in Chapters 4 and 5, the implemented lattice Boltzmanm code was unable to provide a difference in density or significant viscosity ratio between the two fluids being simulated. This meant that in each

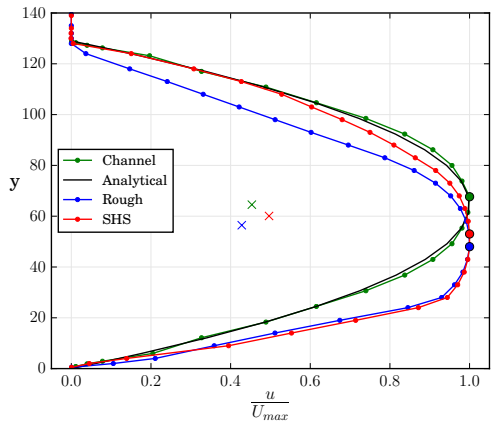

(a) Velocity profiles at $Re_\tau = 50$

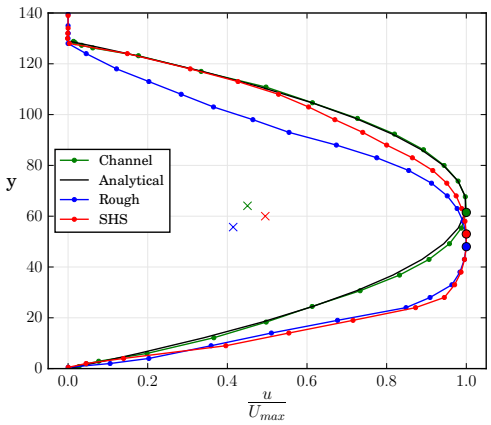

(b) Velocity profiles at $Re_\tau = 100$

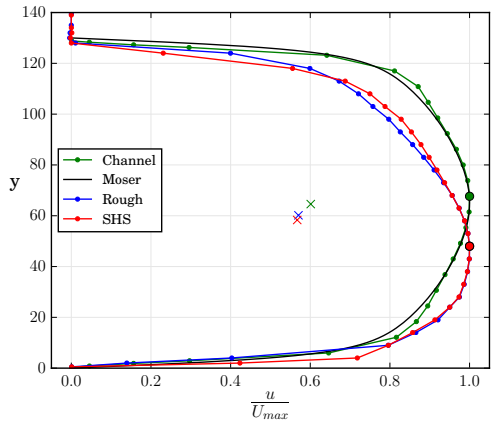

(c) Velocity profiles at $Re_\tau = 180$

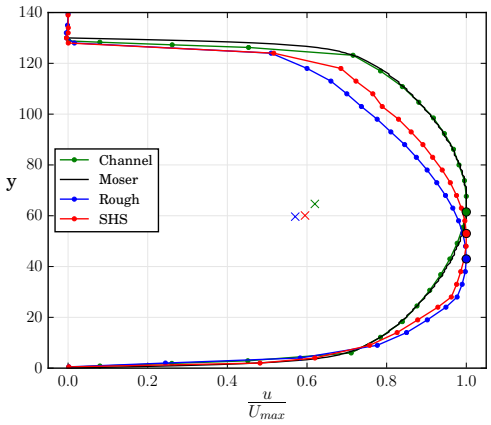

(d) Velocity profiles at $Re_\tau = 395$

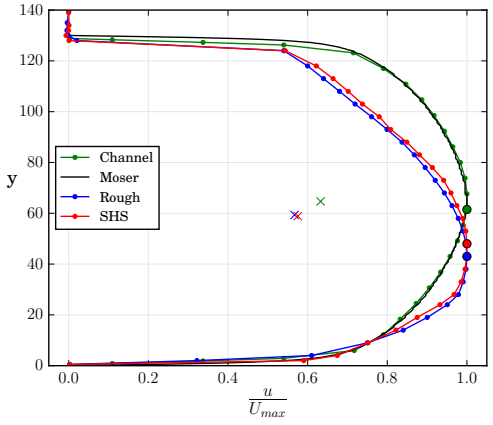

(e) Velocity profiles at $Re_\tau = 590$

Figure 9.4: Velocity profiles from the smooth channel, rough, and hydrophobic surfaces. The velocities have all been normalised by the U_{max} value for each case in order to compare the shape of the profiles and the location of the U_{max} point.

case, the total drag of both the rough surface and hydrophobic surface was almost identical, and in both cases, higher than the drag on the smooth side of the channel. The velocity profiles confirm this, as the peak of the profile in each case is shifted towards the smooth side of the channel, indicating that it has the lower drag. Notwithstanding this, by comparing the locations of the peaks of the velocity profiles for the rough and hydrophobic surfaces, an indication of which of the micro featured surfaces has a lower drag is possible.

The profiles were found by averaging both temporal and spatial results in order to get a representative profile from across the entirety of the surface. Each of the plots compare the smooth channel, the rough surface and the hydrophobic surfaces, each of which have been normalised by their maximum velocities to allow direct comparison between the different surfaces. In each case the profiles have also been compared to either the analytical result for flow through a channel in the case of the laminar flows, or the results from Moser *et. al.* [90] for the turbulent cases. The maximum velocity of each velocity profile is identified by a circle ($\circ$).

Additionally, by studying the position of the moment of area of the velocity profile further information becomes available. The moments of area were found by taking moments about the X and Y axes, as described by Equation 9.1.

$$\mathrm{Mom}_x = \frac{\sum(U \times y)}{\sum U} \qquad \mathrm{Mom}_y = \frac{\sum(U \times y)}{\sum y} \tag{9.1}$$

The moment about the Y axis corresponds to a normalised volumetric flow rate through the channel ($\dot{V} = AU$). As will be shown, with the velocities normalised by peak velocity, there are times in which the hydrophobic surface appears to give a higher flow rate than the other surfaces. The profile area moments are identified by a cross ($\times$).

9.2.1 Spanwise Grooves

The velocity profiles for the spanwise grooved geometries can be seen in Figure 9.4. With the micro-featured side wall at the top of the domain it is immediately obvious that the peaks of the velocity profiles for the rough and hydrophobic surfaces have moved towards the smooth side of the channel. This result is consistent with the results presented in Section 5.3 showing that with the drag

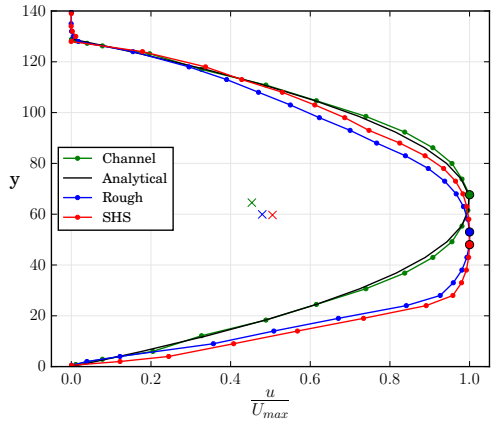

(a) Velocity profiles at $Re_\tau = 50$

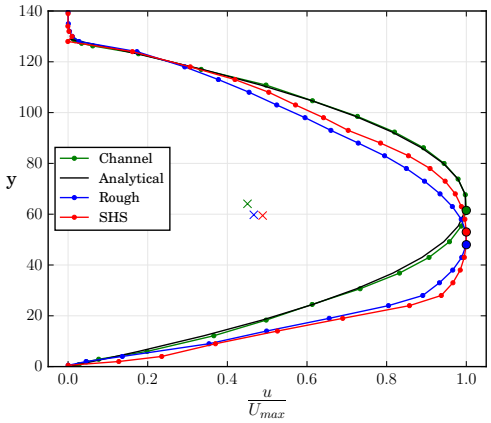

(b) Velocity profiles at $Re_\tau = 100$

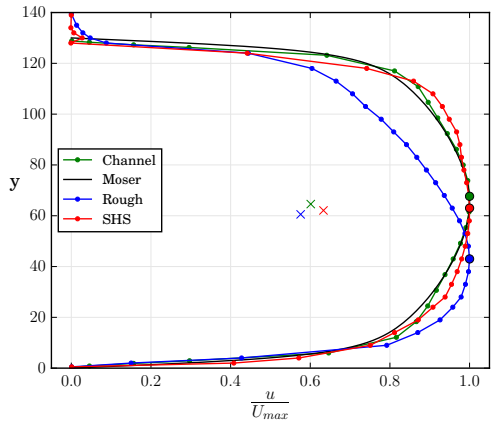

(c) Velocity profiles at $Re_\tau = 180$

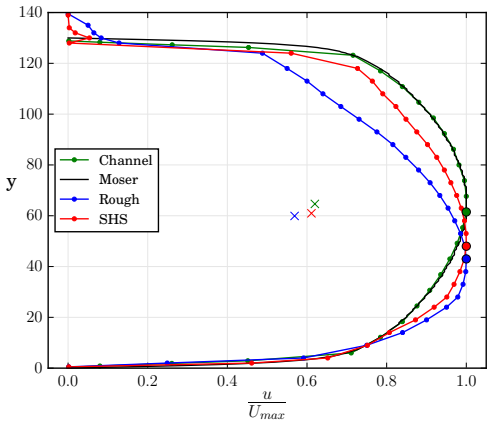

(d) Velocity profiles at $Re_\tau = 395$

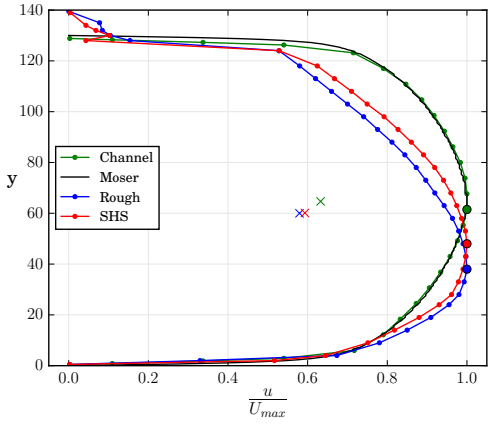

(e) Velocity profiles at $Re_\tau = 590$

Figure 9.5: Velocity profiles from the smooth channel, rough, and hydrophobic surfaces. The velocities have all been normalised by the U_{max} value for each case in order to compare the shape of the profiles and the location of the U_{max} point.

from the "air" included, the total drag on both the rough and hydrophobic surfaces to be almost equal, and higher than that of the smooth wall. The slight reduction in viscosity has had an effect however with the hydrophobic surface exhibiting a slightly lower drag than that of the rough surface. This is indicated by the peak of the hydrophobic profile being closer to the micro-featured wall than it is for the rough surface profile.

Also of interest in these profiles is the moment of area of the profile, marked by the cross ($\times$). This is giving an indication of the volumetric flow rate, and the effective centre of the flow. As would be expected, in the smooth channel cases, the centre of the flow corresponds to the same y value as the peak velocity.

In the laminar flow cases, $Re_\tau = 50$ and $Re_\tau = 100$, the flow rate through the hydrophobic channel appears significantly greater than it does through the rough channel, once again indicating that the drag from the hydrophobic surface is lower than that from the rough surface. This is also demonstrated by the difference in the shape of the profile between the rough and hydrophobic surfaces. In the region near the micro-featured wall the hydrophobic channel profile is identical to that of the smooth channel. The velocity over the rough surface in this region is noticeably lower.

In the turbulent regime, the profiles for the rough and hydrophobic surfaces are more similar with only slight variations between them. This is confirmed by the locations of the moment of area for the two channels being very close together in each turbulent case. In the $Re_\tau = 180$ case, the peak velocities for the micro featured surfaces lie directly on top of each other, meaning no drag reduction should be observed. In both of the higher turbulent cases, the rough surface again appears to have a higher drag as the peak of the profile is closer to the smooth wall.

9.2.2 Streamwise Grooves

The velocity profiles for the streamwise grooved surfaces show different results to those just described. As can be seen in Figure 9.5a, the peak of the rough surface profile is closer to the rough wall than the hydrophobic surface peak. This result is directly contrasted with the flow rate indicator which shows the hydrophobic surface allowing a greater flow rate through the channel. This

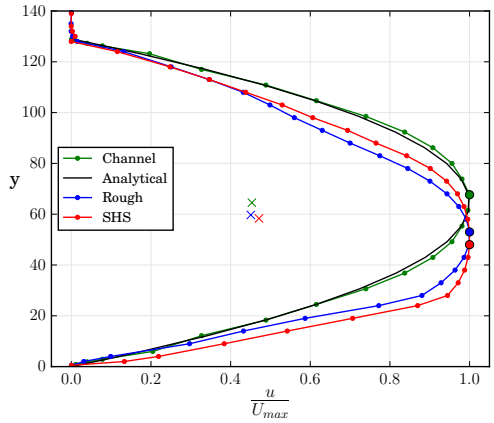

(a) Velocity profiles at $Re_\tau = 50$

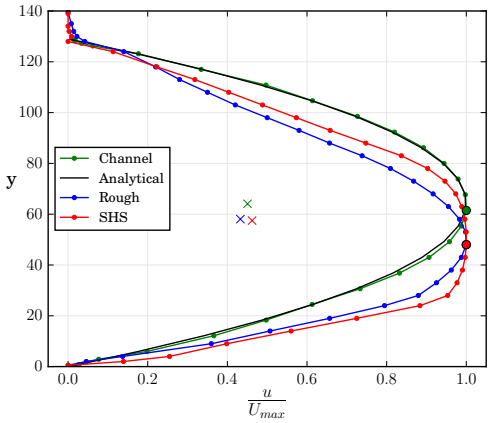

(b) Velocity profiles at $Re_\tau = 100$

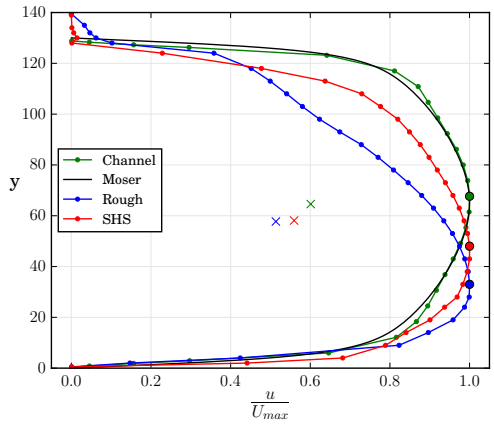

(c) Velocity profiles at $Re_\tau = 180$

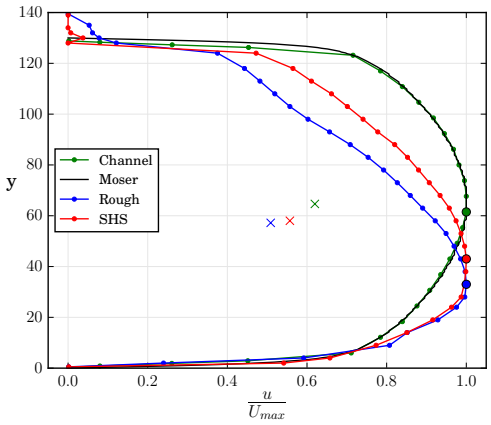

(d) Velocity profiles at $Re_\tau = 395$

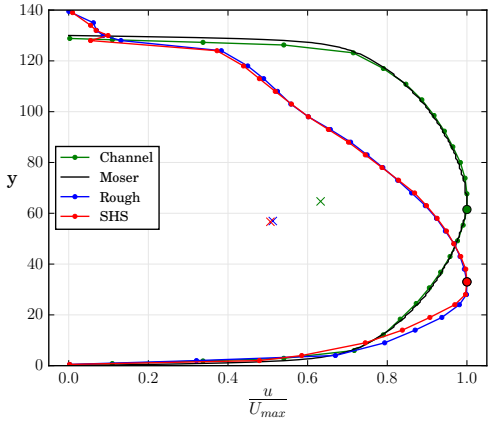

(e) Velocity profiles at $Re_\tau = 590$

Figure 9.6: Velocity profiles from the smooth channel, rough, and hydrophobic surfaces. The velocities have all been normalised by the U_{max} value for each case in order to compare the shape of the profiles and the location of the U_{max} point.

apparent contradiction can be explained by the shape of the hydrophobic profile. With the profile appearing almost flat across the top of the curve, the difference in velocities at the rough surface peak is minimal, with the hydrophobic velocity at that point being 99.99% of the rough surface value.

As can also be seen in Figure 9.5, the profiles for the laminar cases are quite similar. This confirms the results presented in Chapter 6 which indicated that there was minimal drag difference between the rough and hydrophobic streamwise grooved surfaces in low speed flow. Furthermore, the results in Chapter 6 went on to indicate that drag from the streamwise grooved hydrophobic surface were similar to those of the smooth channel in turbulent flow. Looking at the turbulent regime results in Figure 9.5 does nothing to dissuade this idea, with the profile of the flow over the hydrophobic surface quite similar to that of the smooth channel and the results presented by Moser, especially at $Re_\tau = 180$. As the Reynolds number increases from 180 to 590, the profile transitions from that similar to the smooth channel to one more like the rough surface profile.

In each of the turbulent cases, the peak velocities also indicate that the hydrophobic surface should have a lower drag than the rough surface. This is the same result as was suggested in previous chapters which provides further credence of the results presented.

One final point to note is the non-zero velocities within the grooves. Unlike the spanwise grooves cases where the average velocities within the grooves was zero (or very close too), the velocity in the streamwise grooves is noticeable.

9.2.3 Aligned Posts

The aligned posts results, shown in Figure 9.6, are quite similar to those of the streamwise grooves just discussed. Like the streamwise grooves, the laminar velocity profiles for both the rough and hydrophobic surfaces are of similar shape, and based on the location of the peak velocity, again appear to show that the rough surface has less drag than the hydrophobic. The moment of area comparison once again contradicts this with results more in line with those shown in Chapter 7 of the hydrophobic surface having the lower drag of the two micro featured surfaces.

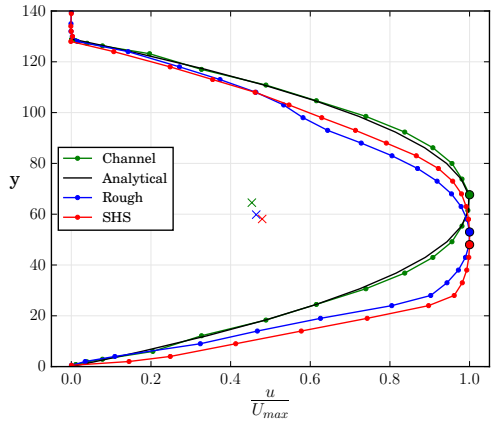

(a) Velocity profiles at $Re_\tau = 50$

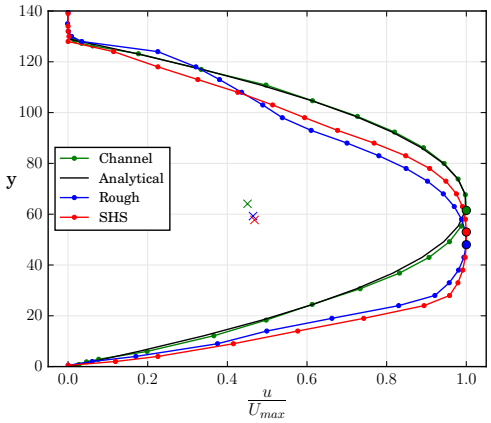

(b) Velocity profiles at $Re_\tau = 100$

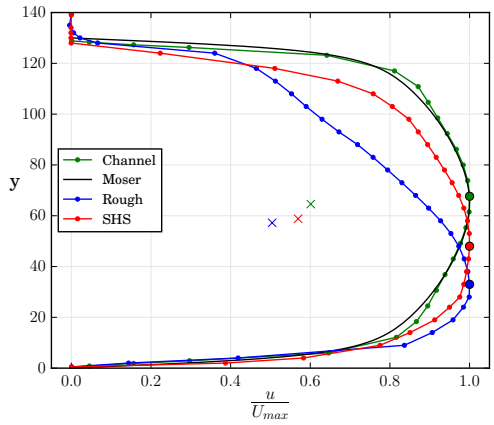

(c) Velocity profiles at $Re_\tau = 180$

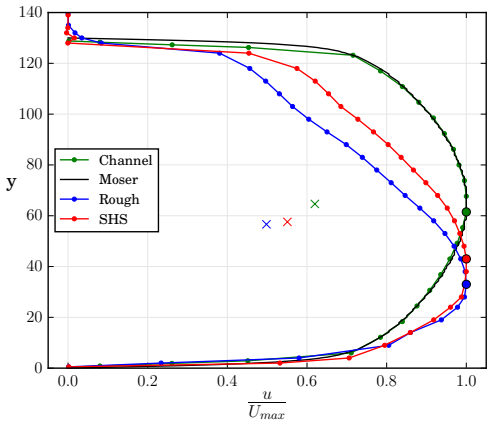

(d) Velocity profiles at $Re_\tau = 395$

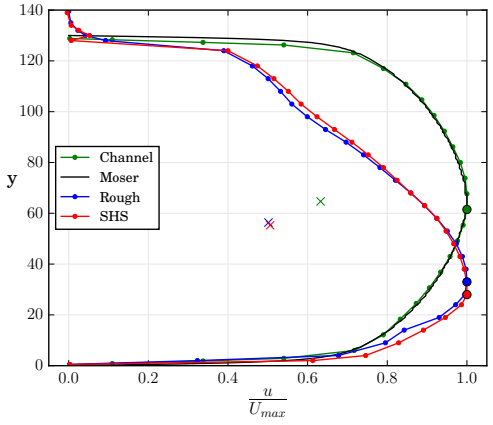

(e) Velocity profiles at $Re_\tau = 590$

Figure 9.7: Velocity profiles from the smooth channel, rough, and hydrophobic surfaces. The velocities have all been normalised by the U_{max} value for each case in order to compare the shape of the profiles and the location of the U_{max} point.

Interestingly, the velocity of fluid within the posts (i.e. above y=130) is quite different between the two surface types in the $Re_\tau = 180$ and $Re_\tau = 395$ cases. The rough surfaces feature higher average velocities in this region than the hydrophobic implying that the free surface, and more specifically, the surface tension of the free surface is acting to insulate the "air" from the fluid in the bulk of the channel. This further reinforces the results shown in Chapter 7.

The turbulent results are also resemblant of those seen in the streamwise grooves case with the hydrophobic profile transitioning from a shape similar to that of the smooth channel at $Re_\tau = 180$ to being identical to that of the rough surface at $Re_\tau = 590$. This again confirms the result shown previously with the hydrophobic surface appearing to have lower drag at $Re_\tau = 180$ and 395 and an almost identical drag at $Re_\tau = 590$.

9.2.4 Offset Posts

The velocity profiles shown in Figure 9.7 for the offset posts surface unsurprisingly are again similar to those already shown for the other surfaces. The laminar regime results show an almost parabolic velocity profile that is offset slightly towards the smooth side of the channel. For the case at $Re_\tau = 50$ the velocity peak again gives a different result to that of the volumteric flow rate analysis. The $Re_\tau = 100$ case shows the rough surface having an abnormally high velocity in the near wall region, a result which has not been seen in any of the other cases. As was shown in Section 7.2, the drag on the rough surface at this Reynolds number appeared higher than expected. This increased near wall velocity goes some way to explaining why the drag is higher and it results in increases to both the pressure and shear drag components.

The turbulent cases are almost identical to those of the aligned posts with the hydrophobic surface appearing to have less drag than the rough surface by both the velocity peak and flow rate analysis methods. The profile shape can once more be seen to transition from the roughly symmetrical power series shape of the smooth channel to the profile expected for turbulent flow through an asymmetric channel.

The results presented in Chapter 7 showed that the rough and hydrophobic surfaces performed almost identically at $Re_\tau = 590$. This result is again confirmed

by this analysis with the profiles with the profile shapes, location of velocity peaks, and locations of the moments of area all being virtually identical.

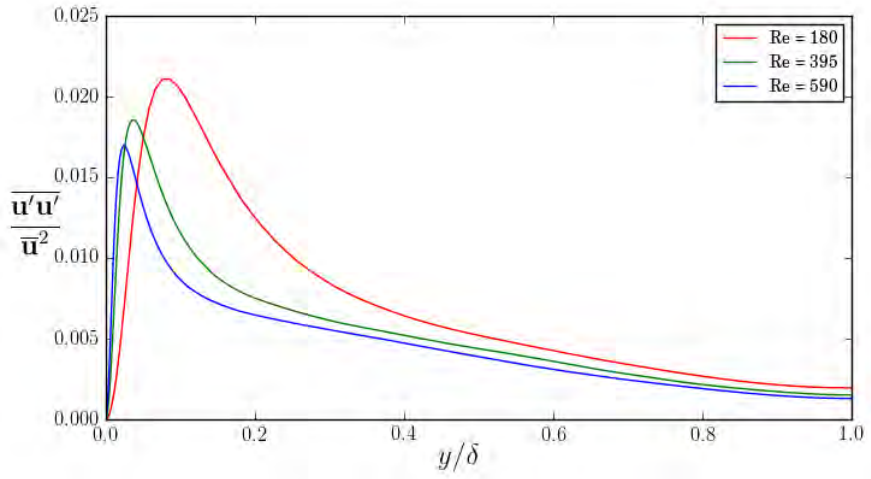

Figure 9.8: Reynolds stresses for channel flows at $Re_\tau = 180,\ 395$ and 590. As can be seen, as the Reynolds number increases the profile becomes pointier, and the peak moves closer to the wall. [90]

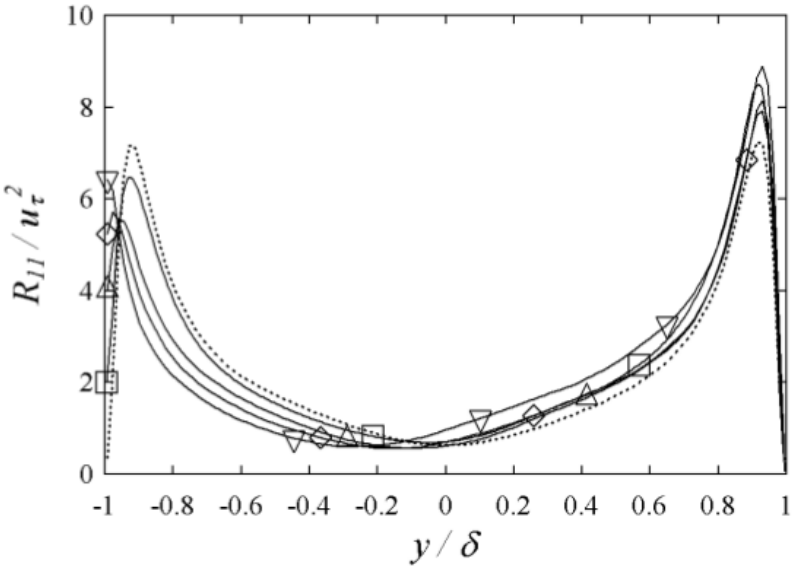

Figure 9.9: Reynolds stresses for a channel featuring alternating slip / no-slip walls at $Re_\tau = 180$. It can be seen that the peaks are lower on the side of the channel with the slip walls. The different lines correspond to different ratio's of slip / no slip area. [84]

9.3 Reynolds Stresses

One final method of analysis has been used to compare the drag on each of the surfaces. By comparing the peaks and shapes of the Reynolds stresses, a further indication of which surface has the lowest drag can be gained.

In order to understand Reynolds stresses, the concept of Reynolds decomposition must first be introduced. In turbulent flow, the velocity of the fluid at any point and time is given by

$$\mathbf{u}(x,t) = \overline{\mathbf{u}(x,t)} + \mathbf{u}'(x,t) \tag{9.2}$$

where $\overline{\mathbf{u}(x,t)}$ is the mean velocity and $\mathbf{u}'(x,t)$ is the fluctuation component of the velocity. The Reynolds stresses are defined as the temporal average of these fluctuating components, as shown in Equation 9.3.

$$\tau'_{ij} = \rho\overline{\mathbf{u}'_i\mathbf{u}'_j} \tag{9.3}$$

Reynolds stresses are referred to as stresses as they transfer momentum in the fluid by the fluctuating velocity field. They are accounted for in a similar way to that of the viscous stresses which transfer momentum at a molecular level; or stresses due to the pressure field. This is better shown by looking at the Reynolds momentum equation, shown in Equation 9.4. This equation is a slightly different form of that shown previously in Section 2.1.2.4 however is otherwise equivalent.

$$\rho\frac{\partial\mathbf{u}}{\partial t} = \frac{\partial}{\partial x_i}\left[\mu\left(\frac{\partial\mathbf{u}_i}{\partial x_j} + \frac{\partial\mathbf{u}_j}{\partial x_i}\right) - \overline{P}\delta_{ij} - \rho\overline{\mathbf{u}'_i\mathbf{u}'_j}\right] \tag{9.4}$$

The terms inside the square brackets represents the stresses acting on the fluid with the term beginning with μ showing the viscous stresses, the $\overline{P}\delta_{ij}$ showing the isotropic stresses from the pressure field, and the $\rho\overline{\mathbf{u}'_i\mathbf{u}'_j}$ being the Reynolds stresses. Further and more detailed descriptions can be found in the textbook by Pope [100].

Figure 9.8 shows the profiles of Reynolds stresses in a smooth channel at Reynolds numbers of 180, 395 and 590. In each case, the Reynolds stresses have been divided by the average channel velocity squared so that the plots are of

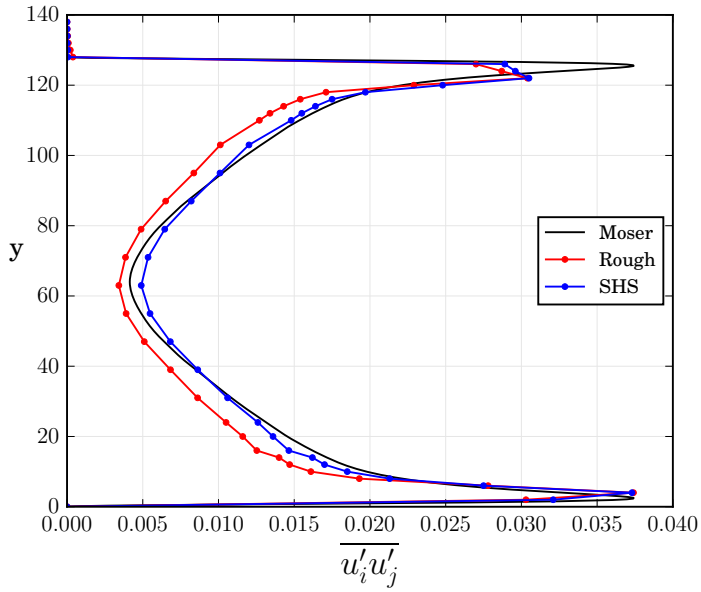

Figure 9.10: Reynolds stresses for the spanwise grooved geometry at $Re_\tau = 395$.

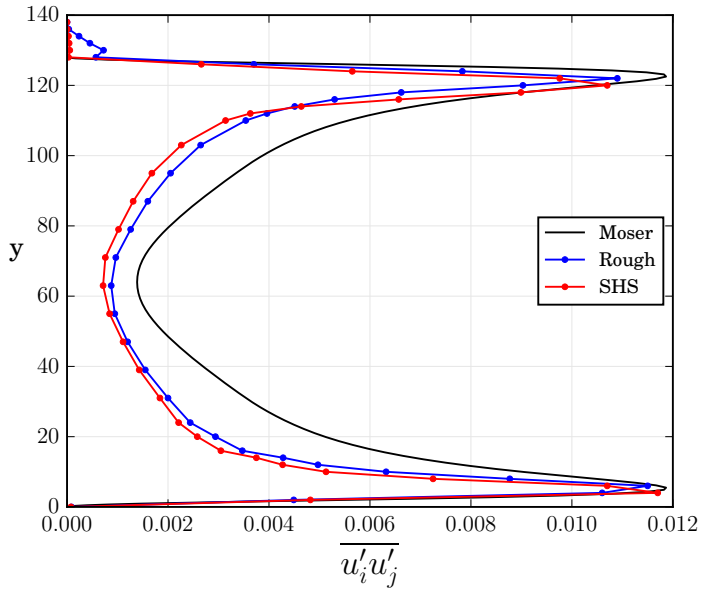

Figure 9.11: Reynolds stresses for the streamwise grooved geometry at $Re_\tau = 180$.

similar magnitude. These results were also taken from the published data of the DNS work performed by Moser *et. al.* [90].

Although Reynolds stresses for all the geometries analysed in the chapter were calculated, only a selection will be shown and discussed as like the velocity profiles, they tend to be quite similar. In order to compare the stresses due to the different surface geometries, the values have been normalised by the peak of the Reynolds stress on the smooth channel side of the domain. This then allows the peak on the micro featured side of the wall to give an indication of the relative drag of the surface. Each plot also shows the Reynolds stresses from the published results of Moser for comparison. Given Reynolds stresses only occur in turbulent flow where there is a fluctuating velocity component, there are only results for the cases where the Reynolds number is 180 or above.

Spanwise Grooves at $Re_\tau = 395$

The first case to be discussed is spanwise grooved geometry at a Reynolds number of $Re_\tau = 395$, which is illustrated in Figure 9.10. Immediately noticeable is that both the rough and hydrophobic surfaces result in a lower Reynolds stress near the wall. This is not unexpected for the hydrophobic surface based on the results of Martell shown in Figure 9.9, however may not be expected for the the rough surface. A study by Antonia and Krogstad [2] in 2000 reported that some three-dimensional roughness features reduced the fluctuating velocities so that the Reynolds stresses for a rough wall could be smaller than those over a flat surface. This finding is also consistent with some of the methods of drag minimisation discussed in the literature review in Chapter 2. It is also worth mentioning at this point that just because the Reynolds stress is lower does not mean that the surface has a lower drag as the total drag is due to the viscous, pressure and Reynolds stresses combined, as was shown in Equation 9.4.

With the exception of the peak on the micro featured side, the Reynolds stress in the channel with the rough surface matches the result by Moser quite closely. The hydrophobic surface however appears to have a lower Reynolds stress across the entirety of the channel. This would also be consistent with the results shown in Section 9.2.1 with the hydrophobic channel having a higher mass flow rate than the rough surface channel.

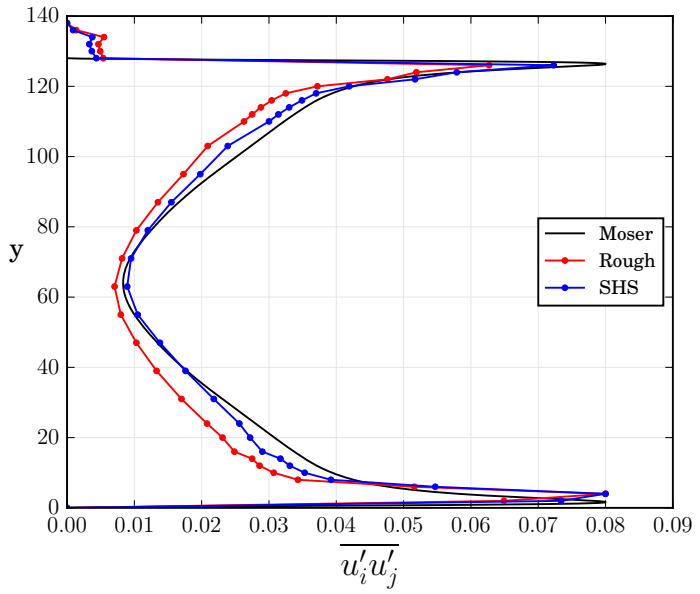

Figure 9.12: Reynolds stresses for the aligned posts geometry at $Re_\tau = 590$.

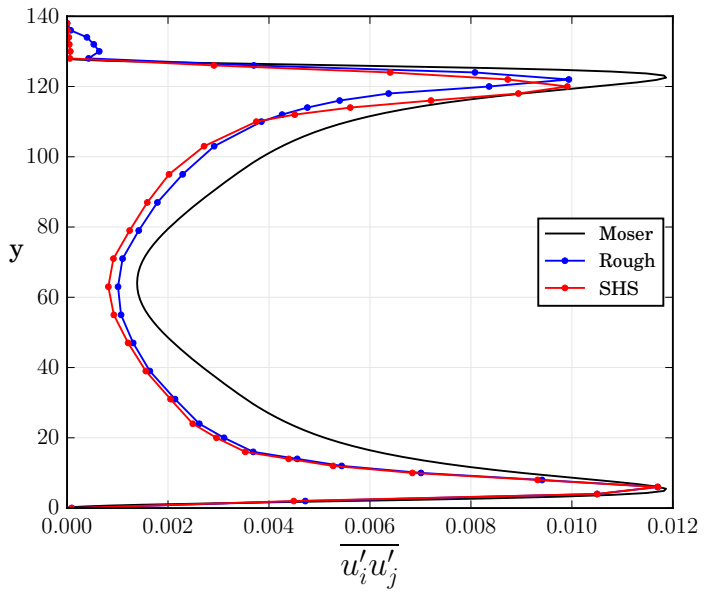

Figure 9.13: Reynolds stresses for the offset posts geometry at $Re_\tau = 180$.

Streamwise Grooves at $Re_\tau = 180$

The next case to be presented is the Reynolds stresses in flow over the streamwise grooved geometry at $Re_\tau = 180$, shown in Figure 9.11. Unlike the the profiles seen for flow over the spanwise grooves, both the rough and hydrophobic surfaces show a distinct reduction in Reynolds stresses in the centre of the channel. Again this is not unexpected based on the studies looking at drag reduction using streamwise grooved surfaces which have been shown to reduce drag. The fact that there is minimal difference between the rough and hydrophobic surface profiles for the Reynolds stresses does not mean that these surfaces are equivalent, it only means that any additional drag reduction possible needs to come from a reduction in either the viscous drag or pressure drag.

Aligned Posts at $Re_\tau = 590$

As can be seen in Figure 9.12, the aligned posts case is similar to the spanwise grooves case in that the Reynolds stresses in flow over the rough surface are quite similar to those expected in a channel. The peak of the hydrophobic profile is roughly 15% lower than that of the rough surface, and combined with the remainder of the profile through the centre of the channel being lower as well results in an overall reduction in Reynolds stress. Unlike any of the other cases presented, the Reynolds stresses on the flow between the grooves is higher in the hydrophobic case than it is for the rough surface.

Offset Posts at $Re_\tau = 180$

The final Reynolds stress case to be shown is for flow over the offset posts at $Re_\tau = 180$ and can be seen in Figure 9.13. This again is quite similar to the streamwise grooves geometry with minimal difference between the surface profiles, but a significant difference to the smooth channel profile. The peaks of both the rough and hydrophobic surface stresses are equal in magnitude, however the peak is slightly closer to the centre of the channel for the hydrophobic surface. As has been seen in all but the aligned posts case, the Reynolds stresses between the posts are again minimal.

9.4 Summary

This chapter has shown that although the fluids being modelled have the same densities and similar viscosities, the hydrophobic surface still gives some level of drag reduction as compared with the rough surface. This was indicated by the peaks of the velocity profiles for the hydrophobic surface being closer to the micro featured surface than those of the rough surface. Comparing the moments of area of the velocity profiles also indicated that the volumetric flow rate through the channel with a hydrophobic wall was also higher than that of the channel with the rough wall.

Additionally, the Reynolds stresses for the fluid flow over the hydrophobic surface are also similar to those shown for the ideal hydrophobic surface modelled as an alternating slip / no-slip boundary. In each case presented, the peak of the Reynolds stress for flow over the hydrophobic surface was equal to or less than that of the rough surface, indicating a slight reduction in Reynolds stresses over the hydrophobic surface. The peak for the hydrophobic surface has also been shifted slightly towards the centre of the channel compared with both the smooth channel results and the flow over the rough surface, an effect that can only be due to the presence of the air water interface near the hydrophobic wall.

Chapter 10

Conclusion

10.1 Summary of Results

The results presented in the previous chapters can best be summarised by comparing the drag of each of the surfaces at the same Reynolds number. This gives a clear indication of which surface exhibits the lowest drag for a given flow. Figures 10.1 to 10.5 show these results.

In each figure, two graphs are presented. The first shows the drag of each surface relative to the drag of the smooth channel as found by the wetted surface analysis performed in Chapters 6, 7 and 8. The second graph indicates the drag difference based on the velocity profile moment of area analysis undertaken in Chapter 9.

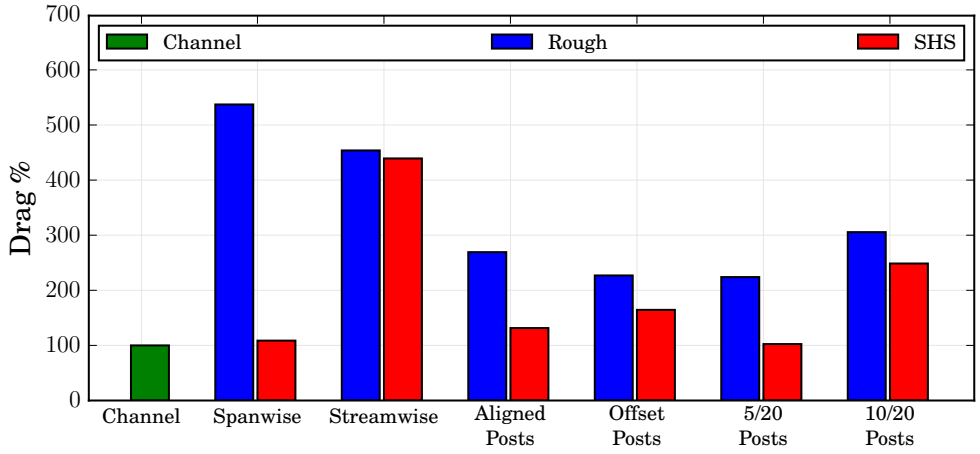

(a) Drag difference from wetted surface area analysis.

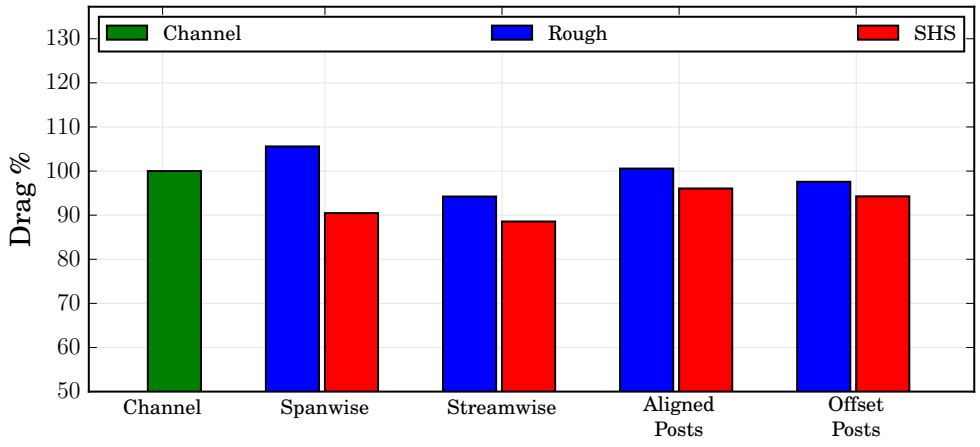

(b) Drag difference from volumetric flow rate analysis.

Figure 10.1: Comparison of drag on the surfaces at $Re_\tau = 50$ shown as a percentage of the drag of the smooth channel. Both methods of analysis show the hydrophobic surfaces have a lower drag for each geometry tested.

10.1.1 $Re_\tau = 50$ Results

Beginning with the results for the $Re_\tau = 50$ case as shown in Figure 10.1 it can be clearly seen that although the magnitudes of the differences in drag between the surfaces are different, the general pattern is the same. In each of the geometries, the hydrophobic surface exhibits a lower drag than that of the rough surface, a fact confirmed by both methods of analysis. The results are also similar in that they both identify the spanwise grooves as giving the biggest drag reduction between the rough and hydrophobic surfaces.

10.1.2 $Re_\tau = 100$ Results

The results at a Reynolds number of 100 are similar to those seen at $Re_\tau = 50$ with both methods of analysis indicating the hydrophobic surface has a lower drag than that of the rough surface, as seen in Figure 10.2. The wetted area analysis shows that the drag on the rough surfaces increases significantly for the offset posts and the cases with larger spacing between posts with the 10/20 posts rough surface showing a drag of over seventeen times that of the smooth channel.

10.1.3 $Re_\tau = 180$ Results

Figure 10.3 gives a summary of the drags of each surface at $Re_\tau = 180$. Unlike the previous cases, there is a discrepancy between the results from the different analysis methods with the wetted surface analysis indicating the spanwise grooves decrease the drag of the hydrophobic surface relative to the rough surface, while the velocity profile analysis indicates the drag will increase. Based on the study undertaken in Section 6.1.2 looking at the expected deformation of the free surface which indicated that the surface should remain non-wetted, and the general trend of the results indicating the hydrophobic surface has a lower drag than the rough surface, the drag reduction shown in Figure 10.3a is probably closer to what would be observed in reality.

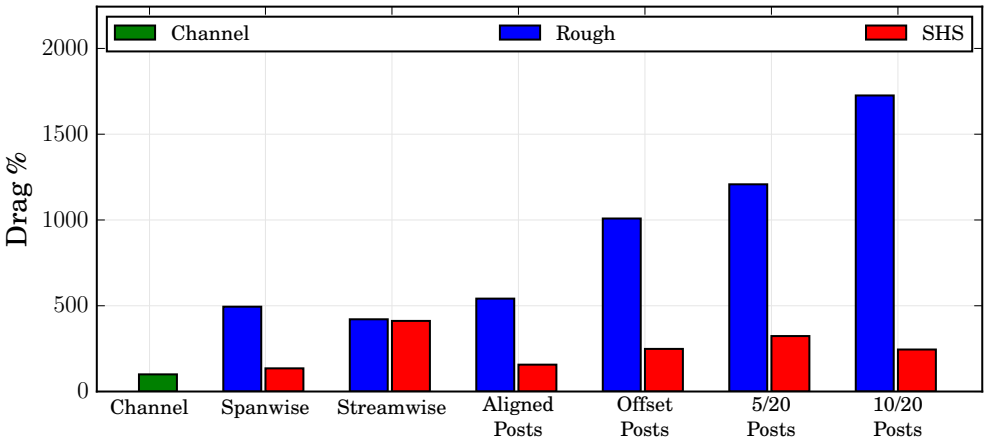

(a) Drag difference from wetted surface area analysis.

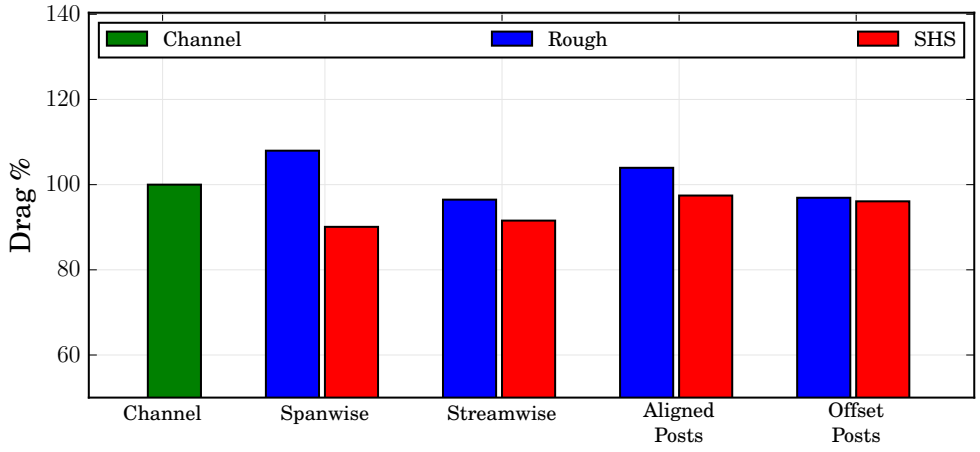

(b) Drag difference from volumetric flow rate analysis.

Figure 10.2: Comparison of drag on the surfaces at $Re_\tau = 100$. The spanwise grooved hydrophobic geometry exhibits the lowest drag. With the exception of the streamwise grooves, all of the other surfaces show a marked reduction in drag between the rough and hydrophobic surfaces.

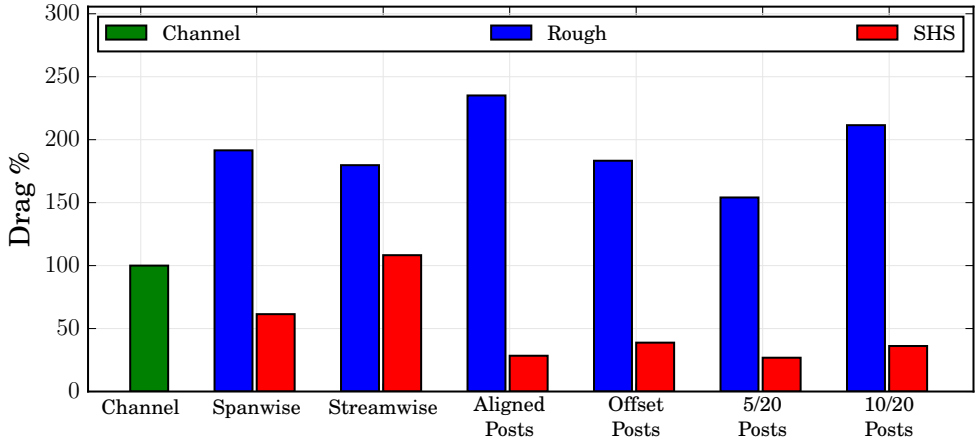

(a) Drag difference from wetted surface area analysis.

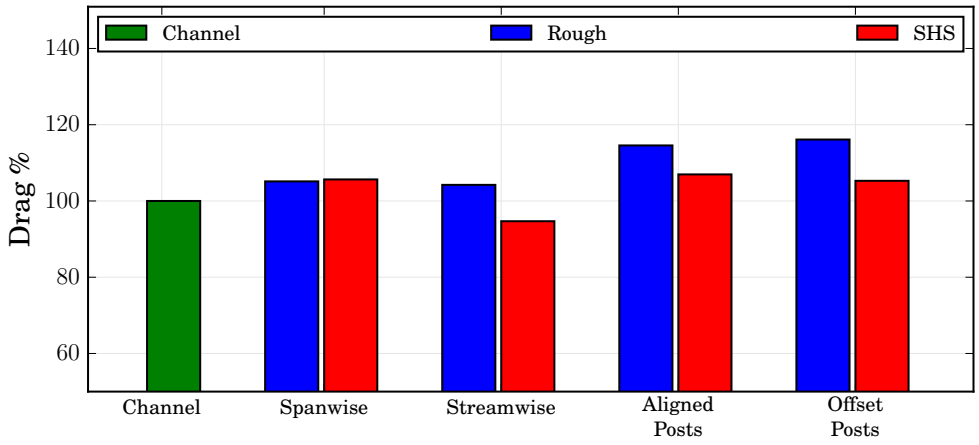

(b) Drag difference from volumetric flow rate analysis.

Figure 10.3: Comparison of Surfaces at $Re_\tau = 180$. With the flow becoming turbulent, the minimal wetted surface area of the posts results in lower drag than the grooved surfaces, a result confirmed by the velocity profile analysis.

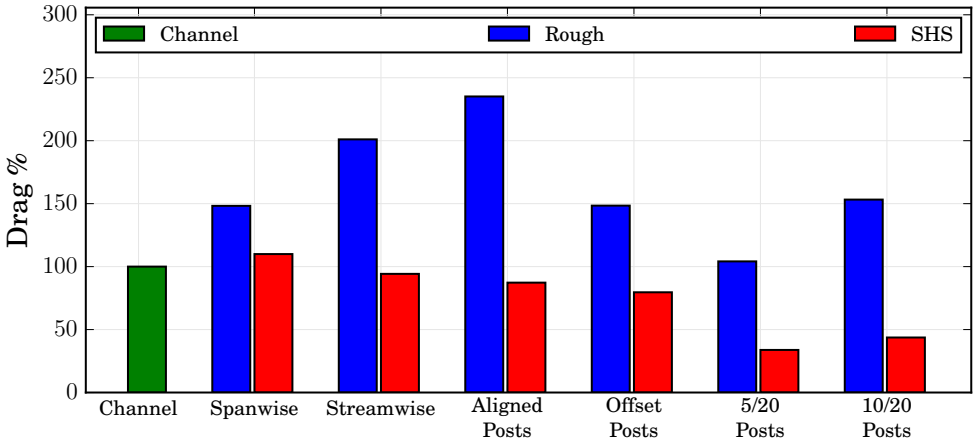

(a) Drag difference from wetted surface area analysis.

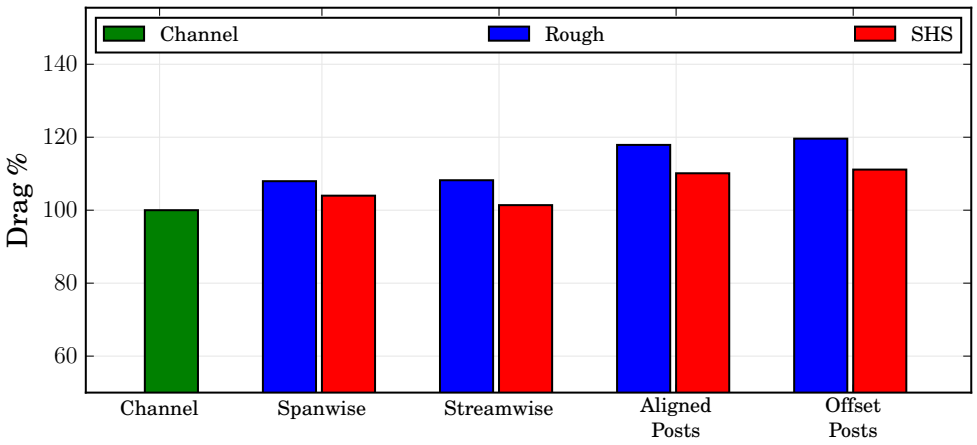

(b) Drag difference from volumetric flow rate analysis.

Figure 10.4: Comparison of Surfaces at $Re_\tau = 395$. Both methods of analysis indicate the hydrophobic surface should have less drag than the rough surface..

10.1.4 $Re_\tau = 395$ Results

As was seen in the laminar regime results, the hydrophobic surface again appears to have a lower drag than the rough surface. This is shown in Figures 10.4a and 10.4b with both graphs giving a similar result. The figures differ in respect to the drag relative to a smooth surface with the wetted surface analysis indicating the hydrophobic surface would have less drag, and the velocity profile analysis indicating an increased drag; however, without the full viscosity ratio difference, the amount of slip near the wall is reduced for the hydrophobic surface leading to a higher drag than should otherwise be expected.

10.1.5 $Re_\tau = 590$ Results

The results presented in Figure 10.5 again show a good level of consistency between the different methods of analysis. With the exception of the streamwise grooved surface, both sets of results indicate that the drag for both the rough and hydrophobic surfaces should be both similar to each other, and greater than the smooth channel. This result is unsurprising given what was shown in Chapters 6, 7, and 8 which indicated that at high Reynolds numbers the air layer was removed from the surface effectively turning the hydrophobic surface into a rough surface.

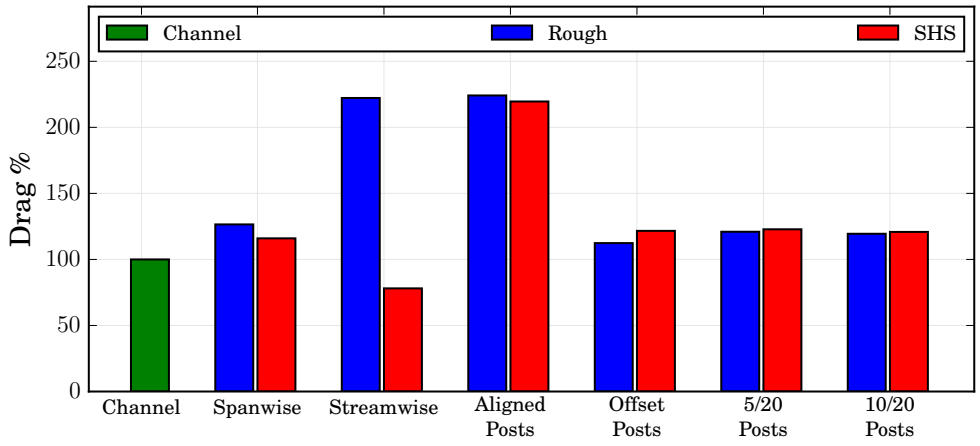

(a) Drag difference from wetted surface area analysis.

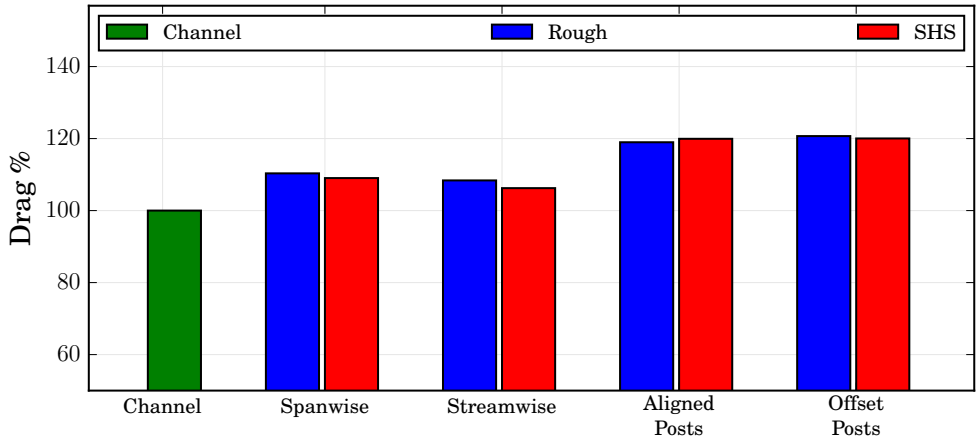

(b) Drag difference from volumetric flow rate analysis.

Figure 10.5: Comparison of Surfaces at $Re_\tau = 590$. The hydrophobic streamwise grooves has both the least drag, and is the only surface to show any significant drag reduction. Each of the other hydrophobic surfaces display similar drag values to the corresponding rough surface.

10.2 Discussion of Key Points

A number of key points have resulted from this research, the first of these being the lattice Boltzmann code itself. Prior to this implementation, there were no other published references to a code capable of modelling turbulent multiphase flow at a direct numerical simulation resolution or accuracy. A code capable of simulating these flow conditions has been devised, implemented, and validated across a range of situations including both laminar and turbulent flow, bubbles, droplets, Rayleigh-Taylor instabilities and low Reynolds number flow over a hydrophobic surface.

Simulation of higher than normally attainable Reynolds numbers for the size of the domain used was achieved by incorporating a fractional propagation scheme. As well as increasing the maximum Reynolds number attainable, this method improved the stability of the simulation, allowing accurate results to be obtained.

This code was further enhanced with a novel mesh refinement method that allows increased resolution of the flow in the near wall regions whilst keeping the total number of elements in the domain to a manageable size. It also combined the best features of the local and multi-block mesh refinement methods resulting in increased efficiency due to its lack of extra interpolation, and ability to optimise distribution of workload across processors.

A multiphase model was implemented, and tuned to give accurate results for flows simulating air and water so as to correctly model both the buoyancy of the differing fluids, and properly capture the interaction between them. This also incorporated a wall wetting model that allowed the surface energy of the wall to be controlled, which enabled the simulations of super hydrophobic surfaces to be undertaken. Although no high density or viscosity difference was present, various techniques were used to minimise the effect that this had on the results.

The implemented code was optimised, and its performance was shown to scale linearly for low numbers of processors allowing multiple simulations to be run concurrently, all at an improved efficiency.

As well as the code, a range of interesting features of flow over super hydrophobic surfaces have been demonstrated in this work. The first of these to be discussed is the effect on the overall drag of the surface that the streamwise channels have, either as grooves or aligned posts. At the high Reynolds numbers

tested, the flow between the posts became just as important as the flow over the tops of the posts. This was due to the increase in shear and pressure forces acting on the sides of the posts resulting from the higher velocities. The geometries that featured streamwise channels, such as the streamwise grooves and the aligned posts geometries tended to display higher reductions in drag; however, they were also more prone to losing the layer of air.

Furthermore, the concept of slip at the surface has previously been used to explain why super hydrophobic surfaces are able to reduce drag, and this appears to be true in cases featuring these streamwise channels. However, in cases such as the spanwise grooves geometry, the flow at the top of the grooves was actually in the negative direction due to the recirculation eddies observed below the free-surface. These results are therefore in agreement with the work by Min and Kim [88, 89] discussed in Chapter 2, who found that slip in the spanwise direction tended to increase the drag of the surface.

Finally, and most importantly, the drag reducing abilities of the superhydrophobic surface appear to be largely due to the location and stability of the free surface. When the free surface extends past the ends of the posts and/or ridges, it acts to deflect the water away from the surface, reducing the distance over which the streamwise component of velocity acts on the surface. The presence of the air layer also insulates the surface from the water, removing the pressure drag component entirely from the total drag. As the location of free-surface shifts further down the height of the post, the pressure drag correspondingly increases until it reaches a maximum when the surface becomes fully wetted like the rough surface.

This shows that the commonly held assumption of a flat and stable free-surface is not true, and cannot be used when dealing with turbulent flow. The analysis of the balance between wall normal forces and the surface tension force demonstrated that it can be predicted as to when the integrity and stability of the free-surface is likely to fail, and hence when the surface will start wetting.

As was discussed in Chapter 2 previous research has found drag reductions from almost none to over 70%. This work has shown that although apparently contradictory, both of these possible finding could be correct depending on the surface geometry and micro feature size tested. The results indicating high drag reductions tended to use streamwise grooved surfaces whilst those with minimal

drag reductions used spanwise grooved surfaces, which is in line with the results shown in Chapters 6.

10.3 Conclusions

The aim of this work was to investigate whether super hydrophobic surfaces have the potential to reduce the drag and resistance of ships. The results presented give limited indication that drag reduction will occur under these conditions. The removal of the air layer from the surface at high Reynolds numbers results in a rough surface which gives only minimal if any benefit.

With the results showing that the streamwise grooved geometry exhibited a reduction in drag compared with both the smooth wall and rough surface even at the highest Reynolds number tested, the theory of drag reduction by surfaces such as this still cannot be entirely discounted. However, in practice, trying to align grooves such that they only ever experience streamwise flow within the boundary layer of a ship, is near impossible, and there are times when the flow will instead be spanwise, leading to both increased drag, and removal of the air from the surface.

10.4 Recommendations and Proposed Work

Although this research has shown that drag reduction in turbulent flow appears to be limited to specific cases, there are some further tests that could be performed to try to broaden the conditions under which drag reduction occurs. The first of these would be again related to the size of the posts and the gaps between them. In this work, the spacing between the gaps was increased, a process that was shown to to increase the drag on the surface at high Reynolds numbers. If instead the size of the posts and gaps were to be reduced, the increased density of the posts may lead to a higher surface tension force supporting the interface, resulting in higher Reynolds numbers being attainable before the air layer is removed from the surface.

Another option would be to investigate differently shaped posts, including the paraboloids that naturally occur on the leaf of a lotus flower. A combination of both microscale and nanoscale roughness could also be introduced, as occurs in nature, to examine if the combination of the two can withstand the high wall-normal forces, and maintain the air layer.

As well as changes to the surfaces, there are some additional improvements that could be made to the lattice Boltzmann code to further improve it's accuracy and efficiency. The first of these would be a process to allow simulation of fluids with high density and viscosity ratios. This would allow the exact physical situation to be correctly simulated and avoid the assumptions that needed to be introduced in this work. Unfortunately, combined with the other techniques implemented to accurately model the turbulent flow, the incorporation of high density ratio method becomes extremely difficult and was therefore left out of this work.

Another feature within the lattice Boltzmann code that would be required to further extend the work is an immersed boundary method. With the lattice Boltzmann method based on square lattices, trying to model curved or irregular shaped surfaces is quite challenging, as was shown with the flow over a NACA 4410 foil in Section 4.4.2.3. An immersed boundary method would allow non-cuboid shapes to be modelled, and would better allow simulations over randomly shaped and orientated series of posts and ridges.

The final feature that could further optimise the implemented code is a change to the domain decomposition technique. As was described in Section 4.8.2, the code currently uses a "book" style method of decomposition. In order to again increase the efficiency, a method that allows decomposition into smaller cubes would further minimise the surface area to volume ratio of the decomposed domains, leading to reduced inter process communication, and more efficient processing.

Another issue that could be addressed differently, as was mentioned in some of the turbulent flow case analysis, is that the reported rough surface results may have been lower than they would otherwise be. This is due to the way that the domains have been constructed, with the depth of the grooves, ridges, posts and gaps added to the top of the original channel. This construction, combined with the fact that no body forces were applied to the fluid contained within this

additional space meant that the measured fluid velocities at the top wall of the domain and around the posts is lower than it should be. In each case where the fluid was free to flow in a streamwise direction, an additional body force could have been applied. This would have increased both the shear drag acting on the posts, and the pressure force being applied to the posts in cases where the posts and top wall were fully wetted (corresponding to all of the rough surface cases and the high Reynolds number turbulent cases). Being within the boundary layer, and to an extent, even below the viscous sub-layer, the magnitude of the body force to be applied is highly dependant on the surface geometry, and extremely difficult to accurately predict, which is why it was not included in this work. Nonetheless, the comparisons between the rough and hydrophobic surfaces are still valid, as are the results between the hydrophobic surface and the smooth channel in cases where the air layer has not been removed. This is further confirmed by both the wetted surface area analysis and the velocity profile analysis indicating the hydrophobic surface had the lower drag in almost all tested cases.

Finally, additional experiments could also give deeper insight into the behaviour of superhydrophobic surfaces in turbulent and transitional flows. With the cavitation tunnel at the Australian Maritime College having a velocity operating range of between 2 and 12 m/s, the flow was already highly turbulent even at the lowest possible speed. Experiments in another facility where lower speeds and Reynolds numbers can be attained would allow further experimental investigation into the exact conditions under which the air layer on the surface is removed, and the corresponding maximum limit of Reynolds number at which drag reduction using superhydrophobic surfaces is possible.

References

[1] Aljallis, E., Sarshar, M.A., Datla, R., Sikka, V., Jones, A. & Choi, C.H. (2013). Experimental study of skin friction drag reduction on superhydrophobic flat plates in high reynolds number boundary layer flow. *Physics of Fluids*, **25**, 025103.

[2] Antonia, R.A. & Krogstad, P.A. (2000). Effect of different surface roughnesses on a turbulent boundary layer. *Journal of the Brazilian Society of Mechanical Sciences*, **22**, 1 – 15.

[3] Baglin, A., Barber, T. & Rosengarten, G. (2014). Development of an effective fvlbm code for the study of turbulent and multiphase flows. *Applied Mechanics and Materials*, **553**, 180–186, (ERA unranked).

[4] Balazs, N., Schlei, B., Strottman, D., Strottman, D. & others (1999). Relativistic flows on a spacetime lattice. *Acta Physica Hungarica A*, **9**, 6798.

[5] Bandyopadhyay, P. & Castano, J. (1996). Micro-tiles for electromagnetic turbulence control in saltwater: Preliminary investigations. *ASME-PUBLICATIONS-FED*, **237**, 5360.

[6] Bechert, D., Bruse, M., Hage, W., Van der Hoeven, J.T. & Hoppe, G. (1997). Experiments on drag-reducing surfaces and their optimization with an adjustable geometry. *Journal of Fluid Mechanics*, **338**, 5987.

[7] Berger, T., Kim, J., Lee, C. & Lim, J. (2000). Turbulent boundary layer control utilizing the lorentz force. *Physics of Fluids*, **12**, 631.

[8] Bespalko, D., Pollard, A. & Uddin, M. (2010). Direct numerical simulation of fully-developed turbulent channel flow using the lattice boltzmann method and analysis of OpenMP scalability. In *High Performance Computing Systems and Applications*, 119.

[9] Bhatnagar, P.L., Gross, E.P. & Krook, M. (1954). A model for collision processes in gases. i. small amplitude processes in charged and neutral one-component systems. *Physical review*, **94**, 511.

[10] Bittoun, E. & Marmur, A. (2009). Optimizing super-hydrophobic surfaces: Criteria for comparison of surface topographies. *Journal of Adhesion Science and Technology*, **23**, 401411.

[11] Blossey, R. (2003). Self-cleaning surfacesvirtual realities. *Nature materials*, **2**, 301306.

[12] Boghosian, B.M. & Taylor, W. (1997). Quantum lattice-gas models for the many-body schrdinger equation. *International Journal of Modern Physics C*, **8**, 705716.

[13] Brandner, P., Lecoffre, Y. & Walker, G. (2006). Development of an australian national facility for cavitation research.

[14] Brandner, P.A., Lecoffre, Y. & Walker, G.J. (2007). Design considerations in the development of a modern cavitation tunnel.

[15] Brandner, P.A., Belle, A., Pearce, B.W. & Holmes, M.J.P. (2012). Artificial thickening of cavitation tunnel boundary layers. In *18th Australasian Fluid Mechanics Conference*, 14.

[16] Briant, A. & Yeomans, J. (2004). Lattice boltzmann simulations of contact line motion. II. binary fluids. *Physical Review E*, **69**.

[17] Briant, A.J. (2002). Lattice boltzmann simulations of contact line motion in a liquid-gas system. *Philosophical Transactions of the Royal Society of London. Series A: Mathematical, Physical and Engineering Sciences*, **360**, 485495.

[18] Byun, D., Park, H.C. *et al.* (2006). Drag reduction on micro-structured super-hydrophobic surface. In *Robotics and Biomimetics, 2006. ROBIO'06. IEEE International Conference on*, 818823.

[19] Cao, N., Chen, S., Jin, S. & Martinez, D. (1997). Physical symmetry and lattice symmetry in the lattice boltzmann method. *Physical Review E*, **55**, R21.

[20] Cassie, A. & Baxter, S. (1944). Wettability of porous surfaces. *Trans. Faraday Soc.*, **40**, 546551.

[21] Chen, H. (1998). Volumetric formulation of the lattice boltzmann method for fluid dynamics: Basic concept. *Phys. Rev. E*, **58**, 39553963.

[22] Chen, S. & Doolen, G.D. (1998). Lattice boltzmann method for fluid flows. *Annual Review of Fluid Mechanics*, **30**, 329–364.

[23] Cheng, Y.T. & Rodak, D.E. (2005). Is the lotus leaf superhydrophobic? *Applied Physics Letters*, **86**, 144101.

[24] Cho, K.L., Liaw, I.I., Wu, A.H.F. & Lamb, R.N. (2010). Influence of roughness on a transparent superhydrophobic coating. *The Journal of Physical Chemistry C*, **114**, 11228–11233.

[25] Choi, H., Moin, P. & Kim, J. (1994). Active turbulence control for drag reduction in wall-bounded flows. *Journal of Fluid Mechanics*, **262**, 7575.

[26] Choi, K.S. & Clayton, B.R. (2001). The mechanism of turbulent drag reduction with wall oscillation. *International journal of heat and fluid flow*, **22**, 19.

[27] Conway, J. (1970). The game of life. *Scientific American*, **223**, 4.

[28] Couser, P., Molland, A., Armstrong, N. & Utama, I. (1997). Calm water powering predictions for high speed catamarans. *Fast97*, 765774.

[29] Crawford, C. & Karniadakis, G. (1997). Reynolds stress analysis of EMHD-controlled wall turbulence. part i. streamwise forcing. *Physics of fluids*, **9**, 788.

[30] Creative-Commons CC-BY-SA (2014). Law of the wall.

[31] Daniello, R.J., Waterhouse, N.E. & Rothstein, J.P. (2009). Drag reduction in turbulent flows over superhydrophobic surfaces. *Physics of Fluids*, **21**, 085103.

[32] De Gennes, P.G. (1985). Wetting: statics and dynamics. *Reviews of modern physics*, **57**, 827.

[33] Dean, B. & Bhushan, B. (2010). Shark-skin surfaces for fluid-drag reduction in turbulent flow: a review. *Philosophical Transactions of the Royal Society A: Mathematical, Physical and Engineering Sciences*, **368**, 47754806.

[34] Decker, L. & Jeulin, D. (1997). Random texture simulation by multi-species lattice-gas models. *Journal of Electronic Imaging*, **6**, 7893.

[35] Dhanak, M. & Si, C. (1999). On reduction of turbulent wall friction through spanwise wall oscillations. *Journal of Fluid Mechanics*, **383**, 175195.

[36] Drela, M. (1989). XFOIL: An Analysis and Design System for Low Reynolds Number Airfoils. In T. Mueller, ed., *Low Reynolds Number Aerodynamics*, vol. 54 of *Lecture Notes in Engineering*, 1–12, Springer Berlin Heidelberg.

[37] Du, Y. (1999). *Parallel DNS of Electro-Magnetic Flow Control.*. PhD thesis, Brown University.

[38] Dupuis, A. & Chopard, B. (2003). Theory and applications of an alternative lattice boltzmann grid refinement algorithm. *Physical Review E*, **67**.

[39] Elizabeth Geller, ed. (2005). *McGraw-Hill concise encyclopedia of science & technology.*. McGraw-Hill, New York.

[40] Emami, B., Hemeda, A.A., Amrei, M.M., Luzar, A., Gad-el Hak, M. & Vahedi Tafreshi, H. (2013). Predicting longevity of submerged superhydrophobic surfaces with parallel grooves. *Physics of Fluids*, **25**, 062108.

[41] Eng Shin Gan (2008). *Testing of Super-insulating Surfaces*. Undergraduate thesis, University of New South Wales.

[42] Filippova, O. & Hanel, D. (1998). Grid refinement for lattice-BGK models. *Journal of Computational Physics*, **147**, 219–228.

[43] Finnie, A.A. & Williams, D.N. (2010). Paint and coatings technology for the control of marine fouling. *Biofouling*, **10**, 9781444315462.

[44] Frisch, U., Hasslacher, B. & Pomeau, Y. (1986). Lattice-gas automata for the navier-stokes equation. *Physical review letters*, **56**, 15051508.

[45] Froude, W. (1872). Experiments on the surface-friction experienced by a plane moving through water. *42nd British Association Report*, 118124.

[46] Fukagata, K., Kasagi, N. & Koumoutsakos, P. (2006). A theoretical prediction of friction drag reduction in turbulent flow by superhydrophobic surfaces. *Physics of Fluids*, **18**, 051703.

[47] Frstner, R., Barthlott, W., Neinhuis, C. & Walzel, P. (2005). Wetting and self-cleaning properties of artificial superhydrophobic surfaces. *Langmuir*, **21**, 956–961.

[48] Glavatskiy, K. & Bedeaux, D. (2008). Nonequilibrium properties of a two-dimensionally isotropic interface in a two-phase mixture as described by the square gradient model. *Physical Review E*, **77**, 061101.

[49] Grosskreutz, R. (1975). An attempt to control boundary-layer turbulence with nonisotropic compliant walls. *University Science Journal Dar es Salaam*, **1**, 6573.

[50] Gunstensen, A. (1987). *Lattice Boltzmann Studies of Multiphase Flows Through Porous Media*. Ph.D. thesis, University of Toronto.

[51] Handbook, D.F. (1992). Thermodynamics, heat transfer and fluid flow. *US Department of Energy*, **1**, 53–96.

[52] Hanjalic, K. & Launder, B.E. (1972). Fully developed asymmetric flow in a plane channel. *Journal of Fluid Mechanics*, **51**, 301–335.

[53] Hardy, J., De Pazzis, O. & Pomeau, Y. (1976). Molecular dynamics of a classical lattice gas: Transport properties and time correlation functions. *Physical review A*, **13**, 1949.

[54] He, X. & Doolen, G.D. (2002). Thermodynamic foundations of kinetic theory and lattice Boltzmann models for multiphase flows. *Journal of Statistical Physics*, **107**, 309–328.

[55] He, X. & Luo, L.S. (1997). Theory of the lattice Boltzmann method: From the Boltzmann equation to the lattice Boltzmann equation. *Physical Review E*, **56**, 6811.

[56] He, X., Luo, L.S. & Dembo, M. (1996). Some progress in lattice boltzmann method. part i. nonuniform mesh grids. *Journal of Computational Physics*, **129**, 357363.

[57] He, X., Zou, Q., Luo, L.S. & Dembo, M. (1997). Analytic solutions of simple flows and analysis of nonslip boundary conditions for the lattice boltzmann BGK model. *Journal of Statistical Physics*, **87**, 115136.

[58] Hefner, J., Weinstein, L. & Bushnell, D. (1980). Large-eddy breakup scheme for turbulent viscous drag reduction. *Viscous flow drag reduction*, 110127.

[59] Henoch, C., Krupenkin, T.N., Kolodner, P., Taylor, J.A., Hodes, M.S., Lyons, A.M., Peguero, C. & Breuer, K. (2006). Turbulent drag reduction using superhydrophobic surfaces. In *3rd AIAA Flow Control Conference*, 58.

[60] Higuera, F.J. & Jimenez, J. (2007). Boltzmann approach to lattice gas simulations. *EPL (Europhysics Letters)*, **9**, 663.

[61] Hoerner, S. (1965). *Fluid-dynamic Drag: Pratical Information on Aerodynamic Drag and Hydrodynamic Resistance*. S. F. Hoerner.

[62] Hou, S., Sterling, J., Chen, S. & Doolen, G. (1996). A lattice boltzmann subgrid model for high reynolds number flows. *Pattern formation and lattice gas automata*, **6**, 151166.

[63] Huang, H., Zheng, H., Lu, X. & Shu, C. (2010). An evaluation of a 3d free-energy-based lattice boltzmann model for multiphase flows with large density ratio. *International journal for numerical methods in fluids*, **63**, 11931207.

[64] Huang, J.J., Shu, C. & Chew, Y.T. (2009). Lattice boltzmann study of droplet motion inside a grooved channel. *Physics of Fluids*, **21**, 022103.

[65] Huang, J.J., Shu, C. & Chew, Y.T. (2009). Mobility-dependent bifurcations in capillarity-driven two-phase fluid systems by using a lattice boltzmann phase-field model. *International journal for numerical methods in fluids*, **60**, 203225.

[66] Inamuro, T., Ogata, T., Tajima, S. & Konishi, N. (2004). A lattice boltzmann method for incompressible two-phase flows with large density differences. *Journal of Computational Physics*, **198**, 628–644.

[67] International Chamber of Shipping (2012). Shipping, world trade and the reduction of CO2 emmissions. Tech. rep., United Nations Framework Convention of Climate Change, International Maritime Organization.

[68] Jain, P.K. & Tentner, A. (2009). A lattice boltzmann framework to simulate boiling water reactor core hydrodynamics. *Computers & Mathematics with Applications*, **58**, 975986.

[69] Jamaluddin, A. & others (2012). Micro-bubble drag reduction on a high speed vessel model. *Journal of Marine Science and Application*, **11**, 301304.

[70] Jan Hoffmann (2013). Review of maritime transport 2013. Tech. rep., United Nations Conference on Trade and Development.

[71] Jimenez, J. & Moin, P. (1991). The minimal flow unit in near-wall turbulence. *Journal of Fluid Mechanics*, **225**.

[72] Jones, A., Lamb, R. & Zhang, H. (2004). *Durable superhydrophobic coating*. Google Patents, US Patent App. 10/552,570.

[73] Koelman, J.M.V.A. (1991). A Simple Lattice Boltzmann Scheme for Navier-Stokes Fluid Flow. *Europhysics Letters (epl)*, **15**, 603–607.

[74] Kramer, M. (1960). Boundary layer stabilization by distributed damping. *Journal of the American Society for Naval Engineers*, **72**, 2534.

[75] Kramer, M. (1965). Hydrodynamics of the dolphin. *Advances in hydroscience*, **2**, 111130.

[76] Latt, J. (2008). Choice of units in lattice boltzamnn simulation. *Lattice Boltzmann Howtos: http://www. lbmethod. org/howtos: main*.

[77] Latt, J., Chopard, B., Malaspinas, O., Deville, M. & Michler, A. (2008). Straight velocity boundaries in the lattice boltzmann method. *Physical Review E*, **77**, 056703.

[78] Lee, C. & Kim, C.J. (2011). Underwater restoration and retention of gases on superhydrophobic surfaces for drag reduction. *Physical Review Letters*, **106**.

[79] Lee, T. & Lin, C.L. (2005). A stable discretization of the lattice boltzmann equation for simulation of incompressible two-phase flows at high density ratio. *Journal of Computational Physics*, **206**, 16–47.

[80] Lim, J., Choi, H. & Kim, J. (1998). Control of streamwise vortices with uniform magnetic fluxes. *Physics of Fluids*, **10**, 1997.

[81] Lin, C.L. & Lai, Y.G. (2000). Lattice boltzmann method on composite grids. *Physical Review E*, **62**, 2219.

[82] Lishchuk, S., Care, C. & Halliday, I. (2003). Lattice boltzmann algorithm for surface tension with greatly reduced microcurrents. *PHYSICAL REVIEW E*, **67**.

[83] Martell, M.B. (2009). *DNS of Superhydrophobic Surfaces*. Ph.D. thesis, University of Massachusetts, Amherst.

[84] Martell, M.B., Perot, J.B. & Rothstein, J.P. (2009). Direct numerical simulations of turbulent flows over superhydrophobic surfaces. *Journal of Fluid Mechanics*, **620**, 31.

[85] Massey, B. & Ward-Smith, J. (1998). *Mechanics of Fluids, Seventh Edition*. No. v. 1 in Mechanics of Series, Taylor & Francis.

[86] McCORMICK, M.E. & Bhattacharyya, R. (1973). Drag reduction of a submersible hull by electrolysis. *Naval Engineers Journal*, **85**, 1116.

[87] Mei, R., Luo, L.S., Lallemand, P. & dHumires, D. (2006). Consistent initial conditions for lattice boltzmann simulations. *Computers & Fluids*, **35**, 855862.

[88] Min, T. & Kim, J. (2004). Effects of hydrophobic surface on skin-friction drag. *Physics of Fluids*, **16**, L55.

[89] Min, T. & Kim, J. (2005). Effects of hydrophobic surface on stability and transition. *Physics of Fluids*, **17**, 108106.

[90] Moser, R., Kim, J. & Mansour, N. (1999). Direct numerical simulation of turbulent channel flow up to re= 590. *Physics of fluids*, **11**, 943.

[91] Motier, J., Chou, L. & Kommareddi, N. (1996). Commercial drag reduction past, present and future. In *The 1996 ASME Fluids Engineering Division Summer Meeting. Part 2(of 3), San Diego, CA, USA, 07/07-11/96*, 229234.

[92] Nannelli, F. & Succi, S. (1992). The lattice boltzmann equation on irregular lattices. *Journal of Statistical Physics*, **68**, 401407.

[93] \"Oner, D. & McCarthy, T.J. (2000). Ultrahydrophobic surfaces. effects of topography length scales on wettability. *Langmuir*, **16**, 7777–7782.

[94] Ou, J., Perot, B. & Rothstein, J. (2004). Laminar drag reduction in microchannels using ultrahydrophobic surfaces. *Physics of fluids*, **16**, 4635.

[95] Papatzacos, P. (2002). Macroscopic two-phase flow in porous media assuming the diffuse-interface model at pore level. *Transport in porous media*, **49**, 139174.

[96] Park, H., Sun, G. & Kim, C.J. (2013). Turbulent drag reduction on superhydrophobic surfaces confirmed by built-in shear sensing. In *Micro Electro Mechanical Systems (MEMS), 2013 IEEE 26th International Conference on*, 11831186, IEEE.

[97] Peguero, C. & Breuer, K. (2009). On drag reduction in turbulent channel flow over superhydrophobic surfaces. In *Advances in Turbulence XII*, 233236, Springer.

[98] PETERLIN, A. (1970). Molecular model of drag reduction by polymer solutes. *Nature*, **227**, 598–599.

[99] Pooley, C.M. & Furtado, K. (2008). Eliminating spurious velocities in the free-energy lattice boltzmann method. *Physical Review E*, **77**, 046702.

[100] Pope, S. (2000). *Turbulent Flows*. Cambridge University Press.

[101] Prandtl, L. (1904). Fluid motion with very small friction. *Proc. 3 Int. Congr. on Mathematics, Heidelberg*.

[102] Qian, Y.H. (1997). Fractional propagation and the elimination of staggered invariants in lattice-BGK models. *International journal of modern physics C*, **8**, 753761.

[103] Qian, Y.H., D'Humires, D. & Lallemand, P. (1992). Lattice BGK models for navier-stokes equation. *EPL (Europhysics Letters)*, **17**, 479.

[104] Read, K. (1984). Experimental investigation of turbulent mixing by Rayleigh-Taylor instability. *Physica D: Nonlinear Phenomena*, **12**, 45–58.

[105] Reshotko, E. (1979). Drag reduction by cooling in hydrogen-fueled aircraft. *J. of Aircraft*, **16**, 584590.

[106] Reynolds, O. (1883). An experimental investigation of the circumstances which determine whether the motion of water shall be direct or sinuous, and of the law of resistance in parallel channels. *Proceedings of the royal society of London*, **35**, 8499.

[107] Reynolds, O. (1895). On the dynamical theory of incompressible viscous fluids and the determination of the criterion. *Philosophical Transactions of the Royal Society of London. A*, 123164.

[108] Richardson, L. (1926). Weather prediction by numerical process, cambridge u. press (1922). In *Proc. Roy. Soc.(London) Al*, vol. 10, 709.

[109] Rohde, M., Kandhai, D., Derksen, J.J. & Van den Akker, H.E.A. (2006). A generic, mass conservative local grid refinement technique for lattice-boltzmann schemes. *International journal for numerical methods in fluids*, **51**, 439468.

[110] Rosengarten, G., Stanley, C. & Kwok, F. (2008). Superinsulating heat transfer surfaces for microfluidic channels. *Int. J. Transp. Phenom*, **10**, 293306.

[111] Rosengarten, G., Tetuko, A., Li, K.K., Wu, A. & Lamb, R. (2011). The effect of nano-structured surfaces on droplet impingement heat transfer. In *ASME 2011 International Mechanical Engineering Congress and Exposition*, 10291036, American Society of Mechanical Engineers.

[112] Roth, J., Sherman, D. & Wilkinson, S. (1998). Boundary layer flow control with a one atmosphere uniform glow discharge surface plasma. In *36th Aerospace Sciences Meeting and Exhibit*, vol. 1.

[113] Roth, J., Nourgostar, S. & Bonds, T. (2007). The one atmosphere uniform glow discharge plasma (OAUGDP)a platform technology for the 21st century. *Plasma Science, IEEE Transactions on*, **35**, 233250.

[114] Rothman, D.H. & Keller, J.M. (1988). Immiscible cellular-automaton fluids. *Journal of Statistical Physics*, **52**, 11191127.

[115] Saha, A.K. (2004). Three-dimensional numerical simulations of the transition of flow past a cube. *Physics of Fluids*, **16**, 1630–1646.

[116] Samaha, M.A., Vahedi Tafreshi, H. & Gad-el Hak, M. (2011). Modeling drag reduction and meniscus stability of superhydrophobic surfaces comprised of random roughness. *Physics of Fluids*, **23**, 012001.

[117] Scardino, A.J., Zhang, H., Cookson, D.J., Lamb, R.N. & Nys, R.d. (2009). The role of nano-roughness in antifouling. *Biofouling*, **25**, 757–767.

[118] Segawa, T., Mizunuma, H., Murakami, K., Li, F.C. & Yoshida, H. (2007). Turbulent drag reduction by means of alternating suction and blowing jets. *Fluid Dynamics Research*, **39**, 552 – 568, in memoriam: Professor Isao Imai, 1914-2004. Vol. {II}.

[119] Slater (2014). Personnal correspondence.

[120] Spong, E., Reizes, J. & Leonardi, E. (2005). Efficiency improvements of electromagnetic flow control. *International Journal of Heat and Fluid Flow*, **26**, 635655.

[121] Succi, S. (2013). *The Lattice Boltzmann Equation: For Fluid Dynamics and Beyond*. Numerical Mathematics and Scientific Computation, OUP Oxford.

[122] Swift, M.R., Osborn, W.R. & Yeomans, J.M. (1995). Lattice boltzmann simulation of nonideal fluids. *Phys. Rev. Lett.*, **75**, 830833.

[123] Teixeira, C. (1998). Incorporating turbulence models into the lattice-boltzmann method. *International Journal of Modern Physics C*, **9**, 11591175.

[124] Teo, C.J. & Khoo, B.C. (2010). Flow past superhydrophobic surfaces containing longitudinal grooves: effects of interface curvature. *Microfluidics and Nanofluidics*, **9**, 499511.

[125] Tretheway, D.C. & Meinhart, C.D. (2002). Apparent fluid slip at hydrophobic microchannel walls. *Physics of Fluids*, **14**, L9.

[126] Tretheway, D.C. & Meinhart, C.D. (2003). Effects of absolute pressure on fluid slip in a hydrophobic microchannel. *ASME-PUBLICATIONS-FED*, **259**, 561564.

[127] Truesdell, R., Mammoli, A., Vorobieff, P., van Swol, F. & Brinker, C. (2006). Drag reduction on a patterned superhydrophobic surface. *Physical Review Letters*, **97**.

[128] Truong, V., Webb, H., Fadeeva, E., Chichkov, B., Wu, A., Lamb, R., Wang, J., Crawford, R. & Ivanova, E. (2012). Air-directed attachment of coccoid bacteria to the surface of superhydrophobic lotus-like titanium. *Biofouling*, **28**, 539550.

[129] Truong, V., Webb, H., Fadeeva, E., Chichkov, B., Wu, A., Lamb, R., Wang, J., Crawford, R. & Ivanova, E. (2012). Air-directed attachment of coccoid bacteria to the surface of superhydrophobic lotus-like titanium. *Biofouling*, **28**, 539–550.

[130] UDAGAWA, H. (1999). Drag reduction of newtonian fluid in a circular pipe with a highly water-repellent wall. *J. Fluid Mech*, **381**, 225238.

[131] Vakarelski, I.U., Marston, J.O., Chan, D.Y.C. & Thoroddsen, S.T. (2011). Drag reduction by leidenfrost vapor layers. *Phys. Rev. Lett.*, **106**, 214501.

[132] Van Manen, J.D. & Van Oossanen, P. (1988). *Principles of Naval Arcitecture, Section 2*, vol. 2. Society of Naval Architects and Marine Engineers.

[133] Vinogradova, O. (1995). Drainage of a thin liquid film confined between hydrophobic surfaces. *Langmuir*, **11**, 22132220.

[134] Vinogradova, O. (1999). Slippage of water over hydrophobic surfaces. *International journal of mineral processing*, **56**, 3160.

[135] Von Karman, T. (1930). Mechanische nlichkeit und turbulenz. *Nachrichten von der Gesellschaft der Wissenschaften zu Gttingen, Mathematisch-Physikalische Klasse*, **1930**, 5876.

[136] Waite, M.E., Ge, S., Spetzler, H. & Bahr, D.B. (1998). The effect of surface geometry on fracture permeability: A case study using a sinusoidal fracture. *Geophysical research letters*, **25**, 813816.

[137] Waite, M.E., Ge, S. & Spetzler, H. (1999). A new conceptual model for fluid flow in discrete fractures: an experimental and numerical study. *Journal of Geophysical Research: Solid Earth (19782012)*, **104**, 1304913059.

[138] Walsh, M. (1980). Drag characteristics of v-groove and transverse curvature riblets. *Viscous flow drag reduction*, 168184.

[139] Walsh, M. (1982). Turbulent boundary layer drag reduction using riblets. In *AIAA, Aerospace Sciences Meeting*, vol. 1.

[140] Wang, C., Wu, A.H. & Lamb, R.N. (2014). Superhydrophobicity and optical transparency in thin films: Criteria for coexistence. *The Journal of Physical Chemistry C*, **118**, 5328–5335.

[141] Wenzel, R. (1936). Resistance of solid surfaces to wetting by water. *Industrial & Engineering Chemistry*, **28**, 988994.

[142] Woolford, B., Prince, J., Maynes, D. & Webb, B.W. (2009). Particle image velocimetry characterization of turbulent channel flow with rib patterned superhydrophobic walls. *Physics of Fluids*, **21**, 085106.

[143] Young, T. (1805). An essay on the cohesion of fluids. *Philosophical Transactions of the Royal Society of London*, **95**, 65–87.

[144] Youngs, D.L. (1984). Numerical simulation of turbulent mixing by rayleigh-taylor instability. *Physica D: Nonlinear Phenomena*, **12**, 32 – 44.

[145] Youngs, D.L. (1991). Three-dimensional numerical simulation of turbulent mixing by rayleightaylor instability. *Physics of Fluids A: Fluid Dynamics*, **3**, 1312.

[146] Yu, D. & Girimaji, S.S. (2006). Multi-block lattice boltzmann method: Extension to 3d and validation in turbulence. *Physica A: Statistical Mechanics and its Applications*, **362**, 118124.

[147] Yu, D., Mei, R. & Shyy, W. (2002). A multi-block lattice boltzmann method for viscous fluid flows. *International Journal for Numerical Methods in Fluids*, **39**, 99–120.

[148] Zecevic, V., Kirkpatrick, M.P. & Armfield, S.W. (2011). The lattice boltzmann method for turbulent channel flows using graphics processing units. In W. McLean & A.J. Roberts, eds., *Proceedings of the 15th Biennial Computational Techniques and Applications Conference, CTAC-2010*, vol. 52 of *ANZIAM J.*, C914C931, http://journal.austms.org.au/ojs/index.php/ANZIAMJ/article/view/3951 [November 10, 2011].

[149] Zhang, R., Chen, H., Qian, Y. & Chen, S. (2001). Effective volumetric lattice boltzmann scheme. *Physical Review E*, **63**.

[150] Zhao, J., Shi, X., Geng, X. & Hou, Z. (2009). Liquid slip over super-hydrophobic surface and its application in drag reduction. *Journal of Ship Mechanics*, **13**, 325330.

[151] Zheng, H., Shu, C. & Chew, Y. (2006). A lattice boltzmann model for multiphase flows with large density ratio. *Journal of Computational Physics*, **218**, 353–371.

[152] Zou, Q. & He, X. (1997). On pressure and velocity boundary conditions for the lattice Boltzmann BGK model. *Physics of Fluids*, **9**, 1591–1598.

Appendix A

System of Units

These are given for reference only and any conversion between physical and lattice Boltzmann quantities should follow the process presented in Section 4.3.2 with a non-dimensionalisation step.

Table A.1: Relationship between SI and LB systems for commonly used units.

Property	Symbol	Dimension	SI unit	LB unit
Length	ℓ	L	m	lu
Time	t	T	sec	ts
Mass	m	M	kg	lu^3
Velocity	u	L/T	m/s	lu/ts
Acceleration	a	L/T^2	m/s^2	lu/ts^2
Force	F	ML/T^2	N	lu^4/ts^2
Pressure	P	M/LT^2	Pa	lu^2/ts^2
Shear Stress	τ_w	M/LT^2	Pa	lu^2/ts^2
Density	ρ	M/V^3	kg/m^3	1^*
Kinematic Viscosity	ν	L^2/T	m^2/s	lu^2/ts
Surface Tension	σ	M/T^2	N/m	lu^3/ts^2

* - Density is the sum of the particle populations and is dimensionless in the lattice Boltzmann Method.

Appendix B

Code Details

B.1 Code Blocks

With the program developed in an object-orientated language, some of the strong features provides by object-oriented programming could be used. By grouping like-with-like, the code could be made to be easily managed. To give some idea of the layout and structure of the program, a diagram is provided in Figure B.1. Each block in this diagram was implemented as a separate instance or class.

B.2 Optimisation

In order to increase efficiency and minimise run time, optimisation of the code has been undertaken. A rule of thumb in computer science known as the "90/10" rule is that 90% of the execution time of a program is spent in 10% of the code. The trick is to find which 10% of the code it is that needs optimisation.

To find the most inefficient 10% of code, both serial and parallel profiling tools were used. These are tools that record the runtime and processor usage statistics while the program is executing in order to determine the efficiency of different parts of the code. Using these, the slowest parts of the code could be found and modified leading to a 30% decrease in total runtime.

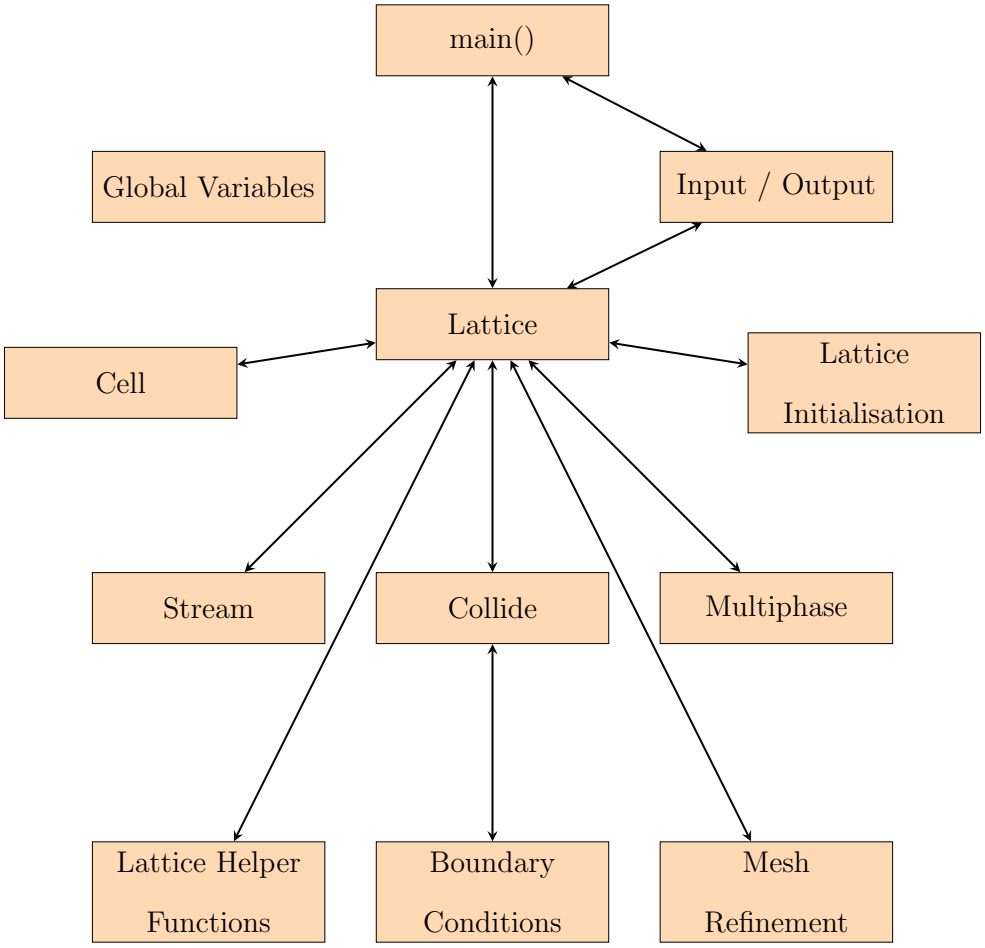

Figure B.1: Diagram of code layout.

Compile time optimisation was also used including Interprocedural Analysis Optimisation (IPA) provided by the Portland Group compiler. This is a feature that re-orders sections of the code to maximise efficiency. Other compile time flags included -O3 and -fastsse in order to get maximum optimisation from the compiler.

main()

The main() function controls the entirety of the program. It creates each of the other classes and control the order of execution of the program including the iteration loop, and when each lattice performs streaming, collision, multiphase interaction, of inter-lattice communication operations.

The outline of the program and main iteration loop can be seen in Section B.3.

Global Variables

Numbers of constants and variables within the program are made global so each class can reference them when required. The global variables class holds each of these allowing values to be changed globally from a single location.

Input / Output

This class both reads input from the user and is used to write results out in two different ways. A minimal output is written to the standard output stream containing data such as iteration number, forces on the walls of the domain, velocity components of the fluid, Reynolds numbers and the fluid mass. A second more detailed output is written directly to a results file and includes all of the other recorded variables in the simulation. The I/O section also writes out backup files that write the contents of the lattice out of memory as a binary file, along with the necessary data to allow it to recreate the lattice and read the data back in. This allows simulations to be stopped and restarted when necessary.

Lattice

The lattice block is where the lattice object is created and acted on, and eventually deleted. It is a parent class for each of the following code blocks which all perform operation on the lattice.

Cell

The cell is the building block of the lattice. Each cell within the lattice is a separate object, each containing it's own dataset including the type of cell (fluid, wall, solid etc), population densities for both the fluid and concentration, velocities of the fluid, and all the other data required. The cell class also includes functions to set, retrieve and modify the data within it.

Stream

The stream block controls the streaming step of the lattice Boltzmann method. As such, it communicates with the surrounding nodes either local to the current processor, or using inter-processor communication to pass the population density data to other compute nodes.

Collide

The collide block controls the collision step including the computation of the equilibrium density functions. If the collision includes a wall, the collide class calls the relevant boundary condition.

Boundary Conditions

The boundary condition code block implements the boundary conditions used in the simulation and also calculates the forces acting on the walls.

Lattice Initialisation

The lattice initialisation block initialises the lattice, and sets up the domain as instructed by the input files. This includes setting the cells to the correct type, and initialising velocities and concentrations throughout the domain.

Mesh Refinement

When using mesh refinement multiple lattices are created. The mesh refinement handles the transfer of data between these lattices.

The main sources used for the mesh refinement method were Rohde [109] and Yu [147].

Multiphase

The multiphase block implements all the functions required to simulate multiphase flow. It calculates the interaction forces between fluids, and controls the fluid-solid interactions.

The main source used for the multiphase method was Huang, Shu & Chew [65].

Helper Functions

The helper functions block holds a host of functions that are used to compute data within the program. This includes functions for finding average velocities of the lattice, calculating global forces, as well as a number of functions to assist in debugging.

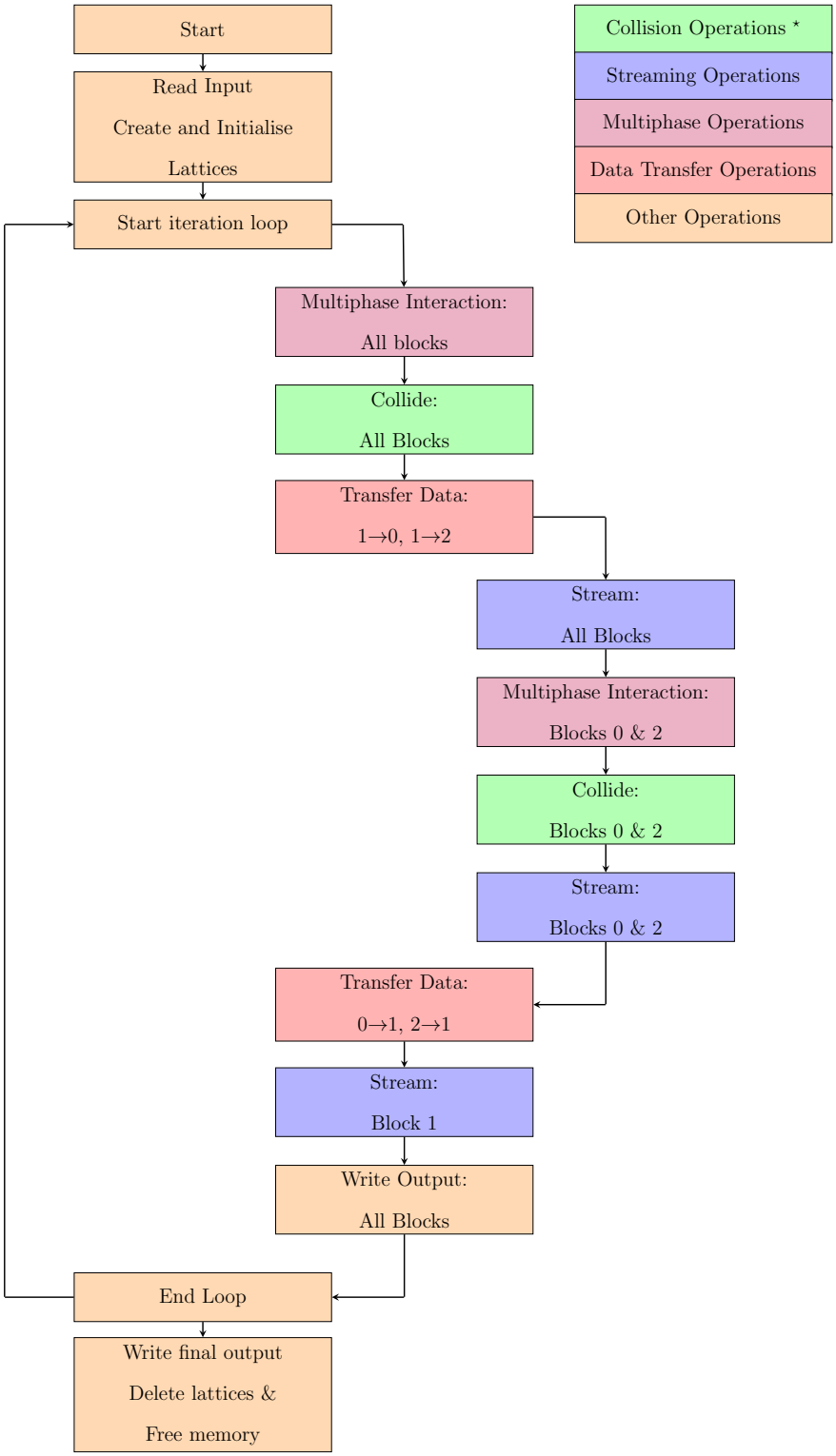

Figure B.2: Code Operation Flowchart

* Collision operations include calculation of f^{eq} and application of boundary conditions if needed.

B.3 Code Operation Example

Figure B.2 shows the program structure and order of execution for the simulation as used for the super hydrophobic surface tests. As can be seen in Figure B.3, the domain features three lattice blocks with those near the walls refined by a factor of two, and also utilises a multiphase model. Chapter 4 gives the details of the equations solved in each of the operations.

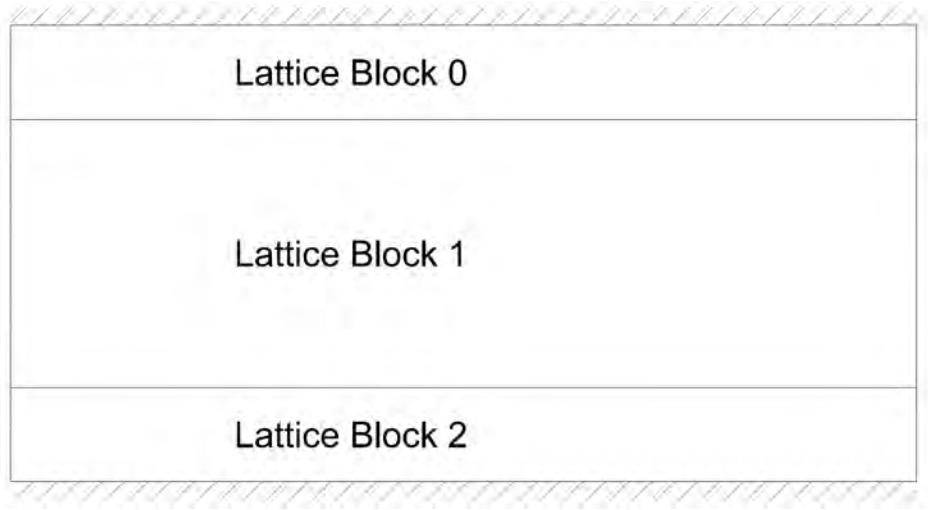

Figure B.3: Domain for code example.

As the code is over 12,500 lines long it has not been included in this document; however, for additional details or a copy of the source code please contact Assoc. Prof. Tracie Barber at *t.barber at unsw.edu.au*

B.4 Hardware

The simulations performed in this work were run on two separate clusters within the University of New South Wales. The first cluster is named *Leonardi* and is composed of 56 HP ProLiant BL685c G7 full-height blade server nodes. Of these, there are 5 different configurations that the blade servers have, ranging from 48 core nodes with 96 GB of memory up to 64 core nodes with 512 GB of memory. *Leonardi* is the main research cluster for the Faculty of Engineering and id capable of 31.6 TFLOPs.

The second cluster utilised is named *Trentino* and features 16 Dell PowerEdge R815 servers. Each of these have four AMD Opteron 6272 2.1GHz 16-core 1600MHz processors giving 64 usable cores per server. They are also equipped with 128GB of 1600 MHz dual-rank RDIMM memory. *Trentino* is a research cluster owned and operated by the School of Mechanical & Manufacturing Engineering and is capable of 17.3 TFLOPs.

Additional information about these clusters can be found at:

Leonardi:
http://leonardi.unsw.wikispaces.net

Trentino:
http://trentino.unsw.wikispaces.net

Appendix C

Equation Derivision

C.1 BGK Collision Operator

Taking Ω_α as the collision operator and expanding about an equilibrium value f^{eq} gives

$$\Omega_i(f) = \Omega_i(f^{eq}) + \frac{\partial \Omega_i(f^{eq})}{\partial f_\beta}\left(f_\beta - f_\beta^{eq}\right) + O\left[\left(f_\beta - f_\beta^{eq}\right)^2\right] \tag{C.1}$$

In the limit of $f \longrightarrow f^{eq}$ it can be seen that $\Omega_i(f^{eq}) \approx 0$. Taking this relation and by neglecting the higher order terms, Equation C.1 can be simplified to

$$\Omega_i(f) \approx \frac{\partial \Omega_i(f^{eq})}{\partial f_\beta}\left(f_\beta - f_\beta^{eq}\right) \tag{C.2}$$

Assuming that the distribution relaxes towards the equilibrium at the rate τ the partial derivative term can be replaced with

$$\frac{\partial \Omega_i(f^{eq})}{\partial f_\beta} = -\frac{1}{\tau}\delta_{\alpha\beta} \tag{C.3}$$

where $\delta_{\alpha\beta}$ is the Kronecker delta. This means Equation C.2 can be rewritten as

$$\Omega_i(f) = -\frac{1}{\tau}\delta_{\alpha\beta}\left(f_\beta - f_\beta^{eq}\right) \tag{C.4}$$

$$= \frac{1}{\tau}\left(f_\alpha^{eq} - f_\alpha\right) \tag{C.5}$$

which is the BGK collision operator

C.2 Grid Refinement

As both the Reynolds numbers and the velocities at the intersection of the coarse (c) and fine (f) grids need to be equal, and recalling that n is the refinement factor between the grids, it can be seen that:

$$Re_c = Re_f \tag{C.6}$$

$$\frac{u_c \Delta x_c}{\nu_c} = \frac{u_f \Delta x_f}{\nu_f} \tag{C.7}$$

$$\text{As } u_c = u_f \text{ and } \Delta x_c = n\Delta x_f \tag{C.8}$$

$$\nu_c = \frac{1}{n}\nu_f \tag{C.9}$$

Then

$$\nu_c = c_s(\tau_c - \frac{1}{2}) \tag{C.10}$$

$$\tau_c = \frac{1}{c_s}\nu_c + \frac{1}{2} \tag{C.11}$$

$$\tau_c = \frac{1}{c_s}\frac{1}{n}\nu_f + \frac{1}{2} \tag{C.12}$$

$$\tau_c = \frac{1}{c_s}\frac{1}{n}c_s(\tau_f - \frac{1}{2}) + \frac{1}{2} \tag{C.13}$$

$$\tau_c = (\tau_f - \frac{1}{2})/n + \frac{1}{2} \tag{C.14}$$

C.3 Shear Reynolds Number / Driving Force

Beginning with $Re_\tau = \frac{u^\star \delta}{\nu}$ and as $u^\star = \sqrt{\frac{\tau_w}{\rho}}$

$$Re_\tau = \frac{\sqrt{\frac{\tau_w}{\rho}}\delta}{\nu} \tag{C.15}$$

$$\frac{Re_\tau \nu}{\delta} = \sqrt{\frac{\tau_w}{\rho}} \tag{C.16}$$

$$\left(\frac{Re_\tau \nu}{\delta}\right)^2 = \frac{\tau_w}{\rho} \tag{C.17}$$

And as $\tau_w = F\delta$

$$\left(\frac{Re_\tau \nu}{\delta}\right)^2 = \frac{F\delta}{\rho} \tag{C.18}$$

$$F = \frac{\rho}{\delta}\left(\frac{Re_\tau \nu}{\delta}\right)^2 \tag{C.19}$$

$$F = \frac{\rho \left(Re_\tau \nu\right)^2}{\delta^3} \tag{C.20}$$

Appendix D

Experimental Equipment Drawings

This appendix contains some of the detail drawings used for construction of the experimental rig.

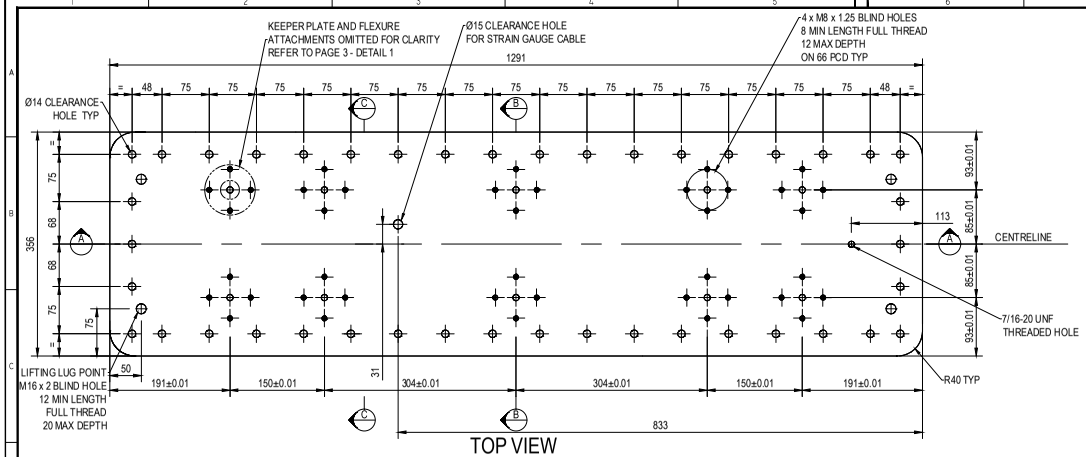

TOP VIEW

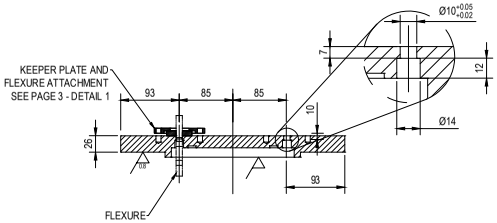

SECTION B-B

SCALE 1:5

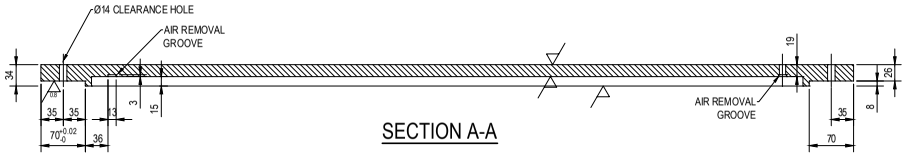

SECTION A-A

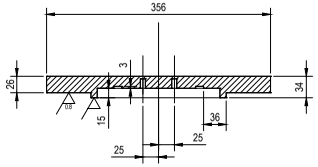

SECTION C-C

SCALE 1:5

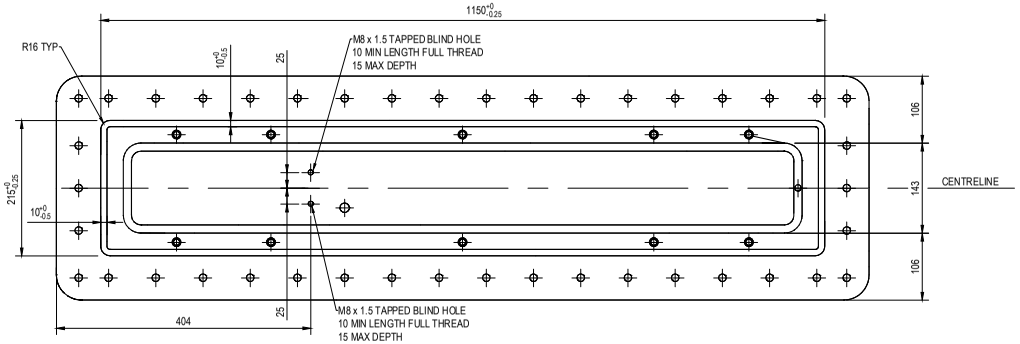

BOTTOM VIEW

NOTES:

1. MATERIAL = 304 STAINLESS STEEL
2. GENERAL TOLERANCE ±0.5MM UNLESS OTHERWISE SPECIFIED
3. 3.2 ALL OVER UNLESS OTHERWISE SPECIFIED

REV	DESCRIPTION	DATE	DRN
C	MODIFIED FOR 34mm PLATE. CORRECTED PCD VALUE. CHANGED AIR GROOVE. ADDED LIFTING LUG HOLES, EXPANDED FLEXURE CLEARANCE HOLES	21.03.11	AKB
B	UPDATED BRACKET HOLES. ADDED TOLERANCES. MODIFIED AIR GROOVE	31.05.10	AKB

TITLE: BOUNDARY LAYER RIG TOP PLATE DETAILS

PROJECT: SHS TURBULENT FLOW TEST

DRAWING No	REVISION	SHEET No	SCALE
2010-002	C	1 OF 4	1:5

DRAWN	DATE	APPROVED
AKB	12.05.2010	

SHEET SIZE: A2

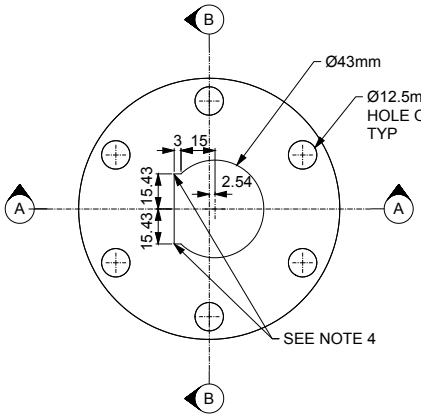

Top View

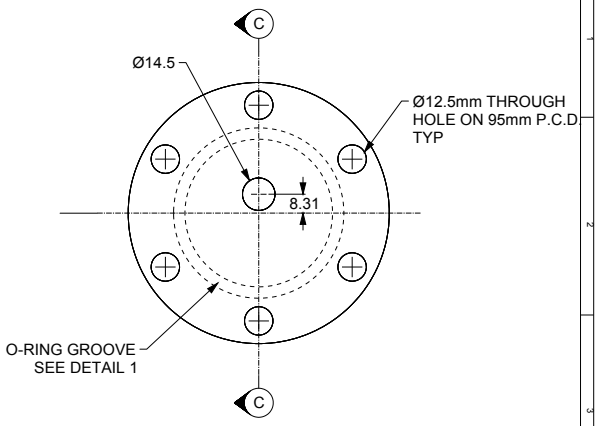

Top View

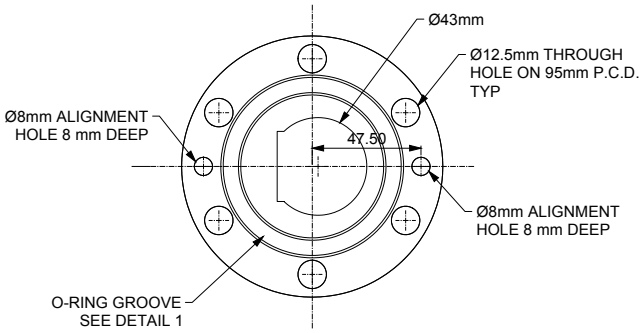

BOTTOM VIEW

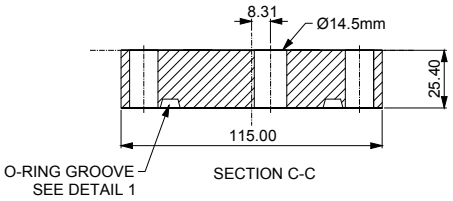

SECTION C-C

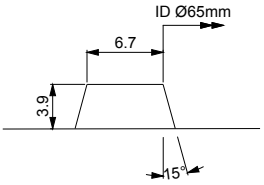

DETAIL 1 - O-RING GROOVE
SCALE 5:1

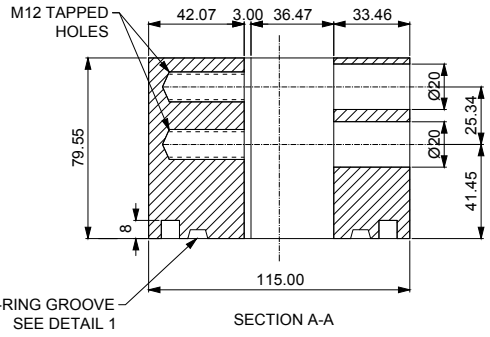

SECTION A-A

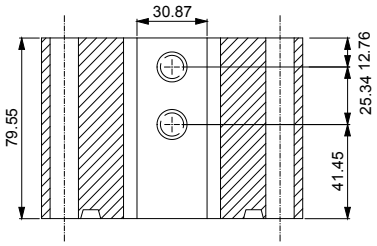

SECTION B-B

NOTES:

1. ALL DIMENSIONS IN MILLIMETRES
2. ALL TOLERANCES TO BE WITHIN 0.01 mm
3. MATERIAL TO BE 304 STAINLESS STEEL
4. ENSURE NO RADIUS ON THIS INTERNAL CORNER

BAGLIN MARINE DESIGNS

TITLE: FLAT PLATE EXPERIMENTAL RIG			
PROJECT: SHS TURBULENT FLOW TEST			
DRAWING No: 2014-001	REVISION: A	SHEET No: 1 OF 1	SCALE: 1:1
DRAWN: AKB	DATE: 14.JAN.14	APPROVED:	

SHEET SIZE: A1

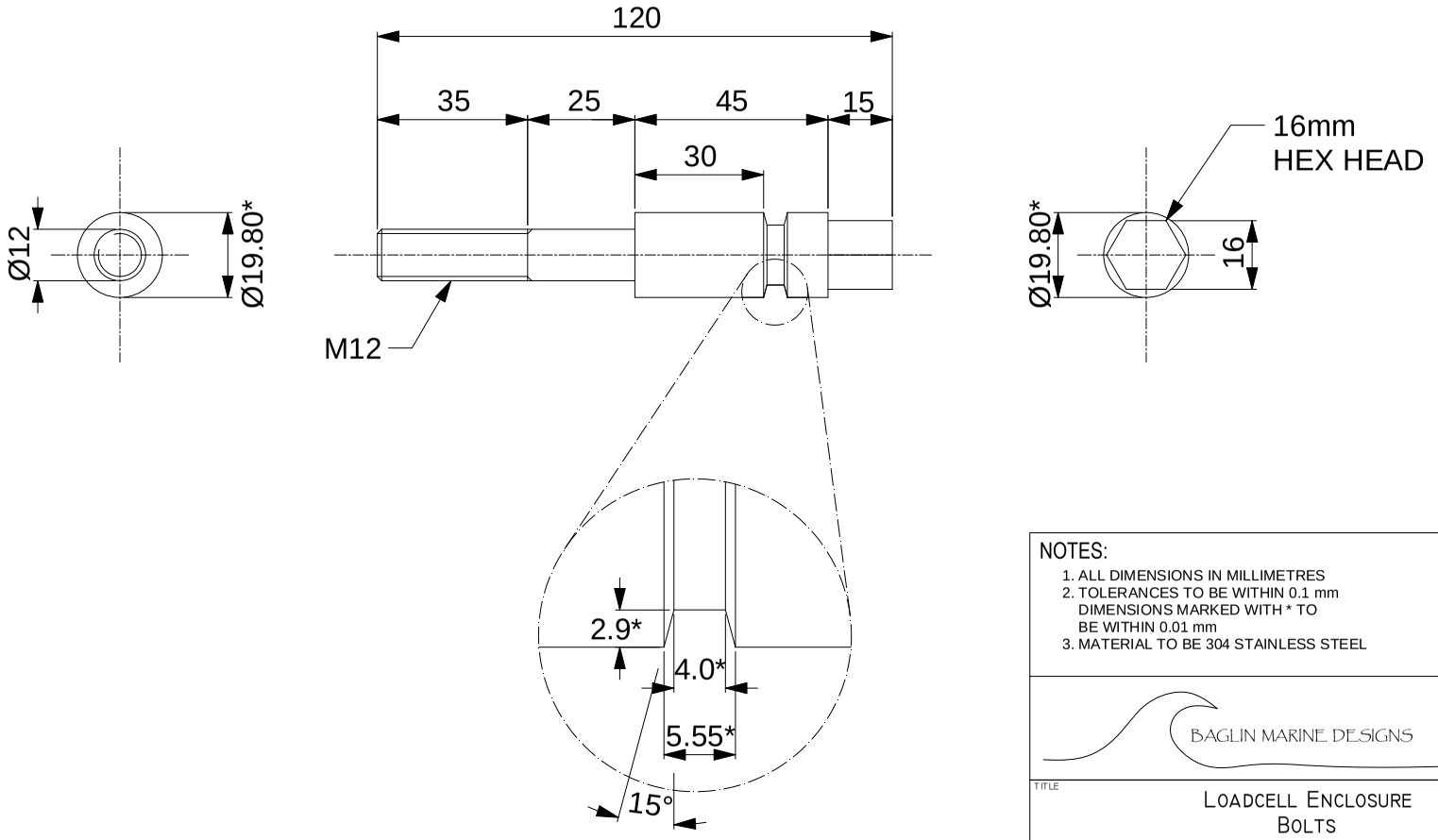

O-Ring Groove Detail

NOTES:

1. ALL DIMENSIONS IN MILLIMETRES
2. TOLERANCES TO BE WITHIN 0.1 mm
   DIMENSIONS MARKED WITH * TO
   BE WITHIN 0.01 mm
3. MATERIAL TO BE 304 STAINLESS STEEL

BAGLIN MARINE DESIGNS

TITLE: LOADCELL ENCLOSURE BOLTS			
PROJECT: SHS TURBULENT FLOW TEST			
DRAWING No: 2014-002	REVISION: A	SHEET No: 1 OF 1	SCALE: 1:1
DRAWN: AKB	DATE: 14.MAR.14	APPROVED:	

SHEET SIZE: A3

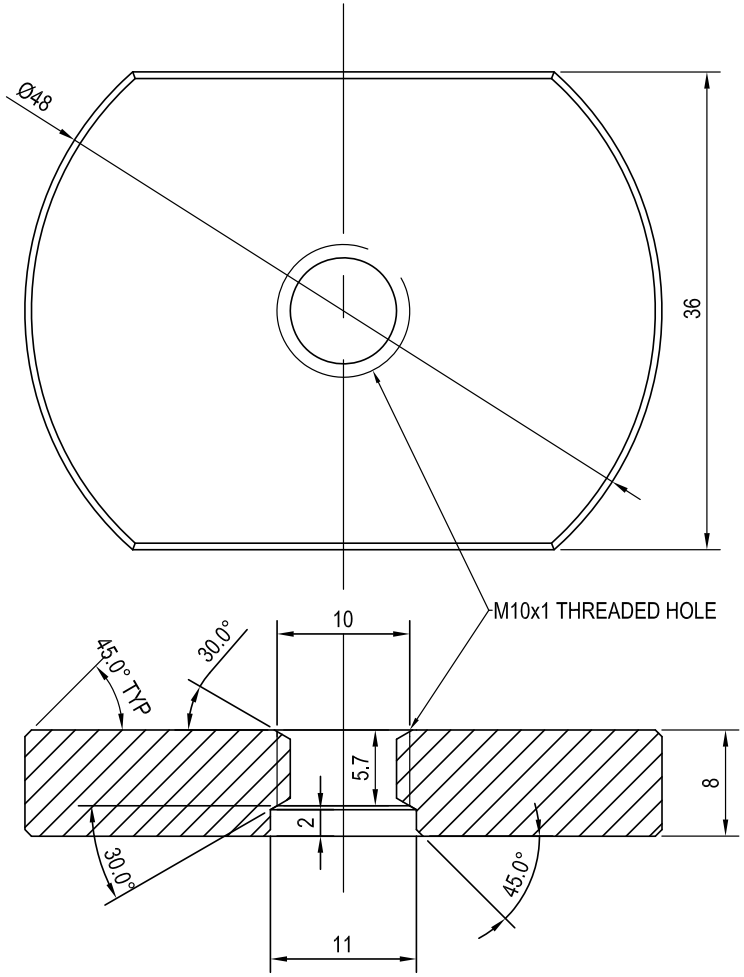

CONSOLE SIDE FLEXURE ATTACHMENT POINTS

6 REQUIRED
SCALE 2:1

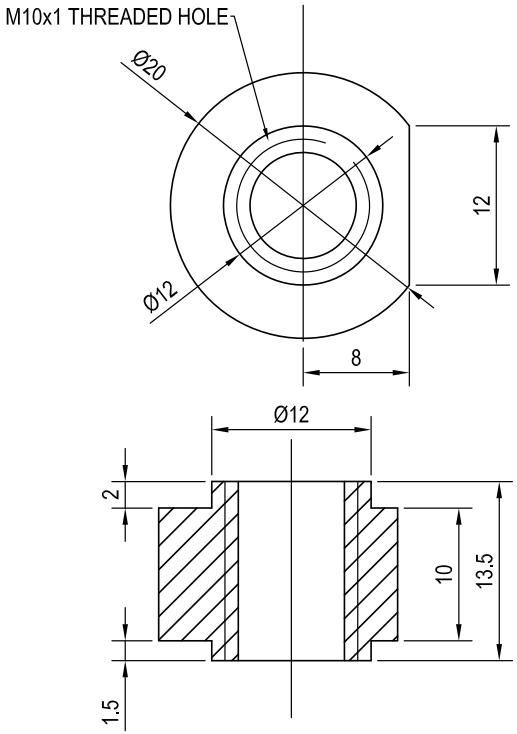

MEASUREMENT SIDE FLEXURE ATTACHMENT POINTS

10 REQUIRED
SCALE 2:1

SHS TURBULENT FLOW TEST
DWG: 2012-001
DRWN BY: ANDREW BAGLIN
DATE: 22/03/2012
SCALE: AS SHOWN

MATERIAL: 304 SS
ALL DIMENSIONS
IN MILLIMETRES

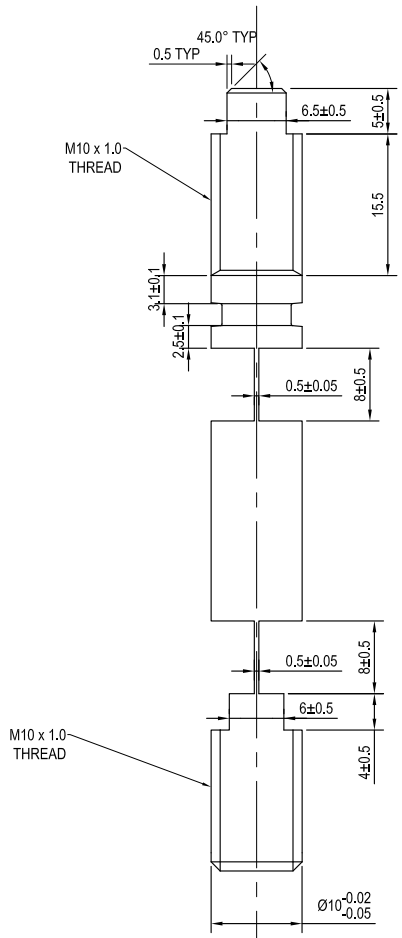

SIDE VIEW

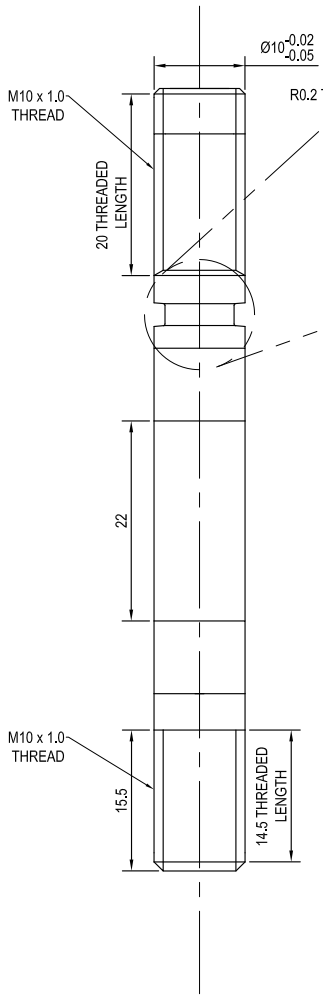

FRONT VIEW

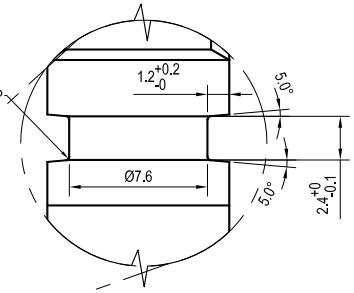

O-RING GROOVE DETAIL

SCALE 4:1

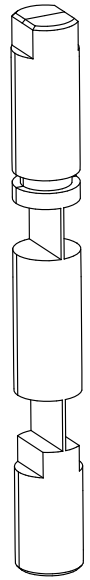

ISOMETRIC VIEW

NOTES:

1. ALL DIMENSIONS IN MILLIMETRES
2. MATERIAL = 304 STAINLESS STEEL
3. M10x1 IS METRIC FINE THREAD
4. ENSURE THREAD SQUARENESS PERPENDICULAR TO AXIS OF ROD

TITLE: FLEXURE DETAILS			
PROJECT: SHS TURBULENT FLOW TEST			
DRAWING No: 2010-002	REVISION: A	SHEET No: 1 OF 1	SCALE: 2:1
DRAWN: AKB	DATE: 2.05.2012	APPROVED:	

SHEET SIZE: A3